Universitat de València
Institut de Física Corpuscular
Departament de Física Teòrica

Programa de Doctorat en Física

PION PHOTO- AND ELECTROPRODUCTION ON NUCLEONS IN RELATIVISTIC CHIRAL PERTURBATION THEORY

Doctoral Thesis

Author:
Gustavo Hazel Guerrero Navarro

Supervisor:
Dr. Manuel José Vicente Vacas

September, 2022

Dr. Manuel José Vicente Vacas, Profesor Titular de Física Teórica de la Universidad de Valencia,

> CERTIFICA: Que la presente memoria *PION PHOTO- AND ELECTROPRODUCTION ON NUCLEONS IN RELATIVISTIC CHIRAL PERTURBATION THEORY* ha sido realizada bajo mi dirección en el Departament de Física Teòrica de la Universitat de València por Gustavo Hazel Guerrero Navarro como tesis para obtener el grado de Doctor en Física.

Y para que así conste presenta la referida Memoria, firmando el presente certificado.

Fdo: Dr. Manuel José Vicente Vacas

For Anna and Itzel

Contents

1 Introduction **1**

2 Theoretical framework: Chiral Perturbation Theory **5**
2.1 QCD and its chiral symmetry 5
2.1.1 The chiral symmetry of the QCD Lagrangian 6
2.1.2 Chiral Symmetry Breaking 8
2.1.3 A Low energy Effective Field Theory Approach 10
2.2 Chiral Perturbation Theory: The low energy effective theory of QCD . 10
2.2.1 Chiral Lagrangian for pions 11
Lowest Order π Lagrangian 11
Couplings to external gauge field sources 13
Higher orders, loops and renormalization 15
Power counting rule for the amplitudes 17
2.2.2 Interaction Lagrangian with nucleons 17
Power Counting Breaking terms and the EOMS renormalization 19
2.2.3 Interaction Lagrangian for the spin-3/2 $\Delta(1232)$ resonance . . . 21
The power counting scheme with Δs 22

3 Formalism for pion EM production on nucleons **25**
3.1 Pion electroproduction on nucleons 25
3.1.1 Matrix element and kinematics 25
3.1.2 Amplitude parametrization 28
3.1.3 Gauge invariant amplitude 30
3.1.4 Observables 32
3.2 Pion photoproduction on nucleons 37
3.2.1 Matrix element and kinematics 38
3.2.2 Amplitude parametrization and gauge invariant amplitude . . . 40
3.2.3 Observables 41
3.3 Isospin amplitudes for pion electromagnetic production 43

4 Amplitudes for pion EM production **47**
4.1 Generation of Feynman graphs 47
4.2 Amplitudes 50
4.2.1 Tree level amplitudes 50
$\mathcal{O}(p^1)$ amplitude 50
$\mathcal{O}(p^2)$ amplitude 52
$\mathcal{O}(p^3)$ amplitude, tree diagrams 53
$\mathcal{O}(p^{5/2})$ amplitude from the Δ mechanisms 55
4.2.2 One-loop level diagrams at $\mathcal{O}(p^3)$ 57
Example: detailed calculation for the (g7) diagram 60
4.2.3 Renormalization 65
4.2.4 EOMS PCBT restoration scheme 66
4.2.5 WFR for the external legs 70

4.3 Further considerations for the $\mathcal{O}(p^3)$ amplitude 72
4.3.1 Diagrams with mass insertions in the propagators 73
4.3.2 Evaluation of the amplitude and the relevant LECs at $\mathcal{O}(p^3)$. 75
4.3.3 Evaluation of the lowest order parameters 77
4.3.4 Relevant LECs at $\mathcal{O}(p^3)$ 80
4.4 Input parameters: LECs from other processes and physical quantities . 86

5 Determination of the low-energy-constants and results 89
5.1 Experimental database for $\gamma^{(*)} + N \longrightarrow \pi + N'$ observables 89
Electroproduction data 90
Photoproduction data 90
5.2 Fitting procedure and error estimation 91
5.2.1 Minimization of the χ^2 function 91
5.2.2 Error estimation for the fitted LECs and the observables 92
5.3 Fit with and without Δ contribution 95
5.3.1 Low-Energy-Constants 95
5.3.2 Contribution of the Δ-resonance 96
5.4 Fit analysis with error propagation from the known LECs 98
5.5 Results for the physical observables 101
5.5.1 Electroproduction observables 101
$\gamma^* + p \longrightarrow \pi^0 + p$ channel 101
$\gamma^* + p \rightarrow \pi^+ + n$ channel 105
5.5.2 Photoproduction observables 106
$\gamma + p \longrightarrow \pi^0 + p$ channel 106
$\gamma + p \longrightarrow \pi^+ + n$ channel 113
$\gamma + n \longrightarrow \pi^- + p$ channel 115

6 Near threshold neutral pion photoproduction off the ^{12}C nucleus 117
6.1 Introduction 117
6.2 Formalism for pion photoproduction off nuclei 119
6.2.1 Matrix elements and elementary amplitudes 120
6.2.2 Calculation of the PWIA cross sections 123
6.2.3 DWIA cross section 125
6.3 Numerical results and comments 126
6.4 Summary and Outlook 128

7 Conclusions 131

8 Resumen en español 137
8.1 Motivación 137
8.2 Metodología 138
8.3 Resultados 141

A Feynman diagram amplitudes 147
Feynman rules for propagators 150
A.1 Vertex Feynman-rules 151
A.1.1 $\mathcal{O}(p^1)$ vertices 151
A.1.2 $\mathcal{O}(p^2)$ vertices 155
A.1.3 $\mathcal{O}(p^3)$ vertices 157
A.1.4 $\mathcal{O}(p^4)$ vertices 159
A.2 Tree level amplitudes 160
A.2.1 Electroproduction 160

$\mathcal{O}(p^1)$ amplitudes 160
$\mathcal{O}(p^2)$ amplitudes 160
$\mathcal{O}(p^3)$ amplitudes 161
$\mathcal{O}(p^{5/2})$ amplitudes 162
A.2.2 Photoproduction 163
$\mathcal{O}(p^1)$ amplitudes 163
$\mathcal{O}(p^2)$ amplitudes 163
$\mathcal{O}(p^3)$ amplitudes 164
$\mathcal{O}(p^{5/2})$ amplitudes 164
A.3 One-loop level $\mathcal{O}(p^3)$ amplitudes 165

B Power counting breaking terms for loop amplitudes 175
B.1 PCBT for pion electroproduction on nucleons 175
B.2 PCBT for pion photoproduction on nucleons 178

C Chiral expansions for physical quantities 181
C.1 Nucleon mass m_N 181
C.2 Pion mass M_π 181
C.3 Axial coupling constant g_A 181
C.4 Pion decay constant F_π 182

D Multipole decomposition 183

E Nuclear form factors 185

List of Figures 187

List of Tables 191

Acknowledgements 193

Bibliography 195

Chapter 1

Introduction

Since the discovery in the early 1950s that pions could be produced by photon beams on nuclei [1], electromagnetic (EM) probes on nucleons have been a very important source of information in the study of hadron interactions, being also crucial in the research of baryonic resonances and their properties. Moreover, hadron interactions are of great interest in the understanding of the fundamental strong interaction. They are described by quantum chromodynamics (QCD), a local non-abelian gauge theory developed in the 1970s in terms of the basic constituents of hadrons, quarks and gluons.

In the study of pion production processes, many theoretical and experimental efforts have been addressed to the intermediate energy region going from the threshold to the region where baryon resonances play an important role. In this work, I focus on the near threshold pion electromagnetic production on nucleons. In detail, I study the effect of the $\Delta(1232)$ resonance for the different charge channels in photo- and electroproduction of pions. I calculate the relevant cross sections, their angular and energy dependence in order to compare with current data. Subsequently, the results obtained from these studies are applied to a sample nuclear reaction, namely the pion photoproduction on the ^{12}C nucleus, where the effect of the Δ can be handled in terms of the elementary amplitude (pion photoproduction on nucleons).

Although QCD successfully describes strong interacting processes at high energies, it cannot be directly applied to the low energy region of hadron processes. This is due to the energy dependence of the strong coupling, α_S. At higher energies, its size is small and QCD is treated as a perturbative quantum field theory (QFT). This is what we know as the *asymptotic freedom* of quark fields. On the other hand, the running α_S is considerably large at low energies and QCD is non-perturbative. This makes the typical perturbative tools of QFT practically useless. Thus, the application of QCD divides into different energy regions, typically separated at the scale $\Lambda_\chi = 1$ GeV. This scale sets the lower limit where the perturbative series of QCD breaks down.

In fact, the energies of the hadron processes investigated here are far below the scale Λ_χ, and they belong to the non-perturbative regime of QCD. The scale Λ_χ can also be understood as the upper limit where quarks interact strongly enough to arrange in confined states, *i.e.* to form hadrons as effective degrees of freedom. We consider, in consequence, an effective field theory (EFT) approach that describes the low energy behaviour of QCD but in terms of interacting hadron fields.

First theoretical attempts to address electromagnetic low energy hadronic processes were made using some phenomenological models that required only gauge and Lorentz invariance, as well as current algebra and partial conservation of the axial current (PCAC). However, these models lacked a systematic way to describe the different processes and failed to reproduce neutral pion photoproduction at some low energy regions.

In this work, we use Chiral Perturbation Theory (ChPT), an EFT that has been developed over the last 40 years. This is a powerful tool for describing the low-energy dynamics of strong processes in terms of effective hadron states. ChPT was formulated as a systematic EFT that fulfills chiral symmetry, its breaking, and all other fundamental properties of QCD. This EFT is aimed to be applied in the non-perturbative energy region, sufficiently lower than 1 GeV. Moreover, ChPT has been shown to reproduce satisfactorily the experimental data for the charged and neutral pion production on nucleons very close to threshold.

The ChPT Lagrangian is written in terms of baryon and meson fields as relevant degrees of freedom, instead of quarks and gluons. Here, we will focus on the lightest baryons and pseudoscalar mesons in the isospin limit: pions, nucleons and the Δ resonances that follow an approximate isospin SU(2) symmetry. Additionally, from the point of view of QCD, those baryons and mesons are composed by the u and d quarks accommodated in a SU(2) flavor symmetry. The quarks fields can be decomposed in left and right components q_L and q_R and in the relativistic limit of vanishing quark masses those components are decoupled in the QCD Lagrangian leading to a global chiral symmetry.

However, the phenomenological observation that the lightest mesons have mass suggests that the chiral symmetry is broken. The masses of the baryon and meson spectra are interpreted as a consequence of the quark masses producing an explicit chiral symmetry breaking. In addition, given that the light meson masses are small compared to the scale Λ_χ, the corresponding pseudoscalar mesons are associated to the Goldstone bosons of a spontaneous symmetry breaking (SSB). Also in the baryon spectrum, the spontaneous symmetry breaking is confirmed by the absence of baryon partners of negative parity with the same masses as the positive parity ones.

Spontaneous and explicit symmetry breaking are basic properties in building the effective Lagrangian of ChPT.
As in any proper effective field theory, the ChPT Lagrangian is ordered according to an expansion in terms of powers of small parameters. In this case, the expansion parameters are given by the small momenta, p/Λ_χ, and the lightest pseudo Goldstone masses, M_π/Λ_χ. This is a suitable approximation method for energies well below the $\Lambda_\chi = 1$ GeV, instead of the running coupling α_S. Also, the relevant degrees of freedom in the small momenta expansion (long distances) are those of asymptotically observed hadrons, since they are the confined states produced by the strong interaction.

Although the idea of an approximation in a series of expansion parameters seems inexact since we cannot calculate infinite terms, the convergence of the series is under control and does not necessarily mean a lack of accuracy. The quality of the convergence depends on the small size of the Goldstone boson masses, which in the flavor SU(2) case is considered a good assumption since $M_\pi << 1$ GeV. Hence, the ChPT approach is accurate enough for the SU(2) multiplet of pseudoscalar pions at low energy. The inclusion of nucleon fields in ChPT as degrees of freedom is also possible at the small momenta limit, but this introduces a new scale, the nucleon mass, which is of similar size to the chiral breaking scale, $m \sim \Lambda_\chi$.

Within the ChPT frame, loop amplitudes can also contribute to amplitude calculations at a given chiral order. Loop amplitudes contain ultraviolet (UV) divergences that can be renormalized with the inclusion of higher order lagrangian counterterms. UV divergences in ChPT, thus, can be renormalized systematically order by order. Furthermore, each of the terms in the infinite series of the ChPT Lagrangian is proportional to a low-energy-constant (LEC). These LECs, lacking a direct extraction

from the low-energy QCD dynamics, are fixed by fitting to a data sample. Then, the resulting Lagrangian can be directly used for further predictions.

However, a technical difficulty arises when loop calculations involving baryons are implemented in ChPT. The inclusion of loops with baryons is known to spoil the chiral power counting in terms of p and M_π for a given amplitude. In particular, nucleon loops can give large contributions of the type m_N/Λ_χ given by the similar size of the nucleon mass to the scale Λ_χ. This conflict was resolved first in the heavy-baryon ChPT approach (HBChPT) at the expense of losing Lorentz invariance, while the original covariant ChPT was abandoned. Then HBChPT became standard in analyses of hadron processes like pion electro- and photoproduction.
While in the non-relativistic HB approach the power counting of nucleon loops was restored , the fact that relativistic corrections may be large in some processes questioned the applicability of this framework. The interest in relativistic methods was renewed and eventually, the conciliation of a consistent power counting with baryon-loops was possible in the original relativistic formulation of ChPT with novel regularization schemes, namely the infrared (IR) [2] and the extended on-mass-shell (EOMS) [3, 4] schemes.
Both solutions, IR and EOMS, extract the conflicting power counting breaking terms (PCBT) from one-loop contributions and reabsorb them into the LECs in addition to the UV renormalization terms. The main difference between the EOMS and the IR schemes is that in EOMS one subtracts exclusively the conflicting terms at lower orders while in the IR renormalization the subtraction also includes higher order terms.

In this thesis, we implement the EOMS renormalization in our calculations. The reasons are twofold: EOMS usually converges faster than HB and (IR)ChPT. As a consequence, this framework has become popular and has been successfully used to describe many observables involving baryons [5–22]. On the other hand, both HB and IRChPT had shown good agreement to EM pion production off nucleons only at very low energies. Extensions to higher chiral orders in IRChPT showed a better agreement for these processes. However, as in the case of HBChPT, the agreement was acceptable only for a still limited range of energies [20] compared to the EOMS approach [21]. Furthermore, the situation became technically complicated due to the large number of still unknown LECs involved at those higher orders.

Besides, recent studies have shown that, in some cases, a simple way to improve the convergence of the chiral series in relativistic ChPT is to include the spin-3/2 resonance Δ as an additional degree of freedom. In fact, the quality and convergence of a given amplitude calculation at higher energies depends on the degrees of freedom taken into account. Moreover, it is well known that additionally to the pion and nucleon fields, the contribution of the $\Delta(1232)$ plays an important role in the neutral pion production off nucleons process due to its proximity to the πN threshold.
The $\Delta(1232)$ resonance, which couples strongly to nucleon and pion, can be easily incorporated in our framework. That means that Δ will be propagated explicitly as an intermediate state in the processes studied here. This particular degree of freedom implies an additional expansion parameter in the chiral series given by the difference between the nucleon and the Δ masses, $\delta = m_\Delta - m_N \approx 300$ MeV. This parameter induces an extension to the power counting rules of the chiral series with nucleon and pion degrees of freedom.

The purpose here is to make a comprehensive analysis within the aforementioned

framework of the pion photo- and electroproduction off nucleons and study the contribution of the $\Delta(1232)$ resonance on them. The neutral pion photoproduction channel has already been investigated in EOMS covariant ChPT with Δ contributions [21,22]. Here, the previous study is extended by adding the photoproduction of charged pions and including the pion electroproduction process for all the neutral and charged pion channels. This allows for the exploration of more interaction vertices with both real and virtual photons and therefore to examine some additional pieces of the chiral Lagrangian.
In this manner, a more complete and better determination of the relevant LECs can be made by comparing the theoretical results with a more complete set of experimental data. Furthermore, some recent data has been incorporated for photoproduction of neutral [23] and charged pions [24], and explicit isospin breaking in the loop calculations has been considered. This latter point considerably improves the agreement with data at low energies.
Finally, a better determination of a more complete set of LECs could be used for predictions as in weak pion production and many other processes.
In particular, the examination of the vector couplings of the nucleons with both real and virtual photons might reduce the large uncertainties that currently hinder the efforts to provide a theoretically well founded prediction of the neutrino induced pion production [25, 26], a very important process in many of the neutrino experiments.

The present thesis includes three main studies: pion photo- and electroproduction on nucleons, as well as pion photoproduction on the ^{12}C nucleus. They are developed through the following chapters: In Chapter 2, the basics of hadron interactions in the relativistic ChPT framework are introduced to be used in the amplitude calculations. In Chapter 3, the general formalism for the pion EM production on nucleons is presented, which includes the parametrizations of the matrix elements and their general properties. Also, the theoretical expressions to calculate the relevant observables to be compared with experimental data are shown. Chapter 4 is dedicated to the tree and loop amplitude calculations within the ChPT approach and the procedure followed in the limit of SU(2) flavor symmetry. Then, the results obtained from the fitting procedure of relevant LECs with data are shown in Chapter 5. Also, the comparison of theoretical observables in ChPT with data is presented here. In this work, we compare two models: one with the inclusion of $\Delta(1232)$ resonance and the other in the Δ-less case. I show the results obtained for the charged and neutral channels of pion photo-and electroproduction on nucleons. Then, Chapter 6 shows a sample study for the neutral pion photo production on nuclei of ^{12}C as an application of the studies from the previous chapters. Finally, I discuss the final results and conclusions in Chapter 7.

Chapter 2

Theoretical framework: Chiral Perturbation Theory

In this chapter, I briefly present the theoretical formalism and methods on which the work throughout this thesis is based. In particular, at the low energies considered, the process of pion production induced by electromagnetic sources on nucleons will be investigated using Chiral Perturbation Theory, an effective field theory based on the underlying symmetry properties from QCD and appropriate for that energy region. Good reviews of ChPT and very detailed presentations can be found in the references [27–31].
Due to the large size of the strong coupling at low energies, it remains a challenge to calculate with perturbative methods and understand the dynamics of the hadrons directly from the QCD Lagrangian in terms of quarks, antiquarks and gluons. This implies that an expansion on the coupling constant for the strong interactions is not viable. Instead, an EFT, such as ChPT, represents the best alternative approach.
In section 2.1, I introduce some QCD properties. I review the chiral symmetry and its spontaneous breaking as a preliminary step for building the effective field theory of QCD in terms of hadronic degrees of freedom. Then, in section 2.2, I present the ChPT Lagrangian, with the inclusion of external electromagnetic fields. It has been formulated systematically in a perturbative expansion of Lagrangian terms organized in powers of small external momenta and light pseudoscalar meson masses. Here, I cover only the Lagrangian terms that describe the interactions between the baryons and mesons involved in the pion production on nucleons. These terms have been formulated for the case of SU(2) flavor fields: pseudoscalar pions, nucleons and $\Delta(1232)$ resonances. Along this section, I outline the power counting rules for the amplitude calculations with ChPT. The power counting problem for diagrams with loops including nucleons will be discussed here, as well as the δ-counting rules when including the $\Delta(1232)$. Additionally, I treat the renormalization methods used in this work.

2.1 QCD and its chiral symmetry

Quantum Chromodynamics (QCD) is believed to be the theory of strong interactions, the gauge field theory that describes the color interactions of quarks and gluons. QCD is based on the color SU(3) local gauge symmetry that leads to the strong interactions through the exchange of colored-gluons. Additionally, there are several symmetries. Among them there are the discrete global symmetries related to space-time coordinates transformations such as C, P and T. Then, we can also find other continuous global symmetries such as the chiral symmetry, related to the invariance under $U(n_f)_L \times U(n_f)_R$ transformations of the left- and right components of the quark fields, for n_f flavors. Chiral symmetry, as I will detail below, plays a central role in the properties of hadron processes driven by the strong interaction, for example the pion

production processes treated in this work. Besides this, the global chiral symmetry is only approximate in the QCD Lagrangian. In fact, it is broken by the quark mass terms. In the particular case of light quarks, this symmetry is softly broken, and thus, one can make many model-independent predictions for physical processes.

2.1.1 The chiral symmetry of the QCD Lagrangian

Let us consider n_f flavors of quarks, collected in a vector field in flavor space: $q^T = (u, d, \dots)$. Color indices are omitted for simplicity. The corresponding SU(3) gauge invariant QCD Lagrangian can be compactly written in the form:

$$\mathcal{L}_{\text{QCD}} = \underbrace{\bar{q}\left[i\not{D} - \mathscr{M}\right] q}_{\mathcal{L}^q_{\text{QCD}}} - \frac{1}{4} G_{a\mu\nu} G_a^{\mu\nu}, \tag{2.1}$$

where the covariant derivative $D_\mu = \partial_\mu - i g_s G^c_\mu \frac{\lambda^c}{2}$ includes the gluon interaction fields G^c_μ and the strong coupling constant g_s. Note that λ^c are the SU(3)-color Gell-Mann matrices, then D_μ acts on the color space and is flavor independent. The quark mass matrix $\mathscr{M}$ is defined in the flavor space as $\mathscr{M} = \text{diag}(m_u, m_d, m_s, \dots, m_{n_f})$. The next term in the Lagrangian (2.1) contains the gluon tensor $G_a^{\mu\nu} = \partial_\mu G^a_\nu - \partial_\nu G^a_\mu + g_s f^{abc} G^b_\mu G^c_\nu$ with f^{abc} the SU(3) structure constants.
We see that $\mathcal{L}_{\text{QCD}}$ can be separated into two parts: the quark interaction term $\mathcal{L}^q_{\text{QCD}}$ that describes the quark propagation and the quark-gluon interactions, and the $G_{c\mu\nu} G_c^{\mu\nu}$ part that governs the gluon self-interactions. The fundamental parameters of QCD are the coupling g_s (or $\alpha_s = \frac{g_s^2}{4\pi}$) and the quark masses m_q.

The analysis of the running of the strong coupling constant given by the renormalization group equation leads to the fact that QCD is a theory with a weak coupling at high energies (asymptotic freedom) and with a strong one at low-energies [32, 33]. In this low energy non-perturbative regime, QCD appears to be confining. This is supported by the experimental evidence that the asymptotically free strong interacting particles at these energies are not quarks and gluons but clusters of them organized in color singlets called hadrons.

In order to treat the strong dynamics at the non-perturbative regime it is useful to analyze the global symmetries of QCD. To do so, we will restrict ourselves to the so-called light sector of QCD, with $n_f = 3$ light quark flavors. Those are the u, d, s quarks, that are much lighter than the so-called heavy quarks: c, b, t. The characteristic hadron scale Λ_χ lies in between both regimes.

To visualize the chiral symmetry properties of the QCD Lagrangian, one decomposes the quark field vector into the left- and right hand fields, $q = q_L + q_R$, where

$$q_R = \frac{1}{2}(\mathbf{1} + \gamma^5) q, \qquad q_L = \frac{1}{2}(\mathbf{1} - \gamma^5) q. \tag{2.2}$$

Then, the quark Lagrangian term $\mathcal{L}^q_{\text{QCD}}$ indicated in Eq. (2.1) can be rewritten as

$$\mathcal{L}^q_{\text{QCD}} = i\bar{q}_L \not{D} q_L + i\bar{q}_R \not{D} q_R \underbrace{- \bar{q}_L \mathscr{M} q_R - \bar{q}_R \mathscr{M} q_L}_{\mathcal{L}_{\mathscr{M}}}, \tag{2.3}$$

where $\mathcal{L}_{\mathscr{M}}$ indicates the masses part of the QCD Lagrangian. Given the flavor independence of the QCD covariant derivative, D_μ, all the terms in $\mathcal{L}_{\rm QCD}$ (2.1), except for $\mathcal{L}_{\mathscr{M}}$, fulfill a global $U(n_f)_L \times U(n_f)_R$ symmetry related to the invariance under the transformations

$$\begin{aligned} q_L &\longmapsto q'_L = u_L q_L = e^{-i\Theta^L_a \frac{\lambda^a}{2}} e^{i\Theta^L} q_L \\ q_R &\longmapsto q'_R = u_R q_R = e^{-i\Theta^R_a \frac{\lambda^a}{2}} e^{i\Theta^R} q_R \end{aligned} \tag{2.4}$$

where $u_{L,R} \in U(n_f)_{L,R}$ are unitary $n_f \times n_f$ matrices in the flavor space[1]. The matrices λ^a are the $SU(n_f)$ generators with Lie algebra $[\lambda^a, \lambda^b] = if_{abc}\lambda^c$ [2]. As shown in Eqs. (2.4), the unitary transformations $u_{L,R}$ are written with separated factors $e^{i\Theta^{L,R}}$ given that they are related to the invariance with respect to a global phase, and both form independent subgroups $U(1)_{L,R}$. In this way, the global symmetry group $U(n_f)_L \times U(n_f)_R$ decomposes into $SU(n_f)_L \times SU(n_f)_R \times U(1)_L \times U(1)_R$ transformations.
In particular, we refer to the invariance under the subgroup $G \equiv SU(n_f)_L \times SU(n_f)_R$ as the **chiral symmetry**. The chiral group G is composed by the chiral transformations $g_L = \exp(-i\Theta^L_a \frac{\lambda^a}{2}) \in SU(n_f)_L$ and $g_R = \exp(-i\Theta^R_a \frac{\lambda^a}{2}) \in SU(n_f)_R$ as in Eqs. (2.4).

In the massless quark limit, when $\mathscr{M} \to 0$, the QCD Lagrangian, Eq. (2.1), is invariant under chiral G transformations and the global phase groups $U(1)_{L,R}$. Then, it posses a total of $2 \times n_f^2$ conserved Noether currents. Namely, from the u_L and u_R transformations (2.4), the conserved currents are: R^μ_a, L^μ_a, correspondingly to the left and right-handed chiral transformations, g_R and g_L. In addition, we have R^μ and L^μ that derive from the unitary transformations $e^{-i\Theta_{R,L}}$. Nevertheless, instead of the separated right and left-handed currents, the description that results more naturally linked with phenomenology (parity) is that in terms of the vector, V, and axial-vector A currents. Specifically,

$$V^\mu_a = R^\mu_a + L^\mu_a = \bar{q}\gamma^\mu \frac{\lambda^a}{2} q, \tag{2.5}$$

$$A^\mu_a = R^\mu_a - L^\mu_a = \bar{q}\gamma^\mu\gamma^5 \frac{\lambda^a}{2} q, \tag{2.6}$$

$$V^\mu = R^\mu + L^\mu = \bar{q}\gamma^\mu q, \tag{2.7}$$

$$A^\mu = R^\mu + L^\mu = \bar{q}\gamma^\mu\gamma^5 q \tag{2.8}$$

Those vector and axial currents transform under parity as $V^\mu(t,\vec{x}) \mapsto V_{\mu(a)}(t,-\vec{x})$ and $A^\mu_{(a)}(t,\vec{x}) \mapsto -A_{\mu(a)}(t,-\vec{x})$. The corresponding invariant charges Q^a_V and Q^a_A serve as generators of the Lie algebra of $SU(n_f)_V$ and $SU(n_f)_A$ and have a different behavior under parity

$$Q^a_V \to Q^a_V; \quad Q^a_A \to -Q^a_A. \tag{2.9}$$

[1]The sum over the indices $a = \{1, 2, \ldots, n_f^2 - 1\}$ for the transformations $\exp\left(-i\Theta^{L,R}_a \frac{\lambda^a}{2}\right)$ in Eq. (2.4) is implicit.

[2]In particular, the generators λ^a are represented by the Pauli (Gell-Mann) matrices for the case of $n_f = 2$ ($n_f = 3$)

2.1.2 Chiral Symmetry Breaking

Explicit χ Symmetry Breaking

The corresponding divergences for the currents (2.5)-(2.8) are [30]

$$\partial_\mu V_a^\mu = i\bar{q}\left[\mathscr{M}, \frac{\lambda^a}{2}\right] q, \tag{2.10}$$

$$\partial_\mu A_a^\mu = i\bar{q}\left\{\mathscr{M}, \frac{\lambda^a}{2}\right\} q, \tag{2.11}$$

$$\partial_\mu V^\mu = 0, \tag{2.12}$$

$$\partial_\mu A^\mu = 2i\bar{q}\gamma^5 \mathscr{M} q + \frac{3g_s^2}{32\pi^2}\varepsilon_{\mu\nu\rho\sigma} G_c^{\mu\nu} G_c^{\rho\sigma}. \tag{2.13}$$

From here, we observe that in the limit of vanishing quark masses ($\mathscr{M} \to 0$), the vector and axial currents, V_a^μ and A_a^μ, are conserved and the chiral symmetry $G = SU(n_f)_L \times SU(n_f)_R$ is then fulfilled. This is why the massless limit is called the chiral limit.

However, since the quarks u, d, s, ... have not zero masses [34], the nonzero matrix $\mathscr{M}$ originates an explicit breaking of the chiral symmetry G, governed by the commutation relations of Eqs. (2.10) and (2.11). Nonetheless, there is a particular situation suggested by the hadron spectrum patterns, where one considers that their constituent quarks have approximately the same mass. It is the case of the low energy regime of QCD with an upper limit scale $\Lambda_\chi \simeq 1$ GeV and restricted to the three lightest quark flavors u, d, s ($n_f = 3$). At the scale Λ_χ, these quarks have approximately the same mass, $m_u \approx m_d \approx m_s << \Lambda_\chi$, thus the assumption of equal quark masses could be a good approximation. In this limit, given that $\mathscr{M}$ is diagonal, the vector currents V_a^μ are conserved, see Eq. (2.10). This is not the case for the axial currents A_a^μ which are broken whenever the mass term $\mathscr{M} \neq 0$, Eq. (2.11).
The singlet vector current V^μ, being the sum of n_f flavor currents, is trivially conserved (2.12) whereas the singlet axial A^μ has an explicit divergence, Eq. (2.13), due to the quark masses and the anomaly due to the quantum loop corrections [35–37]. In consequence, we find that the $U(1)_A$ symmetry will appear always broken. The vector symmetry $U(1)_V$ leads to the conservation of the so-called baryon number, B. This quantum number is used for the classification of the hadron spectrum into mesons ($B = 0$) and baryons ($B \geq 1$). Equivalent considerations applied to independent phase transformations on the different quark flavors lead to the conserved flavor quantum numbers.

In summary, the global symmetry for QCD in the chiral limit is $SU(n_f)_L \times SU(n_f)_R \times U(1)_V$. On the contrary, for the massive case and at low energies, the non-zero matrix $\mathscr{M}$ in the $\mathcal{L}_{\mathscr{M}}$ term (2.3) breaks explicitly the chiral symmetry with pattern:

$$G = SU(n_f)_L \times SU(n_f)_R \longrightarrow H = SU(n_f)_V\,. \tag{2.14}$$

In the physical world, one shall expect chiral symmetry G to be approximately realized for the light quarks and it is natural to explore its breaking pertubatively [33]. Thus, one may consider the massless QCD Lagrangian and later on introduce the quark masses as a small perturbation.

Spontaneous χ Symmetry Breaking and Goldstone Bosons

In addition to the explicit breaking due to the quark masses, chiral symmetry is also spontaneously broken. Since chiral symmetry is a global symmetry, then the Goldstone theorem applies. The Goldstone theorem states as follows: *Given a global continuous symmetry of the Lagrangian; either the vacuum shares the symmetry of the Hamiltonian; or there appear scalar massless particles as a display of Spontaneous Symmetry Breaking. In the last case, for every spontaneously broken symmetry, the theory must contain a massless particle, the so-called Golstone boson.*[3]

In the usual Wigner–Weyl realization of the chiral symmetry, the vector charges annihilate the vacuum,

$$Q_V^a|0\rangle = 0, \tag{2.15}$$

so that it remains invariant under the group of transformations, $U_V = \exp\{i\theta_a Q_V^a)\}$[4]. This implies the existence of degenerate multiplets ϕ_a in the spectrum. For $n_f = 3$, we can find evidence of this in the hadron spectrum [39], where low-lying baryons and mesons sharing the same quantum numbers and approximately the same mass can be grouped into irreducible representations of $SU(3)_V$ [40].
Since parity exchanges left and right, a normal Wigner–Weyl realization of the symmetry would imply degenerate mirror multiplets with opposite chiralities and the chiral symmetry G should be approximately good for the light u, d, s quarks.

On the other hand, when applying an axial transformation U_A over a particle of the lightest meson spectrum, lets say of the pseudoscalar meson octet, we would generate a state with a component of opposite parity. But these mirror states are not observed in nature. Moreover, the octet of pseudoscalar mesons is much lighter than all other hadronic states. These empirical facts clearly indicate that the vacuum is not symmetric under the full chiral group. Specifically, the vacuum is not invariant under axial transformations, *i.e.*

$$Q_A^a|0\rangle \neq |0\rangle, \tag{2.16}$$

which is called the Nambu–Goldstone realization of the symmetry.

Only the transformations with $g_R = g_L$ remain a symmetry of the physical QCD vacuum. Thus, it is said that the **symmetry is spontaneously broken** as $G \equiv SU(3)_L \times SU(3)_R \to H \equiv SU(3)_V$ [see. Eq. (2.14)].[5]

In particular, due to the Goldstone Theorem, for $n_f = 3$ the spectrum contains eight Nambu–Goldstone bosons (NGB), as many as broken generators of $SU(3)_A$. Those NGB fields have the same quantum numbers as Q_A^a : odd parity, and transform under the adjoint representation of $SU(3)_V$. These are the eight lightest hadronic states $(\pi^\pm, \pi^0, \eta, K^\pm, K^0, \overline{K^0})$, whose mass is generated by the quark masses, the ones that explicitly broke the chiral symmetry (2.14)[6]. In this picture, with $n_f = 2$, $q^T = (u, d)$, one recovers the corresponding three NGB identified with the pseudoscalar

[3]There is another important result around the concept of spontaneous symmetry breaking: the Higgs-Kibble mechanism [38] relevant for the case of local gauge symmetries.

[4]In the quantum theory, the conserved charges Q^a become symmetry generators that implement the group of transformations through the unitary operators $U = exp(i\theta_a Q^a)$, being θ_a the continuous parameters characterizing the transformation.

[5] On top of that, another evidence of Spontaneous Symmetry Breaking is the fact that the quark condensate, $\langle 0|\bar{q}q|0\rangle$, the order parameter of this symmetry breaking, has a non zero vacuum expectation value [41–45].

[6]If the breaking is small, we could expect the mass of these bosons to be smaller than the rest of the hadron spectrum.

$SU(2)_V$ pion triplet, (π^-, π^0, π^+).
For a more detailed discussion of the application of Goldstone theorem to the spontaneous chiral symmetry breaking, see Refs. [46, 47].

2.1.3 A Low energy Effective Field Theory Approach

As mentioned before, the large value of the coupling limits the applicability of perturbative QCD with explicit quark and gluon fields. Given the strong coupling dependence on the energy, a typical energy scale, $\Lambda_\chi \simeq 1$ GeV, separates the strong interaction into two different regimes: the low energy $E << \Lambda_\chi$ and the high energy one, $E >> \Lambda_\chi$. The latter is commonly approached as a weakly coupled theory with the perturbative methods of QFT. There, the strong coupling converges asymptotically to small values with increasing energy and is the expansion parameter for the perturbative series. On the contrary, when $E << \Lambda_\chi$, the processes driven by the strong interaction should be treated differently since the coupling increases rapidly as the energy E decreases. For this reason, these low energy processes are usually approached within an EFT formulation. There, one implements an alternative approximation with different expansion parameters and degrees of freedom.

The basic idea to construct an EFT Lagrangian is that all terms compatible with the QCD symmetries should be included, each proportional to some unknown constant that should be determined by fitting to data. In the ChPT case, chiral symmetry and its breaking are the guiding principles in its construction. The Lagrangian terms are organized according to the power of the dimensionless parameters p_{typ}/Λ that each of them contributes to the amplitudes, where p_{typ} are the typical momenta or energies in the process and Λ is some energy scale like, for instance, $\Lambda \approx 1$ GeV. There are infinitely many of those terms in the Lagrangian, but at a given order in p_{typ}/Λ and for a given process only a finite number will contribute. Also, quarks and gluons are integrated out, and the bound states, baryons and mesons, are the relevant degrees of freedom. By construction, this EFT should be valid for energies significantly lower than Λ. Some of the most relevant ideas about EFTs can be found in [48–51].

2.2 Chiral Perturbation Theory: The low energy effective theory of QCD

In this section, I discuss in more detail the fundamentals of the effective theory of QCD at low energies, Chiral Perturbation Theory, ChPT. See reviews [27–31].

Chiral perturbation theory provides a systematic method for discussing the consequences of the global symmetries of QCD at low energies by means of an effective field theory. ChPT is based on an effective Lagrangian built in terms of the asymptotically observed hadronic fields and consistent with all symmetries of QCD. The Lagrangian is organized in the form of a chiral expansion, i.e., an expansion in powers of momenta and light quark masses [52]. Of course, the effective Lagrangian shares the same symmetries with QCD: C, P, T, Lorentz invariance and, in particular, chiral $SU(3)_L \times SU(3)_R$ symmetry and its breaking both explicit and spontaneous.

After introducing the lowest-order effective Lagrangian relevant to the spontaneous breakdown from $SU(3)_L \times SU(3)_R$ to $SU(3)_V$, I will illustrate how Weinberg's power counting scheme allows for a systematic classification of Feynman diagrams in the so-called chiral expansion. The starting point is the sector of the pseudoscalar

mesons. The theory can also be extended to baryons, which are presented in the next subsection. Another important aspect of an effective theory is renormalization, which will be discussed last. In particular, the incorporation of baryon degrees of freedom into the theory complicates this process, which is why the required methods will be explained in more detail.

At low energies, the relevant mesons are just the members of the pseudoscalar octet (π, K, η) which are regarded as the Nambu–Goldstone bosons of the spontaneous breaking of the chiral $SU(3)_L \times SU(3)_R$ symmetry down to $SU(3)_V$. The non-vanishing masses of the light pseudoscalars in the "real" world are related to the explicit symmetry breaking in QCD due to the light quark masses. In this work, we further restrict our investigation to QCD with the two lightest flavors, namely the u and d quarks. Their small masses lead to a faster chiral convergence and the Nambu–Goldstone bosons are just the pions. In this case we have the chiral symmetry breaking pattern

$$G = SU(2)_L \times SU(2)_R \longrightarrow H = SU(2)_V. \tag{2.17}$$

2.2.1 Chiral Lagrangian for pions

Lowest Order π Lagrangian

The standard ChPT description of the light pseudoscalar mesons and their interactions was first formulated by J. Gasser and H. Leutwyler in the 1980s [53, 54] based on the EFT approach of [52]. The group theoretical formalism to construct EFT Lagrangians with spontaneous symmetry breaking was developed by Callan, Coleman, Wess and Zumino (CCWZ) and S. Weinberg [55–57]. In that prescription, the pseudo-Goldstone bosons can be parametrized into a matrix valued field $U \in O(N)$ such that

$$U(x) = \exp\left(i\frac{\vec{\tau}\cdot\vec{\pi}(x)}{F}\right) \tag{2.18}$$

where $\vec{\tau}$ are the set of N broken generators. For the light quarks (u, d) case, the chiral symmetry breaking pattern corresponds to $SU(2)_V$, Eq. (2.17) and $\vec{\tau} = (\tau^1, \tau^2, \tau^3)$ are the Pauli matrices. Hence, $\vec{\pi} = (\pi_1, \pi_2, \pi_3)$ describes the pion modes in a Cartesian basis and F is a normalization constant. The pion field representation can also be given in the physical basis through

$$\vec{\tau}\cdot\vec{\pi} = \begin{pmatrix} \pi_3 & \pi_1 - i\pi_3 \\ \pi_1 + i\pi_2 & -\pi_3 \end{pmatrix} = \begin{pmatrix} \pi^0 & \sqrt{2}\pi^+ \\ \sqrt{2}\pi^- & -\pi^0 \end{pmatrix}, \tag{2.19}$$

where the fields π^0, π^+, and π^- correspond to the physical isospin eigenstates. Given the chiral group $G = SU(2)_L \times SU(2)_R$ the pions matrix U transforms as

$$U(x) \xrightarrow{G} U'(x) = g_L U(x) g_R^\dagger. \tag{2.20}$$

In the context of ChPT, the CCWZ formalism is characterized by Eqs. (2.18) and (2.20) for the pseudoscalar boson fields and their transformation law. The mapping of Goldstone bosons is not unique, but all are equivalent to the exponential realization in Eq. (2.18)[7]. The chiral invariant Lagrangian must be written in terms of the Goldstone bosons collected in the matrix-valued field $U(x)$ (2.18). The construction

[7] Any other choice gives the same results for all observables, such as the S-matrix. A clear explanation about the CCWZ procedure and Goldstone boson parametrization can be found in Ref. [49].

of the effective Lagrangian is based on the vanishing interaction of the Goldstone-bosons at zero momentum. Hence, at low energies the Lagrangian can be organized in terms of increasing powers of momentum (or derivatives),

$$\mathcal{L}_{\text{eff}}(U, \partial U, \partial^2 U, \dots). \tag{2.21}$$

The chiral invariant Lagrangian containing the minimum number of derivatives on the pseudoscalar fields is uniquely given by

$$\mathcal{L}^{(2)}_{\chi S} = \frac{F^2}{4}\text{Tr}\left[\partial^\mu U\,(\partial_\mu U)^\dagger\right]. \tag{2.22}$$

Only even momentum powers will arise since the Lagrangian is a Lorentz scalar which implies that tensor indices of derivatives appear in pairs. The factor $F^2/4$ is fixed by the kinetic term for the pion fields.[8]

The lowest order Lagrangian (2.22) has an exact chiral symmetry. In the real world the quark masses do not vanish and introduce the explicit breaking of chiral symmetry throught the term $\mathcal{L}_{\mathscr{M}}$ (2.3) in the QCD Lagrangian. Here, we take the isospin symmetry case for two flavors where $m_u = m_d$ with the corresponding mass matrix $\mathscr{M} = \text{diag}(m_u, m_d)$.
At the level of the effective field theory, the chiral symmetry breaking patterns of QCD can be reproduced. To this end, the quark mass matrix is interpreted as an external scalar source, $s = \mathscr{M}$,

$$-\mathcal{L}_{\mathscr{M}} = \bar{q}_L \mathscr{M} q_R + \bar{q}_R \mathscr{M} q_L \longrightarrow \bar{q}_L s^\dagger q_R + \bar{q}_R s q_L \tag{2.23}$$

The QCD Lagrangian remains invariant under chiral rotations if the scalar source transforms as

$$s \xrightarrow{G} g_R s g_L^\dagger. \tag{2.24}$$

This implies that the effective Lagrangian must also remain invariant in the presence of s. Hence, the chiral invariant effective Lagrangian Eq. (2.21) is extended with s as an additional building block. At leading chiral order, the new Lagrangian term reads

$$\mathcal{L}^{(2)}_{\chi SB} = \frac{F^2 B}{2}\text{Tr}\left[sU^\dagger + Us^\dagger\right], \tag{2.25}$$

where B is a parameter that relates the quark masses in s with the Goldstone Bosons masses. The explicit mass matrix for the Goldstone bosons is introduced from the standard massive Lagrangian term for π as

$$\chi = 2Bs \tag{2.26}$$

where, in the isospin limit and the $SU(2)$ case, $\chi = \text{diag}(M_\pi^2, M_\pi^2)$. Then, the Lagrangian at the lowest order reads

$$\mathcal{L}^{(2)}_{\text{eff}} = \mathcal{L}^{(2)}_{\chi S} + \mathcal{L}^{(2)}_{\chi SB} = \frac{F^2}{4}\text{Tr}\left[\partial^\mu U\,(\partial_\mu U)^\dagger + \chi U^\dagger + U\chi^\dagger\right], \tag{2.27}$$

[8] An expansion of the exponential term $U = \exp[i\frac{\Phi}{F}] = 1 + i\frac{\Phi}{F} - \frac{1}{2F^2}\Phi^2 + \mathcal{O}(\Phi^3)$ provides all the interactions at LO for increasing number of Goldstone bosons. Thus, the standard kinetic term reads $\mathcal{L}^{(2)}_{\chi S} = \frac{1}{2}\partial_\mu \pi^a \partial^\mu \pi_a + \mathcal{O}(\pi^4)$ such as deduced from (2.22).

The Lagrangian leads to second order terms in powers of momenta and pion masses, the expansion parameters of the EFT at low-energies. Thus, the chiral counting of $\mathcal{L}_{\text{eff}}^{(2)}$ is $\mathcal{O}(p^2)$.

To this lowest chiral order, the strong interactions are characterized by the two scales F and B, the low-energy constants (LECs) of the effective Lagrangian. Those LECs are related to the pion decay constant and to the quark condensate in the chiral limit respectively. The constant B is related to the vacuum expectation values of the scalar quark densities through

$$\langle 0|\bar{q}q|0\rangle = \langle 0|\frac{\partial H_{\text{QCD}}}{\partial m_q}|0\rangle = -\langle 0|\frac{\partial \mathcal{L}_{\text{eff}}}{\partial m_q}|0\rangle = -F^2 B + \mathcal{O}(m_q). \tag{2.28}$$

The constant B is proportional to the quark condensate in the chiral limit, $\langle 0|\bar{u}u|0\rangle = \langle 0|\bar{d}d|0\rangle = -F^2 B$, and it is the order parameter of the spontaneous chiral symmetry breaking. The value of $B \simeq 1800\,\text{MeV}$, is extracted from the sum-rule value $\langle 0|\bar{q}q|0\rangle = -(250\,\text{MeV})^3$ [42].

We can directly read off from (2.26) and (2.27) the pseudoscalar pion masses to leading order in m_q

$$M_{\pi^\pm}^2 = M_{\pi^0}^2 = 2m_q B, \tag{2.29}$$

with $m_q = m_u = m_d$ in the isospin limit. One finds from Eq. (2.29) that the quark masses are proportional to the squared mass of the pion[9] and thus will be counted as $O(p^2)$.

On the other hand, one realizes the physical meaning of the LEC F in the LO effective Lagrangian as the pion decay constant. This interpretation of F is directly inferred by taking the proper matrix element of the axial current from the kinetic term in $\mathcal{L}_{\text{eff}}^{(2)}$ (2.27),

$$\langle 0|J_{A\,a}^{\mu}|\pi_b(p)\rangle = -iFp^\mu \delta_{ab}, \tag{2.30}$$

with $J_{A\,a}^{\mu} = J_{R\,a}^{\mu} - J_{L\,a}^{\mu} = -F\partial^\mu \pi_a + \cdots$, for $a = 1, 2, 3$. The pion decay constant F is then defined in the chiral limit. The experimental value of the π decay rate, $\pi \to \mu\bar{\nu}$, determines its value, $F = 92.4$ MeV [58].[10]

In summary, the lowest-order $\mathcal{L}_{\text{eff}}^{(2)}$ has two LECs: F and B. Moreover, the relation (2.29) gives the Gell-Mann, Oakes and Renner relation [60]. Also, Eq. (2.30) reproduces the hypothesis of the partially conserved axial vector current (PCAC). That is, ChPT at its lowest order reproduces results that had been previously obtained using current algebra.

Couplings to external gauge field sources

It is possible to further extend the pion Lagrangian (2.27) to include interactions with gauge fields, such as photons. Indeed, the mesons do not interact solely among themselves. In addition to the strong interaction, they may also experience electromagnetic and weak interactions.

In our case, this is necessary for the calculation of the pion photo- and electroproduction process which involves vertices with photon couplings. To this aim, one extends $\mathcal{L}_{\text{QCD}}$ (2.1) in the presence of external classical fields coupled to the quark currents

[9] Moreover, similiar relationships are fulfilled for the $SU(3)$ pseudoscalar mesons [28].

[10] Quantum corrections when including higher order calculations lead to different values for the chiral limit $F \approx 88$ MeV since the physical one is $F_\pi = 92.4$ MeV. See for instance [59].

as done in [53, 54],

$$\mathcal{L}_{\rm QCD} = \mathcal{L}^0_{\rm QCD} + \bar{q}\gamma_\mu(v^\mu + \gamma_5 a^\mu)q - \bar{q}(s - i\gamma_5 h)q, \qquad q = \begin{pmatrix} u \\ d \end{pmatrix} \tag{2.31}$$

with $\mathcal{L}^0_{\rm QCD}$ the massless QCD Lagragian. The external fields are used to parametrize the different breakings of chiral symmetry. In detail v^μ, a^μ, s, and h are Hermitian matrices denoting the external vector, axial-vector, scalar, and pseudoscalar fields, respectively. One recovers the original QCD Lagrangian with $v^\mu = a^\mu = h = 0$ and $s = \mathscr{M}$, see Eq. (2.23). The external photons and W bosons are among the gauge fileds v^μ and a^μ. The QCD Lagrangian (2.31) remains invariant under the local chiral $SU(2)_L \times SU(2)_R$ transformations if we demand the sources to transform like

$$q_R \to g_R(x) q_R, \qquad q_L \to g_L(x) q_L, \tag{2.32}$$

$$r_\mu = v_\mu + a_\mu \to g_R(x) r_\mu g_R^\dagger(x) + i g_R(x) \partial_\mu g_R^\dagger(x), \tag{2.33}$$

$$l_\mu = v_\mu - a_\mu \to g_L(x) l_\mu g_L^\dagger(x) + i g_L(x) \partial_\mu g_L(x), \tag{2.34}$$

$$s - ih \to g_R(x)(s - ih) g_L^\dagger(x). \tag{2.35}$$

The effective chiral Lagrangian (2.27) can also be made invariant under the local chiral transformations if one introduces covariant derivatives on the meson fields, including the gauge fields r_μ, l_μ, and replace the quark mass insertions by $\chi = 2Bs$ (with $h = 0$) as previously shown in (2.26). The covariant derivative on GBs, $\nabla_\mu U$, reads

$$\partial_\mu U \to \nabla_\mu U = \partial_\mu U - i l_\mu U + i U r_\mu, \tag{2.36}$$

which transform under chiral rotations as

$$\nabla_\mu U \to g_L(x) \left(\nabla_\mu U\right) g_R^\dagger(x). \tag{2.37}$$

The couplings to the electromagnetic field (photon) $\mathscr{A}^\mu$ are given by $r^\mu = l^\mu = v^\mu = -eQ\mathscr{A}^\mu$, with $Q = (\tau_3 + \mathbb{1})/2$ the electric charge operator in $SU(2)$ and in units of e, the electric charge of the electron.

Finally, the locally chiral invariant Lagrangian of lowest order describing the strong and electromagnetic[11] interactions of mesons is given by

$$\mathcal{L}^{(2)}_\pi = \frac{F^2}{4} \mathrm{Tr}\left[\nabla^\mu U \left(\nabla_\mu U\right)^\dagger + \chi U^\dagger + U \chi^\dagger\right]. \tag{2.38}$$

Furthermore, the vector and axial-vector fields v_μ, a_μ may enter the effective Lagrangian also through the non-Abelian field strength tensors, $F_{R\,\mu\nu}$, $F_{L\,\mu\nu}$,

$$\begin{aligned} F_{R\,\mu\nu} &= \partial_\mu r_\nu - i[r_\mu, r_\nu], \\ F_{L\,\mu\nu} &= \partial_\mu l_\nu - i[l_\mu, l_\nu], \end{aligned} \tag{2.39}$$

with the transformation properties

$$\begin{aligned} F_{R\,\mu\nu} &\to g_R(x) F_{R\,\mu\nu} g_R^\dagger(x), \\ F_{L\,\mu\nu} &\to g_L(x) F_{L\,\mu\nu} g_L^\dagger(x). \end{aligned} \tag{2.40}$$

[11] The weak gauge fields can also be incorporated. See, *e.g.*, [48].

The couplings to the external strength tensor fields contain derivatives on the sources and, in the low-energy limit, they behave as $F_{L\mu\nu} \sim F_{R\mu\nu} \sim \mathcal{O}(p^2)$. Those operators can be classified into a power counting and determine their contribution at low energies as discussed in the following Section.

Higher orders, loops and renormalization

In the previous section, we have shown the lowest order chiral Lagrangian for pions and photons. We have also shown that the construction blocks have a well defined chiral order,

$$U \sim \mathcal{O}(p^0), \qquad D_\mu U,\, v_\mu,\, a_\mu \sim \mathcal{O}(p), \qquad s, p, F^{\mu\nu}_{L,R} \sim \mathcal{O}(p^2). \tag{2.41}$$

One of the most important aspects of ChPT, as an EFT, is the fact that it gives a perfectly defined way of taking into account the next orders in the chiral expansion, included the quantum corrections. In general, the Lagrangian can be written as a sum of terms depending on the powers of mesons momenta and the quark masses,

$$\mathcal{L}_{\text{ChPT}} = \sum_{ij} \mathcal{L}_{ij}, \qquad \mathcal{L}_{ij} = \mathcal{L}(p^i m_q^j) \tag{2.42}$$

As mentioned before, the quark masses count as $m_q \sim \mathcal{O}(p^2)$, and by Lorentz invariance the chiral order of momenta is always given in even numbers, $\mathcal{O}(p^2), \mathcal{O}(p^4), \ldots$. Then, the chiral power counting of the pion Lagrangian can be organized as the series

$$\mathcal{L}_\pi^{\text{eff}} = \sum_n \mathcal{L}_\pi^{(n)} = \mathcal{L}_\pi^{(2)} + \mathcal{L}_\pi^{(4)} + \mathcal{L}_\pi^{(6)} + \cdots, \tag{2.43}$$

where the upper indices refer to the chiral order of each term. In this power expansion, the lowest-order (LO) term $\mathcal{L}_\pi^{(2)}$, already given in Eq. (2.38), gives the dominant behavior at low energies. The following terms in importance are collected in $\mathcal{L}_\pi^{(4)}$ and so on and so forth.

First, let me introduce the effective SU(2) Lagrangian at fourth chiral order, $\mathcal{L}_\pi^{(4)}$, which respects the relevant symmetries of QCD. It is taken from [59] and the relevant terms for the present work are[12],

$$\begin{aligned}\mathcal{L}_\pi^{(4)} = {} & \frac{l_3 + l_4}{16} \text{Tr}\left[\chi U^\dagger + U\chi^\dagger\right]^2 + \frac{l_4}{8} \text{Tr}\left[\nabla_\mu U \left[\nabla^\mu U\right]^\dagger\right] \text{Tr}\left[\chi U^\dagger + U\chi^\dagger\right] \\ & + i\frac{l_6}{2} \text{Tr}\left[F_{R\mu\nu} \nabla^\mu U \left(\nabla^\nu U\right)^\dagger + F_{L\mu\nu} \left(\nabla^\mu U\right)^\dagger \nabla^\nu U\right] + \cdots,\end{aligned} \tag{2.44}$$

where the ellipsis indicates further terms that not contribute in the processes studied here. It contains a total of 10 low-energy-constants l_i corresponding to the number of independent terms. In the electromagnetic case when $r_\mu = l_\mu = v_\mu = eQ\mathscr{A}_\mu$, the tensor field $F_{R\mu\nu} = F_{L\mu\nu} = F_{\mu\nu}$ reads

$$F_{\mu\nu} = eQ(\partial_\mu \mathscr{A}_\nu - \partial_\nu \mathscr{A}_\mu). \tag{2.45}$$

In Eq. (2.44), the LECs l_i parametrize the low energy corrections in the QCD dynamics at fourth chiral order. They are not conditioned by chiral symmetry. They must be

[12] Actually, there are two commonly used Lagrangians that are fully equivalent. Here, we use the version worked out by Gasser, Sainio, and Švarc [59]. The other version is given by Gasser and Leutwyler [53]

determined by comparison with experimental data or derived from phenomenological models, other symmetries, lattice QCD,...[13]

In the evaluation of amplitudes, tree diagrams constructed from the lowest order Lagrangian term $\mathcal{L}_\pi^{(2)}$ give the leading order (LO) contribution. The inclusion of vertices derived from $\mathcal{L}_\pi^{(4)}$ in the tree diagrams calculation provide next-to-leading order (NLO) contributions which give a more accurate calculation when added to the LO ones. See, *e.g.,* App. A. On the other hand, for consistency, loop diagrams with vertices from $\mathcal{L}_\pi^{(2)}$ also must be taken into account as they also contribute at the same, NLO, chiral order[14]. Moreover, they provide the imaginary parts of the amplitudes, needed by unitarity and related with the physical thresholds. However, the loop diagrams contain UV divergences and a regularization scheme is necessary. This scheme must maintain the symmetries of the theory, in particular chiral symmetry[15]. In ChPT, a convenient scheme is dimensional regularization [62]. The basic idea is to change the dimension of the integration loop to an arbitrary dimension $D \in \mathbb{R}$ by making $\int d^4k \to \mu^{4-D} \int d^Dk$, with μ an auxiliary parameter to maintain the mass dimensions. Afterwards, the analytic continuation back to $D \to 4$ is performed. The result is a function of D and after expanding in $D-4$ the integral $\mathcal{A}$ decomposes as

$$\mathcal{A} = f_1 R + f_2 + \mathcal{O}(D-4), \tag{2.46}$$

with R the divergent piece

$$R = \mu^{4-D}\left[\frac{2}{D-4} - \big(\ln 4\pi + 1 + \Gamma'(1)\big)\right]. \tag{2.47}$$

The coefficient f_1 is an analytical function and f_2 corresponds to a finite piece that includes non-analytical terms. We can neglect the remaining terms in $\mathcal{O}(D-4)$ since they vanish in the limit when $D \to 4$.

Dimensional regularization provides a systematic and consistent method to separate the finite terms from the UV divergent ones in the loop integrals. The piece R[16], has always the same structure and can be uniformly subtracted in a renormalization procedure. This topic is further discussed in Sections 4.2.2-4.2.3.

Here, the renormalization of an amplitude consists in the redefinition of the LECs in $\mathcal{L}_\pi^{\text{eff}}$ (2.43), which appear as scale independent parameters in the tree-level amplitudes, in order to cancel the piece $f_1 R$ in (2.46). A complete one-loop calculation with vertices from the lowest-order $\mathcal{L}_\pi^{(2)}$ reveals that divergent parts proportional to R are of chiral order $\mathcal{O}(p^4)$ and analytic in the pion momenta and masses. Hence, the divergent components, f_1, only can be compensated by renormalizing the LECs

[13] At next-to-next-to leading order (NNLO), 53 LECs enter in the SU(2) $\mathcal{L}_\pi^{(6)}$ [61]. That shows a proliferation of unknown couplings with additional order corrections and ChPT seems to lose its predictive power. However, the situation is ameliorated since only a few LECs contribute to each particular process. Furthermore, in practice, in many cases only the LECs from low orders are required. Moreover, the contributions from higher chiral orders are suppressed as they appear with higher powers of small momenta and pion masses.

[14] Regardless of their power counting contribution, loop amplitudes are also required to restore unitarity of the S-matrix, $S = \mathbb{1} + iT$ [62]. The condition $SS^\dagger = \mathbb{1}$ is fulfilled as long as $2\,\text{Im}T = TT^\dagger$. Obviously, tree diagrams cannot satisfy this relation because they do not have an imaginary piece. Thus, unitarity is violated if only tree diagrams are taken into account. In fact, unitarity of the S-matrix is restored by including loop diagrams which have imaginary parts.

[15] One must be careful when employing cutoff regularization schemes since these introduce an additional massive cutoff scale which may spoil chiral symmetry [63].

[16] There are different conventions to define the UV divergent term R. Here, we use the modified subtraction scheme $\widetilde{\text{MS}}$. Other schemes differ on the finite terms in R Eq. (2.47) but all agree on the divergent piece.

at the same chiral order $\mathcal{O}(p^4)$,

$$l_i = l_i^r + \lambda_i R. \tag{2.48}$$

Here, l_i are the LECs in $\mathcal{L}_\pi^{(4)}$ (2.44), such that the sum of loops and tree amplitudes proportional to the LECs remains finite for $D \to 4$. The LEC renormalization in (2.48) is independent of the process (λ_i are unique), then the renormalization method may be generalized to the effective Lagrangian. The corresponding counterterms $\delta\mathcal{L}_\pi^{(4)}$ may be generated and incorporated in $\mathcal{L}_\pi^{(4)}$, Eq. (2.44). I further detail the UV renormalization method within the $\widetilde{\text{MS}}$ scheme in Section 4.2.3.

Power counting rule for the amplitudes

Since the ChPT Lagrangian (2.43) contains an infinite numbers of terms there is the need of a systematic way to organize and quantify the importance of the corresponding amplitudes generated by it. This is achieved by using a power counting scheme.

For any amplitude, the power counting scheme analyses the behavior of a given diagram under a linear rescaling of all the external momenta $p_i \mapsto \delta p_i$, and a quadratic rescaling of the light quark masses, $m_q \mapsto \delta^2 m_q$, which in terms of the Goldstone boson masses, corresponds to $M^2 \mapsto \delta^2 M^2$. Then, the importance of a given amplitude $\mathcal{A}(p_i, m_q)$ is quantified by its chiral order, n, which defined by

$$\mathcal{A}(\delta p_i, \delta^2 m_q) = \delta^n \mathcal{A}(p_i, m_q) \tag{2.49}$$

The order n can be directly deduced from the corresponding amplitude, once its explicit expression is obtained from the corresponding diagram following the Feynman rules derived from the Lagrangian. After some work, it can be shown that the chiral order n of a given Feynman diagram is

$$n = 4L + \sum_d n_d\, d - 2I, \tag{2.50}$$

where L is the number of independent loops, n_d is the number of vertices of order d originating from $\mathcal{L}_\pi^{(d)}$, and I is the number of internal lines corresponding to the mesons propagators [17].

2.2.2 Interaction Lagrangian with nucleons

In the previous section we have introduced the Lagrangian for the purely pionic sector, *i.e.*, the interaction of the Goldstone bosons among themselves or with external sources. As it was firstly suggested by S. Weinberg [52] similar methods to those used in the derivation of a ChPT for Goldstone bosons can be extended to describe the low-energy interaction with baryons or other higher mass states [55–57, 59]. Following the same chiral expansion for ChPT of Eq. (2.42), the corresponding nucleon chiral Lagrangian can be organized order by order as

$$\mathcal{L}_N^{\text{eff}} = \mathcal{L}_N^{(1)} + \mathcal{L}_N^{(2)} + \mathcal{L}_N^{(3)} + \cdots . \tag{2.51}$$

The chiral invariant Lagrangian terms for $SU(2)$ nucleons take the generic form $\bar{N} A^{\mu\nu\cdots} \Theta_{\mu\nu\ldots} N$ + h.c., with $A^{\mu\nu\cdots}$ a product of pion and/or external fields and their

[17] The power counting can be easily understood examining $\mathcal{A}$, where there is a d^4k for each loop integral, each internal boson goes like $\sim 1/k^2$ and each vertex $V^{(d)}$ goes like p^d.

covariant derivatives. On the other hand, $\Theta_{\mu\nu\ldots}$ is a product of the elements 1, γ_5, γ_μ, $\gamma_\mu\gamma_5$, $\sigma_{\mu\nu}$ built from the Dirac gamma matrices, and a properly symmetrized product of covariant derivatives acting on nucleon fields. In the isospin basis, the nucleon field

$$N = \begin{pmatrix} p \\ n \end{pmatrix}, \tag{2.52}$$

denotes the two components for the proton and neutron as four-component Dirac fields. The basic building blocks contained in the nucleon chiral Lagrangian are the pseudoscalar pion field, now realized with $u = U^{1/2}$, and the set of structures

$$u_\mu = iu^\dagger \nabla_\mu U u^\dagger, \tag{2.53}$$

$$\chi_\pm = u^\dagger \chi u^\dagger \pm u \chi^\dagger u, \tag{2.54}$$

$$F^\pm_{\mu\nu} = u^\dagger F_{R\mu\nu} u \pm u F_{L\mu\nu} u^\dagger. \tag{2.55}$$

They provide a convenient choice since they transform in the same way under chiral local transformations, namely,[18]

$$N \to KN \tag{2.56}$$

$$u \to g_L u K^\dagger = K u g_R \tag{2.57}$$

$$X \to KXK^\dagger, \qquad \text{for } X \in \left\{u_\mu, \chi_\pm, F^\pm_{\mu\nu}\right\}, \tag{2.58}$$

where K is a *compensator field* given by

$$K = \left(\sqrt{U g_L^\dagger}\right)^{-1} \left(\sqrt{g_R U}\right). \tag{2.59}$$

On the other hand, the assigned chiral power counting to the Lagrangian operators constructed thereof are

$$\partial_\mu N,\, \bar{N},\, N \sim \mathcal{O}(p^0), \qquad u_\mu \sim \mathcal{O}(p), \qquad \chi_\pm,\, F^\pm_{\mu\nu} \sim \mathcal{O}(p^2), \tag{2.60}$$

whereas derivatives over u_μ, $\chi_\pm$ or $F^\pm_{\mu\nu}$ increase by 1 the order in the counting. With these ingredients, the first order chiral Lagrangian describing the dynamics with nucleons and pions is given by [64]

$$\mathcal{L}_N^{(1)} = \bar{N}\left(i\not{D} - m + \frac{g}{2}\not{u}\gamma_5\right) N, \tag{2.61}$$

where the covariant derivative $D_\mu N$ contains the external gauge fields $\{l_\mu, r_\mu\}$ and it is built in such a manner that transforms as N, (2.56), $D_\mu N \to K D_\mu N$. In detail,

$$D_\mu N = (\partial_\mu + \Gamma_\mu) N, \qquad \Gamma_\mu = \frac{1}{2}[u^\dagger, \partial_\mu u] - \frac{i}{2} u^\dagger r_\mu u - \frac{i}{2} u l_\mu u^\dagger. \tag{2.62}$$

In (2.61), we have assumed that $(i\not{D} - m)N \sim \mathcal{O}(p)$, where m is the mass at leading order for the nucleon doublet N with physical mass m_N. The LEC g is the leading contribution to the physical axial-vector coupling constant $g_A = g + \mathcal{O}(p^2)$, (see App. C). There, the pion fields appear after expanding u_μ.
Following the same naming conventions for the LECs as in Ref. [65], the only relevant

[18] We omit from now on the explicit dependence on x.

terms in the second order Lagrangian are

$$\mathcal{L}_N^{(2)} = \bar{N}\left(c_1 \mathrm{Tr}\left[\chi_+\right] + \frac{c_6}{8m_N} F^+_{\mu\nu}\sigma^{\mu\nu} + \frac{c_7}{8m_N}\mathrm{Tr}\left[F^+_{\mu\nu}\right]\sigma^{\mu\nu}\right) N + \cdots , \tag{2.63}$$

where $\sigma^{\mu\nu} = \frac{i}{2}\left[\gamma^\mu, \gamma^\nu\right]$. For the processes considered here, $\chi_+ = M^2\left(U^\dagger \pm U\right)$ and $F_{R\mu\nu} = F_{L\mu\nu} = F_{\mu\nu}$, Eq. (2.45). The LEC c_1 describes the nucleon self-interaction at $\mathcal{O}(p^2)$ whilst c_6 and c_7 are the nucleon-photon couplings at second chiral order. This Lagrangian contains a total of seven independent LECs and the rest of them correspond to vertices that do not appear in the processes considered in the present work.

Finally, at third order, the relevant terms of the Lagrangian are [65]

$$\begin{aligned}
\mathcal{L}_N^{(3)} &= d_6\bar{N}\left(\frac{1}{2m_N} i[D^\mu, \widetilde{F}^+_{\mu\nu}]D^\nu + \mathrm{H.c.}\right) N \\
&+ d_7\bar{N}\left(\frac{1}{2m_N} i[D^\mu, \mathrm{Tr}\left[F^+_{\mu\nu}\right]]D^\nu + \mathrm{H.c.}\right) N \\
&+ d_8\bar{N}\left(\frac{1}{2m_N} i\epsilon^{\mu\nu\alpha\beta}\mathrm{Tr}\left[\widetilde{F}^+_{\mu\nu}u_\alpha\right] D_\beta + \mathrm{H.c.}\right) N \\
&+ d_9\bar{N}\left(\frac{1}{2m_N} i\epsilon^{\mu\nu\alpha\beta}\mathrm{Tr}\left[F^+_{\mu\nu}\right] u_\alpha D_\beta + \mathrm{H.c.}\right) N \\
&+ d_{16}\bar{N}\left(\frac{1}{2}\gamma^\mu\gamma_5\mathrm{Tr}\left[\chi_+\right] u_\mu\right) N + d_{18}\bar{N}\left(\frac{1}{2}\, i\gamma^\mu\gamma_5[D_\mu, \chi_-]\right) N \\
&+ d_{20}\bar{N}\left(-\frac{1}{8m_N^2} i\gamma^\mu\gamma_5[\widetilde{F}^+_{\mu\nu}, u_\lambda]D^{\lambda\nu} + \mathrm{H.c.}\right) N \\
&+ d_{21}\bar{N}\left(\frac{1}{2} i\gamma^\mu\gamma_5[\widetilde{F}^+_{\mu\nu}, u^\nu]\right) N + d_{22}\bar{N}\left(\frac{1}{2}\,\gamma^\mu\gamma_5[D^\nu, F^-_{\mu\nu}]\right) N + \cdots ,
\end{aligned} \tag{2.64}$$

where d_j $(j = 8, 9, 16, 18, 20, 21, 22)$ are new LECs appearing at $\mathcal{O}(p^3)$. The derivative operator $D_{\mu\nu} = \{D_\mu, D_\nu\}$ acts over the nucleon doublet and

$$\widetilde{F}^+_{\mu\nu} = F^+_{\mu\nu} - \frac{1}{2}\mathrm{Tr}\left[F^+_{\mu\nu}\right] . \tag{2.65}$$

The terms H.c. refer to the Hermitian conjugate field operator and the totally antisymmetric Levi-Civita tensor can be written as $\epsilon^{\mu\nu\alpha\beta} = -\frac{i}{8}\left[\{[\gamma^\mu, \gamma^\nu], \gamma^\alpha\}\gamma^\beta\right]\gamma^5$. While the pions appear through u_μ, the photon is contained in the tensors $F^\pm_{\mu\nu}$, $\widetilde{F}^+_\pm$.

In the present work, the terms $\mathcal{L}_N^{(2)}$ (2.63) and $\mathcal{L}_N^{(3)}$ (2.64) will be used at tree level only, as detailed in Section 4. Nevertheless, the lowest order Lagrangian term $\mathcal{L}_N^{(1)}$ (2.61) will enters in both, tree level and loop contributions.

Power Counting Breaking terms and the EOMS renormalization

At tree level, the lowest-order chiral Lagrangian for nucleons $\mathcal{L}_N^{(1)}$ (2.61) assimilates the successful calculations obtained at low-energy with the methods based on the use of current algebra and PCAC. The Lagrangian formulation for nucleon and pion interactions allows us now to improve those calculations by including higher orders and loop corrections.

As in the case of the purely pseudoscalar meson framework, one should be able to introduce a valid power counting scheme extended to the case with nucleons in order to organize the infinite contributions to a particular amplitude in a series of decreasing

importance. However, in the loop diagrams with inner nucleon lines the naive power counting is broken because of the nonzero nucleon mass, m, in the chiral limit [59]. This makes difficult the development of a scheme that allows for a systematic evaluation of higher orders in the chiral expansion. The reason is that m is of the same order as the scale for the chiral symmetry breaking Λ_χ. Then, contrary to the loops with pions where $M/\Lambda_\chi \sim \mathcal{O}(p)$, the power counting is spoiled. For processes with baryon number $B = 1$, the naive chiral order n of a given Feynman diagram reads

$$n = 4L + \sum_d n_d d - 2I_\pi - I_N, \tag{2.66}$$

for L loops, I_π pion propagators, I_N nucleon propagators and n_d vertices from the d-th order Lagrangian[19]. The formula (2.66) assigns a nominal chiral order for any specific diagram, but n does not necessarily reflects the actual chiral order of the resulting amplitude. Indeed, loop diagrams containing nucleon propagators yield contributions of lower orders.

This problem was first solved in the heavy-baryon (HB)ChPT approach [66, 67], at the expense of losing Lorentz covariance. This is a non-relativistic treatment where baryons are only slighty off-shell, as compared with their masses, whilst it proposes a two-fold expansion in powers of $p/m_N \sim p/\Lambda_\chi$. Then, in the regime of validity of ChPT, the nucleon field and its momentum and hence the nucleon propagator are redefined such that the loop diagrams explicitly fulfill the power counting of Eq. (2.66). As in ChPT for pions, the renormalization of LECs in HBChPT can be implemented order by order.

On the other hand, a comprehensive and precise description of the $SU(3)$ phenomenology, where large relativistic corrections have to be considered because of the K and η masses, has shown to be difficult in the HBChPT approach [68]. Similar problems appear with Born terms [69] where the positions of the poles are moved due to the expansion of the nucleon propagator. Besides that, at one-loop level the HB formalism misses anomalous threshold contributions in triangular graphs what leads to a poor convergence of form factors [2, 70]. Those facts suggested that relativistic corrections may be large and questioned the applicability of the HB expansion in some cases even at low energies.

The convergence problems and the lack of covariance of HBChPT reverted the interest to the original relativistic ChPT approach [59, 71] trying to develop a proper power counting and at the same time obtain the proper analytic structures[20]. The first attempt in that direction was due to Tang and Ellis [72, 73]. The most important step made by Ellis and Tang was to realize that the power counting violating terms were just polynomials. This makes it possible to come back to the relativistic theory and within this framework to get rid of these unwanted terms. Different novel methods were formulated soon after to organize the perturbative series in order to satisfy the formula, Eq. (2.66) [2–4]. See, *e.g.*, Ref. [47] for a review of the various schemes and the discussion in the introduction of Ref. [14]. Of these, we will focus our attention on the Infrared (IR) [2] and the Extended-On-Mass-Shell (EOMS) [4, 74] schemes. We will detail more on the latter, used in this work, in Sec. 4.2.4.

The infrared (IR)BChPT [2] scheme proposes to separate the loop amplitudes into the so-called infrared (I) and regular (R) parts. Given a covariant loop integral which

[19]The nucleon propagator counts like $\sim \mathcal{O}(p^{-1})$ since we assume that $\bar{N}(\not{D} - m)N \sim \mathcal{O}(p)$, Eq. (2.61).

[20]We refer to "proper analytic structures" by those derived from S-matrix theory and implemented automatically in a (Lorentz covariant) quantum field theory of dynamical pions and nucleons.

carries factors of the loop momentum in the numerator, it can be always be reduced to combinations of scalar loop functions:

$$H = \int \frac{d^D k}{(2\pi)^D} \frac{1}{a_1 \cdots a_m b_1 \cdots b_n} \tag{2.67}$$

$$= \int_0^1 dz_1 \cdots = \int_0^\infty dz_1 - \int_1^\infty dz_1 \cdots = I + R \tag{2.68}$$

with m meson-propagator denominators, a, and n baryon propagators, b. The I and R parts are obtained in terms of different integration limits of the Feynman parameters $z_1, ...$ [68]. It has been shown, that the I part contains all the non-analytical pieces and satisfies the power-counting formula, (2.66). The regular R part violates power counting, but it appears in the low energy region as a polynomial expansion in momenta and meson masses. Hence, in the IR formalism one can renormalize the baryon-ChPT by keeping only the I part of any loop amplitude and absorbing the R part in the LECs of the most general chiral Lagrangian.

One should note that the chiral expansion of R, apart from the power counting violating pieces, there is an infinite number of terms that do not violate power counting. In the IR scheme they are all subtracted by absorbing them in Lagrangian counterterms, but it is not necessary to do so. The basic idea behind the EOMS procedure is to keep those terms. In the EOMS scheme, the integrand of the loop integrals is expanded in the small parameters, pion masses and external momenta. Then, after being integrated, the terms violating the power counting are subtracted. The detailed procedure can be found in [30]. The EOMS scheme, in most cases, leads to a faster chiral convergence than HBChPT or IrChPT [10, 12, 14]. Moreover, it has been successfully applied to many processes, among them πN scattering [14, 16, 75, 76] and the pion electromagnetic production on the nucleons [20–22, 77]. Both are directly related to the processes investigated in this work.

2.2.3 Interaction Lagrangian for the spin-3/2 $\Delta(1232)$ resonance

When one considers also the spin-3/2 baryon multiplet, in the $SU(2)$ isospin case the $\Delta(1232)$ resonance, as an explicit degree of freedom, it can appear as an intermediate state in the processes of pion photo- and electroproduction on nucleons. The Δ resonance can interact with the relevant matter fields including pions, nucleons and the external photons. The relevant couplings are those for $\Delta\pi N$ and $\Delta\gamma N$ which are driven by the following Lagrangian terms [78],

$$\mathcal{L}^{(1)}_{\Delta\pi N} = \frac{ih_A}{2Fm_\Delta} \bar{N} T^a \gamma^{\mu\nu\lambda} (\partial_\mu \Delta_\nu) \partial_\lambda \pi^a + \text{H.c.}, \tag{2.69}$$

$$\mathcal{L}^{(2)}_{\Delta\gamma N} = \frac{3ieg_M}{2m_N(m_N + m_\Delta)} \bar{N} T^3 (\partial_\mu \Delta_\nu) \widetilde{f}^{\mu\nu} + \text{H.c.}, \tag{2.70}$$

with m_Δ the mass of the $\Delta(1232)$ and

$$\gamma^{\mu\nu\lambda} = \frac{1}{2} \left\{ \gamma^{\mu\nu}, \gamma^\lambda \right\}, \tag{2.71}$$

$$\gamma^{\mu\nu} = -i\sigma^{\mu\nu} = \frac{1}{2} \left[\gamma^\mu, \gamma^\nu \right], \tag{2.72}$$

$$\widetilde{f}^{\mu\nu} = \frac{1}{2} \varepsilon^{\mu\nu\alpha\beta} f_{\alpha\beta}, \tag{2.73}$$

where the EM field $f_{\alpha\beta} = \partial_\alpha \mathscr{A}_\beta - \partial_\beta \mathscr{A}_\alpha$, similarly to Eq. (2.45). The operator T^a, with $a = 1, 2, 3$ corresponding with the Cartesian pion fields π^a (2.19), is the isospin-3/2 $\mapsto$ 1/2 projector that couples consistently the isospin multiplet $\Delta_\nu = (\Delta_\nu^{++}, \Delta_\nu^{+}, \Delta_\nu^{0}, \Delta_\nu^{-})^T$ with the corresponding nucleon doublet N. The explicit representations of T^a follows the conventions in [31]. In detail,

$$T^1 = \frac{1}{\sqrt{6}} \begin{pmatrix} -\sqrt{3} & 0 & 1 & 0 \\ 0 & -1 & 0 & \sqrt{3} \end{pmatrix}, \tag{2.74}$$

$$T^2 = -\frac{i}{\sqrt{6}} \begin{pmatrix} \sqrt{3} & 0 & 1 & 0 \\ 0 & 1 & 0 & \sqrt{3} \end{pmatrix}, \tag{2.75}$$

$$T^3 = \sqrt{\frac{2}{3}} \begin{pmatrix} 0 & 1 & 0 & 0 \\ 0 & 0 & 1 & 0 \end{pmatrix}. \tag{2.76}$$

They satisfy the relation $T^a T^{\dagger b} = \delta^{ab} - \tau^a \tau^b/3$. The parameter h_A in $\mathcal{L}^{(1)}_{\Delta\pi N}$ (2.69) is the coupling constant related to the $\Delta \to \pi N$ transition at LO. At $\mathcal{O}(p^2)$ the coupling constant g_M in $\mathcal{L}^{(2)}_{\Delta\gamma N}$ (2.70) is related to the electromagnetic transition between the spin-1/2 nucleons and the spin-3/2 Δ resonance. As it will be discussed afterwards in Sec. 4.4, the diagram contributions including the explicit Δ vertices from $\mathcal{L}^{(1)}_{\Delta\pi N}$ and $\mathcal{L}^{(2)}_{\Delta\gamma N}$, do not introduce unknown LECs to be fitted. That is, the parameters h_A and g_M are directly related to the strong and electromagnetic decay of the $\Delta(1232)$ resonance and thus fitted to experimental values (see Table 4.5). The numerical value for h_A is extracted directly from the strong decay width of the $\Delta(1232)$ [79]. Analogously, the parameter g_M can be related directly to the Δ EM decay width, $\Gamma_\Delta^{\rm EM}$, given that it is experimentally known that $\Gamma_\Delta^{\rm EM}/(\Gamma_\Delta^{\rm EM} + \Gamma_\Delta^{\rm strong}) = 0.55\%, ..., 0.65\%$ [34, 80]. Also the parameter g_M has been fixed by other experimental sources related to pion EM production around the resonance peak [81].

The propagator for the spin-3/2 Δ state with momentum P corresponds to the inverse operator of the Rarita-Schwinger Lagrangian form [82],

$$S_\Delta^{\mu\nu}(P) = \frac{\not{P} + m_\Delta}{P^2 - m_\Delta^2 + i\epsilon} \left[-g^{\mu\nu} + \frac{1}{3}\gamma^\mu\gamma^\nu + \frac{(\gamma^\mu P^\nu - \gamma^\nu P^\mu)}{3m_\Delta} + \frac{2}{3m_\Delta^2} P^\mu P^\nu \right]. \tag{2.77}$$

The power counting scheme with Δs

The explicit inclusion of interactions with the $\Delta(1232)$ resonance leads us to an extra power counting problem. In the computation of the diagram amplitudes with the Δ, a small parameter δ/Λ_χ surges in addition to the chiral parameters $p_{\rm ext}/\Lambda_\chi$ and M_π/Λ_χ. The additional parameter appears as the mass splitting $\delta = m_\Delta - m_N \approx 300$ MeV, which is bigger than M_π, but still much smaller than Λ_χ. In consequence, this δ should be considered in a power counting rule that supersedes that of Eq. (2.50).

The dependence on δ of the Δ propagator (2.77), plays a central role to determine the chiral order of the corresponding amplitudes. Given that the Δ resonance surges in the $\gamma^{(*)} + N \longrightarrow \pi + N'$ process, the momentum P can always be written as the sum of a nucleon momentum p_N and an external momentum p_{ext}. Then,

$$\begin{aligned} P^2 - m_\Delta^2 =& (p_N + p_{ext})^2 - m_\Delta^2 = (m_N + m_\Delta)(m_N - m_\Delta) + \mathcal{O}(p_{ext}) \\ =& -(m_N + m_\Delta)\delta + \mathcal{O}(p_{ext}) \end{aligned} \tag{2.78}$$

There are several approaches to incorporate this dependence on the power counting formula, for instance the small-scale expansion (SSE) [83] and the δ-counting scheme

[84]. The δ scheme takes into account the fact that, at very low energies, $\{M_\pi, p_{ext}\} < \delta < \Lambda_\chi$. Then, the parameter δ is considered to count half the power contribution of the pion mass M_π, *i.e.* $\delta \sim \mathcal{O}(p^{1/2})$, since $(\delta/\Lambda_\chi)^2 \approx (M_\pi/\Lambda_\chi)$. In other words, the Δ-propagators, which count as $1/\delta$ will receive a power counting of $\mathcal{O}(p^{-1/2})$. Consequently, the power counting of Eq. (2.50) for any amplitude, but associated to a Feynman diagram with the explicit contribution of the $\Delta(1232)$, is extended as

$$n = 4L + \sum_{k=1}^{\infty} kV^{(k)} - 2N_\pi - N_N - \frac{1}{2}N_\Delta, \tag{2.79}$$

where N_Δ is the number of Δ-propagators. This rule is overall employed along the work presented here, given that the Δ contribution plays an important role in our low-energy calculations. It is worth to insist on the fact that the δ-counting of Eq. (2.79) is only well suited for energy regions well below the actual scale $\delta \approx 300$ MeV, as in the present work. Otherwise, for higher energies such that p_{ext} of similar size to δ, it could be necessary to consider the SSE counting. Both prescriptions have been shown to establish an adequate power counting for the δ parameter depending on the process and the energy range in question, see *e.g.* Refs. [14, 85].

Chapter 3

Formalism for pion EM production on nucleons

In order to detail the calculation of the relevant observables, in this chapter I review some of the general formalism to compute differential cross sections in terms of the scattering amplitude and kinematical functions. The scattering amplitude encodes all the model dependent parts, so I will concentrate here exclusively on the kinematical definitions and the model independent formalism to define the theoretical expressions for the cross sections for single pion production with EM sources. Moreover, I will show along the chapter some of the fundamental properties of the scattering amplitude such as the gauge invariance, crossing symmetry and the isospin decomposition.

In the first section are presented the needed tools for the pion production by electrons on nucleons $e+N \to e+\pi+N'$ within the one-photon exchange approximation. This approximation is useful in decomposing into a lepton and a purely hadron current where the low energy effective theory ChPT is particularly implemented.

In the second section I review the formalism for pion photoproduction on nucleons $\gamma + N \to \pi + N'$ as a limiting case of the pion electroproduction for the kinematical relations. The subsequent amplitude calculation is simply a reduced case of the electroproduction amplitude. Even so, some particular observables in photoproduction are revisited.

The last section addresses the isospin structure of the pion production amplitudes, by introducing the isospin multiplets for pions and nucleons and the corresponding amplitude decomposition for the different physical channels.

3.1 Pion electroproduction on nucleons

In this section I wish to detail the general structure of the pion electroproduction amplitude and to illustrate briefly the specific requirements, such as invariance and conservation laws. Furthermore, I shall develop the derivation of the kinematical relations which are necessary for calculating pion production by electrons.

3.1.1 Matrix element and kinematics

The scattering amplitude for the pion electroproduction on nucleons can be decomposed into a lepton vertex, a virtual photon propagator and a hadron vertex [86], as shown in Fig. 3.1. Then, the corresponding $\mathcal{T}$-matrix element is given by the one-photon exchange approximation as follows

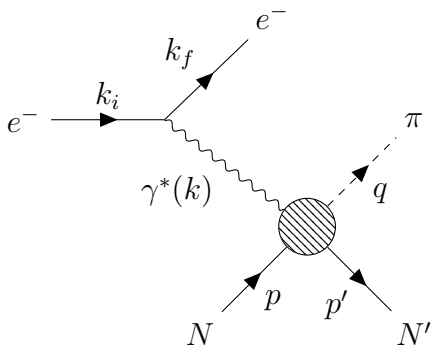

FIGURE 3.1: Diagram for the pion electroproduction on nucleon. The incoming nucleon and electron momenta are denoted by p and k_i, the outgoing nucleon, pion and electron momenta are given by p', q and k_f respectively. The virtual photon γ^* carries the corresponding transferred momentum k. The cross-dashed blob stands for the hadronic vertex.

$$\begin{aligned}\mathcal{T} =& \underbrace{ie\bar{u}(k_f, s_f)\gamma^\nu u(k_i, s_i)}_{\text{Lepton vertex}} \underbrace{\left(i\frac{-g_{\mu\nu}}{k^2 + i\epsilon}\right)}_{\text{Virtual photon propagator}} \underbrace{\left(-ie\langle N'\pi|J^\mu(0)|N\rangle\right)}_{\mathcal{H}^\mu} \\ =& \epsilon_\mu \mathcal{H}^\mu,\end{aligned} \tag{3.1}$$

with $\mathcal{H}^\mu = -ie\langle N'\pi|J^\mu|N\rangle$ the matrix element for the hadronic 4-current, J^μ, corresponding to the initial nucleon N and final nucleon-pion $N'\pi$ states, e is the electric charge, $g_{\mu\nu}$ is the Lorentz metric tensor with components $\mathsf{diag}(1, -1, -1, -1)$, γ^ν the Dirac matrix and $u(k_{i(f)}, s_{i(f)})$ is the Dirac spinor for the initial (final) electron with 4-momentum $k_{i(f)}$ and spin $s_{i(f)}$. Here, the polarization vector is defined as

$$\epsilon^\mu = \frac{e\bar{u}(s_f, k_f)\gamma^\mu u(k_i, s_i)}{k^2}, \tag{3.2}$$

where the 4-momentum components for the virtual-photon, γ^*, are

$$k^\mu = k_i^\mu - k_f^\mu. \tag{3.3}$$

The kinematics of the process displayed in Fig. 3.1 follows the 4-momentum conservation

$$k_i^\mu + p^\mu = k_f^\mu + p'^\mu + q^\mu \qquad \text{or} \qquad k^\mu + p^\mu = p'^\mu + q^\mu, \tag{3.4}$$

in terms of the virtual photon transferred momentum, k^μ as in Eq. (3.3). This is analogue to the four-momenta conservation for the hadron vertex corresponding to the process $\gamma^*(k) + N(p) \to \pi(q) + N'(p')$.

For the 4-momenta appearing in Fig. 3.1, the used notation is given by components as follows

$$\begin{aligned} k_i^\mu &= \left(\mathcal{E}_i, \vec{k}_i\right) \\ k_f^\mu &= \left(\mathcal{E}_f, \vec{k}_f\right) \\ p^\mu &= (E_p, \vec{p}) \\ p'^\mu &= \left(E_{p'}, \vec{p'}\right) \\ k^\mu &= \left(E_\gamma, \vec{k}\right) \\ q^\mu &= (E_\pi, \vec{q}) \end{aligned} \tag{3.5}$$

Considering only the virtual-photon and the hadrons, since we only have three independent impulses, we can use the so-called Mandelstam variables. These are defined as the invariants

$$\begin{aligned} s =& (p+k)^2 = (p'+q)^2, \\ u =& (p-q)^2 = (p'-k)^2, \\ t =& (p-p')^2 = (q-k)^2. \end{aligned} \tag{3.6}$$

Energy-momentum conservation (3.4) and the on-mass-shell restrictions $p^2 = p'^2 = m_N^2$, $q^2 = M_\pi^2$ and $k^2 = -Q^2$ lead to the equation

$$s + t + u = 2m_N^2 + M_\pi^2 - Q^2, \tag{3.7}$$

being Q positively defined for the virtual photon. This leaves only two independent Mandelstam invariants.
Specifically, the computation of the scattering amplitude will be expressed in the $\pi - N'$ final state frame (c.m.), or equivalently the c.m. $\gamma^* - N$ initial state, *i.e.*,

$$\vec{p}^* = -\vec{k}^* \Longleftrightarrow \vec{p'}^* = -\vec{q}^*, \tag{3.8}$$

where the asterisk, $*$, denotes the components as seen from the c.m. frame. On this frame, the energies and momenta can be written in terms of invariant terms as

$$\begin{aligned} E_\gamma^* =& \frac{1}{2\sqrt{s}}\left(s - m_N^2 - Q^2\right), \\ E_\pi^* =& \frac{1}{2\sqrt{s}}\left(s + M_\pi^2 - m_N^2\right), \\ E_p^* =& \frac{1}{2\sqrt{s}}\left(s + m_N^2 + Q^2\right), \\ E_{p'}^* =& \frac{1}{2\sqrt{s}}\left(s + m_N^2 - M_\pi^2\right), \\ |\vec{k}^*| =& \sqrt{E_\gamma^{*2} + Q^2}, \\ |\vec{q}^*| =& \sqrt{E_\pi^{*2} - M_\pi^2}, \\ |\vec{p}^*| =& \sqrt{E_p^{*2} - m_N^2}, \\ |\vec{p'}^*| =& \sqrt{E_{p'}^{*\,2} - m_N^2}. \end{aligned} \tag{3.9}$$

Accordingly to Eq. (3.8) only two of these equations can be independent. Those are very useful given that the frame transformation is straightforward through the Mandelstam invariant, s. In particular, they may be obtained from the Laboratory frame energy as in some typical experimental data where the target nucleon is considered at rest.
In addition to the energy and momentum magnitudes, the process $\gamma^*(k) + N(p) \to \pi(q) + N'(p')$ depends also on the π-γ^* scattering angle (see Fig. 3.2). This angle in the π-N' c.m. frame is given as $\cos\theta^*_\pi = \hat{k^*} \cdot \hat{q^*}$ and enters, by the definition (3.6), exclusively in the Mandelstam invariants u and t. Explicitly, we show one of them:

$$u = -Q^2 + m_N^2 - 2\left(E^*_\gamma E^*_{p'} + |\vec{k}^*||\vec{p'}^*|\cos\theta^*_\pi\right). \tag{3.10}$$

Again, this equation can serve to transform the c.m. angle to any frame through the invariant u (or t). For instance, in the photoproduction case this expression is useful for transforming some experimental data where the angle θ_π is given in the Lab. frame as will be later discussed.
From here, I will write all the 4-vector components in the c.m. frame omitting the *-symbol, except when mentioned explicitly.

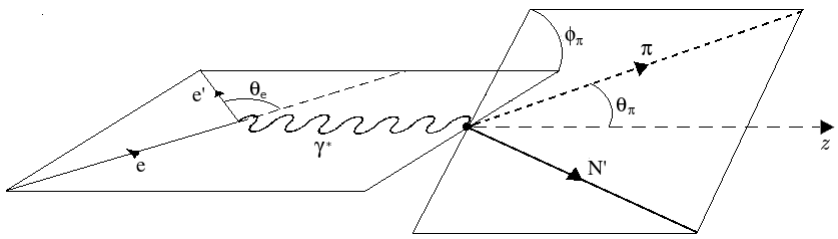

FIGURE 3.2: Kinematics for a typical experiment (in the Lab. frame), leading to out-of-plane pion production. The θ_π angle indicates the deviation of pion 3-momentum from the initial virtual-photon 3-momentum, ϕ_π corresponds to the relative angle between the electron-scattering plane and the pion-nucleon final state plane.

Returning to the scattering amplitude from Eq. (3.1), the hadronic matrix element

$$\mathcal{H}_\mu = -ie\left\langle N', \pi\left|J_\mu(0)\right|N\right\rangle, \tag{3.11}$$

as I will detail in the next part 3.1.2, can be represented in terms of Dirac matrices and 4-momenta. Those, at the same time, are functions of only three independent invariants, for example

$$\mathcal{H}^\mu(s, u, Q^2). \tag{3.12}$$

In the particular π-N' c.m. frame, the matrix $\mathcal{H}^\mu$ can be set, alternatively, as a function on the c.m. energy, $W = (E\gamma + E_p) = \sqrt{s}$, and the c.m. angle $\cos\theta_\pi$, see Eq. (3.10), as given in the electroproduction experimental data used in this work.

3.1.2 Amplitude parametrization

There are several parametrizations concerning the hadron vertex, $\mathcal{H}^\mu$, according with the possible independent combinations in the Dirac-matrix representation that can occur for the analytical $\gamma^* + N \to \pi + N'$ expression. As seen in Eq. (3.11), the 4-current J^μ encoding transition among initial and final states, can be expressed in terms

of the Dirac matrices representation and three independent 4-momenta. Additionally, as the origin of the 4-current relies on the gauge invariance of the ChPT Lagrangian terms, it is a conserved current by definition implying the gauge invariance for the hadron vertex $\mathcal{H}^\mu$, as will be detailed below. From this point, operating the initial and final hadronic states, $|N\rangle$ and $|N'\pi\rangle$, with J^μ for the specific matrix element in Eq. (3.11), the most general expression for $\mathcal{H}^\mu$ can be written in terms of the Ball amplitudes [87],

$$\mathcal{H}^\mu = \bar{u}(p', s') \left(\sum_{i=1}^{8} b_i V_i^\mu \right) u(p, s), \tag{3.13}$$

where $\bar{u}(p', s') = u^\dagger(p', s')\gamma^0$ is the reduced Dirac spinor for the final nucleon field with momentum p' and spin s', $u(p, s)$ the corresponding spinor for the initial nucleon field, b_i are i-th scalar complex functions of (s, u, Q) and the Ball 4-vector basis elements are defined as

$$\begin{aligned} V_1^\mu &= \gamma^\mu\gamma^5, \;\; V_2^\mu = P^\mu\gamma^5, \\ V_3^\mu &= q^\mu\gamma^5, \;\; V_4^\mu = k^\mu\gamma^5, \\ V_5^\mu &= \gamma^\mu \not{k}\gamma^5, \;\; V_6^\mu = P^\mu \not{k}\gamma^5, \\ V_7^\mu &= q^\mu \not{k}\gamma^5, \;\; V_8^\mu = k^\mu \not{k}\gamma^5, \end{aligned} \tag{3.14}$$

where $P^\mu = (p^\mu + p'^\mu)/2$. Although the Ball amplitudes represent an irreducible set of 4-vector combinations, they are not invariant under gauge transformations. However, this amplitude can be further reduced when the gauge invariance condition is introduced. As it was aforementioned, the conserved current, J^μ, obeys the continuity equation, $\partial_\mu J^\mu(x) = 0$. The conservation of the 4-current implies the gauge invariance relation, [1]

$$k_\mu \mathcal{H}^\mu = 0. \tag{3.15}$$

Thus, applying the condition (3.15) to the matrix element in terms of the Ball basis Eq. (3.13), gives us a pair of constraints for the coefficients b_i. Without losing generality we can write in particular that

$$\begin{aligned} b_1 =& - b_6(k \cdot P) - b_7(k \cdot q) + b_8 Q^2, \\ b_2 =& \frac{1}{k \cdot P} \left(Q^2(b_4 + b_5) - b_3(k \cdot q) \right). \end{aligned} \tag{3.16}$$

Satisfying these relations is enough to ensure the gauge invariance for the amplitude $\mathcal{H}^\mu$, Eq. (3.13). Furthermore, by keeping these particular gauge invariance constraints, we can reduce the dimension of the Ball vector basis (3.14) from 8 to 6 independent vectors because of the linear dependence for a couple of coefficients, b_i.

[1] J^μ can be boosted in the space-time as an usual operator like $e^{iP\cdot x} J^\mu(0) e^{-iP\cdot x} = J^\mu(x)$. Then,

$$\begin{aligned} 0 =& - e \left\langle \pi(q), N'(p') \right| \partial_\mu J^\mu(x) \left| N(p) \right\rangle = -e\partial_\mu \left\langle \pi(q), N'(p') \left| e^{iP\cdot x} J^\mu(0) e^{-iP\cdot x} \right| N(p) \right\rangle \\ =& - e\partial_\mu \left\langle \pi(q), N'(p') \left| e^{i(q+p')\cdot x} J^\mu(0) e^{-ip\cdot x} \right| N(p) \right\rangle = -e\partial_\mu e^{i(q+p'-p)\cdot x} \left\langle \pi(q), N'(p') \right| J^\mu(0) \left| N(p) \right\rangle \\ =& - iek_\mu e^{ik\cdot x} \left\langle \pi(q), N'(p') \right| J^\mu(0) \left| N(p) \right\rangle = e^{ik\cdot x} k_\mu \mathcal{H}^\mu. \end{aligned}$$

3.1.3 Gauge invariant amplitude

Another common and useful parametrization is implemented in terms of a covariant and gauge invariant vector basis M_i^μ [88,89]. In this way, the matrix element $\mathcal{H}^\mu$ can be expressed as

$$\mathcal{H}^\mu = \bar{u}(p', s') \left(\sum_{j=1}^{6} A_j M_j^\mu \right) u(p, s) \tag{3.17}$$

with the corresponding scalar complex functions A_j and where

$$\begin{aligned}
M_1^\mu =& -\frac{i}{2}\gamma^5 \left(\gamma^\mu \not{k} - \not{k}\gamma^\mu\right), \\
M_2^\mu =& 2i\gamma^5 \left(P^\mu k \cdot \left(q - \frac{1}{2}k\right) - \left(q - \frac{1}{2}k\right)^\mu k \cdot P \right), \\
M_3^\mu =& -i\gamma^5 \left(\gamma^\mu (k \cdot q) - q^\mu \not{k}\right), \\
M_4^\mu =& i m_N \gamma^5 (\gamma^\mu \not{k} - \not{k}\gamma^\mu) - 2i\gamma^5 (\gamma^\mu k \cdot P - P^\mu \not{k}), \\
M_5^\mu =& i\gamma^5 \left(k^\mu (k \cdot q) + Q^2 q^\mu\right), \\
M_6^\mu =& -i\gamma^5 \left(k^\mu \not{k} + Q^2 \gamma^\mu\right).
\end{aligned} \tag{3.18}$$

The expansion on this basis automatically implements the gauge invariance condition over $\mathcal{H}^\mu$ due to $k_\mu M_j^\mu = 0$ for each j-th basis element. The verification of this property is straightforward using the on mass-shell relations, (3.6) and (3.7).
In principle, as mentioned above, one can discard two of the eight Ball amplitudes. The transformation rules between the parametrizations in the gauge invariant basis (3.17) and the Ball basis (3.13) are obtained by taking

$$\sum_{i=3}^{8} b_i V_i^\mu = \sum_{j=1}^{6} A_j M_j^\mu . \tag{3.19}$$

Then, the corresponding relations among both vector basis are

$$\begin{aligned}
A_1 =& i(b_5 + b_6 m_N), \\
A_2 =& -\frac{i\left(-b_3(k \cdot q) + (b_4 + b_5)Q^2\right)}{(k \cdot P)(2k \cdot q + Q^2)}, \\
A_3 =& i b_7, \\
A_4 =& \frac{i b_6}{2}, \\
A_5 =& -\frac{i(b_3 + 2(b_4 + b_5))}{2k \cdot q + Q^2}, \\
A_6 =& -i b_8 .
\end{aligned} \tag{3.20}$$

In this sense, we can rely on a systematic procedure for going from the most general parametrization form of the hadron vertex $\mathcal{H}^\mu$ (3.13) and translating it into a gauge invariant amplitude using the Eqs. (3.20).

An additional parametrization for the scattering amplitude, $\mathcal{T}$, in Eq. (3.1) was derived by [88,90]. This parametrization allows for a more direct and easier translation for the observable calculations in the c.m. frame. At difference with the previous parametrizations in terms of Dirac matrices, the so-called Chew-Goldberger-Low-Nambu (CGLN) amplitude, $\mathcal{F}$ acts over the Pauli nucleon spinor components, χ^s,

with spin $s = 1/2$. Explicitly,

$$\mathcal{T} = \epsilon^\mu \mathcal{H}_\mu = 4\pi \frac{W}{m_N} \chi_f^\dagger \mathcal{F} \chi_i \,, \tag{3.21}$$

where χ_i and χ_f denote the initial and final Pauli spinors, $W = \sqrt{s}$ is the invariant energy and the matrix $\mathcal{F}$ is written as

$$\begin{aligned} \mathcal{F} =& i\,\vec{\tau}\cdot\vec{a}_\perp\,\mathcal{F}_1 + \vec{\tau}\cdot\hat{q}\,\vec{\tau}\cdot\hat{k}\times\vec{a}_\perp\,\mathcal{F}_2 + i\,\vec{\tau}\cdot\hat{k}\,\hat{q}\cdot\vec{a}_\perp\,\mathcal{F}_3 \\ &+ i\,\vec{\tau}\cdot\hat{q}\,\hat{q}\cdot\vec{a}_\perp\,\mathcal{F}_4 + i\,\vec{\tau}\cdot\hat{k}\,\hat{k}\cdot\vec{a}_\parallel\,\mathcal{F}_5 + i\,\vec{\tau}\cdot\hat{q}\,\hat{k}\cdot\vec{a}_\parallel\,\mathcal{F}_6. \end{aligned} \tag{3.22}$$

Here, $\vec{\tau} = (\tau^1, \tau^2, \tau^3)$ are the Pauli matrices. The particularity of this basis is that the different components are split into transverse and parallel contributions relative to the photon momentum $\vec{k}$. This is organized with the auxiliary polarization vector components $\vec{a}_\perp$ and $\vec{a}_\parallel$. The four-vector a^μ is defined such that its time component is zero [91],

$$a^\mu = \epsilon^\mu - k^\mu \frac{\epsilon_0}{E_\gamma} = \epsilon^\mu - k^\mu \frac{\vec{k}\cdot\vec{\epsilon}}{E_\gamma^2}, \tag{3.23}$$

where the Lorentz condition, $k_\mu \epsilon^\mu = 0$, has been used and

$$\vec{a} = \vec{a}_\parallel + \vec{a}_\perp, \tag{3.24}$$

$$\vec{a}_\parallel = \vec{a}\cdot\hat{k}\hat{k} = \frac{k^2}{E_\gamma^2}\vec{\epsilon}\cdot\hat{k}\hat{k}, \tag{3.25}$$

$$\vec{a}_\perp = \vec{a} - \vec{a}_\parallel = \vec{\epsilon} - \vec{\epsilon}\cdot\hat{k}\hat{k} = \vec{\epsilon}_\perp. \tag{3.26}$$

Again, to complete the last bridge among parametrizations we can go from the invariant basis (3.18) to the CGLN basis (3.22) taking the Eqs. (3.17) and (3.21),

$$\epsilon_\mu \bar{u}(p_f) \left(\sum_{i=1}^{6} A_i M_i^\mu \right) u(p_i) = 4\pi \frac{W}{m_N} \chi_f^\dagger \mathcal{F} \chi_i \,. \tag{3.27}$$

Then, we find, expressed in the c.m. frame, the relations between the coefficients of both parametrizations as [92]

$$\begin{aligned} \mathcal{F}_1 =& \frac{W - m_N}{8\pi W} \sqrt{E_p + m_N}\sqrt{E_{p'} + m_N} \\ &\times \left\{ A_1 + (W - m_N)A_4 - \frac{2m_N \nu_B}{W - m_N}(A_3 - A_4) + \frac{Q^2}{W - m_N} A_6 \right\}, \\ \mathcal{F}_2 =& \frac{W + m_N}{8\pi W} |\vec{q}| \sqrt{\frac{E_p - m_N}{E_{p'} + m_N}} \left\{ -A_1 + (W + m_N)A_4 - \frac{2m_N \nu_B}{W + m_N}(A_3 - A_4) + \frac{Q^2}{W + m_N} A_6 \right\}, \\ \mathcal{F}_3 =& \frac{W + m_N}{8\pi W} |\vec{q}| \sqrt{E_p - m_N}\sqrt{E_{p'} + m_N} \left\{ \frac{2W^2 - 2m_N^2 + Q^2}{2(W + m_N)} A_2 + A_3 - A_4 - \frac{Q^2}{W + m_N} A_5 \right\}, \\ \mathcal{F}_4 =& \frac{W - m_N}{8\pi W} |\vec{q}|^2 \sqrt{\frac{E_p + m_N}{E_{p'} + m_N}} \left\{ -\frac{2W^2 - 2m_N^2 + Q^2}{2(W - m_N)} A_2 + A_3 - A_4 + \frac{Q^2}{W - m_N} A_5 \right\}, \\ \mathcal{F}_5 =& \frac{E_\gamma}{8\pi W} \sqrt{\frac{E_{p'} + m_N}{E_p + m_N}} \Bigg\{ [E_p + m_N] A_1 \end{aligned}$$

$$
\begin{aligned}
&+\left[4m_N\nu_B\left(W-\frac{3}{4}E_\gamma\right)-|\vec{k}|^2W+E_\pi\left(W^2-m_N^2+\frac{1}{2}Q^2\right)\right]A_2\\
&+[E_\pi(W+m_N)+2m_N\nu_B]A_3\\
&+[(E_p+m_N)(W-m_N)-E_\pi(W+m_N)-2m_N\nu_B]A_4\\
&+\left[2m_N\nu_BE_\gamma-E_\pi Q^2\right]A_5-[(E_p+m_N)(W-m_N)]A_6\Bigg\},\\
\mathcal{F}_6=&\frac{E_\gamma}{8\pi W}\frac{|\vec{q}|}{\sqrt{(E_{p'}+m_N)(E_p-m_N)}}\Bigg\{-[Ep-m_N]A_1\\
&+\left[|\vec{k}|^2W-4m_N\nu_B\left(W-\frac{3}{4}E_\gamma\right)-E_\pi\left(W^2-m_N^2+\frac{1}{2}Q^2\right)\right]A_2\\
&+[E_\pi(W-m_N)+2m_N\nu_B]\,A_3\\
&+[(E_p-m_N)(W+m_N)-E_\pi(W-m_N)-2m_N\nu_B]\,A_4\\
&+\left[E_\pi Q^2-2m_N\nu_BE_\gamma\right]A_5-[(E_p-m_N)(W+m_N)]A_6\Bigg\},
\end{aligned}
\tag{3.28}
$$

where $\nu_B=-\dfrac{k\cdot q}{2m_N}=-\dfrac{s+u-2m_N^2}{4m_N}$.

Furthermore, it is common to expand the CGNL amplitudes, $\mathcal{F}_i$, in multipole functions (see App. D), when the contributions for different angular momenta are of interest.

3.1.4 Observables

The cross section for the pion electroproduction process, $e(k_i)+N(p,s)\to e(k_f)+\pi(q)+N'(p',s')$ of Fig. 3.1, in the Bjorken and Drell notation [93], is given by

$$
d\sigma=\frac{1}{\left|\vec{v}_1-\vec{V}_1\right|}\frac{m_e}{\mathcal{E}_i}\frac{m_N}{E_p}\left|\mathcal{T}\right|^2\frac{d^3k_f}{(2\pi)^3}\frac{m_e}{\mathcal{E}_f}\frac{d^3p'}{(2\pi)^3}\frac{m_N}{E_{p'}}\frac{d^3q}{(2\pi)^3}\frac{1}{2E_\pi}(2\pi)^4\delta^4\left(k_i+p-k_f-p'-q\right)
\tag{3.29}
$$

where $\left|\vec{v}_1-\vec{V}_1\right|$ is the flux factor, with $\vec{v}_1$and $\vec{V}_1$ the velocity of the initial electron and nucleon respectively. For practical purposes, lets consider the angular distribution of the pions in the hadronic πN c.m. frame and the energy distribution of the electron at the laboratory frame, where the target nucleon is at rest. In fact $|\vec{v}_1-\vec{V}_1|\mathcal{E}_iE_p$ is a frame invariant quantity. So, we have that

$$
\vec{V}_1=0\qquad\text{and}\qquad\vec{v}_1=\frac{\vec{k}_i}{\mathcal{E}_i}\approx\hat{k}_i,
\tag{3.30}
$$

given that the electron mass, $m_e<<|\vec{k}_i|$. Then, the flux

$$
\left|\vec{v}_1-\vec{V}_1\right|\approx 1,
\tag{3.31}
$$

and we get, under the assumption that the nucleon is not detected in the final state, the differential cross section

$$
\frac{d\sigma}{d\mathcal{E}_fd\Omega_ed\Omega_\pi^*}=\frac{1}{(2\pi)^5}m_e^2\frac{\mathcal{E}_f}{\mathcal{E}_i}\frac{m_N|\vec{q}|}{W}\frac{1}{2}\left|\mathcal{T}\right|^2
\tag{3.32}
$$

with

$$
\begin{aligned}
|\mathcal{T}|^2 &= (\epsilon_\mu \mathcal{H}^\mu)^* \, \epsilon_\nu \mathcal{H}^\nu \\
&= \frac{e^2}{(k^2)^2} \left[\bar{u}(s_f, k_f)\gamma_\mu u(k_i, s_i)\right]^* \left[\bar{u}(s_f, k_f)\gamma_\nu u(k_i, s_i)\right] \underbrace{\mathcal{H}^{\mu *}\mathcal{H}^\nu}_{W^{\mu\nu}} \\
&= \frac{e^2}{(k^2)^2} \eta_{\mu\nu} W^{\mu\nu}. \qquad (3.33)
\end{aligned}
$$

Here, $\eta_{\mu\nu}$ is the leptonic tensor defined by $\epsilon_\mu^* \epsilon_\nu = e^2/(k^2)^2 \eta_{\mu\nu}$, and $W^{\mu\nu} = \mathcal{H}^{\mu *}\mathcal{H}^\nu$ is the corresponding hadronic tensor [see Eq. (3.11)] written as [89]

$$
W^{\mu\nu} = (m_N/4\pi W)^2 \left\langle \chi_f \left| J^\mu \right| \chi_i \right\rangle^* \left\langle \chi_f \left| J^\nu \right| \chi_i \right\rangle, \qquad (3.34)
$$

with $|\chi_{i,f}\rangle$ denoting the initial and final Pauli spinors for nucleons. The 4-current operator is written in the πN c.m. through the CGLN parametrization (3.21) as

$$
\begin{aligned}
\vec{J} =& \frac{4\pi W}{m_N} \Big[i\,\tilde{\vec{\tau}}\,\mathcal{F}_1 + (\vec{\tau}\cdot\hat{q}) \left(\vec{\tau}\times\hat{k}\right) \mathcal{F}_2 + i\tilde{\vec{q}} \left(\vec{\tau}\cdot\hat{k}\right) \mathcal{F}_3 + i\tilde{\vec{q}} (\vec{\tau}\cdot\hat{q})\, \mathcal{F}_4 \\
& + i\hat{k} \left(\vec{\tau}\cdot\hat{k}\right) \mathcal{F}_5 + i\hat{k}\,(\vec{\tau}\cdot\hat{q})\, \mathcal{F}_6 \Big] \qquad (3.35) \\
\rho =& \frac{4\pi W}{m_N} \Big[i\,(\vec{\tau}\cdot\hat{q})\, \mathcal{F}_7 + i(\vec{\tau}\cdot\hat{k})\, \mathcal{F}_8 \Big] = \frac{\vec{k}\cdot\vec{J}}{k_0} \qquad (3.36)
\end{aligned}
$$

with

$$
\tilde{\vec{\tau}} = \vec{\tau} - (\vec{\tau}\cdot\hat{k})\hat{k}, \qquad \tilde{\vec{q}} = \vec{q} - (\vec{q}\cdot\hat{k})\hat{k}. \qquad (3.37)
$$

The right side for ρ in (3.36) is written in terms of the space components $\vec{J}$ due to $k_\mu J^\mu = 0$.

Concerning the leptonic part in (3.33), for unpolarized electrons we average and sum over their initial and final electronic spins respectively, obtaining

$$
\begin{aligned}
\overline{\eta}_{\mu\nu} =& \frac{1}{2} \sum_{s_i, s_f} \left[\bar{u}(s_f, k_f)\gamma_\mu u(k_i, s_i)\right]^* \left[\bar{u}(s_f, k_f)\gamma_\nu u(k_i, s_i)\right] \\
=& \frac{1}{2m_e^2} \left[k_{i\mu} k_{f\nu} + k_{i\nu} k_{f\mu} + g_{\mu\nu} \left(m_e^2 - k_i \cdot k_f\right) \right]. \qquad (3.38)
\end{aligned}
$$

Please note that for unpolarized electrons, this tensor is symmetric for Lorentz components, $\overline{\eta}_{\mu\nu} = \overline{\eta}_{\nu\mu}$. Now, when incoming electrons have a defined helicity polarization the sum runs only over the final spins and results in

$$
\begin{aligned}
\eta_{\mu\nu} =& \sum_{s_f} \left[\bar{u}(s_f, k_f)\gamma_\mu u(k_i, s_i)\right]^* \left[\bar{u}(s_f, k_f)\gamma_\nu u(k_i, s_i)\right] \\
=& \overline{\eta}_{\mu\nu} + \frac{i}{2m_e} h\, \varepsilon_{\mu\nu\sigma\rho} k_i^\sigma k_f^\rho, \qquad (3.39)
\end{aligned}
$$

with $\varepsilon_{0123} = 1$. The helicity for the incoming electron is given here through $h = \vec{\tau}\cdot\hat{k}_i = \pm 1$. I recall again that for this more general tensor, the polarized electron term corresponds to an anti-symmetric tensor part proportional to h.

In order to define the different contributions from the virtual photon polarization components and helicity onto the differential cross section, I consider the following

coordinate system defined by the incoming-outgoing electrons as

$$\hat{e}_z = \hat{k}, \quad \hat{e}_y = \frac{\hat{k}_i \times \hat{k}_f}{\sin\theta_e}, \quad \hat{e}_x = \hat{e}_y \times \hat{e}_z, \tag{3.40}$$

where $\theta_e = \arccos \hat{k}_i \cdot \hat{k}_k$. The transversal polarization of virtual.photon is defined by [91]

$$\varepsilon = \frac{|\mathscr{A}_x|^2 - |\mathscr{A}_y|^2}{|\mathscr{A}_x|^2 + |\mathscr{A}_y|^2} = \frac{\eta_{xx} - \eta_{yy}}{\eta_{xx} + \eta_{yy}}, \tag{3.41}$$

and the longitudinal polarization

$$\varepsilon_L = \frac{|\mathscr{A}_z|^2}{|\mathscr{A}_x|^2 + |\mathscr{A}_y|^2} = \left(\frac{k^2}{k_0^2}\right)^2 \frac{\eta_{zz}}{\eta_{xx} + \eta_{yy}}, \tag{3.42}$$

where $\mathscr{A}_\mu$ are the components of the vector potential for the virtual-photon and $\eta_{\mu\nu}$ is the matrix element of the photon polarization density as in (3.39). The polarization density η_{zz} is defined through the lepton tensor components $\epsilon_z^* \epsilon_z$ and the factor k^2/k_0^2 in (3.42) is a conventional current conserving term that includes the temporal component contributions depending on the coordinate system (3.40), as detailed below.

Some simplifying conventions are introduced here such that our description is reduced to the terms involving only the transversal polarization ε. In detail, we follow the next considerations:

- Applying the Lorentz condition $k_\mu \epsilon^\mu = 0$ then $k^\mu \eta_{\mu\nu} = 0 = \eta_{\mu\nu} k^\nu = 0$, jointly with the current conserved hadron amplitude, $k_\mu \mathcal{H}^\mu = 0$, leads to the similar relation $k_\mu W^{\mu\nu} = 0 = W^{\mu\nu} k_\nu$. Consequently, these relations imply that it is sufficient to consider only space components for ϵ_μ,, $\mathcal{H}^\mu$, $\eta_{\mu\nu}$ and $W^{\mu\nu}$. Therefore, we can write the temporal components in terms of the spatial ones

$$\begin{aligned} \epsilon_0 =& \vec{k} \cdot \vec{\epsilon}/k_0, & \mathcal{H}^0 =& \vec{k} \cdot \vec{\mathcal{H}}/k_0, \\ \eta_{0\nu} =& \frac{k_i}{k_0} \eta_{i\nu}, & W^{0\nu} =& \frac{k_i}{k_0} W^{i\nu}, \end{aligned} \tag{3.43}$$

  for $i = \{x, y, z\}$ as summation index. One gets analogous relations for the exchanged index cases $\eta_{\nu 0}$ and $W^{\nu 0}$.

- The second choice here relies on the convenient direction of the virtual-photon along the z-axis, explicitly $k^\mu = (k_0, 0, 0, |\vec{k}|)^\top$. This additional convention further reduces the 3-momentum scalar products (3.43) to the z-components. Specifically,

$$\epsilon_0 = |\vec{k}| \epsilon_z / k_0, \qquad \mathcal{H}^0 = |\vec{k}| \mathcal{H}_z / k_0 \tag{3.44}$$

$$\eta_{0\nu} = \frac{|\vec{k}|}{k_0} \eta_{z\nu}, \qquad W^{0\nu} = \frac{|\vec{k}|}{k_0} W^{z\nu}. \tag{3.45}$$

As a consequence of the above considerations, the scattering amplitude $\mathcal{T}$ results in only space dependent components,

$$\begin{aligned}\epsilon_\mu \mathcal{H}^\mu =& \epsilon_0 \mathcal{H}^0 - \vec{\epsilon}\cdot\vec{\mathcal{H}} = -\epsilon_x \mathcal{H}_x - \epsilon_x \mathcal{H}_x - \left(1 - \frac{|\vec{k}|^2}{k_0^2}\right)\epsilon_z \mathcal{H}_z \\ =& -\left(\epsilon_x \mathcal{H}_x + \epsilon_y \mathcal{H}_y + \frac{k^2}{k_0^2}\epsilon_z \mathcal{H}_z\right). \end{aligned} \tag{3.46}$$

These relations imply that it is sufficient to consider only the space components of $\eta_{\mu\nu}$ and $W_{\mu\nu}$. We can include the current conservation factor k^2/k_0^2 in the lepton contribution to $|\mathcal{T}|^2$ (3.33) and ignore it in the hadronic part. The same factor appears then in the longitudinal polarization definition as in (3.42).

In detail, the tensor product $\eta_{\mu\nu}W^{\mu\nu}$ in Eq. (3.33), for unpolarized electrons contains just the relevant spatial components from (3.38). Explicitly,

$$\begin{aligned} &\overline{\eta}_{xx} = -\frac{k^2}{4m_e}\frac{1+\varepsilon}{1-\varepsilon}, && \overline{\eta}_{xy} = 0, && \overline{\eta}_{xz} = \frac{k_0\sqrt{-k^2}}{4m_e}\frac{\sqrt{2\varepsilon(1+\varepsilon)}}{1-\varepsilon}, \\ &\overline{\eta}_{yx} = 0, && \overline{\eta}_{yy} = -\frac{k^2}{4m_e^2}, && \overline{\eta}_{yz} = 0, \\ &\overline{\eta}_{zx} = \frac{k_0\sqrt{-k^2}}{4m_e}\frac{\sqrt{2\varepsilon(1+\varepsilon)}}{1-\varepsilon}, && \overline{\eta}_{zy} = 0, && \overline{\eta}_{zz} = \frac{k_0^2}{4m_e^2}\frac{2\varepsilon}{1-\varepsilon}, \end{aligned} \tag{3.47}$$

where, according to (3.41) and for the coordinate system (3.40),

$$\varepsilon = \left(1 + \frac{2|\vec{k}|^2}{Q^2}\tan^2\frac{\theta_e}{2}\right)^{-1} \tag{3.48}$$

is the transverse polarization of the virtual photon [94] with θ_e the electron scattering angle (see Fig. 3.2). As can be noted from the definitions (3.39), (3.41), the parameter ε is an invariant under collinear transformations along $\hat{k}$, *i.e.*, in (3.48) $\vec{k}$ and θ_e may be both expressed in the lab. or in the c.m. frame.
Accordingly, from the definition (3.41) and the components (3.47), the polarization along the z direction is

$$\varepsilon_L = -\frac{k^2}{k_0^2}\varepsilon. \tag{3.49}$$

Finally, and similarly to the time-component reduction in Eq. (3.46), we expand the tensor product for the squared-amplitude $|\mathcal{T}|^2$ in (3.33) with unpolarized and polarized electrons along $\hat{e}_y$ and $\hat{e}_z$ and get

$$\begin{aligned}\eta_{\mu\nu}W^{\mu\nu} = \frac{-k^2}{2m_e^2(1-\varepsilon)}\Bigg[&\frac{W^{xx}+W^{yy}}{2} + \varepsilon\frac{W^{xx}-W^{yy}}{2} + \varepsilon_L W^{zz} - \sqrt{2\varepsilon_L(1+\varepsilon)}\Re e(W^{xz}) \\ &+ h\sqrt{2\varepsilon_L(1-\varepsilon)}\Im m(W^{yz})\Bigg]. \end{aligned} \tag{3.50}$$

Now, if we insert this expression (3.50) into the differential cross section of Eq. (3.32), we obtain

$$\frac{d\sigma}{d\Omega_f d\mathcal{E}_f d\Omega_\pi^*} = \Gamma\frac{W}{m_N k_\gamma^{lab}}|\vec{q}|\Bigg[\frac{W^{xx}+W^{yy}}{2} + \varepsilon\frac{W^{xx}-W^{yy}}{2} + \varepsilon_L W^{zz}$$

$$-\sqrt{2\varepsilon_L(1+\varepsilon)}\Re e(W^{xz}) + h\sqrt{2\varepsilon_L(1-\varepsilon)}\Im m(W^{yz})\Big] , \tag{3.51}$$

where Γ stands for the flux of the virtual photon field,

$$\Gamma = \frac{\alpha}{2\pi^2}\frac{\mathcal{E}_f}{\mathcal{E}_i}\frac{k_\gamma^{lab}}{Q^2}\frac{1}{1-\varepsilon}, \tag{3.52}$$

$k_\gamma^{lab} = (W^2 - m_N^2)/2m_N$ is the equivalent photon energy in the laboratory frame and $\alpha = e^2/4\pi \sim 1/137$. The form of equation (3.51) suggests to introduce the so-called response functions. These are defined as follows:

$$\begin{aligned} R_T =& \frac{1}{2}(W^{xx} + W^{yy}), & R_L =& W^{zz}, \\ \cos\phi_\pi R_{TL} =& -\Re e(W^{xz}), & \cos(2\phi_\pi) R_{TT} =& \frac{1}{2}(W^{xx} - W^{yy}), \\ \sin\phi_\pi R_{LT'} =& \Im m(W^{yz}), \end{aligned} \tag{3.53}$$

with the angular dependence ϕ_π given explicitly, indicating the angle between the electrons plane and the πN reaction plane, as shown Fig. 3.2. The response functions here depend on three independent variables, *e.g.* $R(Q^2, W, \cos\theta_\pi)$. Then, taking (3.51) and (3.54) for an unpolarized electroproduction process, the differential cross section can be written in terms of these response functions [89],

$$\begin{aligned} \frac{d\sigma}{d\Omega_f d\mathcal{E}_f d\Omega_\pi^*} = \Gamma\frac{W}{m_N k_\gamma^{lab}}|\vec{q}|\Big[& R_T + \varepsilon_L R_L + \varepsilon R_{TT}\cos(2\phi_\pi) + \sqrt{2\varepsilon_L(1+\varepsilon)}R_{TL}\cos\phi_\pi \\ & + h\sqrt{2\varepsilon_L(1-\varepsilon)}R_{TL'}\sin\phi_\pi\Big]. \end{aligned} \tag{3.54}$$

We can write this in terms of the virtual photon cross section defined as [91]

$$\frac{d\sigma}{d\Omega_f d\mathcal{E}_f d\Omega_\pi^*} \equiv \Gamma\frac{d\sigma_v}{d\Omega_\pi^*}. \tag{3.55}$$

The virtual photon differential cross section, $d\sigma_v/d\Omega_\pi^*$, for an unpolarized target and without recoil polarization is usually split in the form [77, 89][2]

$$\begin{aligned} \frac{d\sigma_v}{d\Omega_\pi^*} =& \frac{d\sigma_T}{d\Omega_\pi^*} + \varepsilon\frac{d\sigma_L}{d\Omega_\pi^*} + \sqrt{2\varepsilon(1+\varepsilon)}\frac{d\sigma_{LT}}{d\Omega_\pi^*}\cos\phi_\pi + \varepsilon\frac{d\sigma_{TT}}{d\Omega_\pi^*}\cos 2\phi_\pi \\ & + h\sqrt{2\varepsilon(1-\varepsilon)}\frac{d\sigma_{LT'}}{d\Omega_\pi^*}\sin\phi_\pi , \end{aligned} \tag{3.56}$$

where the subscripts refer to the transverse, T, and longitudinal, L, components. The two first terms are independent of the azimuthal angle ϕ_π. The ϕ_π dependence is explicit and is decomposed in the LT and LT' pieces, related to the transverse-longitudinal interference, and the transverse-transverse term, TT, which is proportional to $\sin 2\phi_\pi$. The different components of Eq. (3.56), can be directly given in

[2] A slightly different notation in terms of the longitudinal polarization, $\varepsilon_L = (Q^2/E_\gamma^2)\varepsilon$, is used in Ref. [89].

terms of the diverse longitudinal and transverse response functions [77],

$$\begin{aligned}
\frac{d\sigma_T}{d\Omega_\pi^*} =& \rho_0 R_T, \\
\frac{d\sigma_L}{d\Omega_\pi^*} =& \rho_0 \frac{Q^2}{E_\gamma^2} R_L, \\
\frac{d\sigma_{LT}}{d\Omega_\pi^*} =& \rho_0 \frac{Q}{|E_\gamma|} R_{LT}, \\
\frac{d\sigma_{TT}}{d\Omega_\pi^*} =& \rho_0 R_{TT}, \\
\frac{d\sigma_{LT'}}{d\Omega_\pi^*} =& \rho_0 \frac{Q}{|E_\gamma|} R_{LT'}.
\end{aligned} \tag{3.57}$$

Here, the phase space factor $\rho_0 = |\vec{q}|/k_\gamma^{cm}$ with $k_\gamma^{cm} = k_\gamma^{lab} m_N/W$. Note here that for the longitudinal components, the current conserving term Q/E_γ is introduced compensating the time-component contribution in (3.50). Finally, the response functions, in terms of the CGLN basis, are given by [94]

$$\begin{aligned}
R_T =& |\mathcal{F}_1|^2 + |\mathcal{F}_2|^2 + \frac{\sin^2\theta_\pi}{2}\left(|\mathcal{F}_3|^2 + |\mathcal{F}_4|^2\right) \\
&+ \Re e\left\{\sin^2\theta_\pi\left(\mathcal{F}_2^*\mathcal{F}_3 + \mathcal{F}_1^*\mathcal{F}_4 + \cos\theta_\pi \mathcal{F}_3^*\mathcal{F}_4\right)\right. \\
&\left. -2\cos\theta_\pi \mathcal{F}_1^*\mathcal{F}_2\right\}, \\
R_L =& \Re e\left\{|\mathcal{F}_5|^5 + |\mathcal{F}_6|^2 + 2\cos\theta_\pi \mathcal{F}_5^*\mathcal{F}_6\right\}, \\
R_{LT} =& \sin\theta_\pi \Re e\left\{-\mathcal{F}_2^*\mathcal{F}_5 - \mathcal{F}_3^*\mathcal{F}_5 - \mathcal{F}_1^*\mathcal{F}_6 - \mathcal{F}_4^*\mathcal{F}_6\right. \\
&\left. - \cos\theta_\pi\left(\mathcal{F}_4^*\mathcal{F}_5 + \mathcal{F}_3^*\mathcal{F}_6\right)\right\}, \\
R_{TT} =& \frac{1}{2}\sin^2\theta_\pi\left\{|\mathcal{F}_3|^2 + |\mathcal{F}_4|^2\right\} \\
&+ \sin^2\theta_\pi \Re e\left\{\mathcal{F}_2^*\mathcal{F}_3 + \mathcal{F}_1^*\mathcal{F}_4 + \cos\theta_\pi \mathcal{F}_3^*\mathcal{F}_4\right\}, \\
R_{LT'} =& -\sin\theta_\pi \Im m\left\{\mathcal{F}_2^*\mathcal{F}_5 + \mathcal{F}_3^*\mathcal{F}_5 + \mathcal{F}_1^*\mathcal{F}_6 + \mathcal{F}_4^*\mathcal{F}_6\right. \\
&\left. + \cos\theta_\pi\left(\mathcal{F}_4^*\mathcal{F}_5 + \mathcal{F}_3^*\mathcal{F}_6\right)\right\}.
\end{aligned} \tag{3.58}$$

Most of the experimental data correspond to some of the terms appearing in Eq. (3.56). Additionally, an observable proportional to $d\sigma_{LT'}/d\Omega_\pi^*$ has been measured [95],

$$A_{LT'} = \frac{\sigma^+ - \sigma^-}{\sigma^+ + \sigma^-} = \frac{\sqrt{2\varepsilon(1-\varepsilon)}d\sigma_{LT'}}{d\sigma_T + \varepsilon d\sigma_L - \varepsilon d\sigma_{TT}}, \tag{3.59}$$

where σ^+ and σ^- are the differential cross sections for $\phi_\pi = 90°$ with beam polarization parallel and antiparallel to the beam direction, respectively.

3.2 Pion photoproduction on nucleons

In this subsection I review the particular formal aspects for the $\gamma + N \to \pi + N'$ reaction involving the kinematics and the invariant amplitude parametrizations. Since the hadron vertex in photoproduction is a particular case of the electroproduction vertex $\mathcal{H}^\mu$, Eq. (3.11), the photoproduction scattering amplitude becomes a simplified reduced case, where the reaction is induced by real photons. Following the line of the previous subsection, I present below the definitions for the relevant observables in

pion photoproduction at low energies from threshold. The observables correspond to those where experimental cross-sections data are available.

3.2.1 Matrix element and kinematics

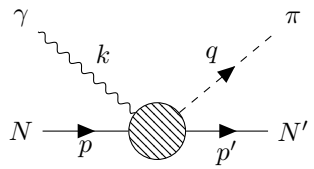

FIGURE 3.3: General diagram for pion photoproduction on nucleons. The corresponding 4-momenta are similar to Fig. 3.1 excluding the lepton vertex and being here γ the incoming real-photon.

As can be seen in Fig. 3.3, in the case of pion photoproduction we will not find the lepton vertex nor the virtual photon propagator in the scattering amplitude but we have, similarly to Eq. (3.1), that the $\mathcal{T}$-matrix will be proportional to the product

$$\mathcal{T} = \epsilon_\mu(\lambda)\mathcal{H}^\mu \tag{3.60}$$

with $\mathcal{H}^\mu$ the hadron matrix element defined as the electromagnetic current of the nucleon Eq. (3.11), and where $\epsilon_\mu(\lambda)$ is the photon polarization vector with zero time component and polarization $\lambda = \pm 1$. Specifically,

$$\epsilon_\mu(\lambda) = \sqrt{\frac{4\pi}{3}} Y_1^\lambda(\theta, \phi)\hat{n}_\pm \tag{3.61}$$

where $Y_1^\lambda(\theta, \phi)$ are the spherical harmonics for the azimuthal and polar angles of $\vec{\epsilon}(\lambda)$, $\hat{n}_\pm = (0, \pm 1, -1, 0)$ is a vector perpendicular to the 3-momentum of the real photon, in particular the 4-momentum is pointed to the z direction, $k^\mu = (k, 0, 0, k)$, and such that the Lorentz condition is still satisfied $k^\mu \epsilon_\mu = 0$. Furthermore, please note that for real photons it is fulfilled

$$\vec{\epsilon} \cdot \vec{k} = 0. \tag{3.62}$$

which is not the case for virtual-photons as in electroproduction (see Eq. (3.25) and Ref. [91]). As seen in Fig. (3.3), the only relevant momenta for the photoproduction process are those in the set $\{p, p', k, q\}$. We have the same 4-momenta conservation rule in the hadron vertex as in Eq. (3.4). Also, we use the same notation for the components for the 4-vector momenta as in (3.5) for the electroproduction case.

The other particularity here is that the real photon 4-momentum, k^μ, is characterized by the invariant identity

$$k^2 = -Q^2 = 0. \tag{3.63}$$

The on-mass shell conditions are still equal for the nucleon and pion momenta, $p^2 = p'^2 = m_N^2$, $q^2 = M_\pi^2$. In consequence the s, t, u invariant representation defined in (3.6) results again in only two independent Mandelstam variables

$$s + t + u = 2m_N^2 + M_\pi^2. \tag{3.64}$$

In addition, the particular components for the 4-momenta p^μ, p'^μ, k^μ and q^μ in the $\pi - N'$ c.m. frame are given previously by Eqs. (3.9) but with $Q^2 = 0$.
On the other hand, the angle θ_π among the outgoing pion and the incoming photon direction enters in the angular dependence of the cross sections. As before, this is given by

$$\cos\theta_\pi = \hat{k} \cdot \hat{q}, \tag{3.65}$$

and is included in the invariant Mandelstam representation as in Eq. (3.10) in the c.m. frame

$$u = m_N^2 - 2\left(E_\gamma E_{p'} + \left|\vec{k}\right|\left|\vec{p'}\right|\cos\theta_\pi\right) \tag{3.66}$$

or

$$t = M_\pi^2 - 2E_\gamma\left(E_\pi - |\vec{q}|\cos\theta_\pi\right), \tag{3.67}$$

with E_γ, $E_{p'}$, E_π, $|\vec{k}|$, $\vec{p'}$, $\vec{q}$ the corresponding energies and momenta as in Eqs. (3.9) for $Q^2 = 0$.
Some of the experimental data in pion photoproduction are given in the Laboratory frame, where the initial target nucleon is at rest. The measured observables are usually functions of the laboratory photon energy, E_γ^{lab}, and the pion scattering angle, $\cos\theta^{lab} = \hat{k} \cdot \hat{q}^{\,lab}$. Here, the 4-momenta components are boosted with respect to the photon 3-momentum such that

$$\begin{aligned} p_{lab}^\mu &= \left(m_N, \vec{0}\right), \\ p_{lab}'^\mu &= \left(E_{p'}^{lab}, \vec{p'}^{\,lab}\right), \\ k_{lab}^\mu &= \left(E_\gamma^{lab}, 0, 0, E_\gamma^{lab}\right), \\ q_{lab}^\mu &= \left(E_\pi^{lab}, \vec{q}^{\,lab}\right). \end{aligned} \tag{3.68}$$

The transformation from the c.m. frame to the Lab. frame is straightforward by using the invariants from Eqs. (3.6) and the expressions for two kinematical degrees of freedom, for example s and t,

$$s = 2E_\gamma^{lab} m_N + m_N^2, \tag{3.69}$$

$$t = M_\pi^2 - 2E_\gamma^{lab}\left(E_\pi^{lab} - |\vec{q}^{\,lab}|\cos\theta_\pi^{lab}\right), \tag{3.70}$$

where

$$E_\pi^{lab} = \frac{m_N^2 + M_\pi^2 - u}{2m_N}, \tag{3.71}$$

$$\left|\vec{q}^{\,lab}\right| = \sqrt{E_\pi^{lab\,2} - M_\pi^2}. \tag{3.72}$$

To summarize, once we get the corresponding amplitude as a function of the invariant kinematical variables, $\mathcal{H}^\mu(s,u)$, we can express them in the c.m. frame $\{s,u\} \to \{W, u(W,\cos\theta)\}$ through Eq. (3.66), or depending on what we shall compare, we can calculate the amplitude in terms of the Lab. frame photon energy and the pion angle production by $\{s,u\} \to \left\{s(E_\gamma^{lab}), u(E_\gamma^{lab}, \cos\theta_\pi^{lab})\right\}$ with Eqs. (3.69), (3.70)

and (3.64). Besides this, when experimental data are provided in terms of the Lab. frame kinematics $E_\gamma^{lab}, \cos\theta_\pi^{lab}$ but we want to compare the angular dependence with other sample of data given in the c.m. frame we can always get the transformations to express $\cos\theta_\pi(\cos\theta_\pi^{lab})$ by combining the equations (3.70) and (3.67).

3.2.2 Amplitude parametrization and gauge invariant amplitude

The matrix amplitude (3.11) for the pion photoproduction process $\gamma(k,\lambda)+N(p,s)\to\pi(q)+N'(p',s')$ can be parametrized as

$$\mathcal{T}=\epsilon_\mu\mathcal{H}^\mu=\bar{u}(p')\left[a_N q\cdot\epsilon\, V_N+a_E\, V_E+a_K q\cdot\epsilon\, V_K+a_{EK}\, V_{EK}\right]u(p), \tag{3.73}$$

with

$$V_N=\gamma^5,\quad V_E=\not{\epsilon}\gamma^5,\quad V_K=\not{k}\gamma^5,\quad V_{EK}=\not{\epsilon}\not{k}\gamma^5 \tag{3.74}$$

the corresponding basis elements. The coefficients a_N, a_E, a_K and a_{EK} are complex scalar functions that can be written in terms of Lorentz invariants s and u. The dependence on the photon polarization, λ, the initial and final nucleon spins, s and s', is understood in the photon polarization vector ϵ_μ, the initial and final nucleon spinors u, $\bar{u}=u^\dagger\gamma^0$, respectively.
This parametrization must satify invariance under gauge transformations considering the full expression, *i.e.*, $k_\mu\mathcal{H}^\mu=0$, and any prior calculation of the scalar set of functions $\{a_N,a_E,a_K,a_{EK}\}$ might be tested afterwards in order to verify the gauge invariance fulfillment. However, following the same line as in the previous subsection for electroproduction and advantageously seeing photoproduction as a particular case ($Q^2=0$), a convenient parametrization is the covariant and current conserving one presented in Eqs.(3.17) and (3.18). Here, the scattering amplitude reads

$$\mathcal{T}=\epsilon_\mu\mathcal{H}^\mu=\epsilon_\mu\bar{u}(p')\left(\sum_{i=1}^{4}A_i M_i^\mu\right)u(p), \tag{3.75}$$

where the vector basis elements M_5^μ and M_6^μ are canceled by the real-photon kinematical condition, $k^2=-Q^2=0$ (3.63), and the Lorentz convention $\epsilon_\mu k^\mu=0$. Then, the remaining vectors of the basis are simply written as

$$\begin{aligned}
\epsilon\cdot M_1 &=\mathrm{i}\not{k}\not{\epsilon}\gamma_5,\\
\epsilon\cdot M_2 &=\mathrm{i}(p'\cdot\epsilon k\cdot q-q\cdot\epsilon k\cdot(p+p'))\gamma_5,\\
\epsilon\cdot M_3 &=\mathrm{i}(\not{\epsilon}k\cdot q-\not{k}q\cdot\epsilon)\gamma_5,\\
\epsilon\cdot M_4 &=\mathrm{i}(\not{\epsilon}k\cdot(p+p')-\not{k}p'\cdot\epsilon-2m_N\not{k}\not{\epsilon})\gamma_5.
\end{aligned} \tag{3.76}$$

Note that in the c.m. system $p\cdot\epsilon=0$. One can easily find the conversion between the two different representations in (3.73) and (3.75) obtaining that

$$A_1=\mathrm{i}\left(a_{EK}-\frac{m_N}{k\cdot p}\left(a_E+k\cdot q\, a_K\right)\right), \tag{3.77}$$

$$A_2=\mathrm{i}\frac{a_N}{2k\cdot p}, \tag{3.78}$$

$$A_3=\mathrm{i}\left(a_K\left(1-\frac{k\cdot q}{2k\cdot p}\right)-\frac{a_E}{2k\cdot p}\right), \tag{3.79}$$

$$A_4=-\frac{\mathrm{i}}{2k\cdot p}\left(a_E+k\cdot q\, a_K\right). \tag{3.80}$$

As our last goal here is to calculate observables, we take advantage of the CGLN parametrization for the amplitude that makes the calculation more straightforward. As in Eq. (3.21),

$$\mathcal{T} = \epsilon_\mu \mathcal{H}^\mu = 4\pi \frac{\sqrt{s}}{m_N}\, \chi_f^\dagger \mathcal{F} \chi_i,$$

where the amplitude $\mathcal{F}$ in photoproduction is reduced only to the perpendicular contributions to the photon momentum, *i.e.* the terms $\mathcal{F}_5$ and $\mathcal{F}_6$ vanish given that the real-photon polarization vector is such that $\vec{k}\cdot\vec{\epsilon}=0$ and the parallel component $\vec{a}_\parallel = 0$ [Eq. (3.25)]. Particularly, as $a^\mu = \epsilon^\mu$ in Eq. (3.23) the CGLN amplitude takes the form [90]

$$\mathcal{F} = i\,\vec{\tau}\cdot\vec{\epsilon}\mathcal{F}_1 + \vec{\tau}\cdot\hat{q}\,\vec{\tau}\cdot\hat{k}\times\vec{\epsilon}\mathcal{F}_2 + i\,\vec{\tau}\cdot\hat{k}\,\hat{q}\cdot\vec{\epsilon}\mathcal{F}_3 + i\,\vec{\tau}\cdot\hat{q}\,\hat{q}\cdot\vec{\epsilon}\mathcal{F}_4, \tag{3.81}$$

being $\mathcal{F}_1, \cdots, \mathcal{F}_4$ the scalar complex functions as in Eqs. (3.28) with $Q^2 = 0$.

3.2.3 Observables

The experimental data compared with the theoretical calculations in ChPT is restricted to the near threshold region, in our case around $E_\gamma^{lab} \approx$70 MeV above the π production threshold. For this energy region the available data correspond to the unpolarized angular and integrated cross section, $d\sigma/d\Omega_\pi$ and σ, as well as the polarized beam and target cross sections, Σ and T, to be detailed subsequently in this subsection. The pion photoproduction off the nucleon, depicted in Fig. (3.3) occurs in four possible physical channels: $\gamma + p \to \pi^0 p$, $\gamma + p \to \pi^+ n$, $\gamma + n \to \pi^- p$ and $\gamma + n \to \pi^0 n$.
The differential cross section for the process $\gamma(k,\lambda) + N(p,s) \to \pi(q) + N'(p',s')$ is written as

$$d\sigma = \frac{1}{\left|\vec{v}_\gamma - \vec{V}_1\right|}\frac{1}{2E_\gamma}\frac{m_N}{E_p}\overline{|\mathcal{T}|^2}\frac{d^3p'}{(2\pi)^3}\frac{m_N}{E_{p'}}\frac{d^3q}{(2\pi)^3}\frac{1}{2E_\pi}(2\pi)^4\delta^4(k+p-p'-q), \tag{3.82}$$

with $\vec{v}_\gamma$, $\vec{V}_1$ the photon and incoming nucleon velocities. The frame invariant flux term is $|\vec{v}_\gamma - \vec{V}_1|E_\gamma E_p = \sqrt{s}|\vec{k}|$ in the c.m. frame. The photoproduction amplitude $\mathcal{T}$ is function of the photon polarization, λ, the nucleon spins s, s' and two independent momenta. It can be depicted as

$$\mathcal{T} = \epsilon_\mu(\lambda)\mathcal{H}^\mu(k;p,s;p',s';q). \tag{3.83}$$

Then, integrating (3.82) over the final momenta, p' and q, the unpolarized angular cross section in the c.m. frame is

$$\begin{aligned}\frac{d\sigma}{d\Omega_\pi^*} &= \frac{(2m_N)^2}{64\pi^2 s}\frac{|\vec{q}|}{|\vec{k}|}\frac{1}{4}\sum_{\lambda,m_i,m_f}|\mathcal{T}|^2 \\ &= \left(\frac{1}{8\pi W}\right)^2\frac{|\vec{q}|}{|\vec{k}|}\frac{\mathrm{Tr}\left[\mathcal{M}^*\cdot(\not{p}'+m_N)\cdot\mathcal{M}\cdot(\not{p}+m_N)\right]}{2},\end{aligned} \tag{3.84}$$

where it has been averaged over the polarization λ and the initial nucleon spin m_i, and summed over the final nucleon spin m_f. $d\Omega_\pi = \sin\theta_\pi d\theta_\pi d\phi_\pi$ is the pion differential solid angle. Here,

$$\mathcal{M} = a_N q\cdot\epsilon V_N + a_E V_E + a_K q\cdot\epsilon V_K + a_{EK} V_{EK} \tag{3.85}$$

$$= \sum_{i=1}^{4} A_i \epsilon\cdot M_i, \tag{3.86}$$

as detailed in Eqs. (3.73)-(3.76). In contrast, using the CGLN basis (3.81), the c.m. expression (3.84) takes the simpler form

$$\frac{d\sigma}{d\Omega_\pi^*} = \frac{|\vec{q}|}{|\vec{k}|}\frac{1}{4}\sum_{m_i,m_f,\lambda}\left|\chi^{(m_f)\dagger}\mathcal{F}\chi^{(m_i)}\right|^2, \tag{3.87}$$

with

$$\chi^{(1/2)} = \begin{pmatrix} 1 \\ 0 \end{pmatrix}, \qquad \chi^{(-1/2)} = \begin{pmatrix} 0 \\ 1 \end{pmatrix}, \tag{3.88}$$

the spinors for the initial and final nucleons for the spin projections, $m = \{1/2, -1/2\}$. Again, when implementing the sum over the unpolarized beam and target spins, the angular cross section is expressed in a compact way as follows [96]

$$\begin{aligned}\frac{d\sigma}{d\Omega_\pi^*} &= \rho_0 \Re e\left\{\mathcal{F}_1^*\mathcal{F}_1 + \mathcal{F}_2^*\mathcal{F}_2 + \sin^2\theta_\pi\left(\mathcal{F}_3^*\mathcal{F}_3 + \mathcal{F}_4^*\mathcal{F}_4\right)/2\right. \\ &\quad \left. + \sin^2\theta_\pi(\mathcal{F}_2^*\mathcal{F}_3 + \mathcal{F}_1^*\mathcal{F}_4 + \cos\theta_\pi\mathcal{F}_3^*\mathcal{F}_4) - 2\cos\theta_\pi\mathcal{F}_1^*\mathcal{F}_2\right\},\end{aligned} \tag{3.89}$$

where the phase space factor evaluated in the c.m. frame is

$$\rho_0 = \frac{|\vec{q}|}{|\vec{k}|}. \tag{3.90}$$

Once the angular cross section, as function of the c.m. energy $\sqrt{s}$ and the pion angle θ_π, is obtained, the integrated total and the polarized beam cross sections can be computed immediately,

$$\sigma(s) = \int \frac{d\sigma}{d\Omega_\pi^*}(s,\cos\theta_\pi)d\Omega_\pi^* = 2\pi\int\frac{d\sigma}{d\Omega_\pi^*}(s,\cos\theta_\pi)d\cos\theta_\pi, \tag{3.91}$$

$$\Sigma \equiv \frac{d\sigma_\perp - d\sigma_\parallel}{d\sigma_\perp + d\sigma_\parallel} \tag{3.92}$$

where $d\sigma_\perp$ corresponds to the angular cross section for beam photon with polarization vector perpendicular to the reaction plane defined by $\hat{k}\times\hat{q}$, while $d\sigma_\parallel$ is the respective angular cross section for polarization vector with only parallel components. In the CGLN representation we can simply write [96]

$$\hat{\Sigma} = -\rho_0\sin^2\theta_\pi\Re e\left\{\left(\mathcal{F}_3^*\mathcal{F}_3 + \mathcal{F}_4^*\mathcal{F}_4\right)/2 + \mathcal{F}_2^*\mathcal{F}_3 + \mathcal{F}_1^*\mathcal{F}_4 + \cos\theta_\pi\mathcal{F}_3^*\mathcal{F}_4\right\}, \tag{3.93}$$

using the profile function, $\hat{\Sigma} = \Sigma\, d\sigma/d\Omega_\pi^*$.
Similarly, an important amount of data belong to the target asymmetry defined by

$$T \equiv \frac{d\sigma_+ - d\sigma_-}{d\sigma_+ + d\sigma_-} \tag{3.94}$$

with $d\sigma_+$ and $d\sigma_-$ the angular cross sections for target nucleons polarized up and down respectively in the direction of the reaction plane given by $\hat{k} \times \hat{q}$. Analogously, we can write in the CGLN framework [96]

$$\hat{T} = +\sin\theta\, \Im m \left\{ \mathcal{F}_1^* \mathcal{F}_3 - \mathcal{F}_2^* \mathcal{F}_4 + \cos\theta_\pi \left(\mathcal{F}_1^* \mathcal{F}_4 - \mathcal{F}_2^* \mathcal{F}_3 \right) - \sin^2\theta \mathcal{F}_3^* \mathcal{F}_4 \right\} \rho_0. \tag{3.95}$$

In this case, $\hat{T} = T\, d\sigma/d\Omega_\pi^*$ corresponds directly to the observable that is currently reported in data at energies close to threshold.

3.3 Isospin amplitudes for pion electromagnetic production

This section is intended to show some properties of the pion production on nucleons with real or virtual-photons when we consider the isospin degrees of freedom to indicate the different physical channels in which can occur the processes. Also here are shown some of the symmetry relations for the amplitude considering the kinematical degrees of freedom.

Since the reaction for photo- (electro-) production $\gamma^{(*)} + N_i \to \pi + N_f$ can occur in four different physical channels

$$\begin{aligned} \gamma^{(*)} + p \to & \pi^0 + p \\ \gamma^{(*)} + p \to & \pi^+ + n \\ \gamma^{(*)} + n \to & \pi^- + p \\ \gamma^{(*)} + n \to & \pi^0 + n \end{aligned} \tag{3.96}$$

we can decompose in the isospin space the invariant amplitude coefficient, A_i, treated in subsections 3.1.3 and 3.2.2.
In a $\gamma^{(*)} + N \to \pi + N'$ reaction the initial state is characterized by a nucleon (isospin $I = 1/2$), which couples to the electromagnetic current J^μ [see Eq. (3.1)]. The isospin structure of the current operator can be described at the quark level by

$$\begin{aligned} J^\mu =& \frac{1}{6} \bar{q} \gamma^\mu q + \bar{q} \gamma^\mu \frac{\tau^3}{2} q \\ =& J^\mu_{(s)} + J^\mu_{(v)}, \end{aligned} \tag{3.97}$$

that contains an isoscalar, J_s^μ $(I = 0)$, and an isovectorial part, J_v^μ $(I = 1)$. The final state is characterized by the isovectorial pion $(I = 1)$ and the outgoing nucleon $(I = 1/2)$. The quark fields are $q = (u, d)^\intercal$ and τ^3 is the third Pauli matrix. Therefore, by using the Wigner-Eckart theorem, it can be shown that the four physical reactions from Eqs. (3.96) are described by only three independent physical amplitudes, as detailed in Table 3.1.

$\langle \pi N' \|$	Tensor operator	$\|N\rangle$		number of amplitudes
$1 \otimes \frac{1}{2} = \frac{3}{2} \oplus \frac{1}{2}$	0	$\otimes$ $\frac{1}{2}$	$= \frac{1}{2}$	1
$1 \otimes \frac{1}{2} = \frac{3}{2} \oplus \frac{1}{2}$	1	$\otimes$ $\frac{1}{2}$	$= \frac{3}{2} \oplus \frac{1}{2}$	2

TABLE 3.1: Source of the isospin amplitudes for pion production in the isospin symmetric limit case. The tensor current operator consists of a isoscalar ($I = 0$) and a isovector ($I = 1$) component as Eq. (3.97).

Assuming the isospin symmetry of the strong interaction, the pion-nucleon interaction in the isospin space must be proportional to $\vec{\tau} \cdot \vec{\pi}$. Thus, the Pauli matrices, which appear in the interaction with the photon and the pion, can be arranged to describe the matrix element in isospin space through

$$A_i(\gamma^* N_i \to \pi^a N_f) = \chi_f^\dagger \left(\frac{1}{2} \left[\tau^{(-a)}, \tau^{(0)} \right] A_i^{(-)} + \tau^{(a)} A_i^{(0)} + \frac{1}{2} \left\{ \tau^{(-a)}, \tau^{(0)} \right\} A_i^{(+)} \right) \chi_i, \tag{3.98}$$

where $\chi_{i,f}$ refers to the nucleon isospinors ($\chi = (1,0)^\top$ for proton and $\chi = (0,1)^\top$ for neutron), a indicates the charge of the generated pion, $a = \{+,-,0\}$ and $i = \{1, \cdots, 6\}$ the different components of the amplitudes as in (3.18). The three isospin amplitudes are denoted by $A^{(0,\pm)}$. The two terms associated with the commutator and the anti-commutator correspond to the isovectorial component of the electromagnetic 4-current, whereas the third term is related to the isoscalar component.

The Pauli matrices $\tau^{(0,\pm)}$ used in (3.98) are in the isospin (or physical) representation and are related to the Cartesian Pauli matrices as follows

$$\tau^{(\pm)} = \frac{1}{\sqrt{2}} \left(\tau^1 \pm i\tau^2 \right), \qquad \tau^{(0)} = \tau^3, \tag{3.99}$$

The respective amplitudes in Cartesian coordinates are

$$A_i(\gamma^* N_i \to \pi^k N_f) = \chi_f^\dagger \left(i\epsilon_{k3n} \tau^n A_i^{(-)} + \tau^k A_i^{(0)} + \delta^{k3} A_i^{(+)} \right) \chi_i, \tag{3.100}$$

where $k = \{1,2,3\}$ indicates the cartesian components instead. The relationship between the physical (3.98) and the latter Cartesian amplitudes is given through

$$A_i(\pi^+) = \frac{1}{\sqrt{2}} \left(A_i(\pi^1) - iA_i(\pi^2) \right), \tag{3.101}$$

$$A_i(\pi^-) = \frac{1}{\sqrt{2}} \left(A_i(\pi^1) + iA_i(\pi^2) \right), \tag{3.102}$$

$$A_i(\pi^0) = A_i(\pi^3). \tag{3.103}$$

On the other hand, when the physical charges are specified the relationship between the isospin amplitudes, $A^{(0,\pm)}$, and the physical amplitudes (3.98) is

$$A_i(\gamma^{(*)} p \to \pi^0 p) = A_i^{(+)} + A_i^{(0)}, \tag{3.104}$$

$$A_i(\gamma^{(*)} p \to \pi^+ n) = \sqrt{2} \left(A_i^{(-)} + A_i^{(0)} \right), \tag{3.105}$$

$$A_i(\gamma^{(*)} n \to \pi^- p) = -\sqrt{2} \left(A_i^{(-)} - A_i^{(0)} \right), \tag{3.106}$$

$$A_i(\gamma^{(*)} n \to \pi^0 n) = A_i^{(+)} - A_i^{(0)}. \tag{3.107}$$

Therefore, the physical amplitudes may be tested through these relations, for example expressing one of them in terms of the other three independent physical channels.

Finally, the isospin amplitudes $A^{(0,\pm)}$ should have crossing-symmetry, referring to the interchange of the Mandelstam variables $s \leftrightarrow u$. Under this permutation, the amplitudes follow the relations

$$\begin{aligned} A_i^{(0,+)} \quad & \overrightarrow{s \leftrightarrow u} \quad \xi A_i^{(0,+)}, \\ A_i^{(-)} \quad & \overrightarrow{s \leftrightarrow u} \quad -\xi A_i^{(-)}, \end{aligned} \tag{3.108}$$

where the ξ coefficient takes the values

$$\xi = \begin{cases} 1, & i = 1, 2, 4 \\ -1, & i = 3, 5, 6. \end{cases}$$

Chapter 4

Amplitudes for pion EM production

In the previous chapter we have presented the formalism for the calculation of physical observables in terms of the scattering amplitude given in any model, while a brief introduction of ChPT was given in Chapter 2. Throughout this chapter I shall develop the systematical procedure for the calculation of the $\gamma^{(*)} + N_i \longrightarrow \pi + N_f$ reaction amplitudes within a fully relativistic ChPT approach.

We are looking to calculate the amplitude contributions up to order $\mathcal{O}(p^3)$ in the chiral expansion using nucleons, pions and the inclusion of explicit Δ's as the degrees of freedom in the process. The several amplitude contributions at $\mathcal{O}(p^n)$ are included following the δ power-counting scheme, Eq. (2.79).
Considering the ChPT Lagrangian terms in Section 2.2, we have generated the explicit Feynman rules from $\mathcal{O}(p^1)$ to $\mathcal{O}(p^4)$ for the building of the different amplitudes associated to the pion photo- and electroproduction off nucleons. The explicit expressions can be found in Appendix A.
Along this chapter, I will show the Feynman diagrams and their corresponding amplitude expressions for the pion photo- and electroproduction reactions at tree and one-loop level, for the 4 possible physical channels, (3.96). Furthermore, the loop amplitudes are renormalized in detail using the $\widetilde{\text{MS}}$ and EOMS schemes.
The full amplitude with all the contributions pieces from the tree and loop level is presented within this renormalization scheme. In order to simplify the evaluation of the amplitude in terms of physical parameters, some approximations valid for an $\mathcal{O}(p^3)$ treatment will be elaborated.

Finally in this chapter, the relevant LECs acting as parameters in the amplitudes for each physical channel are discussed, including the LECs fixed by other processes and physical quantities and the ones that are investigated in this work.

4.1 Generation of Feynman graphs

Considering only the nucleon and pion degrees of freedom, a total of 20 tree Feynman diagrams contribute up to $\mathcal{O}(p^3)$. They are depicted in Fig. 4.1. Also, at this order, there are many diagrams containing loops. We can distinguish two kinds, those that contain loops in the external legs and the rest. The first ones will be accounted for by the Wave Function Renormalization (WFR) of the external legs. The latter ones can be generated from the topologies shown in Fig. 4.2.
Additionally, considering the Δ resonance degree of freedom there are only 2 relevant diagrams at tree level starting from $\mathcal{O}(p^{5/2})$ in the δ-counting, (2.79). Their specific Feynman diagrams are displayed in Fig. 4.3.

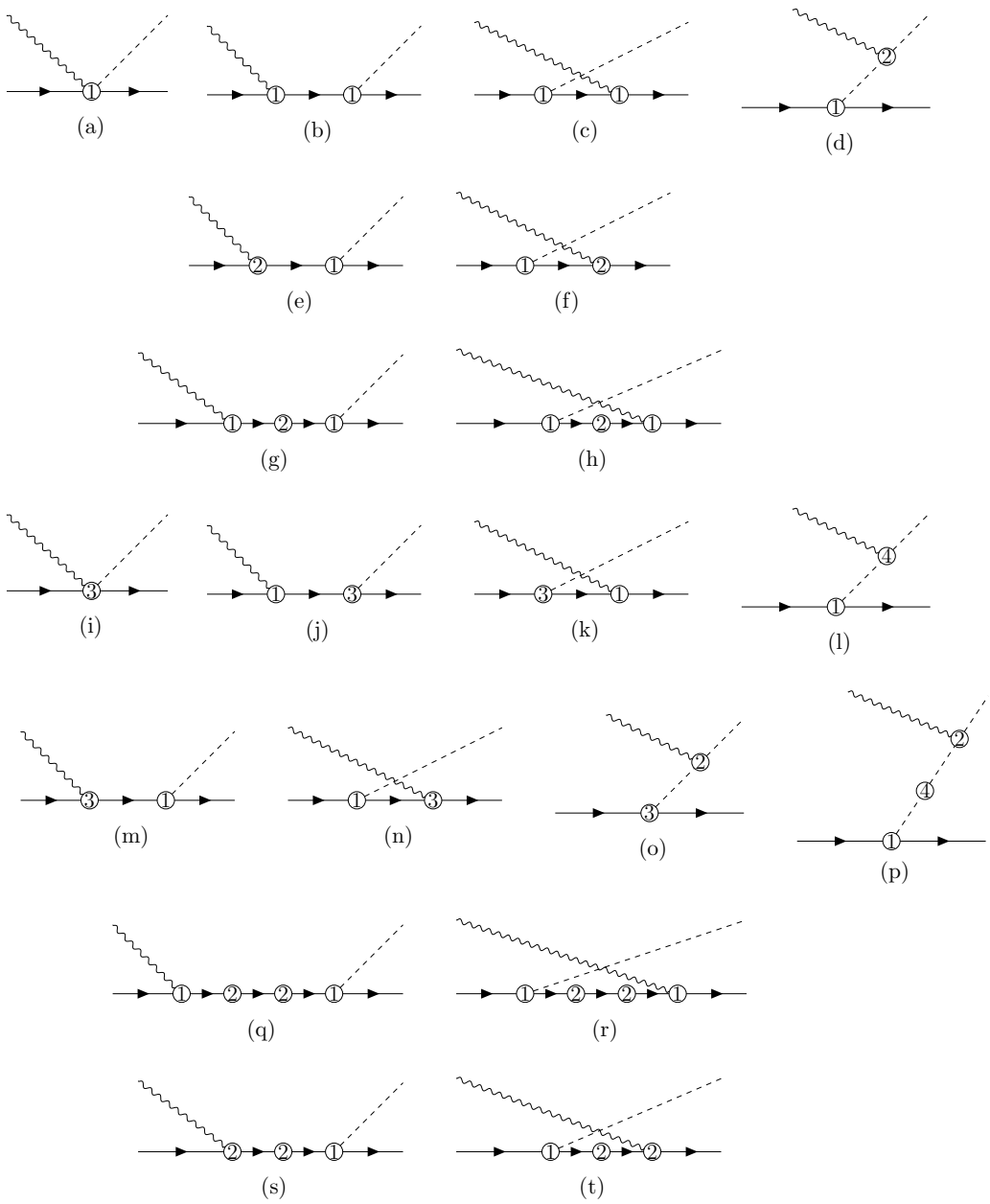

FIGURE 4.1: Tree Feynman diagrams contributing up to $\mathcal{O}(p^3)$ considering only pion and nucleon degrees of freedom. The numbers inside the circles denote the chiral order of the respective vertex. Diagrams from (a) to (d) correspond to the $\mathcal{O}(p^1)$ amplitudes, (e)-(h) are of $\mathcal{O}(p^2)$ order, and (i)-(t) are of $\mathcal{O}(p^3)$ order respectively.

The Feynman diagrams depicted in Figs. 4.1, 4.2 and 4.3 are built systematically following the standard procedure. This procedure relies on the expansion of the S-matrix in the scattering amplitudes, $\langle \pi, N_f | S | \gamma, N_i \rangle$. For the transition $|i\rangle \to |f\rangle$ the scattering amplitude is given by

$$\langle f|S|i\rangle = \delta_{fi} + \left[(2\pi)^4 \delta^4(P_f - P_i) \left(\frac{m_N}{E}\right)^{\frac{1}{2}} \left(\frac{1}{2E_\gamma}\right)^{\frac{1}{2}} \left(\frac{m_N}{E'}\right)^{\frac{1}{2}} \left(\frac{1}{2E_\pi}\right)^{\frac{1}{2}} \right] \mathcal{T}. \quad (4.1)$$

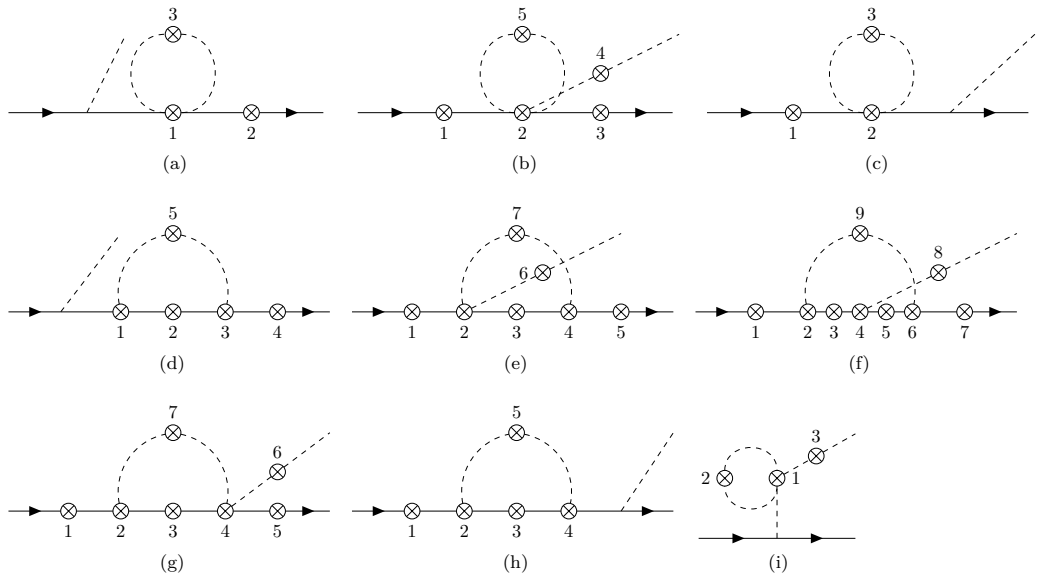

FIGURE 4.2: One-loop Feynman diagram-generating topologies up to the nominal order $\mathcal{O}(p^3)$. Crossed-circles indicate the vertex where one incoming real- or virtual-photon may be placed to generate the corresponding Feynman diagram. Numbers provide the label to identify each diagram generated.

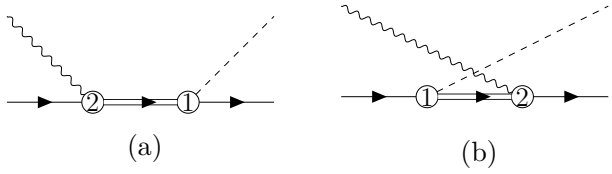

FIGURE 4.3: Tree Feynman diagrams for the $\gamma^{(*)} + N \longrightarrow \pi + N'$ reaction through the explicit $\Delta(1232)$ inclusion. The labels in the circles specify the chiral order of each vertex.

Here, $|i\rangle = |\gamma(k), N_i(p)\rangle$, $|f\rangle = |\pi(q), N_f(p')\rangle$, the initial and final external 4-momenta are $P_i = p+k$, $P_f = p'+q$. $\mathcal{T}$ indicates the total amplitude and is given by the sum of the amplitudes corresponding to the Feynman diagrams. Up to and including $\mathcal{O}(p^3)$ the amplitude, $\mathcal{T}$, is given by

$$\mathcal{T} = \sum_{m=1}^{\infty} \sum_{n=1}^{3} \mathcal{T}_m^{(n)}, \tag{4.2}$$

where the m-th contribution $\mathcal{T}_m^{(n)}$ is obtained by drawing all topologically different, connected Feynman graphs at chiral order $\mathcal{O}(p^n)$ which contain m vertices and the correct external lines.

In the context of ChPT, the contributions to the $\gamma^{(*)} + N_i \longrightarrow \pi + N_f$ amplitude are re-ordered in the power counting scheme, here from $\mathcal{O}(p^1)$ up to $\mathcal{O}(p^3)$. The chiral order $\mathcal{O}(p^n)$ for any given amplitude $\mathcal{T}_m^{(n)}$ is driven by the different vertices and propagators following the δ-counting scheme (2.79). The vertices come from the interaction terms contained in the nucleon, pion and Δ-nucleon Lagrangian terms.

The relevant pieces to take into account are

$$\mathcal{L}_{\rm ChPT} = \sum_{i=1}^{3} \mathcal{L}_N^{(i)} + \sum_{j=1}^{2} \mathcal{L}_{\pi\pi}^{(2j)} + \sum_{k=1}^{2} \mathcal{L}_{\Delta N}^{(k)} \tag{4.3}$$

as in Eqs. (2.61), (2.63) and (2.64) for the nucleon sector Lagrangian terms $\mathcal{L}_N^{(i)}$, Eqs. (2.38) and (2.44) for the purely pion sector $\mathcal{L}_{\pi\pi}^{(2j)}$, and as the Lagrangians terms (2.69) and (2.70) for the $\mathcal{L}_{\Delta N}^{(k)}$ in the nucleon-Δ sector. The needed Feynman rules for all the vertices appearing in the graphs can be derived from the above Lagrangian terms.
In the App. A, I state these Feynman rules for the specific propagators and the needed vertices. Also, throughout this appendix some details in the derivation of the vertex Feynman rules are illustrated.

4.2 Amplitudes

In the following, I shall develop the standard procedure to obtain the specific amplitudes order by order for all the physical channels in the $\gamma^{(*)} + N_i \longrightarrow \pi + N_f$ process, corresponding to the tree and loop Feynman diagrams in Figs. 4.1-4.3. The amplitude contributions are given in the next form, as in (3.1) and (3.60),

$$\mathcal{T} = \epsilon_\mu \overline{u}_{N'}(p') \mathcal{M}^\mu u_N(p), \tag{4.4}$$

where, up to order $\mathcal{O}(p^3)$ in the chiral expansion, there are contributions at tree and one-loop level. According to the δ-counting (2.79) the tree-level amplitudes contribute from $\mathcal{O}(p^1)$ up to $\mathcal{O}(p^3)$, whilst the one-loop level amplitudes start from order $\mathcal{O}(p^3)$. Specifically, as shown in Eq. (4.2) the amplitude $\mathcal{M}^\mu$ is the sum of the different orders

$$\mathcal{M}^\mu = \mathcal{M}_{\rm tree}^{\mu\,(1)} + \mathcal{M}_{\rm tree}^{\mu\,(2)} + \mathcal{M}_{\rm tree}^{\mu\,(5/2)} + \mathcal{M}_{\rm tree}^{\mu\,(3)} + \mathcal{M}_{\rm loop}^{\mu\,(3)} \tag{4.5}$$

where, $\mathcal{M}_{\rm tree}^{\mu\,(n)}$ is the $\mathcal{O}(p^n)$ amplitude contribution from the tree level diagrams and $\mathcal{M}_{\rm loop}^{\mu\,(3)}$ is the one-loop amplitude contribution at the nominal $\mathcal{O}(p^3)$. Below, I detail the tree level pieces of the amplitude, following with the one-loop level contributions in the next section.

4.2.1 Tree level amplitudes

$\mathcal{O}(p^1)$ amplitude

Given the identity (4.4), we have that the $O(p^1)$ amplitude at tree level is $\mathcal{T}_{\rm tree}^{(1)} = \epsilon_\mu \overline{u}_{N'}(p') \mathcal{M}_{\rm tree}^{\mu\,(1)} u_N(p)$. This amplitude is obtained from the sum of the amplitudes corresponding to the diagrams (a)-(d) in Fig. 4.1, as justified by the Eq. (4.2). Then, the $\mathcal{O}(p^1)$ contribution to $\gamma^{(*)} + N \longrightarrow \pi + N'$, is given by

$$\mathcal{M}_{\rm tree}^{\mu\,(1)} = \mathcal{M}_{(a)}^{\mu\,(1)} + \mathcal{M}_{(b)}^{\mu\,(1)} + \mathcal{M}_{(c)}^{\mu\,(1)} + \mathcal{M}_{(d)}^{\mu\,(1)}, \tag{4.6}$$

where the subscripts (a)-(d) indicate the correspondence with the diagrams in the figure 4.1. The amplitude contributions $\mathcal{M}^{\mu\,(1)}_{(a),\cdots,(d)}$ are obtained by using the Feynman rules for the vertices of Eqs. (A.14)-(A.16), (A.20), and the nucleon and pion propagators, (A.22) and (A.21). In detail, the $\mathcal{O}(p^1)$ contributions in (4.6) are calculated as

$$\mathcal{M}^{\mu\,(1)}_{(a)} = \mathcal{V}^{\mu\,(1)}_{\gamma N;\pi N'}, \tag{4.7}$$

$$\mathcal{M}^{\mu\,(1)}_{(b)} = \sum_{N_I} \mathcal{V}^{(1)}_{N_I;N'\pi} iS_{N_I}(p+k)\mathcal{V}^{\mu\,(1)}_{\gamma N;N_I} \tag{4.8}$$

$$\mathcal{M}^{\mu\,(1)}_{(c)} = \sum_{N_I} \mathcal{V}^{\mu\,(1)}_{\gamma N_I;N'} iS_{N_I}(p-q)\mathcal{V}^{(1)}_{N;N_I\pi} \tag{4.9}$$

$$\mathcal{M}^{\mu\,(1)}_{(d)} = \sum_{\pi_I} \mathcal{V}^{\mu\,(1)}_{\gamma\pi_I;\pi} iS_{\pi_I}(q-k)\mathcal{V}^{(1)}_{N;N'\pi_I} \tag{4.10}$$

where $\mathcal{V}^{(1)}_{\text{in;out}}$ are the vertex expressions at $\mathcal{O}(p^1)$ with incoming (in) and outgoing (out) particles such as given by the Feynman rules in App. A.1. For the internal lines in the Feynman diagrams, S_{N_I} and S_{π_I} express the nucleon and pion propagators, as shown in App. A. The inner four-momenta conservation is applied to each vertex as well as $p+k=p'+q$ globally in the hadron part, $\mathcal{M}^{\mu}$. The summation in Eqs. (4.7)-(4.10) is made over the isospin multiplets for the internal lines, such as the nucleon $N_I=\{p,n\}$ and pion $\pi_I=\{\pi^+,\pi^-,\pi^0\}$ propagators connected with the vertices. Let's notice here that the isospin specification for nucleons N_I and pions π_I only affects the explicit expressions for the vertices, due to the isoscalar nature of the propagators.

The above amplitude contributions, $\mathcal{M}^{\mu\,(1)}_{(a),\cdots,(d)}$ (4.7)-(4.10), are constrained by specifying the isospin/charge of the external fields for N, N', π. In consequence, most of the internal lines in the summation are reduced to only one term for each physical channel. Finally, we get

$$\mathcal{M}^{(\mu)}_{(a)} = C^{(1)}_{I}\frac{eg}{F}\gamma^{\mu}\gamma^{5}, \tag{4.11}$$

$$\mathcal{M}^{\mu\,(1)}_{(b)} = C^{(1)}_{II}\frac{eg\not{q}\gamma^5 i\left(\not{p}+\not{k}+m\right)i\gamma^{\mu}}{F\left((p+k)^2-m^2\right)}, \tag{4.12}$$

$$\mathcal{M}^{\mu\,(1)}_{(c)} = C^{(1)}_{III}\frac{egi\gamma^{\mu}i\left(\not{p}'-\not{k}+m\right)\not{q}\gamma^5}{F\left((p'-k)^2-m^2\right)}, \tag{4.13}$$

$$\mathcal{M}^{\mu\,(1)}_{(d)} = C^{(1)}_{IV}\frac{eg(2q-k)^{\mu}(\not{q}-\not{k})\gamma^5}{\sqrt{2}F\left((q-k)^2-M^2\right)}, \tag{4.14}$$

where the constants $C^{(1)}_{I},\ldots,C^{(1)}_{IV}$ are given in Table 4.1 for each channel.

Channel	$C_I^{(1)}$	$C_{II}^{(1)}$	$C_{III}^{(1)}$	$C_{IV}^{(1)}$
$\gamma^{(*)}+p\to p+\pi^0$	0	$\frac{1}{2}$	$\frac{1}{2}$	0
$\gamma^{(*)}+p\to n+\pi^+$	$\frac{1}{\sqrt{2}}$	$\frac{1}{\sqrt{2}}$	0	-1
$\gamma^{(*)}+n\to p+\pi^-$	$-\frac{1}{\sqrt{2}}$	0	$\frac{1}{\sqrt{2}}$	1
$\gamma^{(*)}+n\to n+\pi^0$	0	0	0	0

TABLE 4.1: Tree level amplitude constants for each channel at $\mathcal{O}(p^1)$.

The above amplitudes can be simplified by using the Dirac-matrix algebra, the on-shell conditions for the external legs momenta (throught the physical masses $p^2 = p'^2 = m_N^2$, $q^2 = M_\pi^2$) and applying the Dirac equation for the external spinors $\not{p}u_N(p) = m_N u_N(p)$, $[\overline{u}_N(p_f)\not{p}_f = m_N\overline{u}_N(p_f)]$ given the hadron amplitude $\mathcal{H}^\mu = \overline{u}_{N'}(p')\mathcal{M}^{\mu\,(1)}u_N(p)$ as in Eqs. (3.13) and (3.73). After the algebra simplifications, the amplitude is written in terms of the kinematical variables $\{s, u, Q^2\}$ and the Ball basis as detailed in appendix A.2.

$\mathcal{O}(p^2)$ amplitude

The $\mathcal{O}(p^2)$ contribution to the hadron amplitude $\mathcal{M}^\mu$ in (4.5) includes only the tree level amplitudes

$$\mathcal{M}^{\mu\,(2)}_{\text{tree}} = \mathcal{M}^{\mu\,(2)}_{(e)} + \mathcal{M}^{\mu\,(2)}_{(f)} + \mathcal{M}^{\mu\,(2)}_{(g)} + \mathcal{M}^{\mu\,(2)}_{(h)}, \tag{4.15}$$

with the subscripts (e)-(h) referring to the Feynman topologies in Fig. 4.1. These contributions are calculated as follows,

$$\mathcal{M}^{\mu\,(2)}_{(e)} = \sum_{N_I} \mathcal{V}^{(1)}_{N_I;N'\pi} iS_{N_I}(p+k)\mathcal{V}^{\mu\,(2)}_{\gamma N;N_I}, \tag{4.16}$$

$$\mathcal{M}^{\mu\,(2)}_{(f)} = \sum_{N_I} \mathcal{V}^{\mu\,(2)}_{\gamma N_I;N'} iS_{N_I}(p-q)\mathcal{V}^{(1)}_{N;N_I\pi}, \tag{4.17}$$

$$\mathcal{M}^{\mu\,(2)}_{(g)} = \sum_{N_I} \mathcal{V}^{(1)}_{N_I;N'\pi} iS_{N_I}(p+k)\mathcal{V}^{(2)}_{N_I;N_I} iS_{N_I}(p+k)\mathcal{V}^{\mu\,(1)}_{\gamma N;N_I}, \tag{4.18}$$

$$\mathcal{M}^{\mu\,(2)}_{(h)} = \sum_{N_I} \mathcal{V}^{\mu\,(1)}_{\gamma N_I;N'} iS_{N_I}(p-q)\mathcal{V}^{(2)}_{N_I;N_I} iS_{N_I}(p-q)\mathcal{V}^{(1)}_{N;N_I\pi}, \tag{4.19}$$

where the Feynman rules for the order $\mathcal{O}(p^2)$ vertices, $\mathcal{V}^{(2)}_{\text{vertex}}$, were derived from $\mathcal{L}_N^{(2)}$ (2.63) and can be seen in Appendix A.1. As before with the $\mathcal{O}(p^1)$ amplitude case, the Feynman rules for the vertices can be specified according to the external isospin channel. The hadron amplitudes are then written for each physical channel as

$$\mathcal{M}^{\mu\,(2)}_{(e)} = C_{II}^{(2)} \frac{e\,g\,k_\nu \not{q}\gamma^5(\not{k}+\not{p}+m)\left(\gamma^\mu\gamma^\nu - \gamma^\nu\gamma^\mu\right)}{4Fm_N\left((p+k)^2-m^2\right)}, \tag{4.20}$$

$$\mathcal{M}^{\mu\,(2)}_{(f)} = C_{III}^{(2)} \frac{e\,g\,k_\nu \left(\gamma^\mu\gamma^\nu - \gamma^\nu\gamma^\mu\right)\left(\not{p}'-\not{k}+m\right)\not{q}\gamma^5}{4Fm_N\left((p'-k)^2-m^2\right)}, \tag{4.21}$$

$$\mathcal{M}^{\mu\,(2)}_{(g)} = C_{II}^{(1)} \frac{e\,g\,\not{q}\gamma^5 i\left(\not{p}+\not{k}+m\right)[i4c_1M_\pi^2]i\left(\not{p}+\not{k}+m\right)i\gamma^\mu}{F\left((p+k)^2-m^2\right)^2}, \tag{4.22}$$

$$\mathcal{M}^{\mu\,(2)}_{(h)} = C^{(1)}_{III} \frac{e\,g\,i\gamma^\mu i\left(\not p' - \not k + m\right)[i4c_1 M_\pi^2] i\left(\not p' - \not k + m\right)\not q\gamma^5}{F\left((p'-k)^2 - m^2\right)^2}. \tag{4.23}$$

The coefficients $C^{(2)}_{II}$ and $C^{(2)}_{III}$ are found in the Table 4.2. The constants $C^{(1)}_{II}$, $C^{(1)}_{III}$ coincide with those appearing in Table 4.1, given the similarity between diagrams (b) and (g), and the crossed ones (c) and (h) in Fig. 4.1.

Channel	$C^{(2)}_{II}$	$C^{(2)}_{III}$
$\gamma + p \to p + \pi^0$	$\frac{1}{2}(c_6 + c_7)$	$\frac{1}{2}(c_6 + c_7)$
$\gamma + p \to n + \pi^+$	$\frac{1}{\sqrt{2}}(c_6 + c_7)$	$\frac{1}{\sqrt{2}}c_7$
$\gamma + n \to p + \pi^-$	$\frac{1}{\sqrt{2}}c_7$	$\frac{1}{\sqrt{2}}(c_6 + c_7)$
$\gamma + n \to n + \pi^0$	$-\frac{1}{2}c_7$	$-\frac{1}{2}c_7$

TABLE 4.2: Tree level amplitude constants for each channel at $\mathcal{O}(p^2)$.

$\mathcal{O}(p^3)$ amplitude, tree diagrams

The tree level contribution at $\mathcal{O}(p^3)$ in the $\gamma^{(*)} + N \longrightarrow \pi + N'$ amplitude of Eq. (4.5) is obtained as the sum of the following pieces

$$\begin{aligned}\mathcal{M}^{\mu\,(3)}_{\text{tree}} =& \mathcal{M}^{\mu\,(3)}_{(i)} + \mathcal{M}^{\mu\,(3)}_{(j)} + \mathcal{M}^{\mu\,(3)}_{(k)} + \mathcal{M}^{\mu\,(3)}_{(l)} + \mathcal{M}^{\mu\,(3)}_{(m)} + \mathcal{M}^{\mu\,(3)}_{(n)} + \mathcal{M}^{\mu\,(3)}_{(o)} \\ &+ \mathcal{M}^{\mu\,(3)}_{(p)} + \mathcal{M}^{\mu\,(3)}_{(q)} + \mathcal{M}^{\mu\,(3)}_{(r)} + \mathcal{M}^{\mu\,(3)}_{(s)} + \mathcal{M}^{\mu\,(3)}_{(t)},\end{aligned} \tag{4.24}$$

corresponding to the diagrams (i)-(t) in Fig. 4.1. These diagrams contain vertices derived from the Lagrangian terms $\mathcal{L}^{(3)}_N$ (2.64), $\mathcal{L}^{GSS(4)}_{\pi\pi}$ (2.44), and other vertices from the lower order Lagrangian pieces. According to the δ power counting rule (2.79), all possible $\mathcal{O}(p^3)$ tree level contributions include only the pion and nucleon sectors. The calculation of the amplitudes in $\mathcal{M}^{\mu\,(3)}_{\text{tree}}$ (4.24) is performed as follows

$$\mathcal{M}^{\mu\,(3)}_{(i)} = \mathcal{V}^{\mu\,(3)}_{\gamma N;\pi N'}, \tag{4.25}$$

$$\mathcal{M}^{\mu\,(3)}_{(j)} = \sum_{N_I} \mathcal{V}^{(3)}_{N_I;N'\pi} iS_N(p+k)\mathcal{V}^{\mu\,(1)}_{\gamma N;N_I} \tag{4.26}$$

$$\mathcal{M}^{\mu\,(3)}_{(k)} = \sum_{N_I} \mathcal{V}^{\mu\,(1)}_{\gamma N_I;N'} iS_N(p-q)\mathcal{V}^{(3)}_{N;N_I\pi} \tag{4.27}$$

$$\mathcal{M}^{\mu\,(3)}_{(l)} = \sum_{\pi_I} \mathcal{V}^{\mu\,(4)}_{\gamma\pi_I;\pi} iS_\pi(q-k)\mathcal{V}^{(1)}_{N;N'\pi_I} \tag{4.28}$$

$$\mathcal{M}^{\mu\,(3)}_{(m)} = \sum_{N_I} \mathcal{V}^{(1)}_{N_I;N'\pi} iS_N(p+k)\mathcal{V}^{\mu\,(3)}_{\gamma N;N_I} \tag{4.29}$$

$$\mathcal{M}^{\mu\,(3)}_{(n)} = \sum_{N_I} \mathcal{V}^{\mu\,(3)}_{\gamma N_I;N'} iS_N(p-q)\mathcal{V}^{(1)}_{N;N_I\pi} \tag{4.30}$$

$$\mathcal{M}^{\mu\,(3)}_{(o)} = \sum_{\pi_I} \mathcal{V}^{\mu\,(2)}_{\gamma\pi_I;\pi} iS_\pi(q-k)\mathcal{V}^{(3)}_{N;N'\pi_I} \tag{4.31}$$

$$\mathcal{M}^{\mu\,(3)}_{(p)} = \sum_{\pi_I} \mathcal{V}^{\mu\,(2)}_{\gamma\pi_I;\pi} iS_\pi(q-k)\mathcal{V}^{(4)}_{\pi_I;\pi_I} iS_\pi(q-k)\mathcal{V}^{(1)}_{N;N'\pi_I} \tag{4.32}$$

$$\mathcal{M}^{\mu\,(3)}_{(q)} = \sum_{N_I} \mathcal{V}^{(1)}_{N_I;N'\pi} iS_{N_I}(p+k)\mathcal{V}^{(2)}_{N_I;N_I} iS_{N_I}(p+k)\mathcal{V}^{(2)}_{N_I;N_I} iS_{N_I}(p+k)\mathcal{V}^{\mu\,(1)}_{\gamma N;N_I} \tag{4.33}$$

$$\mathcal{M}^{\mu\,(3)}_{(r)} = \sum_{N_I} \mathcal{V}^{\mu\,(1)}_{\gamma N_I;N'} iS_{N_I}(p-q)\mathcal{V}^{(2)}_{N_I;N_I} iS_{N_I}(p-q)\mathcal{V}^{(2)}_{N_I;N_I} iS_{N_I}(p-q)\mathcal{V}^{(1)}_{N;N_I\pi} \tag{4.34}$$

$$\mathcal{M}^{\mu\,(3)}_{(s)} = \sum_{N_I} \mathcal{V}^{(1)}_{N_I;N'\pi} iS_{N_I}(p+k)\mathcal{V}^{(2)}_{N_I;N_I} iS_{N_I}(p+k)\mathcal{V}^{\mu\,(2)}_{\gamma N;N_I} \tag{4.35}$$

$$\mathcal{M}^{\mu\,(3)}_{(t)} = \sum_{N_I} \mathcal{V}^{\mu\,(2)}_{\gamma N_I;N'} iS_{N_I}(p-q)\mathcal{V}^{(2)}_{N_I;N_I} iS_{N_I}(p-q)\mathcal{V}^{(1)}_{N;N_I\pi} \tag{4.36}$$

where the Feynman rules for the propagators S_N, S_π and vertices $\mathcal{V}^{(1)}_{\text{vertex}}, \ldots, \mathcal{V}^{(4)}_{\text{vertex}}$ are given in the appendix A. For all the four physical channels, the above expressions are summarized and written in terms of Dirac matrices, momenta, and LECs as

$$\begin{aligned}
\mathcal{M}^{\mu\,(3)}_{(i)} &= C^{(3)}_{Ia} \frac{ie}{m_N F} 2\varepsilon^{\mu\nu\alpha\beta}\, k_\nu (p_\beta + p'_\beta) q_\alpha \\
&+ C^{(3)}_{Ib} \Bigg[\frac{\sqrt{2}\,(d_{18} - 2d_{16})\, eM^2 \gamma^\mu \gamma^5}{F} \\
&- \frac{d_{20} e}{\sqrt{2} F m_N^2} k_\nu \Big[\gamma^\mu \gamma^5 \left(p'^\nu q \cdot p' + p^\nu p \cdot q \right) - \gamma^\nu \gamma^5 \left(p'^\mu q \cdot p' + p^\mu p \cdot q \right) \Big] \\
&- \frac{\sqrt{2} d_{21} e}{F} k_\nu \left(q^\nu \gamma^\mu \gamma^5 - q^\mu \gamma^\nu \gamma^5 \right) + \frac{d_{22} e}{\sqrt{2} F} k_\nu \left(\gamma^\mu \gamma^5 \left(q^\nu - k^\nu \right) - \gamma^\nu \gamma^5 \left(q^\mu - k^\mu \right) \right) \Bigg],
\end{aligned} \tag{4.37}$$

$$\mathcal{M}^{\mu\,(3)}_{(j)} = C^{(3)}_{IIa} \frac{eM^2}{F} \not{q} \gamma^5 \frac{(\not{p} + \not{k} + m)}{(p+k)^2 - m^2} \gamma^\mu (d_{18} - 2d_{16}), \tag{4.38}$$

$$\mathcal{M}^{\mu\,(3)}_{(k)} = C^{(3)}_{IIIa} \frac{eM^2}{F} \gamma^\mu \frac{(\not{p}' - \not{k} + m)}{(p'-k)^2 - m^2} \not{q} \gamma^5 (d_{18} - 2d_{16}), \tag{4.39}$$

$$\begin{aligned}
\mathcal{M}^{\mu\,(3)}_{(l)} &= C^{(3)}_{IV} \frac{2ie\, g\, (\not{q} - \not{k}) \gamma^5}{\sqrt{2} F \left((q-k)^2 - M^2 \right)} \\
&\left(\frac{i l_4 M^2 (2q-k)^\mu}{F^2} + \frac{i l_6 k^\nu \left(q^\mu (q-k)^\nu - q^\nu (q-k)^\mu \right)}{F^2} \right),
\end{aligned} \tag{4.40}$$

$$\mathcal{M}^{\mu\,(3)}_{(m)} = C^{(3)}_{IIb} \frac{e\, g\, k_\nu \Big[k^\nu \left((k+p)^\mu + p^\mu \right) - k^\mu \left((k+p)^\nu + p^\nu \right) \Big] \not{q} \gamma^5 (\not{p} + \not{k} + m)}{4 F m_N \left((p+k)^2 - m^2 \right)}, \tag{4.41}$$

$$\mathcal{M}^{\mu\,(3)}_{(n)} = C^{(3)}_{IIIb} \frac{e\, g\, k_\nu \Big[k^\nu \left((p'-k)^\mu + p'^\mu \right) - k^\mu \left((p'-k)^\nu + p'^\nu \right) \Big] \left(\not{p}' - \not{k} + m \right) \not{q} \gamma^5}{4 F m_N \left((p'-k)^2 - m^2 \right)}, \tag{4.42}$$

$$\mathcal{M}^{\mu\,(3)}_{(o)} = C^{(3)}_{IV} \frac{\sqrt{2} eM^2}{F} \frac{(\not{q} - \not{k})}{(q-k)^2 - M^2} (2q-k)^\mu \gamma^5 (d_{18} - 2d_{16}), \tag{4.43}$$

$$\mathcal{M}^{\mu\,(3)}_{(p)} = C^{(1)}_{IV} \frac{e\, g\, (2q-k)^\mu (\not{q} - \not{k}) \gamma^5}{\sqrt{2} F \left((q-k)^2 - M^2 \right)} \xi, \tag{4.44}$$

$$\mathcal{M}^{\mu\,(3)}_{(q)} = C^{(1)}_{II} \frac{e\, g\, \not{q} \gamma^5 i \left(\not{p} + \not{k} + m \right) [i 4 c_1 M_\pi^2] i \left(\not{p} + \not{k} + m \right) [i 4 c_1 M_\pi^2] i \left(\not{p} + \not{k} + m \right) i \gamma^\mu}{F \left((p+k)^2 - m^2 \right)^3}, \tag{4.45}$$

$$\mathcal{M}^{\mu\,(3)}_{(r)} = C^{(1)}_{III} \frac{e\,g\,i\gamma^\mu i\left(\not p' - \not k + m\right)[i4c_1M_\pi^2]i\left(\not p' - \not k + m\right)[i4c_1M_\pi^2]i\left(\not p' - \not k + m\right)\not q\gamma^5}{F\left((p'-k)^2 - m^2\right)^3}, \tag{4.46}$$

$$\mathcal{M}^{\mu\,(3)}_{(s)} = C^{(2)}_{II} \frac{e\,g\,k_\nu \not q\gamma^5(\not k + \not p + m)[i4c_1M_\pi^2]i\left(\not p + \not k + m\right)\left(\gamma^\mu\gamma^\nu - \gamma^\nu\gamma^\mu\right)}{4Fm_N\left((p+k)^2 - m^2\right)^2}, \tag{4.47}$$

$$\mathcal{M}^{\mu\,(3)}_{(t)} = C^{(2)}_{III} \frac{e\,g\,k_\nu\left(\gamma^\mu\gamma^\nu - \gamma^\nu\gamma^\mu\right)\left(\not p' - \not k + m\right)[i4c_1M_\pi^2]i\left(\not p' - \not k + m\right)\not q\gamma^5}{4Fm_N\left((p'-k)^2 - m^2\right)^2}. \tag{4.48}$$

The corresponding constants, $C^{(3)}_{Ia}, \ldots, C^{(3)}_{IV}$, are given in Table 4.3 for each channel. In the particular amplitude $\mathcal{M}^{\mu\,(3)}_{(p)}$, the coefficient ξ is an $O(p^2)$ function given by

$$\begin{aligned}\xi =& \frac{2M^2}{F^2}\left(\frac{M^2}{(q-k)^2 - M^2}l_3 - l_4\right)\\ =& \frac{2M^2}{F^2}\left(\frac{M^2}{2m_N^2 - Q^2 - s - u}l_3 - l_4\right)\end{aligned} \tag{4.49}$$

and the constant $C^{(1)}_{IV}$ is that given in Table. 4.1. In fact,

$$\mathcal{M}^{\mu\,(3)}_{(p)} = \mathcal{M}^{\mu\,(1)}_{(d)}\xi. \tag{4.50}$$

The other coefficients $C^{(1)}_{II}$, $C^{(1)}_{III}$,$C^{(2)}_{II}$ and $C^{(2)}_{III}$ for the amplitude contributions $\mathcal{M}^{\mu\,(3)}_{(q)}$, $\ldots$, $\mathcal{M}^{\mu\,(3)}_{(t)}$ appeared already in Tables 4.1 and 4.2. These amplitudes are proportional to the same coefficients because they include only extra momenta-independent vertices, $\mathcal{V}^{(2)}_{N_I,N_I} = 4ic_1M^2$, inserted in the nucleon propagator for the diagrams (b), (c) and (e), (f) [see Fig. 4.1].

Channel	$C^{(3)}_{Ia}$	$C^{(3)}_{Ib}$	$C^{(3)}_{IIa}$	$C^{(3)}_{IIb}$	$C^{(3)}_{IIIa}$	$C^{(3)}_{IIIb}$	$C^{(3)}_{IV}$
$\gamma^*p \to p\pi^0$	$d_8 + d_9$	0	1	$2d_7 + d_6$	1	$2d_7 + d_6$	0
$\gamma^*p \to n\pi^+$	$\sqrt{2}d_9$	-1	$\sqrt{2}$	$\sqrt{2}(2d_7 + d_6)$	0	$\sqrt{2}(2d_7 - d_6)$	1
$\gamma^*n \to p\pi^-$	$\sqrt{2}d_9$	1	0	$\sqrt{2}(2d_7 - d_6)$	$\sqrt{2}$	$\sqrt{2}(2d_7 + d_6)$	-1
$\gamma^*n \to n\pi^0$	$d_8 - d_9$	0	0	$-(2d_7 - d_6)$	0	$-(2d_7 - d_6)$	0

TABLE 4.3: Tree level amplitude constants for each channel at $\mathcal{O}(p^3)$.

$\mathcal{O}(p^{5/2})$ amplitude from the Δ mechanisms

In the δ-power counting scheme, (2.79), the $\Delta(1232)$ contribution for the EM pion production amplitude starts from $\mathcal{O}(p^{5/2})$ at tree level. The diagrams are depicted in Fig. 4.3. Further contributions with the Δ resonance include tree and loop-level amplitudes at $\mathcal{O}(p^{7/2})$ which are above our considerations up to $\mathcal{O}(p^3)$[1].
The different couplings needed to build the corresponding diagrams are driven by the interaction vertices $\Delta N\pi$ and $\Delta N\gamma$. They are encoded in the vertex Feynman rules

[1]The effect of the $\mathcal{O}(p^{5/2})$ Δ contributions at tree and loop level has been studied in detail for the $\gamma + p \longrightarrow \pi^0 + p$ channel at low energies in the same model considered here in Ref. [22]. They have shown that the $\mathcal{O}(p^{7/2})$ contributions produce quite small changes in comparison with the $\mathcal{O}(p^3)$ calculation.

derived from $\mathcal{L}^{(1)}_{\Delta\pi N}$ (2.69) and $\mathcal{L}^{(2)}_{\Delta\gamma N}$ (2.70). In this way, the amplitude contribution from the Δ mechanisms in $\mathcal{M}^{\mu}$ (4.5) is given by

$$\mathcal{M}^{\mu\,(5/2)}_{\text{tree}\Delta} = \mathcal{M}^{\mu\,(5/2)}_{(a)} + \mathcal{M}^{\mu\,(5/2)}_{(b)} \tag{4.51}$$

where $\mathcal{M}^{\mu\,(5/2)}_{(a)}$ and $\mathcal{M}^{\mu\,(5/2)}_{(b)}$ indicate the amplitudes of the corresponding diagrams of Fig. 4.3. The above amplitudes are calculated with the Feynman rules for the Rarita-Schwinger Δ-propagator, (A.23), and the vertices, $\mathcal{V}^{\nu\mu\,(2)}_{\gamma N;\Delta}$ and $\mathcal{V}^{\mu\,(1)}_{\Delta;N\pi}$ given explicitly in App. A, as follows

$$\mathcal{M}^{\mu\,(5/2)}_{(a)} = \sum_{\Delta_I} \mathcal{V}^{\eta\,(1)}_{\Delta_I;N'\pi} iS^{\Delta}{}_{\eta\nu}(p+k)\mathcal{V}^{\nu\mu\,(2)}_{\gamma N;\Delta_I}\,, \tag{4.52}$$

$$\mathcal{M}^{\mu\,(5/2)}_{(b)} = \sum_{\Delta_I} \mathcal{V}^{\eta\mu\,(2)}_{\gamma\Delta_I;N'} iS^{\Delta}{}_{\eta\nu}(p-q)\mathcal{V}^{\nu\,(1)}_{N;\Delta_I\pi}. \tag{4.53}$$

The summation for the different isospin states of the Δ, $\Delta_I = \{\Delta^{++}, \Delta^{+}, \Delta^{0}, \Delta^{-}\}$, is reduced to only one term for each physical channel due to the charge conservation in the vertices depending of the external fields γ, N, π, N'. Indicating the external particles for the four channels, the amplitudes can be written as

$$\mathcal{M}^{\mu\,(5/2)}_{(a)} = D_{II}\frac{eh_A g_M}{2F_\pi m_N m_\Delta(m_N+m_\Delta)} P_\rho q_\lambda \gamma^{\rho\mu\lambda} iS^{\Delta}_{\mu\nu}(P)\varepsilon^{\sigma\nu\alpha\beta}k_\alpha\epsilon_\beta P_\sigma\,, \tag{4.54}$$

$$\mathcal{M}^{\mu\,(5/2)}_{(b)} = D_{III}\frac{eh_A g_M}{2F_\pi m_N m_\Delta(m_N+m_\Delta)} \varepsilon^{\rho\mu\alpha\beta}k_\alpha\epsilon_\beta P'_\rho iS^{\Delta}_{\mu\nu}(P')\gamma^{\sigma\nu\lambda}P'_\sigma q_\lambda\,, \tag{4.55}$$

where the coefficients D_{II} and D_{III} are displayed in Table 4.4, $P = p + k$ and $P' = p' - k$ are the 4-momenta of the Δ resonance for the respective amplitudes, $\mathcal{M}^{\mu\,(5/2)}_{(a)}$ and $\mathcal{M}^{\mu\,(5/2)}_{(b)}$.

Channel	D_{II}	D_{III}
$\gamma^{(*)} + p \to p + \pi^0$	1	-1
$\gamma^{(*)} + p \to n + \pi^+$	$-\frac{1}{\sqrt{2}}$	$-\frac{1}{\sqrt{2}}$
$\gamma^{(*)} + n \to p + \pi^-$	$\frac{1}{\sqrt{2}}$	$\frac{1}{\sqrt{2}}$
$\gamma^{(*)} + n \to n + \pi^0$	1	-1

TABLE 4.4: Tree level amplitude constants for each channel at $\mathcal{O}(p^{5/2})$.

Additionally, in the above Δ-exchange amplitudes, the Δ-width effect can be included through the modification of the Δ propagator (A.23) by making the following substitution within $iS^{\mu\nu}_{\Delta}(p_\Delta)$,

$$\frac{1}{m_\Delta^2 - p_\Delta^2 - i\epsilon} \to \frac{1}{m_\Delta^2 - im_\Delta\Gamma_\Delta(p_\Delta^2) - p_\Delta^2}, \tag{4.56}$$

where $\Gamma_\Delta(p_\Delta^2)$ is the energy-dependent width given by [97]

$$\Gamma_\Delta(p_\Delta^2) = \frac{[h_A/2]^2\Lambda^{3/2}(p_\Delta^2, M_\pi^2, m_N^2)}{192\pi F_\pi [p_\Delta^2]^3}\left[(p_\Delta^2 - M_\pi^2 + m_N^2)m_\Delta + 2p_\Delta^2 m_N\right]\theta\left(p_\Delta^2 - (m_N + M_\pi)^2\right), \tag{4.57}$$

with $\Lambda(x,y,z) = (x-y-z)^2 - 4yz$ the Källén function and $\theta(x)$ the unit step function. Since the step function $\theta(x)$ in (4.57) filters the Δ width effect only above the physical threshold, the function Γ_Δ is only relevant to the $\mathcal{M}^{\mu\,(5/2)}_{(a)}$ piece.

In fact, the Δ width will only affect the s-channel process, given by $\mathcal{M}^{\mu\,(5/2)}_{(a)}$, where it always occurs that the Δ four-momentum, $p_\Delta^2 = (p+k)^2 \geqslant (m_N + M_\pi)^2$. On the other hand, for the u-channel amplitude, $\mathcal{M}^{\mu\,(5/2)}_{(b)}$, corresponding to the crossed-diagram 4.3 (b), we have that the Δ momentum is always below the physical threshold, $p_\Delta^2 = (p-q)^2 \leqslant (m_N + M_\pi)^2$.

4.2.2 One-loop level diagrams at $\mathcal{O}(p^3)$

As it was indicated in Eq. (4.5), the amplitude $\mathcal{M}^\mu$ up to $\mathcal{O}(p^3)$ contains contributions from the loop amplitudes, there denoted as $\mathcal{M}^{\mu\,(3)}_{\text{loop}}$. The loop contribution can be separated into two kinds:

- The loops appearing in external legs through the WFR. In this case, for the hadronic current, they are the initial and final nucleons and the outgoing pion[2]. Their contribution can be factorized from the hadron current amplitude, $\mathcal{M}^\mu$, as a multiplicative function for each external hadron leg via the Lehmann-Symanzik-Zimmermann (LSZ) reduction formula[3]

$$\hat{\mathcal{M}}^\mu = \mathcal{Z}_N\sqrt{\mathcal{Z}}_\pi\mathcal{M}^\mu \tag{4.58}$$

  The functions $\mathcal{Z}_N$ and $\mathcal{Z}_\pi$ are well known up to and including $\mathcal{O}(p^2)$ in the same covariant ChPT approach used here. The explicit expressions are given in Eqs. (4.102) and (4.104).

- Apart from the loops in the external legs, there are 47 $\mathcal{O}(p^3)$ loop diagrams for the $\gamma^{(*)} + N \longrightarrow \pi + N'$ process that can be generated from the LO Lagrangians $\mathcal{L}_N^{(1)}$ and $\mathcal{L}_{\pi\pi}^{GSS\,(2)}$. First of all, I will treat them in more detail in the following.

The 47 loop diagrams can be built from the topologies of Fig. 4.2. They generate the Feynman diagrams by inserting in each specific crossed-dot vertex an incoming real or virtual photon, *e.g.* the topology 4.2-(c) can generate three diagrams for each of the three crossed-dot vertex as shown in Fig. 4.4.[4]

[2]The QED loop corrections for the external electrons or the real photon are negligible in the energy region treated here.

[3]This point will be discussed in detail in 4.2.5.

[4] In this way, all the diagrams generated are tagged with the label set {a1–3, b1–5, c1–3, d1–5, e1–7, f1–9, g1–7, h1–5, i1–3}. For instance, in Fig. 4.4, the diagrams (c1), (c2) and (c3) are displayed.

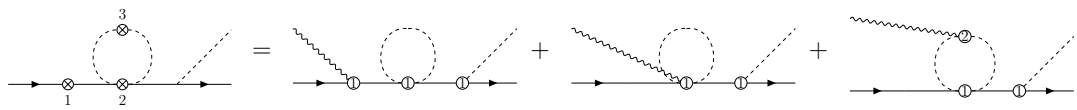

(c) (c1) (c2) (c3)

FIGURE 4.4: Example of Feynman diagrams generated by the topology in Fig. 4.2 -(c).

As before, the loop contribution to the pion EM production amplitude $\mathcal{M}^{\mu}$ (4.5) is the sum of the amplitudes associated with the Feynman diagrams from Fig. 4.2 such as,

$$\mathcal{M}^{\mu\,(3)}_{\text{loop}} = \sum_{topo=a1}^{i3} \mathcal{M}^{\mu\,(3)}_{(topo)}. \tag{4.59}$$

Using the Feynman rules shown in appendix A, the amplitude pieces $\mathcal{M}^{\mu\,(3)}_{(topo)}$ are written in detail in A.3 for the four physical channels. There are different types of loop amplitudes depending on the number of vertices the loop is connected to. In this work, the loops connect from 1 vertex (tadpoles) up to 4 vertices. For instance, the loop in the diagram from Fig. 4.2-(a1) is connected to a single vertex point while diagram (f3) is connected to 4 vertices. Another classification of the loop diagrams is related to the kind of propagators involved in the loop. In our case, we have purely meson loops for the topologies (a), (b), (c) and (i) in Fig. 4.2 and combined ones including meson-baryon loops for the rest of topologies in the same Figure. We will use this classification later to discuss some of the power counting issues.

Obviously, the calculation of loops involves an integral over the loop internal momenta. Moreover, some of these integrals are divergent and, since the propagators involved in those loop integrals are for massive particles, we only have ultraviolet (UV) divergences. In this work, we implement the method of dimensional regularization to remove them[5]. This method is characterized by the generalization of the loop integral from four to $D = 4 - 2\epsilon_{UV}$ continuum dimensions and the introduction of a multiplicative parameter $\mu^{2\epsilon_{UV}}$, (μ the renormalization scale). Then, in the limit of $\epsilon_{UV} \to 0$, the integral is separated into a series of $\mathcal{O}(\frac{1}{\epsilon_{UV}})$ and a finite part depending on μ. The UV renormalization of the theory consists on the absorption of the divergent terms of $\mathcal{O}(\frac{1}{\epsilon_{UV}})$ by the redefinition of LECs in the Lagrangian. There is still some freedom in the method used to accomplish that. As customary in ChPT, we use here the modified minimal subtraction $\widetilde{MS}$ scheme that will be described later. For full details of the scheme see Ref. [30].

Some self-energy types of diagrams are relatively easy to calculate. For instance, see a few examples in appendix C. Normally, the integral has a simple form or can be reduced into simple forms. After some algebra, these forms lead to simple expressions in terms of $\mathcal{O}(\frac{1}{\epsilon_{UV}})$, logarithms and some analytic terms.[6]

[5] There are many other methods used to regularize the UV divergences. Among them we could mention the radial cutoff approach [30, 98], which introduces suitable cutoffs Λ_i in the momentum integrations.

[6] For instance, the Feynman parametrization of the integrals may lead to some well known expressions. See, *e. g.,* the appendix in [62]).

In general, any of the loop amplitudes can be written as a combination of n-points integral functions $\mathcal{T}_n^{\mu_1\cdots\mu_p}$. Then, they are further simplified through Feynman parametrization to combinations of known integrals $I_n^{\mu_1\cdots\mu_p}$ as

$$\mathcal{T}_n^{\mu_1\cdots\mu_p} = \int \frac{d^D z}{(2\pi)^D} \frac{z^{\mu_1}\cdots z^{\mu_p}}{D_0 D_1 D_2 \ldots D_{n-1}} \longrightarrow I_n^{\mu_1\cdots\mu_p} = \int \frac{d^D l}{(2\pi)^D} \frac{l^{\mu_1}\cdots l^{\mu_p}}{(l^2 - \triangle^2)^n} \tag{4.60}$$

where $D_i = (z + r_i)^2 - m_i + i\epsilon$ is the denominator propagator in the loop with mass m_i and momenta $(z + r_i)$, r_i is related to the external momenta and $r_0 = 0$. l^μ and $\triangle$ are functions of the external momenta. Then, the integrals can be solved by known UV dimensional regularization expressions, which can be found, *e. g.,* in Ref. [62]. To do this extensive work, it is possible to combine calculations by hand with the help of specialized software. An example of this can be found in the previous work on pion photoproduction off protons [99].

Despite of the usefulness of the above approach, the task becomes quite complicated if one wants to calculate each of the 47 UV dimensional regularized integrals, $\mathcal{M}^{\mu\,(3)}_{(topo)}$, for the 4 physical channels (3.96) and for 2 reactions. That means for pion photo- and electroproduction a total of $47 \times 4 \times 2 = 376$ different loop integrals. To overcome this problem, I have implemented an automatized code based on a fully equivalent approach first proposed by Passarino and Veltman [100]. In detail, similarly to the tree-level amplitudes, we can simplify all the integrals for $\mathcal{M}^{\mu\,(3)}_{(topo)}$ after some Dirac matrix algebra into one-loop tensor integrals of the form

$$\mathcal{T}_n^{\mu_1\cdots\mu_p} = \frac{(2\pi\mu)^{4-D}}{i\pi^2} \int d^D z \frac{z^{\mu_1}\cdots z^{\mu_p}}{D_0 D_1 D_2 \ldots D_{n-1}}. \tag{4.61}$$

Then, the integral (4.61) can be reduced to combinations of four independent scalar Passarino-Veltman integrals

$$A_0[m_0^2] = \frac{(2\pi\mu)^{4-D}}{i\pi^2} \int d^D z \frac{1}{z^2 - m_0^2} \tag{4.62}$$

$$B_0[r_{10}^2, m_0^2, m_1^2] = \frac{(2\pi\mu)^{4-D}}{i\pi^2} \int d^D z \prod_{i=0}^{1} \frac{1}{[(z + r_i)^2 - m_i^2]} \tag{4.63}$$

$$C_0[r_{10}^2, r_{12}^2, r_{20}^2, m_0^2, m_1^2, m_2^2] = \frac{(2\pi\mu)^{4-D}}{i\pi^2} \int d^D z \prod_{i=0}^{2} \frac{1}{[(z + r_i)^2 - m_i^2]} \tag{4.64}$$

$$D_0[r_{10}^2, r_{12}^2, r_{23}^2, r_{30}^2, r_{20}^2, r_{13}^2, m_0^2, m_1^2, m_2^2, m_3^2] = \frac{(2\pi\mu)^{4-D}}{i\pi^2} \int d^D z \prod_{i=0}^{3} \frac{1}{[(z + r_i)^2 - m_i^2]} \tag{4.65}$$

where $r_{ij}^2 = (r_i - r_j)^2$ with the convention $r_0 = 0$.[7] I take advantage of this method where the above Passarino-Veltman functions have been implemented in the

[7] In all these expressions the $i\epsilon$ part of the denominators is omitted.

`Mathematica` package `FeynCalc` [101, 102]. Subsequently, I can express the full loop amplitude (4.59) as follows,

$$\mathcal{M}^{\mu(3)}_{loop} = \mu^{4-D} \sum_{topo=a1}^{i3} \mathcal{M}^{\mu}_{(topo)} \tag{4.66}$$

$$= f\left(A_0\left[M^2\right], B_0\left[s, M^2, m^2\right], \ldots, C_0[...], D_0[...]\right), \tag{4.67}$$

where μ^{4-D} is the scaling parameter in the dimensional regularization. Although there are known expressions for the Passarino-Veltman functions in dimensional regularization[8], we can evaluate numerically the finite part of these functions directly with the help of the `LoopTools` package [103, 104]. The calculation of all the loop amplitudes is still delicate and quite lengthy. For this reason, they need to be tested algebraically, *e.g.*, checking the fulfillment of the isospin symmetry, (3.104)-(3.107) and the crossing symmetry relations, (3.108). Further numerical probes have been made for the particular π^0 photoproduction channel comparing with previous results [99], obtained by solving the integrals with the Feynman parametrization method.

I will illustrate with further detail the steps for the complete procedure in the next section with a representative 3-point loop integral example. In addition, I will explain the breaking of the power counting for some of the integrals and its restoration.

Example: detailed calculation for the (g7) diagram

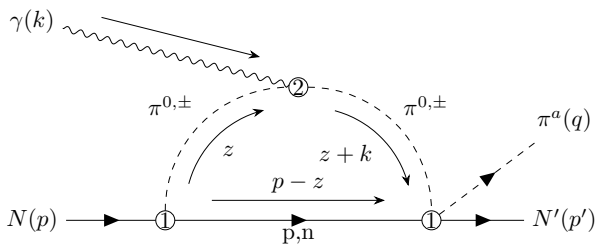

FIGURE 4.5: Feynman diagram for the one-loop diagram topology (g7) of Fig. 4.2 corresponding to the $\mathcal{O}(p^3)$ amplitude for the $\gamma^{(*)} + N \longrightarrow \pi^a + N'$ reaction. The numbers inside the circles indicate the chiral order of the vertices. The labels $\pi^{0,\pm}$ and p,n denote the possible charges of the loop lines, and z is the inner momentum in the loop integral.

As an example, I will show the detailed calculation for one of the loop diagrams. Using the Feynman rules for vertices and propagators given in appendix A, the corresponding momentum space amplitude, $\mathcal{M}^{\mu\,(3)}_{(topo)}$, can be written for the channel $\gamma^{(*)} + N \longrightarrow \pi^a + N'$ as

$$\mathcal{M}^{\mu\,(3)}_{(\mathrm{g7})} = \int \frac{dz^D}{(2\pi)^D} \sum_{N_I} \sum_{\pi_I} \mathcal{V}^{(1)}_{N_I\pi_I;N'\pi^a} iS_\pi(z+k) iS_N(p-z) \mathcal{V}^{\mu\,(2)}_{\gamma\pi_I;\pi_I} iS_\pi(z) \mathcal{V}^{(1)}_{N;N_I\pi_I}, \tag{4.68}$$

[8]Some of these analytical expressions are very complicated and/or have strong numerical instabilities due to large cancellations.

where the sums and integral are made over the degrees of freedom of the internal loop lines. The sums are made over the isospin states $N_I \in \{\text{p,n}\}$ and $\pi_I \in \{\pi^+, \pi^-, \pi^0\}$, while the integral is made over the inner loop momentum z. Specifying the charge of the external legs, I write down the amplitude for each physical channel.

- For the $\gamma^{(*)} + p \longrightarrow \pi^0 + p$ channel:

$$\mathcal{M}^{\mu\,(3)}_{(\text{g7})} = \int \frac{dz^D}{(2\pi)^D} \frac{i\,e\,g\,(k+2z)^\mu \left((\not{k}+\not{z})+\not{q}\right)\left(m_n + (\not{p}-\not{z})\right)\not{z}\gamma^5}{4F^3\left(z^2 - M^2_{\pi^+}\right)\left((k+z)^2 - M^2_{\pi^+}\right)\left((p-z)^2 - m_n^2\right)} \tag{4.69}$$

- For the $\gamma^{(*)} + p \longrightarrow \pi^+ + n$ channel:

$$\mathcal{M}^{\mu\,(3)}_{(\text{g7})} = \int \frac{dz^D}{(2\pi)^D} \frac{i\,e\,g\,(k+2z)^\mu \left((\not{k}+\not{z})+\not{q}\right)\left(m_n + (\not{p}-\not{z})\right)\not{z}\gamma^5}{4\sqrt{2}F^3\left(z^2 - M^2_{\pi^+}\right)\left((k+z)^2 - M^2_{\pi^+}\right)\left((p-z)^2 - m_n^2\right)} \tag{4.70}$$

- For the $\gamma^{(*)} + n \longrightarrow \pi^- + p$ channel:

$$\mathcal{M}^{\mu\,(3)}_{(\text{g7})} = \int \frac{dz^D}{(2\pi)^D} \frac{-i\,e\,g\,(-k-2z)^\mu \left((-\not{k}-\not{z})-\not{q}\right)\left(m_p + (\not{p}-\not{z})\right)\not{z}\gamma^5}{4\sqrt{2}F^3\left(z^2 - M^2_{\pi^-}\right)\left((k+z)^2 - M^2_{\pi^-}\right)\left((p-z)^2 - m_p^2\right)} \tag{4.71}$$

- For the $\gamma^{(*)} + n \longrightarrow \pi^0 + n$ channel:

$$\mathcal{M}^{\mu\,(3)}_{(\text{g7})} = \int \frac{dz^D}{(2\pi)^D} \frac{i\,e\,g\,(-k-2z)^\mu \left((-\not{k}-\not{z})-\not{q}\right)\left(m_p + (\not{p}-\not{z})\right)\not{z}\gamma^5}{4F^3\left(z^2 - M^2_{\pi^-}\right)\left((k+z)^2 - M^2_{\pi^-}\right)\left((p-z)^2 - m_p^2\right)} \tag{4.72}$$

where I have distinguished in the propagators the corresponding physical masses for the neutral and charged pions, M_{π^0} and $M_{\pi^\pm}$ respectively. Analogously, the corresponding neutron and proton propagators are differentiated with masses m_n and m_p. This distinction was made to account for the isospin breaking effects, relevant close to the threshold, which come from the different mass gaps between the physical threshold of the reaction, $W_{th} = (m_N + M_{\pi^a})$, and the thresholds for the opening of the loop channels: $W_{th-loop} = (m_{N_I} + M_{\pi_I})$, where m_{N_I} and M_{π_I} are taken as the physical masses[9].

These effects can be better appreciated when the physical threshold of the reaction, W_{th}, is lower than the total mass of the loop masses, *i.e.*, $(m_N + M_{\pi^a}) < (m_{N_I} + M_{\pi_I})$. This is the case for loops involved in the neutral pion production channels: $\gamma^{(*)} + p \longrightarrow \pi^0 + p$ and $\gamma^{(*)} + n \longrightarrow \pi^0 + n$. For example, in the photoproduction channel $\gamma + p \longrightarrow \pi^0 + p$, the above loop amplitude $\mathcal{M}^{\mu\,(3)}_{(\text{g7})}$ will account differently for the near threshold energies, W, such that $(m_p + M_{\pi^0}) < W < (m_n + M_{\pi^+})$ than for the higher energy region $W > (m_n + M_{\pi^+})$.

[9]Formally, given that the propagators are derived from the LO ChPT Lagrangian in an SU(2) isospin symmetric ChPT, we should include the masses in the chiral limit and the isospin limit. However, the inclusion of the physical masses instead of the chiral masses introduces differences of order $\mathcal{O}(p^4)$ or higher and do not alter the power counting at $\mathcal{O}(p^3)$; see section 4.3.3. Hence, I have considered in the loop lines the physical masses for the different charges of pions and nucleons in a more phenomenological approach to better describe isospin effects.

In detail, when the above contribution with a positive pion in the loop is evaluated near the threshold region, 1073.25 MeV $< W <$ 1078.49 MeV, it returns a purely real result, while for higher energies, $W >$ 1078.49, the loop results in a combination of real and imaginary components. In other words, it occurs a loop opening-channel from 1078.49 MeV. Thus, an abrupt behavior change at $W =$ 1078.49 MeV, known as a cusp effect, can be appreciated in some observables[10]. At much higher energies, the numerical differences are marginal between the isosymmetric loop amplitudes and the loops with isospin breaking. However, the isospin symmetric calculations badly fail to reproduce the very precise data near threshold.

At tree level, there are no such strong isospin breaking effects for the neutral pion channels $\pi^0 N$. On the other hand, for the charged pion channels, $\gamma^{(*)}+N \longrightarrow \pi^{\pm}+N'$, this effect is marginal given that it is related to only the smaller mass difference between the neutron and proton. Moreover, this difference is negligible and the phase space widely dominates the behaviour of the cross sections close to the threshold for these cases.

I shall highlight now the computing procedure I follow in general for the loop amplitudes. I take the channel $\gamma^* + p \longrightarrow \pi^0 + p$. Both, Dirac matrices and momenta are set in an analytically extended D-dimensional Minkowski space. The calculation steps proceed as follows:

- As the D-dimensional algebra for the Dirac matrices and scalar products [62] has been implemented in the `FeynCalc` package, I define in a `Mathematica` notebook the D dimensional on-shell scalar products for the external momenta, the Feynman rules, and the external momenta conservation (3.4).

- I type the integrand of the amplitude (4.69), expand the numerator part and reduce all possible terms into scalar products of type $p{\cdot}k$, $q{\cdot}p'$, $k{\cdot}q$, $p{\cdot}p'$, $p'{\cdot}k$, $p{\cdot}q$ including the on-shell conditions $p^2 = p'^2 = m_N^2, q^2 = M_\pi^2, k^2 = -Q^2$.

- I apply the Dirac equation to the integrand part in $\bar{u}_{N'}(p')\mathcal{M}^{\nu\,(3)}_{(g7)}u_N(p)$ for the external initial and final nucleon D-momenta $\not{p}u_N = m_N u_N$, with u_N the D-dimensional nucleon Dirac-spinor. This considerably simplifies the expressions.

- To implement the integration over the loop momentum, z, with dimensional regularization, the `TID` command in `FeynCalc` has been recently developed. This command does a one-loop tensor integral decomposition, transforming the Lorentz indices away from the integration momentum, z, and identifies the split terms with the scalar and tensorial Passarino-Veltman functions $A_0[m_p^2]$, $B_0[s, M_{\pi^+}^2, m_n^2]$,..., etc. The introduction of the t'Hooft parameter μ^{4-D} for dimension $D = 4 - 2\epsilon_{UV}$ has been encoded within `FeynCalc`.

- Finally, the scalar products among momenta are written in terms of the Mandelstam representation, s and u, using Eqs. (3.6) and (3.7).

After the above steps, the amplitude contribution (4.69) is written in the form

$$\mu^{4-D}\mathcal{M}^{\mu\,(3)}_{(g7)} = \frac{e\,g\,(m_n+m_p)}{16\pi^2 F^3}\Bigg[-\frac{\mathrm{A}_0\left[m_n^2\right]\gamma^5\left(k^\mu+p^\mu\right)}{2s} + \left(\frac{\gamma^\mu\gamma^5 Q^2-(D-2)k^\mu\not{k}\gamma^5}{4(D-1)Q^2\,(m_n+m_p)}+\frac{\left(k^\mu+p^\mu\right)\gamma^5}{2s}\right)\mathrm{A}_0\left[M_{\pi^+}^2\right]$$

[10] This isospin breaking effect has been studied earlier for some electroproduction observables. See, *e.g.*, Ref. [105].

$$
\begin{aligned}
&+ \frac{\gamma^5\left(k^\mu\left(m_n^2 - M_{\pi^+}^2\right) - p^\mu\left(M_{\pi^+}^2 - m_n^2 + s\right)\right)}{2s}\mathrm{B}_0\left[s, M_{\pi^+}^2, m_n^2\right] \\
&+ \frac{\left(4M_{\pi^+}^2 + Q^2\right)\left(\gamma^\mu\gamma^5 Q^2 + k^\mu \not{k}\gamma^5\right)}{8(D-1)Q^2\left(m_n + m_p\right)}\mathrm{B}_0\left[-Q^2, M_{\pi^+}^2, M_{\pi^+}^2\right] \\
&+ \frac{1}{4}k^\mu\left(2\not{k}\gamma^5\left(m_n - m_p\right) + \gamma^5\left(\left(m_p - m_n\right)^2 - 2M_{\pi^+}^2\right)\right) \\
&\qquad\qquad \times \mathrm{C}_0\left[m_p^2, -Q^2, s, m_n^2, M_{\pi^+}^2, M_{\pi^+}^2\right] \\
&+ \frac{1}{4}k^\mu\left(5\not{k}\gamma^5\left(m_n - m_p\right) + 2\gamma^5\left(Q^2 + \left(m_p - m_n\right)^2 - 2M_{\pi^+}^2\right)\right) \\
&\qquad\qquad \times \mathrm{C}_1\left[-Q^2, s, m_p^2, M_{\pi^+}^2, M_{\pi^+}^2, m_n^2\right] \\
&- \left(\left(p^\mu \not{k}\gamma^5 - \frac{m_p}{4}k^\mu\gamma^5\right)\left(m_n - m_p\right) + \frac{m_p}{2}k^\mu\not{k}\gamma^5 + p^\mu\gamma^5\frac{\left(m_n - m_p\right)^2 - 2M_{\pi^+}^2}{2}\right) \\
&\qquad\qquad \times \mathrm{C}_2\left[-Q^2, s, m_p^2, M_{\pi^+}^2, M_{\pi^+}^2, m_n^2\right] \\
&+ \frac{1}{2}p^\mu m_p\left(2\not{k}\gamma^5 + \gamma^5\left(m_p - m_n\right)\right)\mathrm{C}_{22}\left[-Q^2, s, m_p^2, M_{\pi^+}^2, M_{\pi^+}^2, m_n^2\right] \\
&- \frac{1}{2}\left(2\not{k}\gamma^\mu\gamma^5 + \gamma^\mu\gamma^5\left(m_p - m_n\right)\right)\mathrm{C}_{00}\left[-Q^2, s, m_p^2, M_{\pi^+}^2, M_{\pi^+}^2, m_n^2\right] \\
&- \frac{1}{2}k^\mu\left(\not{k}\gamma^5\left(m_p - m_n\right) - 2Q^2\gamma^5\right)\mathrm{C}_{11}\left[-Q^2, s, m_p^2, M_{\pi^+}^2, M_{\pi^+}^2, m_n^2\right] \\
&- \left(\left(Q^2 p^\mu\gamma^5 + m_p k^\mu\not{k}\gamma^5\right) + \left(p^\mu\not{k}\gamma^5 - m_p k^\mu\not{k}\gamma^5\right)\frac{\left(m_n - m_p\right)}{2}\right) \\
&\qquad\qquad \times \mathrm{C}_{12}\left[-Q^2, s, m_p^2, M_{\pi^+}^2, M_{\pi^+}^2, m_n^2\right]\Bigg]
\end{aligned}
\tag{4.73}
$$

where A_0, B_0, and C_0 are the 1-point, 2-points and 3-points scalar Passarino-Veltman integral functions defined in (4.62)-(4.64), respectively. The 3-point functions C_1, C_2,C_{22}, C_{11}, C_{00}, C_{12} are defined through the 3-point tensorial Passarino-Veltman integrals C^μ and $C^{\mu\nu}$

$$
C^\mu = r_1^\mu C_1 + r_2^\mu C_2\,, \tag{4.74}
$$

$$
C^{\mu\nu} = g^{\mu\nu}C_{00} + \sum_{i,j=1}^{2} r_i^\mu r_j^\nu C_{ij}\,, \tag{4.75}
$$

with

$$
C^\mu = \frac{(2\pi\mu)^{4-D}}{i\pi^2}\int d^D z z^\mu \prod_{i=0}^{2}\frac{1}{\left[(z+r_i)^2 - m_i\right]}, \tag{4.76}
$$

$$
C^{\mu\nu} = \frac{(2\pi\mu)^{4-D}}{i\pi^2}\int d^D z z^\mu z^\nu \prod_{i=0}^{2}\frac{1}{\left[(z+r_i)^2 - m_i\right]}. \tag{4.77}
$$

where r_i is related to the external momenta [see argument dependence as given in (4.64)]. For this example, it is deduced that $r_0 = 0$, $r_1 = -k$ and $r_2 = p$. Once we have our amplitude integrated and given in terms of the Passarino-Veltman functions, we are able to evaluate numerically all these functions using the `LoopTools` package for any c.m. energy $W = \sqrt{s}$ and pion angle. In the `LoopTools` package, it

is possible to evaluate Passarino-Veltman functions in UV dimensional regularization, implement any of the renormalization conventions to subtract the term containing $1/\varepsilon_{UV}$ and define the scale parameter at will. We choose $\mu = m_N$ as customary in BChPT calculations.

The tensorial Passarino-Veltman functions C_{ij}, C_i that appear in the amplitude (4.73) can be further decomposed into only scalar functions A_0, B_0, C_0 [11] and, as it was pointed out in (4.67), all the loop amplitudes can be written in terms of only scalar Passarino-Veltman functions[12]. Alternatively, we can evaluate directly the tensorial functions C_{ij} and C_i with `LoopTools`. Despite the equivalence among both approaches, at very low energies we reach a higher numerical precision in `LoopTools` with the tensorial Passarino-Veltman version and we obtain a very smooth behavior. On the other hand, with the scalar functions sometimes there are numerical issues due to cancellations among very large numerical quantities and the evaluated energy dependence becomes quite unstable close to the threshold.

Finally, as can be noticed in (4.73), there is still some remaining dependence on the dimension D for some terms multiplying the Passarino-Veltman functions[13]. These D's should not be naively substituted by four. In order to remove the UV term $1/\epsilon_{UV}$ and hold the adequate finite part, we need to take special care with terms that contain UV divergences. Here, this only applies to the terms with A_0, B_0 and C_{00}. The correct way to tackle this problem is to expand the expression obtained after making the substitution, $D = 4 - 2\epsilon_{UV}$, as a power series in ϵ_{UV}. Then, the resulting linear part in ϵ_{UV} will be multiplied by the divergent part of the respective Passarino-Veltman functions. This gives in return finite terms which need to be taken into account. For instance, in this example, it can occur that

$$D\ \mathrm{Div}[A_0[M_\pi^2]] = DM_\pi^2 \frac{1}{\epsilon_{UV}} \tag{4.78}$$

$$= (4 - 2\epsilon_{UV}) M_\pi^2 \frac{1}{\epsilon_{UV}} \tag{4.79}$$

$$= 4M_\pi^2 \frac{1}{\varepsilon_{UV}} - 2M_\pi^2, \tag{4.80}$$

where $\mathrm{Div}[A_0[M_\pi^2]]$ refers to the UV divergent part for $A_0[M_\pi^2]$ in dimensional regularization[14]. The term proportional to $\frac{1}{\varepsilon_{UV}}$ is systematically taken out in the regularization procedure while we hold the resulting finite term, $-2M_\pi^2$.

The procedure here presented has been applied for each loop amplitude given in appendix A.3 in a systematical automatized code in `Mathematica`. The algebraic manipulations with Dirac matrices and Passarino-Veltman functions were delegated to `FeynCalc` and the numerical evaluations to `LoopTools` in `FORTRAN` for faster numerical calculations. I have taken care of the conventions, comparing loop by loop with previous works [107] and in parallel with loop amplitudes for other similar reactions [25]. The algebraical testing has been ran in Mathematica for the isospin symmetry relations (3.104)-(3.107) and the crossing symmetry relations (3.108).

[11] We can do this with `FeynCalc` using the command `PaVeReduce` in `Mathematica`. This reduction is not unique but all the options give the same numerical results.

[12] D_0 only appears when we consider a 4-point one-loop integral

[13] The D dependence comes from the Dirac matrices manipulation in D dimensions, for instance when we use some identities like $g_{\mu\nu}\gamma^\mu\gamma^\nu = D$.

[14] The extraction of the divergent part for all the Passarino-Veltman functions has been implemented in `PackageX` [106], an auxiliary package for `FeynCalc`.

4.2.3 Renormalization

Once the one-loop integrals are dimensionally regularized, the UV divergences of the integrals are canceled by the counter-terms obtained by adjusting the bare LECs of the ChPT Lagrangian so that the resulting amplitude is expressed in terms of the renormalized LECs. The absorption of the UV divergences into the LECs is namely the renormalization procedure.

There are several conventions to cancel the divergences for a dimensional regularized loop amplitude. Some of the most popular are the minimal subtraction scheme, $\overline{MS}$, commonly used in Standard Model calculations, and the modified minimal subtraction scheme, $\overline{MS}-1$ (or $\widetilde{MS}$), widely used in ChPT.
In this work, we follow the $\widetilde{MS}$ scheme for the renormalization of the ChPT Lagrangian. In this scheme, one is looking to re-absorb in the LECs multiples of

$$R = \gamma_E - \frac{1}{\epsilon_{UV}} - \log(4\pi) - 1, \tag{4.81}$$

where $\gamma_E = -\Gamma'(1) = 0.5772\ldots$ is the Euler constant and $\epsilon_{UV} = (4-D)/2$, see Eq. (2.47) [15]. To illustrate this procedure and without losing generality, if one writes the regularized loop amplitude, $\mathcal{M}^{\mu\,(3)}_{loop}$, in terms of only scalar Passarino-Veltman functions, (4.67), the divergent part, R, appears in the one-point and two-point one-loop functions, (4.62) and (4.63) respectively. The R dependence can be seen through their expanded expressions around $\epsilon_{UV} \to 0$:

$$A_0[m_0^2] = -\, m_0^2 \left(R + \ln \frac{m_a^2}{\mu^2} \right), \tag{4.82}$$

$$\begin{aligned} B_0[r_{10}^2, m_0^2, m_1^2] = &-\, R + 1 - \ln \frac{m_1^2}{\mu^2} + \frac{m_0^2 - m_1^2 - r_{10}^2}{2r_{10}^2} \ln \frac{m_1^2}{m_0^2} \\ &+ \frac{r_{10}^2 - (m_0 - m_1)^2}{p^2} \rho_{ab}(r_{10}^2) \ln \frac{\rho_{ab}(r_{10}^2) - 1}{\rho_{ab}(r_{10}^2) + 1}, \end{aligned} \tag{4.83}$$

with

$$\rho_{ab}(r_{10}^2) \equiv \sqrt{\frac{r_{10}^2 - (m_0 + m_1)^2}{r_{10}^2 - (m_0 - m_1)^2}}. \tag{4.84}$$

In practice, we just drop all the terms proportional to R to regularize the loop amplitudes and, hence, treat the LECs appearing at the tree level amplitude as renormalized in the $\widetilde{MS}$ scheme.[16] Nonetheless, formally, we can always find the specific UV shift, β, for the LECs:

$$X = X^r + \frac{\beta_X}{16\pi^2} R, \qquad X \in \{m, g, c_i, d_j, l_k\} \tag{4.85}$$

such that for the complete amplitude, as in (4.5), including tree and loop contributions becomes

[15] Instead, in $\overline{MS}$ one subtracts multiples of $\gamma_E - \frac{1}{\epsilon_{UV}} - \log(4\pi)$.

[16] Taking $R = 0$ can be readily implemented in the `LoopTools` package [103] when we numerically evaluate the amplitudes.

$$\begin{aligned}&\mathcal{M}^{\mu}_{tree}[m,g,c_i,d_j,l_k]+\mathcal{M}^{\mu\,(3)}_{loops}\left(A_0\left[M^2\right],B_0\left[s,M^2,m^2\right],\ldots,C_0[...],D_0[...]\right)\\&=\underbrace{\mathcal{M}^{\mu}_{tree}[m^r,g^r,c^r_i,d^r_j,l^r_k]+\mathcal{M}^{\mu\,(3)}_{loops}\left(\overline{A}_0\left[M^2\right],\overline{B}_0\left[s,M^2,m^2\right],\ldots,C_0[...],D_0[...]\right)}_{\widetilde{MS}-\text{regularized amplitude without UV divergences}}\end{aligned} \tag{4.86}$$

where X are the non-renormalized LECs, m, g and the values for the indices i,j,k refers to those LECs involved in the Lagrangian terms (2.61), (2.63), (2.64) and (2.44). X^r stand for the $\widetilde{MS}$ renormalized LECs. $\mathcal{M}^{\mu}_{tree}$ indicates the amplitude at tree level, Eq. (4.5), and $\mathcal{M}^{\mu\,(3)}_{loops}$ is the loop amplitude, Eq. (4.67), that also includes the loops for the external legs, (see sect. 4.2.5). The functions $\overline{A}_0$ and $\overline{B}_0$ in Eq. (4.86) are the $\widetilde{MS}$ renormalized functions as in Eqs. (4.82) and (4.83) with $R=0$.
The UV β functions of Eq. (4.85) should be the adequate ones to cancel terms proportional to R involved in $\mathcal{M}^{\mu\,(3)}_{loops}$. In principle, those β functions are unique and most of them were derived from other processes and are well known. See, *e.g.*, Ref. [25].

In a more general case, when the tensorial Passarino-Veltman functions are used in the evaluation of $\mathcal{M}^{\mu\,(3)}_{loops}$, the procedure is equivalent given that the divergent part is always proportional to $1/\epsilon_{UV}$: First, we extract the terms proportional to R from the tensorial Passarino-Veltman functions in $\mathcal{M}^{\mu\,(3)}_{loops}$ [17]; Second, we subtract the terms going as $1/\epsilon_{UV}$ by doing $R\to 0$ (or $1/\epsilon_{UV}\to\gamma_E-\log(4\pi)-1$).

4.2.4 EOMS PCBT restoration scheme

According to the power-counting rule of Eq. (2.66), the $\widetilde{MS}$-renormalized loop amplitude, $\mathcal{M}^{\mu\,(3)}_{\text{loop}}$ (4.86), is supposed to be of order $\mathcal{O}(p^3)$. However, as it was pointed out in section 2.2.2, when one considers baryons in the loops, such as those derived from the baryonic $\mathcal{L}^{(1)}_N$ (2.61) [64], there may appear terms which are inconsistent with the power-counting [59]. These power-counting breaking terms (PCBT) are finite and of lower orders than the nominal one given by Eq. (2.66). In this sense, loops with nucleons in a baryon ChPT calculation lead us to a power-counting problem. As always, tree-level diagrams and those diagrams that exclusively contain mesons in the loops are still consistent with the power-counting defined in Eq. (2.66).
The main idea of the EOMS scheme is to absorb only the PCBT by performing finite subtractions, in addition to those of the $\widetilde{MS}$ renormalization procedure, such that the resulting expressions for the amplitudes of the corresponding diagrams satisfy the power-counting rule. Specifically, the EOMS renormalization consists of the cancellation of the PCBT appearing in the loop amplitudes obtained by performing a suitable finite shift of the LECs in the ChPT Lagrangian. These shifted constants alter the tree amplitudes in such a manner that the PCBT are exactly removed.

In particular, the power-counting violating loop amplitudes for $\gamma^{(*)}+N\longrightarrow\pi+N'$ are those involving nucleon propagators in the loops. They correspond to the topologies (d), (e), (f), (g) and (h) in Fig. 4.2. These loop amplitudes are not purely of order $\mathcal{O}(p^3)$, but contain PCBTs of lower orders: $\mathcal{O}(p^1)$ and $\mathcal{O}(p^2)$. These terms spoil the power-counting of Eqs. (2.66) and (2.79) for the given amplitudes $\mathcal{M}^{\mu\,(3)}_{topo}$.

[17] This is readily performed in `FeynCalc` jointly with the auxiliary software `PackageX`.

The commonly used procedure to implement the EOMS scheme in order to restore the power-counting in the aforementioned loop amplitudes goes as follows. The first step is to find the PCBTs by expanding the amplitudes in a series of the appropriate chiral parameters. For example, in [22] and [14], the parameters M_π, of order $\mathcal{O}(p)$, the Mandelstam variable t and $\nu = (s-u)/4m_N$, both of $\mathcal{O}(p^2)$, with s and u Mandelstam variables, were chosen for the expansion. As the PCBTs correspond to lower orders than the nominal $\mathcal{O}(p^3)$, all the PCBT of order $\mathcal{O}(p^2)$ or lower are identified and summed[18]. Please notice that to accomplish this, to have the analytical expressions of the integrated amplitudes is, normally, necessary[19].
The second step to regularize the loops in the EOMS scheme is to subtract the PCBT from $\mathcal{M}^{\mu(3)}_{loop}$, (4.86). Explicitly, we have that

$$\mathcal{M}^{\mu(3)}_{loop} = \sum_n \mathrm{PCBT}^{(n)} + \widetilde{\mathcal{M}}^{\mu(3)}_{loop} \tag{4.87}$$

where $\mathcal{M}^{\mu(3)}_{loop}$ is the $\widetilde{MS}$-regularized loop amplitude, $\mathrm{PCBT}^{(n)}$ is the PCBT of order $\mathcal{O}(p^n)$ with $n < 3$, and $\widetilde{\mathcal{M}}^{\mu(3)}_{loop}$ is the $\widetilde{MS}$ and EOMS-regularized loop amplitude. Please notice that the new amplitude $\widetilde{\mathcal{M}}^{\mu(3)}_{loop}$ starts now at $\mathcal{O}(p^3)$ and therefore satisfies the power-counting rule. From here, we can simply remove each $\mathrm{PCBT}^{(n)}$ and only keep the fully regularized $\mathcal{O}(p^3)$ amplitude, $\widetilde{\mathcal{M}}^{\mu(3)}_{loop}$. Finally, the LECs supposed to re-absorb the PCBT are already found renormalized in the EOMS scheme.

This method was performed in Ref. [22] in a study the neutral pion photoproduction on protons. They used the same theoretical model as here. Thus, they had similar loop amplitudes. Although their results were satisfactory with this method, the calculation for the four physical channels and the generalization to virtual photons for the electro-production process would be far more delicate and lead to a substantially larger task.

For that reason, and given that PCBT can be absorbed by shifts in the LECs, I have implemented, instead, an equivalent method by using the EOMS-renormalized LECs and their corresponding finite shifts. The corresponding shifts have been obtained first by T. Fuchs *et al.* in Ref. [6].
These EOMS shifts in the LECs allow us to generate the adequate counter-terms that cancel the PCBTs in the loops from the tree-level amplitudes. This straightforward method is based on the preliminary method working exclusively with loops as described above (4.60), but here we are only required to work with the tree-level amplitudes while the loop terms can be directly evaluated without modifications or further subtractions. This approach is much simpler and we are able to automatize efficiently the task for all the four physical channels and the pion electro- and photoproduction amplitudes.

In detail, the approach I follow introduces the EOMS-renormalized LECs, $\widetilde{X}$,

[18] Although there may be some PCBT cancellations among different loop diagrams, we still have some persistent PCBT for the total sum of topologies.

[19] It is possible to subtract the PCBTs without calculating explicitly the full integrals. The detailed procedure is explained in Ref. [30]. Basically, the integrands are modified with the subtraction of the suitable counter terms. To find them, the integrands are expanded in a series, and the problematic terms must be identified. The method is laborious but is well defined and systematic.

$$X^r = \widetilde{X} + \frac{m\,\widetilde{\beta}_X}{16\pi^2 F^2} \tag{4.88}$$

with X^r the $\widetilde{MS}$-renormalized LECs of Eq. (4.85). The functions $\widetilde{\beta}_X$ suitably shift the X^r LECs, such that, with the $\widetilde{MS}$-regularized tree amplitude we can systematically generate the PCBTs to be canceled up to $\mathcal{O}(p^2)$. That is, when we apply Eq. (4.88) to the tree level amplitude from Eq. (4.86) we get for the complete $\widetilde{MS}$-regularized amplitude that

$$\begin{aligned}\mathcal{M}^\mu =& \mathcal{M}^\mu_{tree}[m^r, g^r, c_i^r, d_j^r, l_k^r] + \mathcal{M}^{\mu\,(3)}_{loop} \\ =& \left[\mathcal{M}^\mu_{tree}(\widetilde{m}, \widetilde{g}, \widetilde{c}_i, d_j^r, l_k^r) - \sum_{n=1}^{2} \mathrm{PCBT}^{(n)}\right] + \mathcal{M}^{\mu\,(3)}_{loop}.\end{aligned} \tag{4.89}$$

In our case, the EOMS-renormalization shifts apply only to $X^r \in \{m^r, g^r, c_1^r, c_6^r, c_7^r\}$. Their $\widetilde{\beta}$-functions are given in Eqs. (4.91)-(4.93). Those few LECs are sufficient to generate the PCBT up to $\mathcal{O}(p^2)$. The EOMS-renormalization for the d_j, l_k LECs would produce contributions of $\mathcal{O}(p^3)$ or higher, which would not correspond to the PCBT treated here.
Additionally, we can notice from (4.87) and the loop contribution $\mathcal{M}^{\mu\,(3)}_{loop}$ in (4.89), the cancellation of PCBT up to $\mathcal{O}(p^2)$ and the EOMS regularization becomes evident. Thus

$$\begin{aligned}\mathcal{M}^\mu =& \mathcal{M}^\mu_{tree}[m^r, g^r, c_i^r, d_j^r, l_k^r] + \mathcal{M}^{\mu\,(3)}_{loop} \\ =& \mathcal{M}^\mu_{tree}[\widetilde{m}, \widetilde{g}, \widetilde{c}_i, d_j^r, l_k^r] + \widetilde{\mathcal{M}}^{\mu\,(3)}_{loop}.\end{aligned} \tag{4.90}$$

The EOMS $\widetilde{\beta}$-functions required in this work are readily available. They had already been obtained in the analysis of electromagnetic form factors of the nucleon [6], pion nucleon scattering [14], weak pion electroproduction [25] and others.
For the LO parameters m and g, from $\mathcal{L}^{(1)}_{\pi N}$, we have

$$\widetilde{\beta}_m = -\frac{3}{2} g^2 \overline{A}_0\left[m^2\right], \qquad \widetilde{\beta}_g = g^3 m + \frac{\left(2-g^2\right) g}{m} \overline{A}_0\left[m^2\right], \tag{4.91}$$

where

$$\overline{A}_0[m^2] = -m^2 \log \frac{m^2}{\mu^2}, \tag{4.92}$$

is the $\widetilde{\mathrm{MS}}$-renormalized scalar 1-point Passarino-Veltman function, (4.82), with μ the renormalization scale introduced in dimensional regularization[20].

[20] To be rigorous, we have included the $\overline{A}_0\left[m^2\right]$ terms that are sometimes omitted in the literature. The reason is that in those cases, like in this work, the renormalization scale is set to be the nucleon mass, $\mu = m$. Thus, $\overline{A}_0\left[m^2\right] \to 0$.

For the second order LECs appearing in $\mathcal{L}_N^{(2)}$ we get[21]

$$\widetilde{\beta}_{c_1} = \frac{3}{8}g^2 + \frac{3g^2}{8m^2}\overline{A}_0[m^2], \qquad \widetilde{\beta}_{c_6} = -5g^2 m, \qquad \widetilde{\beta}_{c_7} = 4g^2 m. \tag{4.93}$$

In the following, I will show briefly how the PCBT have been generated order by order from the tree-level amplitudes of $\mathcal{O}(p)$ and $\mathcal{O}(p^2)$. For each channel, I perform the calculations in the way of Eq. (4.89) to restore in the EOMS scheme the power-counting of the loop amplitudes.

First, we take the amplitude $\mathcal{M}_{tree}^{\mu(1)}$ of $\mathcal{O}(p)$, after the $\widetilde{MS}$-renormalization of the relevant LECs (g^r, m^r). As the renormalization scheme preserves the structure of the Lagrangian, the amplitude still has the same form. Thus, we can simply rename the LECs X as X^r. In the EOMS approach, we need to further modify the LECs $\{m^r, g^r\}$. To do that, we shift them in the amplitude $\mathcal{M}_{tree}^{\mu(1)}$ (4.6) using the equations (4.88) and (4.91). Then, expanding at first order in $\widetilde{\beta}_X$, we get[22]

$$\begin{aligned}\mathcal{M}_{tree}^{\mu\,(1)}[g^r, F, M, m^r] =& \mathcal{M}_{tree}^{\mu(1)}[\widetilde{g}, F, M, \widetilde{m}] + \mathrm{PCBT}_1 \\ =& \widetilde{\mathcal{M}}_{tree}^{\mu(1)} + \mathrm{PCBT}_1,\end{aligned} \tag{4.94}$$

where $\widetilde{\mathcal{M}}_{tree}^{\mu(1)} = \mathcal{M}_{tree}^{\mu(1)}[\widetilde{g}, F^r, M^r, \widetilde{m}]$ is the EOMS $\mathcal{O}(p^1)$ tree amplitude[23] The term PCBT_1 is a combination of $\mathcal{O}(p)$ and $\mathcal{O}(p^2)$ terms corresponding to some PCBT pieces, with a minus sign as compared to corresponding terms of the loop amplitude, (4.87). The explicit expressions of PCBT_1 for all physical channels and studied reactions are given in the appendix B.
Secondly, the additional LECs $\{c_1^r, c_6^r, c_7^r\}$ appearing in the amplitude $\mathcal{M}_{tree}^{\mu\,(2)}$, (4.15), are redefined in EOMS by using the equations (4.88), (4.91) and (4.93). Then, as before for the $\mathcal{O}(p^1)$ case

$$\begin{aligned}\mathcal{M}_{tree}^{\mu(2)}[c_1^r, c_6^r, c_7^r, m^r, g^r, F] =& \mathcal{M}_{tree}^{\mu(2)}[\widetilde{c}_1, \widetilde{c}_6, \widetilde{c}_7, \widetilde{m}, \widetilde{g}, F] + \mathrm{PCBT}_2 \\ =& \widetilde{\mathcal{M}}_{tree}^{\mu(2)} + \mathrm{PCBT}_2\end{aligned} \tag{4.95}$$

with $\widetilde{\mathcal{M}}_{tree}^{\mu(2)} = \mathcal{M}_{tree}^{\mu(2)}[\widetilde{c}_1, \widetilde{c}_6, \widetilde{c}_7, \widetilde{m}, \widetilde{g}, F]$ the $\mathcal{O}(p^2)$ tree amplitude in the EOMS scheme and of the same form as in Eq. (4.15). The generated PCBT_2 are shown explicitly in App. B.

Therefore, as it was mentioned above, the EOMS $\widetilde{\beta}$-functions are built to cancel, up to $\mathcal{O}(p^2)$, the PCBT that spoil the power-counting in the loop amplitudes. The complete set of PCBT, fully generated from only the amplitudes $\mathcal{M}_{tree}^{\mu(1)}$ and $\mathcal{M}_{tree}^{\mu(2)}$, corresponds to the sum of PCBT_2 and PCBT_2, *i.e.*,

[21] Note that the EOMS shifts applied to the c_6 and c_7 parameters in Ref. [6] are different, since their Lagrangian has an alternative arrangement so that: $c_6 = 4mc_6^F, c_7 = m\left(c_7^F - 2c_6^F\right)$, where the superscript F is just to identify the LECs of Ref. [6].

[22] Otherwise, given that m^r appears in the propagator denominator, without implementing any further expansion we could neither isolate the corresponding $\mathcal{M}_{tree}^{\mu\,(1)}(\widetilde{g}, F^r, M^r, \widetilde{m})$ nor identify the extracted PCBT_1. Both approaches do not produce any important numerical difference and, analytically, the discrepancies are of a higher chiral order than the present work.

[23] I recall here that in these $\mathcal{O}(p)$ amplitudes, the nucleon and pion masses, $\{\widetilde{m}, M\}$, which appear for instance in the propagators take their LO values.

$$\mathrm{PCBT}_1 + \mathrm{PCBT}_2 = -\sum_{n=1}^{2} \mathrm{PCBT}^{(\mathrm{n})}. \tag{4.96}$$

In order to test the correct calculation of the PCBT, the above terms PCBT_1 and PCBT_2 were checked to respect the symmetry relations for the isospin amplitudes (3.104)-(3.107) and the crossing symmetry relations (3.108) as well as the gauge invariance condition. Additionally, the PCBT derived with the $\widetilde{\beta}$-functions approach have been compared with those derived from the explicit calculation of the loops, given in Ref. [22] for the photoproduction channel $\gamma + p \longrightarrow \pi^0 + p$. We found that they coincide up to and including $\mathcal{O}(p^2)$[24].

In summary, once the PCBT were generated from the respective tree-level amplitudes, we can write the total regularized amplitude with all the contributions from the tree and loop diagrams of Figs. 4.1 and 4.2. Using the EOMS renormalization of the tree amplitudes of $\mathcal{O}(p)$ and $\mathcal{O}(p^2)$, the total amplitude reads

$$\mathcal{M}^\mu = \mathcal{M}^{\mu(1)}_{tree} + \mathcal{M}^{\mu(2)}_{tree} + \mathcal{M}^{\mu(3)}_{tree} + \mathcal{M}^{\mu(5/2)}_{tree\Delta} + \mathcal{M}^{\mu(3)}_{loop} \tag{4.97}$$

$$= \widetilde{\mathcal{M}}^{\mu(1)}_{tree} + \widetilde{\mathcal{M}}^{\mu(2)}_{tree} + \mathcal{M}^{\mu(3)}_{tree} + \mathcal{M}^{\mu(5/2)}_{tree\Delta} + \left(\mathrm{PCBT}_1 + \mathrm{PCBT}_2 + \mathcal{M}^{\mu(3)}_{loop}\right), \tag{4.98}$$

with $\mathcal{M}^{\mu(3)}_{loop}$ the UV $\widetilde{MS}$-regularized loop amplitude that breaks the power-counting. Then, using Eqs. (4.87) and (4.96), we have that

$$\mathcal{M}^\mu = \widetilde{\mathcal{M}}^{\mu(1)}_{tree} + \widetilde{\mathcal{M}}^{\mu(2)}_{tree} + \mathcal{M}^{\mu(3)}_{tree} + \mathcal{M}^{\mu(5/2)}_{tree\Delta} + \widetilde{\mathcal{M}}^{\mu(3)}_{loop}, \tag{4.99}$$

is the EOMS regularized amplitude, where $\widetilde{\mathcal{M}}^{\mu(3)}_{loop} = \mathrm{PCBT}_1 + \mathrm{PCBT}_2 + \mathcal{M}^{\mu(3)}_{loop}$ follows the nominal power-counting. The tree amplitudes in the EOMS scheme, $\widetilde{\mathcal{M}}^{\mu(1)}_{tree}$ and $\widetilde{\mathcal{M}}^{\mu(2)}_{tree}$, are defined in Eqs. (4.94) and (4.95) respectively. All the individual pieces for PCBT_1, PCBT_2 and $\mathcal{M}^{\mu(3)}_{loop}$ are provided in the appendices A.3 and B.

The above expression (4.99) is written in such a manner that is consistent with the power-counting rule given in Eq. (2.79), specially the loop amplitude, $\widetilde{\mathcal{M}}^{\mu(3)}_{loop}$. We should remark that also the EOMS and the non-EOMS regularized tree amplitudes obey the power-counting rule and start contributing at the order given by the superscript.

4.2.5 WFR for the external legs

To fully consider the loop contributions for the $\gamma^{(*)} + N \longrightarrow \pi + N'$ amplitude we should introduce the diagrams obtained from the previous ones when the external hadronic legs are modified including self-energy loops or insertions, as shown in Fig. 4.6. These diagrams need to be taken into account in this work given that they can contribute to $\mathcal{O}(p^3)$. As it was mentioned at the beginning of the section 4.2.2, the effects of this kind of loops can be included as a correction called wave function renormalization (WFR), because it can be absorbed into a rescaling of the fields. As

[24]The difference in the treatment of higher orders leads to some really small numerical differences between the corrected amplitudes in the full set of the kinematical regions given in data between both approaches. All this indicates that both versions are sufficient, and they remove the same $\mathcal{O}(p^2)$ power-counting violating pieces from the loops.

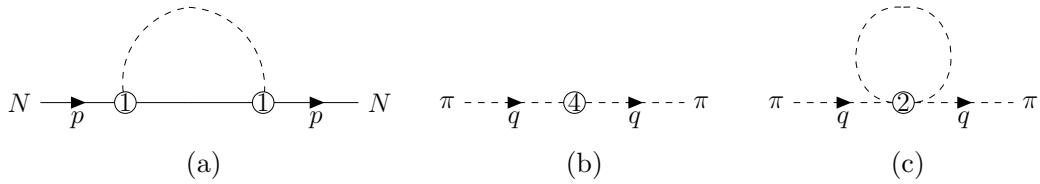

FIGURE 4.6: Self energy diagrams contributing to the wave function renormalization of the external nucleon with momentum p, (a), and the external pion with momentum q, (b), (c).

they are presented in the ChPT Lagrangian (4.3), the rescaling of the external nucleon and pion fields are $N \to \sqrt{\mathcal{Z}_N} N$ and $\phi \to \sqrt{\mathcal{Z}_\pi}\phi$. The correction functions are given by [62]

$$\mathcal{Z}_N = \frac{1}{1 - \frac{d}{d\not{p}}\Sigma_N(\not{p})}\bigg|_{\not{p}=m_N}, \qquad \mathcal{Z}_\pi = \frac{1}{1 - \frac{d}{dq^2}\Sigma_\pi(q^2)}\bigg|_{q^2=M_\pi^2}, \tag{4.100}$$

with Σ_B the self-energy for the corresponding hadron field, $B \in \{N, \pi\}$. Σ_B is a function of the pion or nucleon momentum, q or p respectively. The derivative implies that only the momentum dependent terms in the self-energy amplitude contribute to the WFR. In fact, the only contributing diagrams to the rescaling functions, $\mathcal{Z}_B$, at the order required for our calculation are those displayed in Fig. 4.6.

The renormalization of external fields follows the LSZ formula [62]. In our case, the total amplitude from the $\gamma^{(*)} + N \longrightarrow \pi + N'$ process (4.99) is completed with the loop corrections in the external legs by rescaling the initial and final nucleons and pion fields, as in (4.58)

$$\hat{\mathcal{M}}^\mu = \sqrt{\mathcal{Z}_\pi}\mathcal{Z}_N\mathcal{M}^\mu \tag{4.101}$$

with $\hat{\mathcal{M}}^\mu$ the full definitive amplitude at $\mathcal{O}(p^3)$ to be worked out for the calculation of physical observables.
In the framework of ChPT, the self-energies Σ_B and the rescaling constants $\mathcal{Z}_B$ are straightforwardly obtained from the chiral Lagrangian terms. the nucleon rescaling constant $\mathcal{Z}_N$ has been obtained in Ref. [14] in a calculation with the same $\widetilde{MS}$ renormalization and in the EOMS scheme. The wave function renormalization for the external nucleon legs can be written as

$$\mathcal{Z}_N = 1 + \widetilde{\delta}^{(2)}_{\mathcal{Z}_N} + \mathcal{O}(p^3), \tag{4.102}$$

where, according to Eq. (4.100), $\widetilde{\delta}^{(2)}_{\mathcal{Z}_N} = \frac{d}{d\not{p}}\Sigma_N(\not{p})\big|_{\not{p}=m_N}$ is the $\mathcal{O}(p^2)$ loop contribution[25] regularized in the EOMS scheme. From the evaluation of the diagram in

[25]Please, notice that the self energy contribution to $\Sigma_N(\not{p})$ from the diagram in Fig. 4.6-(a) is of $\mathcal{O}(p^3)$.

Fig. 4.6-(a) one obtains

$$\widetilde{\delta}^{(2)}_{\mathcal{Z}_N} = -\frac{3g_A^2}{64\pi^2 F_\pi^2\left(M_\pi^2-4m_N^2\right)}\Bigg\{4M_\pi^2\Big(\overline{A}_0\left[m_N^2\right]+\left(M_\pi^2-3m_N^2\right)\overline{B}_0\left[m_N^2,M_\pi^2,m_N^2\right]-m_N^2\Big) + \left(12m_N^2-5M_\pi^2\right)\overline{A}_0\left[M_\pi^2\right]\Bigg\}, \tag{4.103}$$

where $\overline{A}_0$ and $\overline{B}_0$ are the $\widetilde{MS}$ renormalized Passarino-Veltman functions given in Eqs. (4.82) and (4.83) with $R \to 0$.

In the same way, the rescaling constant for the final pion field, $\mathcal{Z}_\pi$, has been obtained by Gasser *et al.* in Ref. [53]. The only diagrams that can contribute to the wave function renormalization up to $\mathcal{O}(p^2)$ are those in Fig. 4.6-(b),(c) through the self-energy $\Sigma_\pi(q^2)$ and using Eq. (4.100).
The pion scaling function can be expanded as

$$\mathcal{Z}_\pi^{(2)} = 1 + \widetilde{\delta}^{(2)}_{\mathcal{Z}_\pi} + \mathcal{O}(p^3), \tag{4.104}$$

where $\delta^{(2)}_{\mathcal{Z}_\pi} = \frac{d}{dq^2}\Sigma_\pi(q^2)\big|_{q^2=M_\pi^2}$ is the $\mathcal{O}(p^2)$ contribution given explicitly as

$$\delta^{(2)}_{\mathcal{Z}_\pi} = -\frac{2}{3F_\pi^2}\left\{3l_4^r M_\pi^2 + \frac{\overline{A}_0\left[M_\pi^2\right]}{16\pi^2}\right\}, \tag{4.105}$$

with l_4^r the corresponding $\widetilde{MS}$ renormalized LEC from the Lagrangian term $\mathcal{L}_{\pi\pi}^{GSS(4)}$ of Eq. (2.44).

Although the loop contributions to the WFR actually depend on the chiral limit masses and constants, m, M, g and F, all these parameters are replaced by the physical quantities m_N, M_π, g_A and F_π. By doing this, the change produced in the WFR is at least of $\mathcal{O}(p^3)$[26] for the scaling factors, $\mathcal{Z}_\mathcal{B}$, of Eqs. (4.102) and (4.104). Thus, this modification of $\mathcal{O}(p^3)$ multiplied by the amputated amplitude, $\mathcal{M}^\mu$, as in Eq. (4.101), will produce terms from $\mathcal{O}(p^4)$, which are beyond the order of our calculations, $\mathcal{O}(p^3)$. I will review in more detail this kind of approximations in the next section.

4.3 Further considerations for the $\mathcal{O}(p^3)$ amplitude

In the present subsection, I would like to describe briefly some algebraical tools used here to simplify and implement the calculations of the amputated total amplitude $\mathcal{M}^\mu$ at $\mathcal{O}(p^3)$ [Eq. (4.99)]. First, I will discuss the behavior of the tree level amplitudes involving nucleon and pion propagators when the chiral expansions of the masses are taken into account. Secondly, I will follow with a discussion on the contributing LECs in the full amplitude up to an $\mathcal{O}(p^3)$ approximation. Lastly, I will review the evaluation of the chiral parameters in terms of physical quantities, order by order in the amplitude terms.

[26] See, *e.g.*, appendix C.

4.3.1 Diagrams with mass insertions in the propagators

One of the simplifications that can be made is related to the diagrams with mass insertions in the nucleon propagators, such as the diagrams depicted in Fig. 4.1 (g), (h), (q), (r), (s) and (t). All the amplitudes related to these diagrams can be generated from the corresponding diagrams without propagator insertions, namely the diagrams 4.1 (b), (c), (e) and (f). In fact, with only the four latter diagrams we can calculate all the ten diagram amplitudes mentioned before by simply replacing the chiral nucleon mass, m, in the propagator denominator by $m - 4c_1 M_\pi^2$, which includes the second chiral order correction. This shortcut will automatically reproduce all the original amplitudes (b), (c), (e), (f), (g), (h), (q), (r), (s) and (t) at the expense of getting an extra $O(p^4)$ contribution.

This approach is based on the chiral expansion of the nucleon mass, m_N, up to $\mathcal{O}(p^2)$ in terms of the LO parameters. As it is shown in App. C, the nucleon mass corrections in the $\widetilde{MS}$ and EOMS scheme are given by

$$m_N = \underbrace{\widetilde{m} - 4\widetilde{c}_1 M_\pi^2}_{\widetilde{m}_2} + \widetilde{\delta}^{(3)}_{m_N} + \mathcal{O}(p^4) \tag{4.106}$$

with $\widetilde{m}_2$ the nucleon mass up to $\mathcal{O}(p^2)$ and $\widetilde{\delta}^{(3)}_{m_N}$ is the corresponding $\mathcal{O}(p^3)$ contribution given in Eq. (C.3). Then, when we make the substitution

$$\widetilde{m} \to \widetilde{m}_2 = \widetilde{m} - 4\widetilde{c}_1 M_\pi^2 \tag{4.107}$$

in the nucleon propagator, (A.22), and we expand it over the pion mass M_π, it results in[27]

$$\begin{aligned}
iS_N(p)\{m \to m_2\} =& i\frac{\not{p} + m_2}{p^2 - m_2^2} \\
=& i\frac{\not{p} + m}{p^2 - m^2} \\
&+ i\frac{\not{p} + m}{p^2 - m^2}\left(i4c_1 M_\pi^2\right) i\frac{\not{p} + m}{p^2 - m^2} \\
&+ i\frac{\not{p} + m}{p^2 - m^2}\left(i4c_1 M_\pi^2\right) i\frac{\not{p} + m}{p^2 - m^2}\left(i4c_1 M_\pi^2\right) i\frac{\not{p} + m}{p^2 - m^2} + \mathcal{O}(p^2) \\
=& \, iS_N(p) \\
&+ \, iS_N(p)\left(\mathcal{V}^{(2)}_{N;N}\right) iS_N(p) \\
&+ \, iS_N(p)\left(\mathcal{V}^{(2)}_{N;N}\right) iS_N(p)\left(\mathcal{V}^{(2)}_{N;N}\right) iS_N(p) + \mathcal{O}(p^2).
\end{aligned} \tag{4.108}$$

[27] Tildes are omitted for simplicity in the next equations. This will be discussed below.

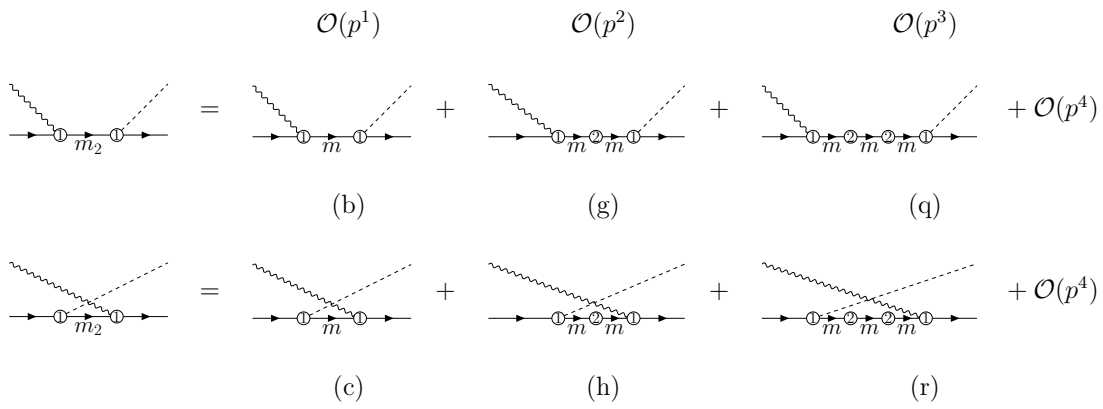

FIGURE 4.7: Feynman diagrams showing the generation of amplitudes of higher orders in the chiral expansion when we substitute the nucleon mass m by m_2, Eq. (4.107), in the nucleon propagator of two $\mathcal{O}(p^1)$ amplitudes, $\mathcal{M}^{\mu\,(1)}_{(b)}$, (4.12), and $\mathcal{M}^{\mu\,(1)}_{(c)}$, (4.13).

As we can see in the expressions for $\mathcal{M}^{\mu\,(1)}_{(b)}$ (4.12), $\mathcal{M}^{\mu\,(2)}_{(g)}$ (4.18) and $\mathcal{M}^{\mu\,(3)}_{(q)}$ (4.33), the above expansion terms precisely appear in the intermediate blocks of their respective amplitudes. The same occurs for the crossed diagram amplitudes (4.13), (4.19) and (4.34). Therefore, applying the substitution (4.107) in the LO amplitudes $\mathcal{M}^{\mu\,(1)}_{(b)}$ (4.12), $\mathcal{M}^{\mu\,(1)}_{(c)}$ (4.13), we have following relations:

$$\mathcal{M}^{\mu\,(1)}_{(b)}[m \to m_2] = \mathcal{M}^{\mu\,(1)}_{(b)}[m] + \mathcal{M}^{\mu\,(2)}_{(g)}[m] + \mathcal{M}^{\mu\,(3)}_{(q)}[m] + \mathcal{O}(p^4), \tag{4.109}$$

$$\mathcal{M}^{\mu\,(1)}_{(c)}[m \to m_2] = \mathcal{M}^{\mu\,(1)}_{(c)}[m] + \mathcal{M}^{\mu\,(2)}_{(h)}[m] + \mathcal{M}^{\mu\,(3)}_{(r)}[m] + \mathcal{O}(p^4), \tag{4.110}$$

which introduces a negligible difference of higher order, $\mathcal{O}(p^4)$, in the amplitude, as it was previously mentioned. This shortcut is illustrated in Fig. 4.7. In other words, when we use m_2 instead of m in the LO amplitudes we are considering all[28] the required diagrams with mass insertions. In the discussions, for simplicity, I have omitted the tilde for the masses. The result and its derivation are quite general. Actually, all the expressions remain the same in the EOMS framework. From the definition of the $\mathcal{O}(p^2)$ nucleon mass $\widetilde{m}_2$ in Eq. (4.107), we can alternatively derive from $\mathcal{M}^{\mu\,(1)}_{(b),(c)}[m_2]$ (4.109),(4.110), the respective PCBT to be subtracted with the EOMS beta functions for m and c_1, Eqs. (4.91)-(4.93). The corresponding EOMS shift for m_2 is

$$m_2 = \widetilde{m}_2 + \frac{m\left(\widetilde{\beta}_m - 4M_\pi^2\widetilde{\beta}_{c_1}\right)}{16\pi^2F^2}. \tag{4.111}$$

[28] Up to $\mathcal{O}(p^3)$.

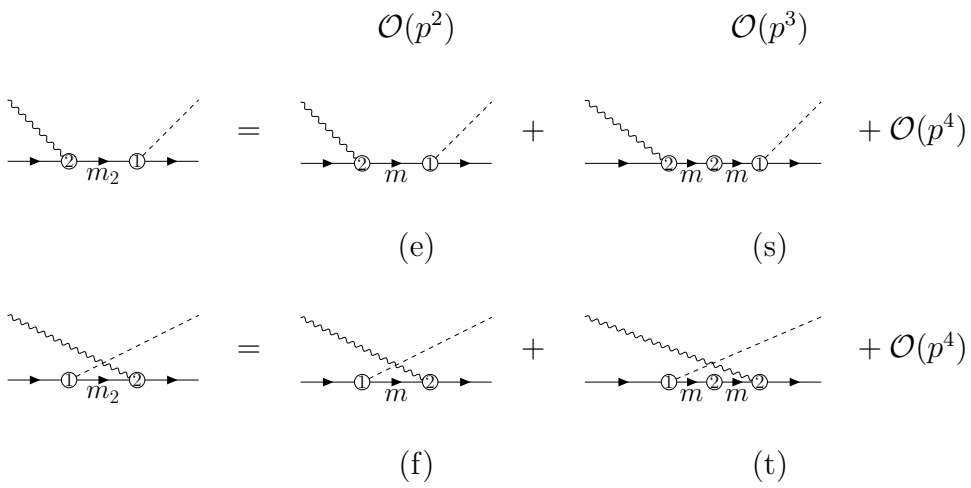

FIGURE 4.8: Feynman diagrams indicating the generation of amplitudes the by chiral expansion when we substitute the nucleon mass m by m_2, Eq. (4.107), in the nucleon propagator of the $\mathcal{O}(p^2)$ amplitudes, $\mathcal{M}^{\mu\,(2)}_{(e)}$, Eq. (4.20) and $\mathcal{M}^{\mu\,(2)}_{(f)}$, Eq. (4.21).

Likewise, the same approach was used for the $\mathcal{O}(p^2)$ amplitudes $\mathcal{M}^{\mu\,(2)}_{(e)}$ and $\mathcal{M}^{\mu\,(2)}_{(f)}$. In this case, applying the substitution $m \to m_2$ (4.107) we can find that

$$\mathcal{M}^{\mu\,(2)}_{(e)}[m \to m_2] = \mathcal{M}^{\mu\,(2)}_{(e)}[m] + \mathcal{M}^{\mu\,(3)}_{(s)}[m] + \mathcal{O}(p^4), \tag{4.112}$$

$$\mathcal{M}^{\mu\,(2)}_{(f)}[m \to m_2] = \mathcal{M}^{\mu\,(2)}_{(f)}[m] + \mathcal{M}^{\mu\,(3)}_{(t)}[m] + \mathcal{O}(p^4), \tag{4.113}$$

where the amplitudes $\mathcal{M}^{\mu\,(2)}_{(e)}$, $\mathcal{M}^{\mu\,(2)}_{(f)}$, $\mathcal{M}^{\mu\,(3)}_{(s)}$ and $\mathcal{M}^{\mu\,(3)}_{(t)}$ are given in Eqs. (4.16), (4.17), (4.35) and (4.35) respectively. The EOMS version is still the same by replacing directly $\widetilde{m}$ by $\widetilde{m}_2$ in the propagator if one has already generated the PCBT. The Feynman diagrams for the amplitude expansions of the Eqs. (4.112) and (4.113) are depicted in Fig. 4.8.

To conclude, the approach presented here allows us to evaluate some contributions to the amplitude in a more straightforward way. In this sense, we do not need to calculate the diagrams with vertex insertions in their nucleon propagators.

Furthermore, this procedure is particularly convenient in evaluating the LECs $\widetilde{m}$ and $\widetilde{c}_1$ up to $\mathcal{O}(p^3)$ through the parameter $\widetilde{m}_2$ in terms of well known physical quantities like m_N, M_π and F_π, see Eq. (C.2). In the next sections, I will treat more deeply this and further simplifications that result in the evaluation of the chiral parameters in the amplitude.

4.3.2 Evaluation of the amplitude and the relevant LECs at $\mathcal{O}(p^3)$

In this subsection, I review some of the basic ingredients of this work related to the evaluation of the amplitude $\hat{\mathcal{M}}^\mu$, (4.101), as a function of the chiral parameters and LECs. First, I detail the evaluation of the lowest-order parameters g, m, M and F, order by order, to express them in terms of physical quantities. Second, I explain briefly which are the relevant LECs that will contribute to the amplitude $\hat{\mathcal{M}}^\mu$ for an $\mathcal{O}(p^3)$ calculation.

At this point, I would like to recall the full amplitude for $\gamma^{(*)} + N \longrightarrow \pi + N'$ split order by order as in the previous sections. According to Eq. (4.99) and to the simplifications of Eqs. (4.109)-(4.113), the $\widetilde{MS}$-EOMS regularized amputated amplitude can be written as

$$\begin{aligned}
\mathcal{M}^{\mu} = & \mathcal{M}^{\mu\,(1)}_{\text{tree}}[s,u,Q^2,\widetilde{g},F,M,\widetilde{m}_2] \\
& + \mathcal{M}^{\mu\,(2)}_{\text{tree}}[s,u,Q^2,\widetilde{g},F,\widetilde{m}_2,\widetilde{c}_6,\widetilde{c}_7] \\
& + \mathcal{M}^{\mu\,(3)}_{\text{tree}}[s,u,Q^2,g^r,F,M,m^r,d^r_6,d^r_7,d^r_8,d^r_9,d^r_{16},d^r_{18},d^r_{20},d^r_{21},d^r_{22},l^r_3,l^r_4,l^r_6] \\
& + \mathcal{M}^{\mu(5/2)}_{tree\Delta}[s,u,Q^2,g_M,h_A) \\
& + \widetilde{\mathcal{M}}^{\mu(3)}_{loop}[s,u,Q^2,g^r,F,M,m^r] + \mathcal{O}(p^4),
\end{aligned} \tag{4.114}$$

where is given explicitly the dependence on the kinematical variables $\{s,u,Q^2\}$ and the relevant LECs, $\{\widetilde{g},g^r,F,M,\widetilde{m}_2,m^r,\widetilde{c}_6,\widetilde{c}_7,d^r_8,d^r_9,,d^r_{16},d^r_{18},d^r_{20},d^r_{21},d^r_{22},l^r_3,l^r_4,l^r_6,g_M,h_A\}$. The amplitude for the Δ mechanisms, $\mathcal{M}^{\mu(5/2)}_{tree\Delta}$, is given as in Eq. (4.51) and the contribution of the loop diagrams, $\widetilde{\mathcal{M}}^{\mu(3)}_{loop}$, as in Eq. (4.87). As always, the amplitude dependence on the masses $\{\widetilde{m}_2,m^r,M\}$ refers to how they appear in their corresponding propagators. As it was treated in Sec. 4.3.1, the amplitudes with nucleon vertex insertions were absorbed into other amplitudes [see Eqs. (4.109)-(4.113)]. Then, the tree level amplitude contributions are re-organized order by order as

$$\begin{aligned}
\mathcal{M}^{\mu\,(1)}_{\text{tree}}[\widetilde{g},F,M,\widetilde{m}_2] = & \mathcal{M}^{\mu\,(1)}_{(a)}[\widetilde{g},F] + \mathcal{M}^{\mu\,(1)}_{(b)}[\widetilde{g},F,\widetilde{m}_2] \\
& + \mathcal{M}^{\mu\,(1)}_{(c)}[\widetilde{g},F,\widetilde{m}_2] + \mathcal{M}^{\mu\,(1)}_{(d)}[\widetilde{g},F,M],
\end{aligned} \tag{4.115}$$

$$\mathcal{M}^{\mu\,(2)}_{\text{tree}}[\widetilde{g},F,\widetilde{m}_2,\widetilde{c}_6,\widetilde{c}_7] = \mathcal{M}^{\mu\,(2)}_{(e)}[\widetilde{g},F,\widetilde{m}_2,\widetilde{c}_6,\widetilde{c}_7] + \mathcal{M}^{\mu\,(2)}_{(f)}[\widetilde{g},F,\widetilde{m}_2,\widetilde{c}_6,\widetilde{c}_7], \tag{4.116}$$

$$\begin{aligned}
\mathcal{M}^{\mu\,(3)}_{\text{tree}}[g^r,F,M,m^r,d^r_j,l^r_k] = & \mathcal{M}^{\mu\,(3)}_{(i)}[F,M,d^r_8,d^r_9,d^r_{16},d^r_{18},d^r_{20},d^r_{21},d^r_{22}] \\
& + \mathcal{M}^{\mu\,(3)}_{(j)}[F,M,m^r,d^r_{16},d^r_{18}] \\
& + \mathcal{M}^{\mu\,(3)}_{(k)}[F,M,m^r,d^r_{16},d^r_{18}] \\
& + \mathcal{M}^{\mu\,(3)}_{(l)}[g^r,F,M,l^r_4,l^r_6] \\
& + \mathcal{M}^{\mu\,(3)}_{(m)}[g^r,m^r,d^r_6,d^r_7] \\
& + \mathcal{M}^{\mu\,(3)}_{(n)}[g^r,m^r,d^r_6,d^r_7] \\
& + \mathcal{M}^{\mu\,(3)}_{(o)}[M,F,d^r_{16},d^r_{18}] \\
& + \mathcal{M}^{\mu\,(3)}_{(p)}[g^r,M,F,l^r_3,l^r_4],
\end{aligned} \tag{4.117}$$

where I have omitted the kinematical variables $\{s,u,Q^2\}$. Each individual amplitude piece corresponds to the labeled Feynman diagrams of Figure 4.1. The $\mathcal{O}(p^1)$ amplitudes $\mathcal{M}^{\mu\,(1)}_{(a)}$ and $\mathcal{M}^{\mu\,(1)}_{(d)}$ are given in Eqs. (4.11) and (4.14), while $\mathcal{M}^{\mu\,(1)}_{(b)}$ and $\mathcal{M}^{\mu\,(1)}_{(c)}$ are given in Eqs. (4.12) and (4.13), but with the replacement $m \to m_2$. Now, the

$\mathcal{O}(p^2)$ contribution has only two terms, at difference with Eq. (4.15)[29]. These amplitudes, $\mathcal{M}^{\mu\,(2)}_{(e)}$ and $\mathcal{M}^{\mu\,(2)}_{(f)}$, are obtained from Eqs. (4.20) and (4.21) with the $m \to m_2$ change.
For the $\mathcal{O}(p^3)$ tree contributions, the rest of the terms, $\mathcal{M}^{\mu\,(3)}_{(i)}, \ldots, \mathcal{M}^{\mu\,(3)}_{(p)}$ are given in Eqs. (4.37)-(4.44). The $\mathcal{O}(p^3)$ amplitudes $\mathcal{M}^{\mu\,(3)}_{(q)} \ldots \mathcal{M}^{\mu\,(3)}_{(t)}$ with insertions in the nucleon propagators have been reabsorbed into the LO amplitudes as it was explained in the previous section.

As we can see in Eqs. (4.115)-(4.117), each one of the tree-level pieces depends on a few specific LECs. Some of them, defined in the chiral limit, can be directly related to physical quantities. They are the axial coupling, $\widetilde{g}$, the nucleon and pion masses, m^r and M respectively, and the pion decay constant F; see appendix C. In the next part, I detail the evaluation of these LO parameters in terms of physical measurable quantities, following with a discussion of the rest of the relevant LECs, $\{c_i, d_j, l_k\}$.

4.3.3 Evaluation of the lowest order parameters

As is shown in appendix C, the LECs involved in the $\mathcal{O}(p^1)$ amplitude, Eq. (4.115), are $\{\widetilde{g}, F, M, \widetilde{m}_2\}$ and all of them can be expanded in terms of physical quantities and some other LECs. In particular, the EOMS $\mathcal{O}(p^2)$ nucleon mass, $\widetilde{m}_2$, can be evaluated easily from Eq. (4.106),

$$\widetilde{m}_2 = m_N - \widetilde{\delta}^{(3)}_{m_N} + \mathcal{O}(p^4). \tag{4.118}$$

Similarly, the chiral parameters $\widetilde{g}$, F and M can be written in an expansion with only physical quantities using Eqs. (C.6), (C.8) and (C.4) respectively. Then,

$$\widetilde{g} = g_A - 4d^r_{16}M^2_\pi - g_A\widetilde{\delta}^{(2)}_{g_A} + \mathcal{O}(p^4), \tag{4.119}$$

$$F = F_\pi(1 - \delta^{(2)}_{F_\pi}[l^r_4]) + \mathcal{O}(p^4), \tag{4.120}$$

$$M^2 = M^2_\pi\left(1 - \delta^{(2)}_{M_\pi}[l^r_3]\right) + \mathcal{O}(p^6), \tag{4.121}$$

with $\widetilde{\delta}^{(2)}_{g_A}$ a function of m_N, M_π, g_A and F_π given in Eq. (C.7) and

$$\delta^{(2)}_{F_\pi}[l^r_4] = \frac{l^r_4 M^2_\pi}{F^2_\pi} + \frac{\overline{A}_0\left[M^2_\pi\right]}{16\pi^2 F^2_\pi}, \tag{4.122}$$

$$\delta^{(2)}_{M_\pi}[l^r_3] = \frac{2l^r_3 M^2_\pi}{F^2_\pi} - \frac{\overline{A}_0[M^2_\pi]}{32\pi^2 F^2_\pi}. \tag{4.123}$$

These expansions can be directly substituted in the amplitude if one knows the values for the physical g_A, F_π M_π, m_N and the extra LECs d^r_{16}, l^r_3 and l^r_4. Nevertheless, if we further substitute the above expressions for $\widetilde{g}$, F and M in the amplitude $\mathcal{M}^\mu$, Eq. (4.114), and simplify up to an accuracy of $\mathcal{O}(p^3)$, then the pieces with these LECs, (d^r_{16}, l^r_3 and l^r_4) are actually canceled at that order with other pieces in the full amplitude, $\hat{\mathcal{M}}^\mu$, Eq. (4.101).

[29]The other two amplitudes, $\mathcal{M}^{\mu\,(2)}_{(g)}$ and $\mathcal{M}^{\mu\,(2)}_{(h)}$, were absorbed in $\mathcal{M}^{\mu\,(1)}_{(b)}$, $\mathcal{M}^{\mu\,(1)}_{(c)}$, as shown in Eqs. (4.109) and (4.110).

Furthermore, since in the $\mathcal{O}(p^1)$ amplitude, $\widetilde{\mathcal{M}}^{\mu\,(1)}_{\text{tree}}$, (4.115), the LECs $\widetilde{g}$ and F always appear in the combination $\widetilde{g}/F$, then, using the Eqs. (4.118), (4.119) and (4.120), we can recast the expressions as

$$\begin{aligned}\mathcal{M}^{\mu\,(1)}_{\text{tree}}[\widetilde{g},F,M,\widetilde{m}_2] =&\mathcal{M}^{\mu\,(1)}_{\text{tree}}[g_A,F_\pi,M,m_N-\widetilde{\delta}^{(3)}_{m_N}]\left(1-\frac{4d^r_{16}M^2_\pi}{g_A}-\widetilde{\delta}^{(2)}_{g_A}+\delta^{(2)}_{F_\pi}[l^r_4]\right)+\mathcal{O}(p^4)\\ =&\mathcal{M}^{\mu\,(1)}_{(a)}[g_A,F_\pi]\left(1-\frac{4d^r_{16}M^2_\pi}{g_A}-\widetilde{\delta}^{(2)}_{g_A}+\delta^{(2)}_{F_\pi}[l^r_4]\right)\\ &+\mathcal{M}^{\mu\,(1)}_{(b)}[g_A,F_\pi,m_N-\widetilde{\delta}^{(3)}_{m_N}]\left(1-\frac{4d^r_{16}M^2_\pi}{g_A}-\widetilde{\delta}^{(2)}_{g_A}+\delta^{(2)}_{F_\pi}[l^r_4]\right)\\ &+\mathcal{M}^{\mu\,(1)}_{(c)}[g_A,F_\pi,m_N-\widetilde{\delta}^{(3)}_{m_N}]\left(1-\frac{4d^r_{16}M^2_\pi}{g_A}-\widetilde{\delta}^{(2)}_{g_A}+\delta^{(2)}_{F_\pi}[l^r_4]\right)\\ &+\mathcal{M}^{\mu\,(1)}_{(d)}[g_A,F_\pi,M]\left(1-\frac{4d^r_{16}M^2_\pi}{g_A}-\widetilde{\delta}^{(2)}_{g_A}+\delta^{(2)}_{F_\pi}[l^r_4]\right)+\mathcal{O}(p^4).\end{aligned} \tag{4.124}$$

As we can see above, the pieces $\mathcal{M}^{\mu\,(1)}_{(a)}$, $\mathcal{M}^{\mu\,(1)}_{(b)}$ and $\mathcal{M}^{\mu\,(1)}_{(c)}$ are fully expressed in terms of physical magnitudes and the LECs d^r_{16} and l^r_4. Also, it is necessary to expand the dependence on the chiral pion mass, M, which is only relevant in the term $\mathcal{M}^{\mu\,(1)}_{(d)}$. This expansion up to $\mathcal{O}(p^3)$ will make explicit the dependence in l^r_4. Taking the amplitude expression for $\mathcal{M}^{\mu\,(1)}_{(d)}$ as it is given in Eq. (4.124) and substituting the expansion for M, Eq. (4.121), we have that

$$\begin{aligned}&\mathcal{M}^{\mu\,(1)}_{(d)}[g_A,F_\pi,M]=C^{(1)}_{IV}\frac{eg_A(2q-k)^\mu(\not{q}-\not{k})\gamma^5}{\sqrt{2}F_\pi\left((q-k)^2-M^2\right)}\\ &=\underbrace{C^{(1)}_{IV}\frac{eg_A(2q-k)^\mu(\not{q}-\not{k})\gamma^5}{\sqrt{2}F_\pi\left((q-k)^2-\overline{M}^2_\pi\right)}}_{\mathcal{M}^{\mu\,(1)}_{(d)}[g_A,F_\pi,\overline{M}_\pi]}-\underbrace{C^{(1)}_{IV}\frac{2eg_AM^4_\pi(2q-k)^\mu(\not{q}-\not{k})\gamma^5}{\sqrt{2}F^3_\pi\left((q-k)^2-M^2_\pi\right)^2}l^r_3}_{\mathcal{M}^{\mu\,(3)}_{(d)R}[M_\pi,l^r_3]}+\mathcal{O}(p^5)\end{aligned} \tag{4.125}$$

where $\mathcal{M}^{\mu\,(3)}_{(d)R}$ is the correction term at $\mathcal{O}(p^3)$. The mass $\overline{M}_\pi$ is defined from Eq. (4.123) in terms of the physical pion mass[30]

$$\overline{M}^2_\pi=M^2_\pi+M^2_\pi\frac{\overline{\mathrm{A}}_0[M^2_\pi]}{32\pi^2F^2_\pi}. \tag{4.126}$$

In summary, the evaluation of the $\mathcal{O}(p^1)$ amplitude $\mathcal{M}^{\mu\,(1)}_{(d)}[\widetilde{g},F,M]$, (4.115), in terms of physical quantities and LECs can be expressed as an expansion up to $\mathcal{O}(p^3)$ as

$$\begin{aligned}\mathcal{M}^{\mu\,(1)}_{(d)}[\widetilde{g},F,M]=&\mathcal{M}^{\mu\,(1)}_{(d)}[g_A,F_\pi,\overline{M}_\pi]\left(1-\frac{4d^r_{16}M^2_\pi}{g_A}-\widetilde{\delta}^{(2)}_{g_A}+\delta^{(2)}_{F_\pi}[l^r_4]\right)\\ &-\mathcal{M}^{\mu\,(3)}_{(d)R}[M_\pi,l^r_3]+\mathcal{O}(p^4)\end{aligned} \tag{4.127}$$

[30] For the pion mass expansion included in the propagator I have used the expression $\frac{1}{z^2-M^2}=\frac{1}{z^2-M^2_\pi}-\frac{1}{z^2-M^2_\pi}\left(M^2_\pi\delta^{(2)}_{M_\pi}\right)\frac{1}{z^2-M^2_\pi}+\mathcal{O}(p^2)$

with $\mathcal{M}^{\mu\,(1)}_{(d)}[g_A, F_\pi, \overline{M}_\pi]$ and $\mathcal{M}^{\mu\,(3)}_{(d)R}[M_\pi, l^r_3]$ indicated in Eq. (4.125).

LECs in the $\mathcal{O}(p^2)$ tree amplitude

For the $\mathcal{O}(p^2)$ amplitude terms of Eq. (4.116), the handling of the chiral parameters is more straightforward than for the $\mathcal{O}(p^1)$ one. In this case, when we expand there the involved parameters, $\widetilde{g}$, F and $\widetilde{m}_2$, using the Eqs. (4.118)-(4.120), we get

$$\mathcal{M}^{\mu\,(2)}_{tree}[\widetilde{g}, F, \widetilde{m}_2, \widetilde{c}_6, \widetilde{c}_7] = \mathcal{M}^{\mu\,(2)}_{tree}[g_A, F_\pi, m_N, \widetilde{c}_6, \widetilde{c}_7] + \mathcal{O}(p^4) \tag{4.128}$$

where only remain the LECs $\widetilde{c}_6$ and $\widetilde{c}_7$ from the chiral Lagrangian. I will treat their evaluation below. For the above amplitude the expansion of the chiral parameters return the same amplitude evaluated directly with the physical parameters except for higher order terms of $\mathcal{O}(p^4)$ that we can neglect.

Parameters in the $\mathcal{O}(p^3)$ tree and loop amplitude

As we can see in Eq. (4.117), the tree amplitude at $\mathcal{O}(p^3)$ depends on $\{g^r, F, M, m^r, d^r_j, l^r_k\}$ for $j \in \{6, 7, 8, 9, 16, 18, 20, 21, 22\}$ and $k \in \{4, 6\}$. Here, the LECs are only given in the $\widetilde{MS}$ scheme but not in EOMS, since at $\mathcal{O}(p^3)$ we do not need to renormalize them to generate PCBT. Furthermore, as we use the scale parameter $\mu = m_N$ for the loop functions, then $\overline{\mathrm{A}}_0[m_N] = 0$ and the LO parameters m^r and g^r are related to their analogous ones in EOMS as [see Eqs. (4.88), (4.91)]

$$m^r = \widetilde{m}, \tag{4.129}$$

$$g^r = \widetilde{g} + \frac{{m_N}^2 g_A^3}{16\pi^2 F_\pi^2}. \tag{4.130}$$

Substituting (4.129) and (4.130) in the corresponding expansions, (4.106) and (4.119), we have that

$$m^r = m_N + \mathcal{O}(p^2), \tag{4.131}$$

$$g^r = g_A + \mathcal{O}(p^2). \tag{4.132}$$

This, together with the chiral expansions for F (4.120) and M (4.121), implies that the $\mathcal{O}(p^3)$ tree amplitude of Eq. (4.117) can be expressed as

$$\mathcal{M}^{\mu\,(3)}_{\mathrm{tree}}[g^r, F, M, m^r, d^r_j, l^r_k] = \mathcal{M}^{\mu\,(3)}_{\mathrm{tree}}[g_A, F_\pi, M_\pi, m_N, d^r_j, l^r_k] + \mathcal{O}(p^4). \tag{4.133}$$

Similarly for the loop amplitude we have

$$\widetilde{\mathcal{M}}^{\mu(3)}_{loop}[g^r, F, M, m^r] = \widetilde{\mathcal{M}}^{\mu(3)}_{loop}[g_A, F_\pi, M_\pi, m_N] + \mathcal{O}(p^4). \tag{4.134}$$

By consistency, this identity also affects the corresponding PCBT that should be removed from the amplitudes $\mathcal{M}^{\mu(3)}_{loop}$ of Eq. (4.67)[31]. That is because $\widetilde{\mathcal{M}}^{\mu(3)}_{loop} =$

[31] I refer to the loop amplitude which is already UV regularized in the $\widetilde{MS}$ scheme as in Eq. (4.86).

$\mathrm{PCBT}_1 + \mathrm{PCBT}_2 + \mathcal{M}^{\mu(3)}_{loop}$ [see Eq. (4.98)]. For this reason, the PCBT are given too in terms of the physical parameters g_A,F_π,M_π and m_N in appendix B.

Finally, all the pieces involved in the total amputated amplitude $\mathcal{M}^\mu$, (4.114), can be evaluated in terms of the known physical masses for the nucleon, m_N, the pion, M_π, the axial coupling, g_A, and the pion decay constant, F_π. Although the set of the other required LECs $\{\widetilde{c}_6, \widetilde{c}_7, d^r_6, d^r_7, d^r_8, d^r_9, d^r_{16}, d^r_{18}, d^r_{20}, d^r_{21}, d^r_{22}, l^r_3, l^r_4, l^r_6, h_A, g_M\}$ is quite large, as it was aforementioned, some of these LECs become irrelevant in an $\mathcal{O}(p^3)$ calculation. Explicitly, when we sum all the pieces together in $\mathcal{M}^\mu$ (4.114) and multiply the result by the WFR factor $\sqrt{\mathcal{Z}_\pi}\mathcal{Z}_N$, the LECs d^r_{16}, l^r_3 and l^r_4, which appear in different pieces of the amplitude, either cancel or can be reabsorbed by other LECS.

4.3.4 Relevant LECs at $\mathcal{O}(p^3)$

Here, I detail which are the relevant LECs at $\mathcal{O}(p^3)$ for the $\gamma^{(*)} + N \longrightarrow \pi + N'$ reaction. Cancellations between different terms and a proper analysis of the chiral order of each contribution are taken into account. Namely,

- there is a direct cancellation of terms proportional to l^r_4 when the individual tree amplitudes at $\mathcal{O}(p^3)$, Eq. (4.117), are added up. Also, among the same diagrams, the LEC l^r_3 involved in the pion exchange amplitudes in $\mathcal{M}^{\mu\,(3)}_{\mathrm{tree}}$ is canceled by the chiral limit mass M in $\mathcal{M}^{\mu\,(1)}_{\mathrm{tree}}$, which is expressed in terms of l^r_3 and other physical quantities.
- The second point is related to the re-absorption of the LEC d^r_{16} in $\mathcal{M}^{\mu\,(3)}_{\mathrm{tree}}$ by the expansion at $\mathcal{O}(p^3)$ of the LEC $\widetilde{g}$ in $\mathcal{M}^{\mu\,(1)}_{\mathrm{tree}}$ in the amputated amplitude (4.114).
- The last step is related to the inclusion of the WFR correction $\sqrt{\mathcal{Z}_\pi}$ and its further expansion up to $\mathcal{O}(p^3)$ that results in the re-absorbtion of l^r_4 by the chiral limit parameter F in $\mathcal{M}^{\mu\,(1)}_{\mathrm{tree}}$.

Recollecting the previous results, once the amputated amplitude $\mathcal{M}^\mu$, (4.114), has been evaluated in terms of the physical parameters and the related LECs, the full amplitude including WFR can be computed as

$$\begin{aligned}
\hat{\mathcal{M}}^\mu &= \sqrt{\mathcal{Z}_\pi}\mathcal{Z}_N\mathcal{M}^\mu \\
&= \sqrt{\mathcal{Z}_\pi}\mathcal{Z}_N\Bigg\{\mathcal{M}^{\mu\,(1)}_{\mathrm{tree}}[s,u,Q^2,\widetilde{g},F,M,\widetilde{m}_2] \\
&\quad + \mathcal{M}^{\mu\,(2)}_{\mathrm{tree}}[s,u,Q^2,g_A,F_\pi,m_N,\widetilde{c}_6,\widetilde{c}_7] \\
&\quad + \mathcal{M}^{\mu\,(3)}_{\mathrm{tree}}[s,u,Q^2,g_A,F_\pi,M_\pi,m_N,d^r_6,d^r_7,d^r_8,d^r_9,d^r_{16},d^r_{18},d^r_{20},d^r_{21},d^r_{22},l^r_3,l^r_4,l^r_6] \\
&\quad + \mathcal{M}^{\mu(5/2)}_{tree\Delta}[s,u,Q^2,g_M,h_A) \\
&\quad + \widetilde{\mathcal{M}}^{\mu(3)}_{loop}[s,u,Q^2,m_N,M_\pi,g_A,F_\pi] + \mathcal{O}(p^4)\Bigg\},
\end{aligned} \tag{4.135}$$

where the $\mathcal{O}(p^1)$ amplitude, taking Eqs. (4.124) and (4.127), is written as

$$\mathcal{M}^{\mu\,(1)}_{\mathrm{tree}}[\widetilde{g},F,M,\widetilde{m}_2] = \left(1 - \frac{4d^r_{16}M^2_\pi}{g_A} - \widetilde{\delta}^{(2)}_{g_A} + \delta^{(2)}_{F_\pi}[l^r_4]\right) \times$$

$$\Bigg(\mathcal{M}^{\mu\,(1)}_{(a)}[g_A, F_\pi] + \mathcal{M}^{\mu\,(1)}_{(b)}[g_A, F_\pi, m_N - \widetilde{\delta}^{(3)}_{m_N}]$$
$$+ \mathcal{M}^{\mu\,(1)}_{(c)}[g_A, F_\pi, m_N - \widetilde{\delta}^{(3)}_{m_N}] + \mathcal{M}^{\mu\,(1)}_{(d)}[g_A, F_\pi, \overline{M}_\pi]\Bigg)$$
$$- \mathcal{M}^{\mu\,(3)}_{(d)R}[M_\pi, l_3^r], \tag{4.136}$$

where the amplitude pieces $\mathcal{M}^{\mu\,(1)}_{(a)}[g_A, F_\pi]$, $\mathcal{M}^{\mu\,(1)}_{(b)}[g_A, F_\pi, m_N - \widetilde{\delta}^{(3)}_{m_N}]$, $\mathcal{M}^{\mu\,(1)}_{(c)}[g_A, F_\pi, m_N - \widetilde{\delta}^{(3)}_{m_N}]$ and $\mathcal{M}^{\mu\,(1)}_{(d)}[g_A, F_\pi, M]$ are taken from Eqs. (4.11), (4.12), (4.13) and (4.14) respectively [32]. The functions $\widetilde{\delta}^{(2)}_{g_A}$ and $\delta^{(2)}_{F_\pi}[l_4^r]$ are correspondingly given in (C.7) and (C.9).

The $\mathcal{O}(p^2)$ amplitude term of Eq. (4.135) is given by Eq. (4.116) and evaluated as shown in Eq. (4.128),

$$\mathcal{M}^{\mu\,(2)}_{\text{tree}}[g_A, F_\pi, m_N, \widetilde{c}_6, \widetilde{c}_7] = \mathcal{M}^{\mu\,(2)}_{(e)}[g_A, F_\pi, m_N, \widetilde{c}_6, \widetilde{c}_7] + \mathcal{M}^{\mu\,(2)}_{(f)}[g_A, F_\pi, m_N, \widetilde{c}_6, \widetilde{c}_7], \tag{4.137}$$

where the explicit expressions can be found in Eqs. (4.20) and (4.21), with the respective parameter dependence as displayed here.

Finally, the $\mathcal{O}(p^3)$ amplitude piece of Eq. (4.135) is split as shown in Eq. (4.117) and reshaped as in Eq. (4.133)

$$\begin{aligned}\mathcal{M}^{\mu\,(3)}_{\text{tree}}[g_A, F_\pi, M_\pi, m_N, d_j^r, l_k^r] =& \mathcal{M}^{\mu\,(3)}_{(i)}[F_\pi, M_\pi, d_8^r, d_9^r, d_{16}^r, d_{18}^r, d_{20}^r, d_{21}^r, d_{22}^r]\\ &+\mathcal{M}^{\mu\,(3)}_{(j)}[F_\pi, M_\pi, m_N, d_{16}^r, d_{18}^r]\\ &+\mathcal{M}^{\mu\,(3)}_{(k)}[F_\pi, M_\pi, m_N, d_{16}^r, d_{18}^r]\\ &+\mathcal{M}^{\mu\,(3)}_{(l)}[g_A, F_\pi, M_\pi, l_4^r, l_6^r]\\ &+\mathcal{M}^{\mu\,(3)}_{(m)}[g_A, m_N, d_6^r, d_7^r]\\ &+\mathcal{M}^{\mu\,(3)}_{(n)}[g_A, m_N, d_6^r, d_7^r]\\ &+\mathcal{M}^{\mu\,(3)}_{(o)}[M_\pi, F_\pi, d_{16}^r, d_{18}^r]\\ &+\mathcal{M}^{\mu\,(3)}_{(p)}[g_A, M_\pi, F_\pi, l_3^r, l_4^r].\end{aligned} \tag{4.138}$$

We start discussing some simplifications related to the LECs $\{l_3^r,\, l_4^r\}$. The summed amplitudes involved here, at tree level and involving pion propagators, are $\mathcal{M}^{\mu\,(1)}_{(d)}[g_A, F_\pi, M]$, $\mathcal{M}^{\mu\,(3)}_{(p)}[g_A, M_\pi, F_\pi, l_3^r, l_4^r]$ and $\mathcal{M}^{\mu\,(3)}_{(l)}[g_A, F_\pi, M_\pi, l_4^r, l_6^r]$. Using the expansion of Eq. (4.125) for M in the $\mathcal{O}(p^1)$ amplitude and after some algebra, the cancellation for l_3^r, l_4^r looks like

$$\begin{aligned}&\mathcal{M}^{\mu\,(1)}_{(d)}[g_A, F_\pi, M] + \mathcal{M}^{\mu\,(3)}_{(p)}[g_A, M_\pi, F_\pi, l_3^r, l_4^r] + \mathcal{M}^{\mu\,(3)}_{(l)}[g_A, F_\pi, M_\pi, l_4^r, l_6^r]\\ &= \mathcal{M}^{\mu\,(1)}_{(d)}[g_A, F_\pi, M] + \mathcal{M}^{\mu\,(3)}_{(p)}[g_A, M_\pi, F_\pi, l_3^r, \cancel{l_4^r}] + \mathcal{M}^{\mu\,(3)}_{(l)}[g_A, F_\pi, M_\pi, \cancel{l_4^r}, l_6^r]\end{aligned}$$

[32] The referred amplitudes from section 4.2.1 are taken by replacing there the parameters $g \to g_A$, $m \to m_N - \widetilde{\delta}^{(3)}_{m_N}$, $F \to F_\pi$, $M \to \overline{M}_\pi$.

$$
\begin{aligned}
&= \left(\mathcal{M}^{\mu\,(1)}_{(d)}[g_A, F_\pi, \overline{M}_\pi] - \mathcal{M}^{\mu\,(3)}_{(d)R}[M_\pi, l_3^r] + \mathcal{O}(p^5)\right) + \mathcal{M}^{\mu\,(3)}_{(p)}[g_A, M_\pi, F_\pi, l_3^r, l_4^r = 0] \\
&\qquad + \mathcal{M}^{\mu\,(3)}_{(l)}[g_A, F_\pi, M_\pi, l_4^r = 0, l_6^r] \\
&= \mathcal{M}^{\mu\,(1)}_{(d)}[g_A, F_\pi, \overline{M}_\pi] - \cancel{\mathcal{M}^{\mu\,(3)}_{(d)R}[M_\pi, l_3^r]} + \cancel{\mathcal{M}^{\mu\,(3)}_{(p)}[g_A, M_\pi, F_\pi, l_3^r, l_4^r = 0]} \\
&\qquad + \mathcal{M}^{\mu\,(3)}_{(l)}[g_A, F_\pi, M_\pi, l_4^r = 0, l_6^r] + \mathcal{O}(p^5) \\
&= \mathcal{M}^{\mu\,(1)}_{(d)}[\widetilde{g}, F, \overline{M}_\pi] + \mathcal{M}^{\mu\,(3)}_{(l)}[g_A, F_\pi, M_\pi, l_4^r = 0, l_6^r] + \mathcal{O}(p^5),
\end{aligned}
\tag{4.139}
$$

with $\overline{M}_\pi$ defined in Eq. (4.126). In this way, the above amplitudes corresponding to the tree Feynman diagrams (d), (p) and (l) of Fig. 4.1 are reduced to just the amplitude of diagrams (d) and (l), without any dependence on $\{l_3^r, l_4^r\}$. This is also illustrated in Fig. 4.9.

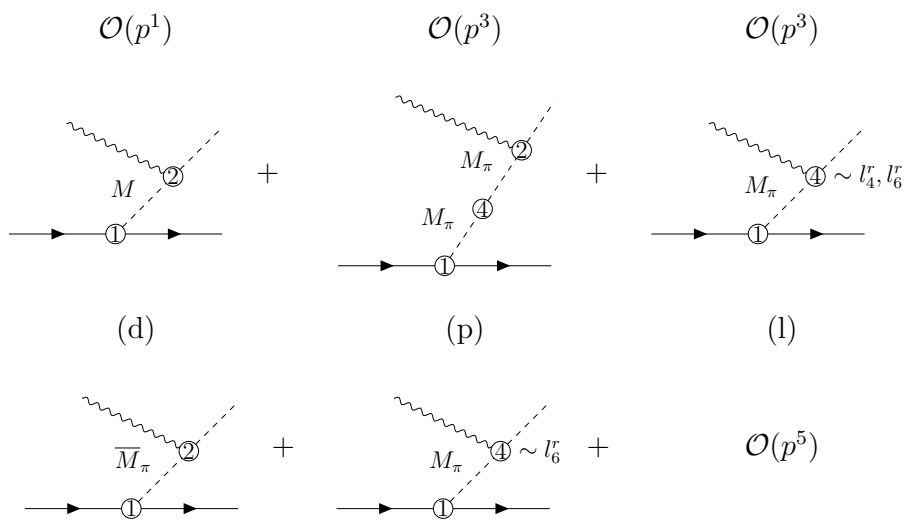

FIGURE 4.9: Feynman diagrams indicating the reduction to the relevant amplitudes and LECs shown in Eq. (4.139).

An additional simplification is related to the LEC d_{16}^r for the amputated amplitude $\mathcal{M}^\mu$, Eq. (4.135). Similarly to the previous example for l_3^r and l_4^r, the summation of all the pieces containing terms proportional to d_{16}^r are re-absorbed when $\widetilde{g}$ is expanded up to $O(p^3)$ as a function of g_A. In detail, using the amplitudes which depend on d_{16}^r, (4.136), (4.138) together with (4.139) we have that

$$
\begin{aligned}
&\mathcal{M}^{\mu\,(1)}_{\text{tree}}[\widetilde{g}, F, M, \widetilde{m}_2] + \mathcal{M}^{\mu\,(3)}_{\text{tree}}[g_A, F_\pi, M_\pi, m_N, d_j^r, l_k^r] \\
&= \left(1 - \cancel{\frac{4d_{16}^r M_\pi^2}{g_A}} - \widetilde{\delta}^{(2)}_{g_A} + \delta^{(2)}_{F_\pi}[l_4^r]\right) \times \\
&\quad \Bigg(\mathcal{M}^{\mu\,(1)}_{(a)}[g_A, F_\pi] + \mathcal{M}^{\mu\,(1)}_{(b)}[g_A, F_\pi, m_N - \widetilde{\delta}^{(3)}_{m_N}] \\
&\quad + \mathcal{M}^{\mu\,(1)}_{(c)}[g_A, F_\pi, m_N - \widetilde{\delta}^{(3)}_{m_N}] + \mathcal{M}^{\mu\,(1)}_{(d)}[g_A, F_\pi, \overline{M}_\pi]\Bigg) \\
&\quad + \mathcal{M}^{\mu\,(3)}_{(i)}[F_\pi, M_\pi, d_8^r, d_9^r, \cancel{d_{16}^r}, d_{18}^r, d_{20}^r, d_{21}^r, d_{22}^r]
\end{aligned}
$$

$$
\begin{aligned}
&+\mathcal{M}^{\mu\,(3)}_{(j)}[F_\pi, M_\pi, m_N, \cancel{d^r_{16}}, d^r_{18}] + \mathcal{M}^{\mu\,(3)}_{(k)}[F_\pi, M_\pi, m_N, \cancel{d^r_{16}}, d^r_{18}] \\
&+\mathcal{M}^{\mu\,(3)}_{(l)}[g_A, F_\pi, M_\pi, l^r_4 = 0, l^r_6] + \mathcal{M}^{\mu\,(3)}_{(m)}[g_A, m_N, d^r_6, d^r_7] \\
&+\mathcal{M}^{\mu\,(3)}_{(n)}[g_A, m_N, d^r_6, d^r_7] + \mathcal{M}^{\mu\,(3)}_{(o)}[M_\pi, F_\pi, \cancel{d^r_{16}}, d^r_{18}]
\end{aligned}
\tag{4.140}
$$

In summary, once the amputated amplitude has been summed, in particular the terms $\mathcal{M}^{\mu\,(1)}_{\text{tree}}[\widetilde{g}, F, M, \widetilde{m}_2] + \mathcal{M}^{\mu\,(3)}_{\text{tree}}[g_A, F_\pi, m_N, d^r_j, l^r_k]$, as shown in Eq. (4.140), we find that we can discard completely the LECs d^r_{16} and l^r_3 and the amplitude $\mathcal{M}^{\mu\,(3)}_{(p)}$ in an $\mathcal{O}(p^3)$ calculation. On the other hand, the LEC l^r_4 does not appear any longer in the $\mathcal{O}(p^3)$ tree amplitudes, as shown in Eq. (4.139). Still, at first sight, there is a residual l^r_4 dependence which appears in the chiral expansion for F, as a function of F_π, from the $\mathcal{O}(p^1)$ amplitude. This will be discussed below.
Thus, the evaluated amputated-amplitude $\mathcal{M}^\mu$ (4.135) in terms of physical quantities and LECs[33] has a simpler form. Namely, the following particular pieces can be replaced by

$$
\mathcal{M}^{\mu\,(1)}_{\text{tree}}[\widetilde{g}, F, M, \widetilde{m}_2] \longrightarrow \left(1 - \widetilde{\delta}^{(2)}_{g_A} + \delta^{(2)}_{F_\pi}[l^r_4]\right)\mathcal{M}^{\mu\,(1)}_{\text{tree}}[g_A, F_\pi, \overline{M}_\pi, m_N - \widetilde{\delta}^{(3)}_{m_N}],
\tag{4.141}
$$

$$
\begin{aligned}
\mathcal{M}^{\mu\,(3)}_{\text{tree}}[g_A, F_\pi, m_N, d^r_j, l^r_k] \longrightarrow &\mathcal{M}^{\mu\,(3)}_{(i)}[F_\pi, M_\pi, d^r_8, d^r_9, d^r_{16} = 0, d^r_{18}, d^r_{20}, d^r_{21}, d^r_{22}] \\
&+\mathcal{M}^{\mu\,(3)}_{(j)}[F_\pi, M_\pi, m_N, d^r_{16} = 0, d^r_{18}] \\
&+\mathcal{M}^{\mu\,(3)}_{(k)}[F_\pi, M_\pi, m_N, d^r_{16} = 0, d^r_{18}] \\
&+\mathcal{M}^{\mu\,(3)}_{(l)}[g_A, F_\pi, M_\pi, l^r_4 = 0, l^r_6] + \mathcal{M}^{\mu\,(3)}_{(m)}[g_A, m_N, d^r_6, d^r_7] \\
&+\mathcal{M}^{\mu\,(3)}_{(n)}[g_A, m_N, d^r_6, d^r_7] + \mathcal{M}^{\mu\,(3)}_{(o)}[M_\pi, F_\pi, d^r_{16} = 0, d^r_{18}],
\end{aligned}
\tag{4.142}
$$

with

$$
\begin{aligned}
\mathcal{M}^{\mu\,(1)}_{\text{tree}}[g_A, F_\pi, \overline{M}_\pi, m_N - \widetilde{\delta}^{(3)}_{m_N}] =&\mathcal{M}^{\mu\,(1)}_{(a)}[g_A, F_\pi] + \mathcal{M}^{\mu\,(1)}_{(b)}[g_A, F_\pi, m_N - \widetilde{\delta}^{(3)}_{m_N}] \\
&+\mathcal{M}^{\mu\,(1)}_{(c)}[g_A, F_\pi, m_N - \widetilde{\delta}^{(3)}_{m_N}] + \mathcal{M}^{\mu\,(1)}_{(d)}[g_A, F_\pi, \overline{M}_\pi].
\end{aligned}
\tag{4.143}
$$

A final simplification of the amplitude is related to the dependence on the parameter l^r_4 when we consider the full amplitude with the WFR of the external fields. The LEC l^r_4 appears both in the LO amplitude through $\delta^{(2)}_{F_\pi}[l^r_4]$ in the expansion for F and in the scaling constant $\sqrt{\mathcal{Z}_\pi}$ [see. Eq. (4.104)]. In detail, the full amplitude as shown in Eq. (4.135) contains the scaling factor $\sqrt{\mathcal{Z}_\pi}\mathcal{Z}_N$ for each order in the amputated contribution. Subsequently, these WFR scaling factors multiply all the amputated amplitudes from $\mathcal{O}(p^1)$ to $\mathcal{O}(p^3)$ and introduces higher order corrections.
The most interesting case is for the $\mathcal{O}(p^1)$ term $\sqrt{\mathcal{Z}_\pi}\mathcal{Z}_N\mathcal{M}^{\mu\,(1)}$ from Eq. (4.135). Using the simplification of Eq. (4.141), this term is

[33] Assuming that all the amplitude pieces also depend on the kinematical variables $\{s, u, Q^2\}$.

$$\sqrt{\mathcal{Z}_\pi}\mathcal{Z}_N\mathcal{M}^{\mu\,(1)}_{\text{tree}}[\widetilde{g},F,M,\widetilde{m}_2]=\sqrt{\mathcal{Z}_\pi}\mathcal{Z}_N\left(1-\widetilde{\delta}^{(2)}_{g_A}+\delta^{(2)}_{F_\pi}[l_4^r]\right)\mathcal{M}^{\mu\,(1)}_{\text{tree}}[g_A,F_\pi,\overline{M}_\pi,m_N-\widetilde{\delta}^{(3)}_{m_N}], \tag{4.144}$$

where the series $(1+\delta^{(2)}_{F_\pi}[l_4^r]+\dots)$ comes from the chiral expansion of the LO parameters F and $\widetilde{g}$ within the amplitude $\mathcal{M}^{\mu\,(1)}_{\text{tree}}[\widetilde{g},F,M,\widetilde{m}_2]$ [see Eq. (4.3.3)]. In a $\mathcal{O}(p^3)$ expansion, F contains explicitly a linear dependence on l_4^r, as well as it does the expansion for $\sqrt{\mathcal{Z}_\pi}$. Using the equations for $\delta^{(2)}_{\mathcal{Z}_\pi}[l_4^r]$, (4.105), and $\delta^{(2)}_{F_\pi}[l_4^r]$, (4.123), we get

$$\begin{aligned}\sqrt{\mathcal{Z}_\pi}\left(1+\delta^{(2)}_{F_\pi}[l_4^r]-\widetilde{\delta}^{(2)}_{g_A}\right)=&\left(1+\frac{1}{2}\delta^{(2)}_{\mathcal{Z}_\pi}[l_4^r]+\mathcal{O}(p^3)\right)\left(1+\delta^{(2)}_{F_\pi}[l_4^r]-\widetilde{\delta}^{(2)}_{g_A}\right)\\ =&1+\frac{1}{2}\delta^{(2)}_{\mathcal{Z}_\pi}[l_4^r]+\delta^{(2)}_{F_\pi}[l_4^r]-\widetilde{\delta}^{(2)}_{g_A}+\mathcal{O}(p^3)\\ =&1+\frac{2}{3}\frac{\overline{A}_0[M_\pi^2]}{16\pi^2F_\pi^2}-\widetilde{\delta}^{(2)}_{g_A}+\mathcal{O}(p^3)\end{aligned} \tag{4.145}$$

where in $\frac{1}{2}\delta^{(2)}_{\mathcal{Z}_\pi}[l_4^r]+\delta^{(2)}_{F_\pi}[l_4^r]$ the terms with l_4^r have canceled. Thus, expanding also $\mathcal{Z}_N$ as in (4.102), the equation (4.144) is written as

$$\begin{aligned}\sqrt{\mathcal{Z}_\pi}\mathcal{Z}_N\mathcal{M}^{\mu\,(1)}_{\text{tree}}[\widetilde{g},F,M,\widetilde{m}_2]=&\left(1+\frac{\overline{A}_0[M_\pi^2]}{24\pi^2F_\pi^2}+\widetilde{\delta}^{(2)}_{\mathcal{Z}_N}-\widetilde{\delta}^{(2)}_{g_A}\right)\mathcal{M}^{\mu\,(1)}_{\text{tree}}[g_A,F_\pi,\overline{M}_\pi,m_N-\widetilde{\delta}^{(3)}_{m_N}]\\ &+\mathcal{O}(p^4)\end{aligned} \tag{4.146}$$

where it is clear that there is not further dependence on l_4^r up to the $\mathcal{O}(p^3)$ considered.

For the following higher order terms the situation is simpler because the l_4^r dependence coming from the WFR factor can be neglected because is of order higher than three. Indeed, using Eqs. (4.102) and (4.104) we have

$$\begin{aligned}\sqrt{\mathcal{Z}_\pi}\mathcal{Z}_N=&\left(1+\delta^{(2)}_{\mathcal{Z}_\pi}[l_4^r]+\mathcal{O}(p^3)\right)^{1/2}\left(1+\delta^{(2)}_{\mathcal{Z}_N}+\mathcal{O}(p^3)\right)\\ =&1+\frac{1}{2}\delta^{(2)}_{\mathcal{Z}_\pi}[l_4^r]+\delta^{(2)}_{\mathcal{Z}_N}+\mathcal{O}(p^3).\end{aligned} \tag{4.147}$$

Taking the rest of the amplitude terms: $\widetilde{\mathcal{M}}^{\mu\,(2)}_{tree}$, $\mathcal{M}^{\mu\,(3)}_{tree}$, $\mathcal{M}^{\mu\,(5/2)}_{tree\Delta}$ and $\widetilde{\mathcal{M}}^{\mu\,(3)}_{loop}$ such as they appear in Eq. (4.135), we multiply them by the WFR factor and we obtain

$$\begin{aligned}\sqrt{\mathcal{Z}_\pi}\mathcal{Z}_N\widetilde{\mathcal{M}}^{\mu(2)}_{tree}=&\left(1+\frac{1}{2}\delta^{(2)}_{\mathcal{Z}_\pi}(l_4,M_\pi,F_\pi)+\delta^{(2)}_{\mathcal{Z}_N}(m_N,M_\pi,g_A,F_\pi)+\mathcal{O}(p^3)\right)\widetilde{\mathcal{M}}^{\mu(2)}_{tree}\\ =&\widetilde{\mathcal{M}}^{\mu(2)}_{tree}+\mathcal{O}(p^4)\end{aligned} \tag{4.148}$$

$$\begin{aligned}\sqrt{\mathcal{Z}_\pi}\mathcal{Z}_N\mathcal{M}^{\mu(3)}_{tree}=&\left(1+\frac{1}{2}\delta^{(2)}_{\mathcal{Z}_\pi}(l_4,M_\pi,F_\pi)+\delta^{(2)}_{\mathcal{Z}_N}(m_N,M_\pi,g_A,F_\pi)+\mathcal{O}(p^3)\right)\mathcal{M}^{\mu(3)}_{tree}\\ =&\mathcal{M}^{\mu(3)}_{tree}+\mathcal{O}(p^5)\end{aligned} \tag{4.149}$$

$$\sqrt{\mathcal{Z}_\pi}\mathcal{Z}_N\mathcal{M}^{\mu(5/2)}_{tree\Delta} = \left(1+\frac{1}{2}\delta^{(2)}_{\mathcal{Z}_\pi}(l_4,M_\pi,F_\pi)+\delta^{(2)}_{\mathcal{Z}_N}(m_N,M_\pi,g_A,F_\pi)+\mathcal{O}(p^3)\right)\mathcal{M}^{\mu(5/2)}_{tree\Delta}$$
$$=\mathcal{M}^{\mu(5/2)}_{tree\Delta}+\mathcal{O}(p^{9/2}) \tag{4.150}$$
$$\sqrt{\mathcal{Z}_\pi}\mathcal{Z}_N\widetilde{\mathcal{M}}^{\mu(3)}_{loop} = \left(1+\frac{1}{2}\delta^{(2)}_{\mathcal{Z}_\pi}(l_4,M_\pi,F_\pi)+\delta^{(2)}_{\mathcal{Z}_N}(m_N,M_\pi,g_A,F_\pi)+\mathcal{O}(p^3)\right)\widetilde{\mathcal{M}}^{\mu(3)}_{loop}$$
$$=\widetilde{\mathcal{M}}^{\mu(3)}_{loop}+\mathcal{O}(p^5) \tag{4.151}$$

These relations show that the WFR corrections start to contribute at two orders higher than the corresponding amputated amplitudes. That means that the loop corrections in the external legs are of $\mathcal{O}(p^4)$ or higher and can be neglected. We observe here that one can opt to include or not the WFR for the amputated amplitude from $\mathcal{O}(p^2)$ and higher. However, these choices have been tested to produce inappreciable differences. In contrast, the effect of WFR in $\mathcal{M}^{\mu\,(1)}_{\text{tree}}$ is sizable and becomes relevant to reproduce the data.

To summarize the treatment of the full amplitude and to show the final form that it takes, I write it down such as I use it for the calculation of physical observables for the $\gamma^{(*)}+N\longrightarrow\pi+N'$ reaction. That is, the full $\widetilde{\text{MS}}$ and EOMS regularized amplitude, Eq. (4.135), results in

$$\begin{aligned}\hat{\mathcal{M}}^\mu &= \sqrt{\mathcal{Z}_\pi}\mathcal{Z}_N\mathcal{M}^\mu\\
&= \left(1+\frac{\overline{A}_0[M_\pi^2]}{24\pi^2F_\pi^2}+\widetilde{\delta}^{(2)}_{\mathcal{Z}_N}-\widetilde{\delta}^{(2)}_{g_A}\right)\mathcal{M}^{\mu\,(1)}_{\text{tree}}[s,u,Q^2,g_A,F_\pi,\overline{M}_\pi,m_N-\widetilde{\delta}^{(2)}_{m_N}]\\
&\quad+\mathcal{M}^{\mu\,(2)}_{\text{tree}}[s,u,Q^2,g_A,F_\pi,m_N,\widetilde{c}_6,\widetilde{c}_7]\\
&\quad+\mathcal{M}^{\mu\,(3)}_{\text{tree}}[s,u,Q^2,g_A,F_\pi,M_\pi,m_N,d^r_6,d^r_7,d^r_8,d^r_9,d^r_{18},d^r_{20},d^r_{21},d^r_{22},l^r_6]\\
&\quad+\mathcal{M}^{\mu(5/2)}_{tree\Delta}[s,u,Q^2,g_M,h_A]\\
&\quad+\widetilde{\mathcal{M}}^{\mu(3)}_{loop}[s,u,Q^2,m_N,M_\pi,g_A,F_\pi]+\mathcal{O}(p^4),\end{aligned} \tag{4.152}$$

where $\widetilde{\delta}^{(2)}_{\mathcal{Z}_N}$ is given by Eq. (4.103) and $\widetilde{\delta}^{(2)}_{g_A}$ is shown in (C.7). The amplitudes, where the kinematical dependence $\{s,u,Q^2\}$ is understood, are evaluated after the LEC simplification for $\mathcal{M}^{\mu\,(1)}_{\text{tree}}[g_A,F_\pi,\overline{M}_\pi,m_N-\widetilde{\delta}^{(2)}_{m_N}]$ as in (4.143); the amplitude term $\mathcal{M}^{\mu\,(2)}_{\text{tree}}[g_A,F_\pi,m_N,\widetilde{c}_6,\widetilde{c}_7]$ is simply evaluated as in Eq. (4.143); the amplitude for $\mathcal{M}^{\mu\,(3)}_{\text{tree}}[g_A,F_\pi,m_N,d^r_j]$ is evaluated as in (4.142) where the LECs d^r_{16},l^r_3,l^r_4 contribution are neglected; as always, the Δ contribution amplitude is evaluated as in (4.51). Finally the amputated loop contribution is evaluated as

$$\widetilde{\mathcal{M}}^{\mu(3)}_{loop}[m_N,M_\pi,g_A,F_\pi] = \text{PCBT}_1+\text{PCBT}_2+\sum_{topo=a1}^{i3}\mathcal{M}^{\mu\,(3)}_{(topo)}[m_N,M_\pi,g_A,F_\pi]. \tag{4.153}$$

The tree level amplitude pieces given here, although they are given in this chapter, also can be found along the app. A.2 in terms of the kinematical variables $\{s,u,Q^2\}$ and written in the Ball basis for photoproduction (3.74) and electroproducion (3.14). Similarly, the PCBT are provided explicitly in App. B for each physical channel and both reactions. This is especially useful in the calculation of the physical observables studied in Ch. 3 and as I will discuss in the next chapter.

The loop amplitudes $\mathcal{M}^{\mu\,(3)}_{(topo)}$ when are integrated and written in terms of the Ball basis and Passarino-Veltman functions, they result in very large expressions. Nevertheless, these loop amplitudes are given explicitly in A.3 in the integral form for the four physical channels of pion production.

4.4 Input parameters: LECs from other processes and physical quantities

Apart from the well known physical parameters $\{g_A, F_\pi, M_\pi, m_N\}$ [34], the LECs dependence of the full $\mathcal{O}(p^3)$ amplitude (4.152) is displayed in

$$\hat{\mathcal{M}}^\mu = \hat{\mathcal{M}}^\mu[\widetilde{c}_6, \widetilde{c}_7, d^r_6, d^r_7, d^r_8, d^r_9, d^r_{18}, d^r_{20}, d^r_{21}, d^r_{22}, l^r_6, h_A, g_M]. \tag{4.154}$$

On the other hand, within the EOMS framework and at $\mathcal{O}(p^3)$ [34], many of the LECs involved in the amplitude for the pion photo- and electroproduction on nucleons have been investigated through the analysis of several other processes. They are the set of LECs $\{\widetilde{c}_6, \widetilde{c}_7, d^r_6, d^r_7, d^r_{18}, l^r_6\}$. Their specific values and references are shown in Table 4.5.

TABLE 4.5: Values of the $\mathcal{O}(p^3)$ EOMS LECs determined from other processes.

	LEC	Value	Source
$\mathcal{L}^{(2)}_N$	$\widetilde{c}_6$	5.07 ± 0.15	μ_p and μ_n [25, 34, 108]
	$\widetilde{c}_7$	-2.68 ± 0.08	μ_p and μ_n [26, 34, 108]
$\mathcal{L}^{(3)}_N$	d^r_6	-0.70 GeV^{-2}	N EM Form factor [6]
	d^r_7	-0.49 GeV^{-2}	N EM Form factor [6]
	d^r_{18}	-0.20 ± 0.80 GeV^{-2}	πN scattering [14]
$\mathcal{L}^{(4)}_{\pi\pi}$	l^r_6	$(-1.34 \pm 0.12) \times 10^{-2}$	$\langle r^2 \rangle_\pi$ [25]
$\mathcal{L}^{(1)}_{\Delta N\pi}$	h_A	2.87 ± 0.03	$\Gamma^{\text{strong}}_\Delta$ [79]
$\mathcal{L}^{(2)}_{\Delta N\gamma}$	g_M	3.16 ± 0.16	$\Gamma^{\text{EM}}_\Delta$ [80]

For the leading order Lagrangian and the rest of physical quantities we take $g_A = 1.27$, $F_\pi = 92.42$ MeV, $M_{\pi^0} = 134.9767$ MeV, $M_{\pi^\pm} = 139.5702$ MeV, $m_p = 938.272081$ MeV, $m_n = 939.565413$ MeV, $m_\Delta = 1232$ MeV and $e^2 = 4\pi/137$.

Finally, we only keep five undetermined parameters $\{d^r_8, d^r_9, d^r_{20}, d^r_{21}, d^r_{22}\}$ that are involved in our amplitudes and need to be determined from the available data [see. Sec. 5.1]. Specifically, they appear only at the tree $\mathcal{O}(p^3)$ amplitudes. In particular, the combination $\{d^r_8 + d^r_9\}$ appears exclusively in the $\pi^0 p$ channel, whilst the set $\{d^r_9, d^r_{20}, d^r_{21}, d^r_{22}\}$ contributes only to the charged pion channels, as shown in Sec. 4.2.1. In Ref. [109], d^r_{22}, related to the nucleon axial radius, was fixed from a fit to lattice data at unphysical pion masses [110]. However, the quoted error bars might be underestimated [35] and we prefer to fix it independently. Furthermore, in the previous studies

[34] Furthermore, the quoted studies have also used $\widetilde{MS}$ regularization and explicit Δ's when relevant.

[35] See Fig. 4 of Ref. [110], to fully appreciate the uncertainties of that fit.

of pion photoproduction, its value could not be well assessed because, at $Q^2 = 0$, its contribution is fully correlated to that of d^r_{21}. Thus, for $Q^2 \neq 0$, the inclusion of electroproduction in the current analysis could lead to a more reliable determination of this parameter.
Additionally to the value for g_M as given in Tab. 4.5, the values reported in the literature, using the same Lagrangian as in the present work, vary from 2.6 ± 0.2 [84] in a heavy-baryon calculation of Compton scattering to $g_M = 2.8 \pm 0.2$ [111] (in pion photoproduction) and $g_M = 2.9$ [81, 112] (in pion electroproduction). For this reason and the importance of the Δ mechanism in the agreement with photo- and electroproduction data, we opt to leave the parameter g_M fluctuate within the quoted ranges and take it as a constrained fitting parameter.
Considering the loop contribution in an EOMS renormalization scheme, we investigate these free parameters in the next chapter through the comparison with the experimental data for the $\gamma^{(*)} + N \longrightarrow \pi + N'$ observables.

Chapter 5

Determination of the low-energy-constants and results

This chapter is aimed to describe the procedure to determine the values for the relevant LECs in pion photo- and electroproduction on nucleons, and to present the theoretical results for the physical observables compared with their corresponding experimental measurements.
First, we specify the used experimental database for the electroproduction and the photoproduction processes within an adequate kinematical region given our ChPT model. We include data in the invariant energy range from threshold up to the first 60 MeV (W =1133 MeV). For the electroproduction case, the collected experimental data also include angular cross sections at different transfer momenta, Q^2, up to $0.15\,\mathrm{GeV}^2$.
Next, we detail the LEC fitting procedure where the theoretical model is compared with the experimental database and the minimization of the χ^2 function is performed. The fitting parameters considered here are the free LECs, $\{d_8^r, d_9^r, d_{20}^r, d_{21}^r, d_{22}^r\}$ and g_M, whose numerical values are reported here as result of the corresponding χ^2 minimization procedure. Additionally, an estimate of the errors for the LECs and calculations of observables is detailed, taking into account the systematical and statistical errors from different sources.
In the last section, the theoretical calculations for the $\gamma^{(*)} + N \longrightarrow \pi + N'$ observables are compared with data for different kinematical regions, and the results are discussed. The electroproduction observables are presented as a function of the c.m. energy (W), the transfer momenta (Q^2), and the pion angle production (θ_π). For the photoproduction reaction, the kinematical results are shown as a function of the photon energy in the lab. frame (E_γ^{lab}) and the c.m. angle (θ_π). The propagation of the systematical and statistical uncertainties are also plotted.

5.1 Experimental database for $\gamma^{(*)} + N \longrightarrow \pi + N'$ observables

In ChPT we assume that the expansion parameters, the external momenta and pion mass, are small enough compared with the $\Lambda \sim m_N$ scale. As the momenta depend on the energy, these parameters are kept small when the energy is close enough to the threshold. Because of this, we compare our model to the available experimental data with some kinematical limits to ensure small external momenta. Thus, we have taken the invariant energy of the πN system, W, ranging from threshold up to 1133 MeV. Furthermore, from the study of the nucleon electromagnetic form factors [108, 113] it is known that a good description beyond $Q^2 \sim 0.2$ GeV^2 requires the inclusion of vector mesons in the model. Therefore, we have selected data with transfer momentum

within the interval $0 \leq Q^2 \leq 0.15$ GeV^2. This choice guarantees that the external pion momentum is small enough to stay well below the $\Delta(1232)$ resonance peak of the cross sections. In particular, the case for $Q^2 = 0$ corresponds to pion photoproduction data. We expect the $\mathcal{O}(p^3)$ ChPT calculation with explicit Δ's to be well suited for the description of the phenomenology in this kinematical region.
In the following, the experimental data used in the fitting procedure will be described.

Electroproduction data

In the single pion electroproduction case, $\gamma^* N \longrightarrow \pi N'$, the available experimental data at low energies are related to the target- and recoil unpolarized virtual cross section $d\sigma_v/d\Omega_\pi$ and its transverse-longitudinal decomposition as shown in Eq. (3.56).

The largest amount of data corresponds to the $\gamma^* p \to \pi^0 p$ channel. Specifically, from the late nineties, we include data for the virtual angular cross section $d\sigma_v/d\Omega_\pi^*$ at $Q^2 = 0.1$ GeV^2, obtained by the Amsterdam Pulse Stretcher facility [114], and data from MAMI [115] for the observables $d\sigma_{TT}/d\Omega_\pi^*$, $d\sigma_{TL}/d\Omega_\pi^*$ and the combination $(d\sigma_T/d\Omega_\pi^* + \varepsilon d\sigma_L/d\Omega_\pi^*)$. Later, very precise energy dependence data have been obtained at $Q^2 = 0.05$ GeV^2 in Mainz [95] for the observables $d\sigma_{TT}/d\Omega_\pi^*$, $d\sigma_{TL}/d\Omega_\pi^*$, $(d\sigma_T/d\Omega_\pi^* + \varepsilon d\sigma_L/d\Omega_\pi^*)$ and the asymmetry $A_{LT'}$ [see Eq. (3.59)]. More recently, data for $d\sigma_{TL}/d\Omega_\pi^*$ and $(d\sigma_T/d\Omega_\pi^* + \varepsilon d\sigma_L/d\Omega_\pi^*)$ were published for additional Q^2 values [116].

There are far less data for the pion charged channel $\gamma^* p \to \pi^+ n$. Nonetheless, they are crucial to determine LECs like d_{20}^r, d_{21}^r and d_{22}^r. We consider data on $d\sigma_T/d\Omega_\pi^*$, $d\sigma_L/d\Omega_\pi^*$, $d\sigma_{TL}/d\Omega_\pi^*$ and the total $d\sigma_v/d\Omega_\pi^*$ at a fixed $Q^2 = 0.117$ GeV^2 measured at Mainz [117]. Later, the experiment was extended to other Q^2 values for $d\sigma_T/d\Omega_\pi^*$, $d\sigma_L/d\Omega_\pi^*$ and $d\sigma_v/d\Omega_\pi^*$ [118, 119], and more recently to lower energies [120].

The total amount of used data in the electroproduction case contains 769 points. Specifically, 751 of them correspond to the $\gamma^* p \to \pi^0 p$ channel whilst only 18 points correspond to the $\gamma^* p \to \pi^+ n$ channel.

Photoproduction data

In the study of the photoproduction reaction, $\gamma N \longrightarrow \pi N'$, we constrain the data collection to the same energy region as in the electroproduction case, $W = \sqrt{s} \in [1073, 1133]$ MeV. Usually, the photoproduction data are reported in terms of the lab. frame photon energy (3.69), *i.e.*, $E_\gamma^{lab} \in [145, 215]$ MeV.

Also here, the larger part of the database corresponds to the $\gamma p \to \pi^0 p$ process. Furthermore, the experimental errors are relatively smaller when compared to the other channels. As a consequence, the neutral pion production has a preeminent weight in the fits. There have been extensive measurements in the near threshold region [121–124], although the largest contribution comes from the comprehensive set of data on angular cross sections, $d\sigma/d\Omega_\pi^*$ (3.84), and photon asymmetries, Σ (3.92), obtained at MAMI [125]. [1]
At the higher end of our energy range there are a few data points measured by the LEGS facility at the Brookhaven National Laboratory [126].
In addition, we have considered more recent measurements on transverse protons from Ref. [23]. They correspond to the physical observable $T\, d\sigma/d\Omega_\pi^*$, defined in Eq. (3.95), with T the target asymmetry and $d\sigma/d\Omega_\pi^*$ the angular cross section.

[1] The data from Refs. [122, 123] are not unfolded from the angular spectrometer distortion and have not been included in the fit.

In contrast, the experimental data are scarce at low energies for the charged pions channels and there are only a few recent experiments on them.
For the channel $\gamma n \to \pi^- p$, we use the angular distributions and total cross sections from Refs. [127–130]. There are no low energy data on polarization observables yet. The early experiments at Frascati [127] and DESY [128] actually measured the reaction on deuterium and then, the cross sections on the neutron were obtained using the spectator model. On the other hand, the experiments at TRIUMF [129, 130] correspond to the inverse reaction: radiative pion capture on the proton. There are some later measurements from the early 1990s, also at TRIUMF, quoted by SAID [131], but they are unfortunately unpublished. Only recently, the near threshold π^- photoproduction on the deuteron has been measured again at the MAX IV Laboratory [132], and the derivation of the total cross section for the $\gamma n \longrightarrow \pi^- p$ elementary reaction has been published in [24]. We have included these latter data in our fit since they are crucial for a better determination of the LECs.

There are some more data for the $\gamma p \to \pi^+ n$ channel, which can be measured more directly. They are mostly angular and total cross sections but they also include some photon asymmetries. We take the data from Refs. [126, 133–135].
In total, the photoproduction database contains 1917 points. Specifically, 1716 correspond to the $\gamma p \to \pi^0 p$ channel, 126 data for the $\gamma p \to \pi^+ n$ and 75 data for the $\gamma n \to \pi^- p$ reaction. For most of them the total error estimation (statistic plus systematic) was given in the original references. A typical 5% systematic error has been added in quadrature for the few points where only the statistical error was provided [127–129].

5.2 Fitting procedure and error estimation

In the ChPT calculation for a process at a given chiral order, besides the theoretical uncertainty introduced by the finite number of terms considered in the expansion, the predictive power of this effective theory is quantified with the low-energy constants. The numerical values of the LECs are determined with the aforementioned experimental data. Here we show the procedure in fitting the undetermined LECs that are relevant in the processes studied in this work.

5.2.1 Minimization of the χ^2 function

In order to find the values for the parameters, $\{d_8^r, d_9^r, d_{20}^r, d_{21}^r, d_{22}^r, g_M\}$ that best reproduce the data, the theoretical model has been compared with the full photoproduction and electroproduction database previously introduced, minimizing the χ-squared function by varying the values of the free LECs and leaving fixed the rest of parameters. The fixed LECs are those already determined by other processes and quantities to the values given in Tab. 4.5.
Explicitly, the fitting LECs have real values such that the χ^2 function, given by

$$\chi^2(\mathbf{x}) = \sum_i \left(\frac{\overline{y}_i - \mathcal{O}^{th}(a_i, \mathbf{x})}{\delta y_i} \right)^2 , \tag{5.1}$$

has a global minimum in a particular $\overline{\mathbf{x}}$, with $\mathbf{x} = (d_8^r, d_9^r, d_{20}^r, d_{21}^r, d_{22}^r, g_M)$ the fitting parameters vector. The values δy_i are the uncertainties in the i-th experimental

measurements $\overline{y}_i$ for a given observable[2]. The values $\mathcal{O}^{th}(a_i, \mathbf{x})$ indicate the theoretical calculation of the observable evaluated in the particular kinematic variable set $a_i = \{Q_i^2, s_i, u_i\}$, where the experimental data measurements $\overline{y}_i \pm \delta y_i$ are defined.

For convenience, we omit the dependence on the fixed LECs into the theoretical calculation of the observable $\mathcal{O}^{th}$. Only the free LEC dependence on $\mathbf{x}$ is displayed explicitly into the ChPT model to be fitted, $\mathcal{O}^{th}(a, \mathbf{x})$.

The minimization procedure of the χ^2 function has been implemented numerically with the help of the `MINUIT` package provided by the CERN software library.
As we consider the data sets for the two reactions, photo- and electroproduction, the above function, Eq. (5.1), can be split as

$$\chi^2 = \chi^2_\gamma + \chi^2_e, \tag{5.2}$$

with χ^2_γ and χ^2_e the chi-square functions for the photoproduction and electroproduction data respectively. This distinction allows us to quantify the accordance between theory and experiment for each separated reaction in the global fit. As it was mentioned before, most of the LO parameters are known or determined by the analysis of other processes studied in the same approach, $\widetilde{\text{MS}}$ and EOMS-regularized ChPT. Within this approach, the novel contribution in our model stresses the explicit inclusion of the Δ-resonance. To study the effect of this Δ inclusion, we compare the quality and the chiral convergence as a function of energy of the theoretical model through two different approaches, one with only the nucleon and pion contributions and other with the explicit inclusion of the Δ mechanisms. In detail, we have proceeded to fit the free LECs including Δ in the $\gamma^{(*)}N \longrightarrow \pi N'$ amplitude (4.154) and compared to the corresponding fit when using the Δ-less amplitude[3]. The results will be shown in Table. 5.1 and discussed afterwards in Section 5.3.

5.2.2 Error estimation for the fitted LECs and the observables

After the minimization procedure of the χ^2 function, we can find the optimal values for the fitted LECs that best reproduce the data. However, these low-energy parameters have an associated uncertainty due to many different error sources. Moreover, the subsequent calculation of the observables in our ChPT model inherits such uncertainty.

In the computation of the fitting LECs and the observables, we can calculate an estimate of the corresponding uncertainties to explore the confidence limits in our theoretical results. The uncertainties for both the observables and fitting LECs come from the propagation of systematical and statistical sources of error. Among them, we distinguish in our calculations three different types:

- Error bars in the experimental data.
- Systematical uncertainties in our theoretical calculation of observables truncated at $\mathcal{O}(p^3)$ in the chiral power counting, since we consider only a finite number of terms in the chiral expansion.
- Errors in the fixed LECs given by the study of other processes and quantities, see Table 4.5.

[2]The observables to be compared are those of the indicated database described in Section 5.1, namely, $\{d\sigma/d\Omega^*_\pi, \sigma, \Sigma, \hat{T}\}$ for photoproduction and $\{d\sigma_v/d\Omega^*_\pi,\ d\sigma_T/d\Omega^*_\pi,\ d\sigma_L/d\Omega^*_\pi,\ d\sigma_{TT}/d\Omega^*_\pi,\ d\sigma_{TL}/d\Omega^*_\pi,\ (d\sigma_T + \varepsilon d\sigma_L)/d\Omega^*_\pi,\ A_{LT'}\}$ for electroproduction of pions on nucleons respectively. See Sections 3.1.4 and 3.2.3 for the explicit definitions.

[3]In practice, this is equivalent to set the value $g_M = 0$

Once the fit of the undetermined LECs is made, we estimate the propagated uncertainties to our results from these sources. To do that, we follow a systematic procedure depending on the error source. Hence, the obtained results for the fitting LECs, $\mathbf{x}$, and the corresponding observables, $\mathcal{O}^{th}(\mathbf{x})$, will be given with their mean values and error deviations, respectively. The propagation of the uncertainties in these results is detailed below for each case.

Statistical error from the experimental data points

In the fitting procedure, the error bars δy_i in the experimental data lead to an statistical error for the fitting LECs. In detail, the fit result for a LEC vector is given by

$$x_j = \overline{x}_j \pm \delta x_j, \qquad \text{for } x_j \in \{d_8^r, d_9^r, d_{20}^r, d_{21}^r, d_{22}^r, g_M\}\,, \tag{5.3}$$

where the global minimum of the χ^2 function is obtained at the best fit values $\overline{x}_j$. The δx_j is the statistical error for the LECs in 1-σ, and can be obtained systematically in `MINUIT` assuming that the behavior of the χ^2 function is nearly quadratic around each individual $\bar{x}_j$. In detail, δx_j for the LEC x_j is obtained as a parabolic error such that for each minimum $\left|\chi^2(\bar{x}_j) - \chi^2(\bar{x}_j \pm \delta x_j)\right| = 1$.

On the other hand, we propagate the statistical error from the fitting LECs, δx_j, to any observable $\mathcal{O}^{th}$ such that its associated error, $\delta\mathcal{O}^{th}_{\text{Stat}}$, is derived through the relation

$$\delta\mathcal{O}^{th}_{\text{Stat}}(\overline{\mathbf{x}}) = \left(\sum_{j,k}\left[\text{Corr}(x_j, x_k)\right]\frac{\partial\mathcal{O}^{th}(\overline{\mathbf{x}})}{\partial x_j}\delta x_j\frac{\partial\mathcal{O}^{th}(\overline{\mathbf{x}})}{\partial x_k}\delta x_k\right)^{1/2}, \tag{5.4}$$

where $\text{Corr}(x_k, x_j)$ indicates the (k, j)-th element of the correlation matrix, giving the estimated correlation among the x_k and x_j LECs. This correlation function is directly provided after the minimization process by the `MINUIT` program. The partial derivatives respect to an individual LEC dependence are evaluated over the fitted LECs, $\frac{\partial}{\partial x_j}\mathcal{O}^{th}(\overline{\mathbf{x}})$. It is worthy to mention here that, after the fitting procedure, the best estimation for the observables including only the statistical error is then given by

$$\mathcal{O}^{th}\left(a_i, \overline{\mathbf{x}}\right) \pm \delta\mathcal{O}^{th}_{\text{Stat}}(a_i, \overline{\mathbf{x}}) \tag{5.5}$$

for any i-th kinematical configuration $a_i = \{Q_i^2, s_i, u_i\}$ of the data of pion electromagnetic production on nucleons.

Systematical error from chiral truncation at $\mathcal{O}(p^3)$

Another source of uncertainty is the systematical error of the theory due to the truncation of the chiral series expansion at a given order. The calculation of the physical observables is based in the amplitude, $\hat{\mathcal{M}}^{\mu}$ (4.152), that contains a systematic error of chiral order $\mathcal{O}(p^4)$. To estimate it, we use the method of Refs. [76, 136]. Namely, for an order n observable calculation, $\mathcal{O}^{th}$, this systematical error is given by

$$\delta\mathcal{O}^{(n)}_{\text{Syst}} = \max\left(\left|\mathcal{O}^{(n_{LO})}\right| B^{n-n_{LO}+1}, \left\{\left|\mathcal{O}^{(k)} - \mathcal{O}^{(l)}\right| B^{n-l}\right\}\right), \qquad n_{LO} \leq l \leq k \leq n. \tag{5.6}$$

We take $B = M_\pi/\Lambda_\chi$ as in Ref. [110] with Λ_χ the breakdown scale of the chiral expansion, $\Lambda_\chi = 4\pi F_\pi \sim 1$ GeV. In the present work we have $n_{LO} = 1$ as the lowest order and the upper order is $n = 3$.
To take into account this piece in the final results, we add it in quadrature to the statistical error. Thus, the fitted results for the observables are

$$\mathcal{O}^{th}\left(a_i, \overline{\mathbf{x}}\right) \pm \sqrt{\delta\mathcal{O}^{th}_{\text{Stat}}(a_i, \overline{\mathbf{x}})^2 + \delta\mathcal{O}^{(3)}_{\text{Syst}}(a_i, \overline{\mathbf{x}})^2} \tag{5.7}$$

Error from uncertainties in fixed LECs

In addition, we can explore the extent and limits of our estimations by considering the uncertainties of the fixed LECs previously determined by other studies, as shown in Table 4.5. The already determined LECs have an associated error that comes from their respective fits to other data. Those errors may be originated by any statistical or systematical source. Nonetheless, we can include them in our fitting procedure without knowing *a priori* the details of their analyses.

On the other hand, the minimization routines in `MINUIT` are of limited use for the inclusion of errors in non-fitting parameters and a more adequate treatment of them is not direct. In consequence we must implement a more exhaustive fitting procedure to the routine based on the minimization of χ^2 (5.1).

To take into account the uncertainties of the fixed parameters, we follow an usual Bootstrap method [137]. To do that, we simulate a random sample of $N = 1000$ values for each known LEC, Tab. 4.5, with a proper probabilistic Gaussian distribution. There, we assume a simple scenario where the fixed LECs are uncorrelated and independent of each other. Thus, these non-fitting LECs are simulated such that their central and error values correspond to the mean and standard deviation of their respective Gaussian distributed samples.
Then, we proceed with the fitting procedure for the free LECs with data by minimizing the χ-squared, but repeating the process for each of the $N = 1000$ simulated sets of fixed LECs.[4]

The obtained results for the central values of both the fitted LECs and the observables remained the same as if no error in the fixed LECs were considered. We have taken this bootstrap procedure as an extension of the fitting procedure where the known LECs are fixed to their central values. For convenience, the inclusion and propagation of the error associated with the known LECs will be detailed below in section 5.4.

[4]It is worth mentioning that this method based on Monte Carlo techniques, where the non-fitting parameters are simulated to be normally distributed, has also been applied in other similar ChPT calculations [138] for the propagation of errors from experimental data and fixed LECs to the relevant LECs to be fitted.

5.3 Fit with and without Δ contribution

5.3.1 Low-Energy-Constants

In a first step, we minimize the χ^2 function of Eqs. (5.1), (5.2). The results are obtained for two different models, with and without the inclusion of the Δ, as they appear in Tab. 5.1. The Full model fit corresponds to the $\mathcal{O}(p^3)$ calculation when the Δ-resonance is included explicitly in the amplitude (4.152), as described in the previous chapter.

In this calculation, we have fixed the LECs from Table 4.5 to their central values, except for g_M. We have let the $\gamma\Delta N$ coupling, g_M, which proved of paramount significance in the description of π^0 photoproduction [21], to fluctuate around the central value according to the electromagnetic Δ width.

The LECs values obtained by the fits are presented together with the full χ^2 per degree of freedom [5], and the partial contributions of photo-(χ^2_γ) and electroproduction (χ^2_e). Here, the shown LECs errors are purely statistical and propagated from data error bars. The effects of the uncertainties of the fixed LECs are treated later.

TABLE 5.1: Fit results for the LECs. The coupling g_M is dimensionless and d_i in units of GeV^{-2}.

LECs	Full model	Δ-less
$d_8^r + d_9^r$	1.12 ± 0.01	3.44 ± 0.01
$d_8^r - d_9^r$	0.63 ± 0.15	4.75 ± 0.18
d_{20}^r	-0.29 ± 0.09	-3.01 ± 0.09
d_{21}^r	1.64 ± 0.06	4.50 ± 0.06
d_{22}^r	0.95 ± 0.13	0.45 ± 0.12
g_M	2.90 ± 0.01	—
χ^2/dof	2.7	13.2
χ^2_γ/dof	1.7	16.8
χ^2_e/dof	5.1	4.4

In this minimization procedure, we have chosen to fit the combinations $(d_8^r + d_9^r)$ and $(d_8^r - d_9^r)$, instead of the individual constants, because of the strong correlation among d_8^r and d_9^r. Actually, they appear in the amplitudes for π^0 production just in the combination $(d_8^r + d_9^r)$, while the charged $\pi^\pm$ channels depend only on d_9. Given that the $\gamma^{(*)} + p \longrightarrow \pi^0 + p$ processes represent, so far, the most precise and largest amount of data, its particular dependence on the $(d_8^r + d_9^r)$ combination can be determined with a high accuracy. Evidently, better data for the $\pi^\pm$ channels, would be essential to obtain more precise results for d_9^r or, similarly, for $(d_8^r - d_9^r)$. Given that the χ^2 value is not affected by the combination choice for d_8^r and d_9^r, the choice mentioned above is only important for the precise evaluation of the observables for π^0 or $\pi^\pm$ channels when the correlation matrix from the fits is not provided.

Alternatively, we could have fitted $(d_8^r + d_9^r)$ and d_9^r, such as they appear directly in the amplitudes. For the full model, the resulting fit leads to the same value for $(d_8^r + d_9^r)$ and $d_9^r = 0.25 \pm 0.08$. For the Δ-less model, again $(d_8^r + d_9^r)$ is not affected and $d_9^r = -0.66 \pm 0.09$. In both cases the results are fully consistent with those of Table 5.1 and can also be obtained from them using the correlation matrix and Eq. (5.5).

[5] The degrees of freedom corresponds to $dof = n_{data} - n_{par}$, where n_{data} in the number of data points used in the corresponding χ^2-function and n_{par} is the number of parameters to be fitted (See Section 5.1). Here, $n_{par} = 6$ for the Full model and $n_{par} = 5$ for the Δ-less case.

The parameters $\{d^r_{20}, d^r_{21}, d^r_{22}\}$ are only relevant for the charged channels $\gamma^{(*)}p \longrightarrow \pi^+ n$ and $\gamma^{(*)}n \longrightarrow \pi^- p$. The relatively low precision of the data and their scarcity limits the precision of their determination. Furthermore, these channels are already rather well described by the lower order predictions and in consequence the $\mathcal{O}(p^3)$ LECs play a small role. It is worth mentioning that in photoproduction, d^r_{21} and d^r_{22} appear only in the combination $(2d^r_{21} - d^r_{22})$ while for electroproduction that is not anymore the case (see App. Sec. A.2). Therefore, the full correlation between d^r_{21} and d^r_{22} is broken once electroproduction is considered in the fit.

Clearly, pion electroproduction reactions probe the Q^2 dependence of the scattering amplitude. Thus, it would allow for the exploration of already known LECs like $\{d^r_6, d^r_7, l^r_6\}$, which are relevant for the description of the nucleon EM form factors and the pion charge radius and which appear in the electroproduction case.

The parameter g_M takes a value consistent with that obtained from the electromagnetic Δ decay width. The results for g_M and $(d^r_8 + d^r_9)$ agree well with those obtained in the analysis of Ref. [109], which studied photoproduction within the same framework but imposed full isospin symmetry on the loop calculation. Our change with respect to that previous work, using physical masses in the loops, has led to a substantial improvement by lowering the χ^2_γ value and to some small changes in $(d^r_8 - d^r_9)$ and d^r_{20}. A larger variation can be observed in d^r_{21} and d^r_{22} but this could be deceptive. The photoproduction amplitude only depends on the combination $(2d^r_{21} - d^r_{22})$, which it has changed little. The separation of the two constants made in Ref. [109] was based on the use of $d_{22} = 5.20$ GeV^{-2}, taken from Ref. [110]. This value, obtained from the lattice and already discussed, is clearly disfavoured by the electroproduction data. However, our result is close to an alternative fit of Ref. [110] that restricted lattice data to low Q^2 values.

All the fitted d_i's are of natural size and, thus, the contribution of the associated $O(p^3)$ mechanisms is relatively small at low energies. While the global result is acceptable, as it will be better shown in the detailed comparison with various observables (Section 5.5), we can see that the model reproduces to a greater degree the photoproduction data.

5.3.2 Contribution of the Δ-resonance

To explore the importance of the explicit inclusion of the $\Delta(1232)$ in the model, we repeated the fit without the corresponding mechanisms. The results for the LECs and χ^2 are shown in the second column of Table 5.1.

Comparing the absolute values of χ^2/dof, we see that the $O(p^3)$ calculation without Δ gives $\chi^2/dof = 13.2$. This number is mostly driven by the contributions of the $\gamma^{(*)}p \to \pi^0 p$ channel, whereas the contribution of the channels with charged pions to χ-squared is barely modified. The total χ^2 value is substantially reduced to $\chi^2/dof = 2.7$ with the explicit inclusion of the Δ (Full model fit), still at $O(p^3)$ and even when the Δ coupling constants are previously fixed. A reduction can also be obtained at a more limited energy range without the Δ by doing an $O(p^4)$ calculation [20, 139]. However, apart from requiring a number of extra parameters, in the Δ-less calculations the fit quality diminishes rapidly as a function of the energy.

Removing the Δ mechanisms, we see that, with the current data set, the χ^2_γ for photoproduction is considerably worsened, whereas for electroproduction χ^2_e is little modified, even showing a little improvement. In particular, we have found that Δ inclusion worsens the overestimation for $(d\sigma_T/d\Omega^*_\pi + \varepsilon d\sigma_L/d\Omega^*_\pi)$ in Fig. 5.7. However, it improves the agreement with the other observables of the same figure. This point is relevant, because that observable has the largest, may be excessive, weight in the

χ^2 calculation among the full electroproduction data set, followed by $d\sigma_{TT}/d\Omega_\pi^*$ from the same experiment [95]. This is due to the large number of points and their quoted precision.

Within our model is not possible to reproduce well the full set of data from Ref. [95], neither with nor without Δ. We should remark that similar discrepancies have been found in other Δ-less chiral calculations, both covariant and HBChPT as shown in Refs. [77, 95], even at $O(p^4)$. Barring experimental problems or some underestimation of the uncertainties, these difficulties may point out to the need of a higher order calculation. In fact, this set of data is well reproduced by the phenomenological DMT model [140, 141] which includes explicitly vector mesons, the Δ and several heavier resonances.

In contrast, the Δ contribution, which depends only on well constrained parameters, (h_A and g_M), improves substantially the global agreement with data. It is also noteworthy that most of the fitted d_i LECs have much larger values in the Δ-less fit. This clearly shows the sensitivity of the pion photo- and electroproduction to the Δ resonance even at the low energies investigated. In fact, removing the Δ mechanisms we get a much worse agreement with data. The reshuffling of the free parameters is ineffective in describing the rapid growth of the cross section of the π^0 channel, indicating the need of a more important third order and a slower chiral convergence. The importance of the resonant mechanisms can be also appreciated in Fig. 5.1, where I compare the χ^2 per degree of freedom as a function of the invariant maximum energy, W, of the data included in the fitting procedure.

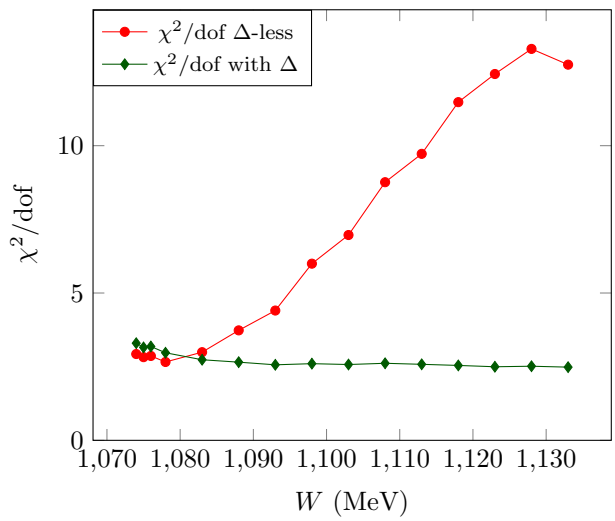

FIGURE 5.1: χ^2/dof as function of the maximum W considered in the fitting procedure. Full model at $\mathcal{O}(p^3)$ with Δ (green diamonds) and without Δ (red circles).

The quality of the agreement decreases rapidly as a function of the maximum W, in the Δ-less case, whereas it is practically stable for the full model. This behavior (rapid growth of χ^2 as a function of energy) can also be seen even for the $O(p^4)$ covariant and HB calculations that do not include the Δ resonance explicitly. See, e.g., Figs. 2 of Refs. [20, 77] and Fig. 1 of Ref. [139] [6].

[6]The two figures from Refs. [20, 139] only consider the π^0 photoproduction channel, whereas Fig. 5.1 includes all the channels and both photo-and electroproduction reactions. Still, the comparison is fair as the χ^2 is basically driven by the π^0 channel and we obtain a similar figure for that restricted case.

It is remarkable that the Δ role in photoproduction is of the utmost importance to reproduce the energy dependence of data. The Δ-less model is unable to describe the energy evolution of the cross sections, mostly in the π^0 channel, even with the inclusion of the $\mathcal{O}(p^3)$ one-loop amplitudes. This failure can be appreciated in Fig. 5.1. The quality of the agreement remains stable for the full model whereas without explicit Δ the χ^2 function grows fast as a function of the energy and it is impossible to describe data at this chiral order.

5.4 Fit analysis with error propagation from the known LECs

This section is meant to analyze the propagation of the errors present in the known LECs of Table 4.5 to the results for the fitted LECs, $\{d_8^r, d_9^r, d_{20}^r, d_{21}^r, d_{22}^r\}$, and the subsequent observable calculations.
Here, we extend the fit of the previous Section 5.3, where the previously known LECs have been fixed to their central values shown in Tab. 4.5, by including their corresponding uncertainties in the fitting procedure and further calculations. As mentioned above in Sec. 5.2.2, we can consider the uncertainties and mean values of the fixed LECs with a Monte Carlo simulation of normally distributed samples. In the following, we briefly detail the fitting procedure within a usual Bootstrap method [137].

(1) In a first step, for each fixed LEC we simulate a sample of $N = 1000$ random values obeying normal distributions such that their mean and 1-σ width correspond to the central and error values. For each $n \in [1, 1000]$ we define the LEC vector

$$c_{[n]} = (\widetilde{c}_{6[n]}, \widetilde{c}_{7[n]}, d^r_{6[n]}, d^r_{7[n]}, d^r_{18[n]}, l^r_{6[n]}). \tag{5.8}$$

We assume that they are uncorrelated from each other as an approximate scenario[7]. The rest of the physical parameters determined with higher accuracy: e, g_A, F_π, M_π, m_N, m_Δ and h_A, were just fixed to their central values [34]. To compare more directly our results with the previous fit, we have also preferred to leave g_M fixed to their best value, given in Tab. 5.1.

(2) Then, we minimize the respective χ-squared function for each n-th LECs vector by taking

$$\chi^2\left(x_{[n]}\right) = \sum_i \left(\frac{\overline{y}_i - \mathcal{O}^{th}\left(a_i, c_{[n]}, x_{[n]}\right)}{\delta y_i} \right)^2, \tag{5.9}$$

where the χ-squared function and the fitting LECs, $x_{[n]}$, are given similarly to Eq. (5.1) and lead to a n-th fitted array

$$x_{[n]} = (d^r_{8[n]}, d^r_{9[n]}, d^r_{20[n]}, d^r_{21[n]}, d^r_{22[n]}). \tag{5.10}$$

[7]Since the underlying processes and the nature of the data constraining the LECs in Tab. 4.5 are not considered, we only take as relevant information the central and error values for the fixed LECs without any correlation. Otherwise, in a more detailed study, we should include their correlations numerically, see Ref. [138].

(3) Finally, after the minimization procedure for each $\chi^2(x_{[n]})$ minimum, one obtains a collection of $N = 1000$ sets of fitted LECs, $x_{[n]}$. As before, we can choose the combination $x_{[n]} = (d_{8[n]}^r + d_{9[n]}^r, d_{8[n]}^r - d_{9[n]}^r, d_{20[n]}^r, d_{21[n]}^r, d_{22[n]}^r)$[8]. Thus, the central and 1-σ error values can be calculated as the mean and normal standard deviation respectively,

$$\bar{x}_j = \sum_{n=1}^{1000} \frac{x_{j[n]}}{n}, \qquad \delta x_j = \left(\sum_{n=1}^{1000} \frac{\left(x_{j[n]} - \bar{x}_j\right)^2}{n} \right)^{1/2}, \tag{5.11}$$

for $x_j \in \{d_8^r + d_9^r, d_8^r - d_9^r, d_{20}^r, d_{21}^r, d_{22}^r\}$ the fitted LECs[9]. This procedure also generates the correlations between the known LECs, $c_{[n]}$ (5.8), and the fitting parameters, $x_{[n]}$, (5.10). To illustrate this, we show in Figure 5.2 the results for the LEC distributions obtained in this approach.

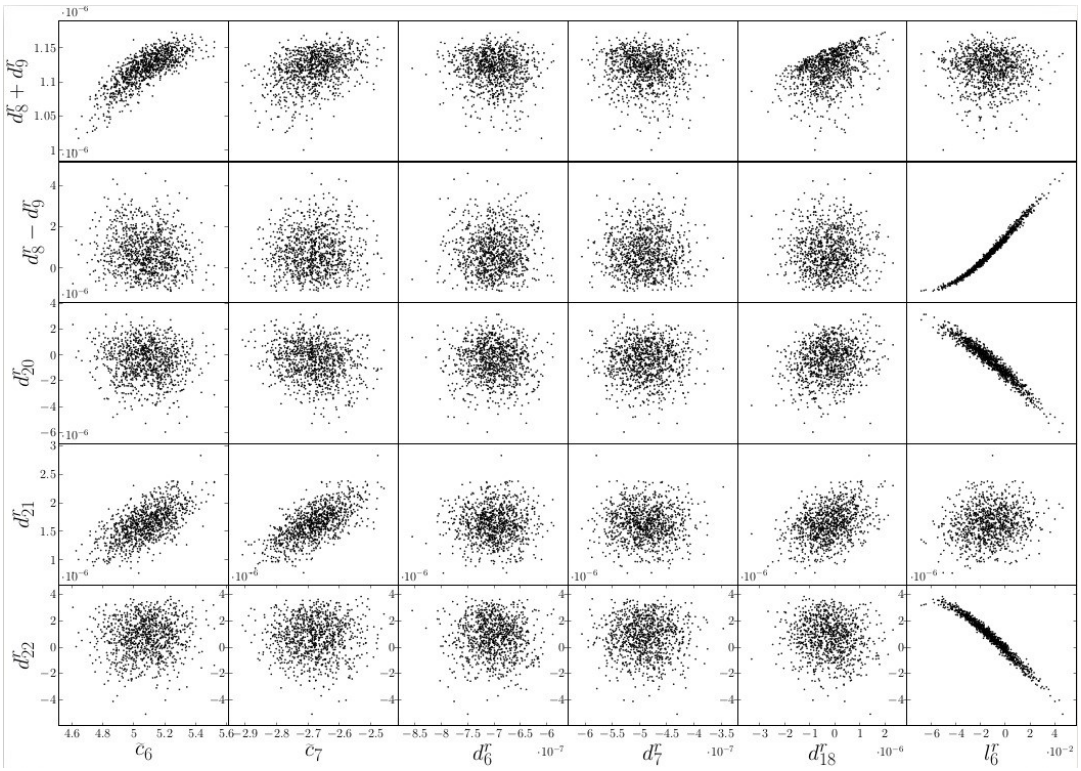

FIGURE 5.2: Two dimensional distributions of the fixed low-energy constants $\{\widetilde{c}_6, \widetilde{c}_7, d_6^r, d_7^r, d_{18}^r, l_6^r\}$ generated via Monte Carlo simulation versus the resulting fitted LECs $\{d_8^r + d_9^r, d_8^r - d_9^r, d_{20}^r, d_{21}^r, d_{22}^r\}$ for $N = 1000$ samples. Each point corresponds to a particular fit where the χ^2 function is minimized.

From the resulting LEC samples $x_{[n]}$ and using Eq. (5.11), we get the values for the fitted LECs corresponding to their means and 1-σ deviations. In Table 5.2, we compare these results to the previous full model fit given in Table 5.1.

[8]They are also Gaussian distributed around the global minimum. This has been confirmed by the corresponding frequency histograms

[9] Even though this procedure generates correlations between the fitted LECs, we do not need to compute their explicit values to estimate the LECs uncertainties, as was the case in Eq. (5.4).

TABLE 5.2: Values of the fitted LECs in the full model. LECs are dimensionless for g_M and in units of GeV^{-2} for d's. Fit I refers to the previous fit from Tab. 5.1. Fit II refers to a new fit taking into account the uncertainties of the previously known LECs, Tab. 4.5. Both of them correspond to the full model including Δ mechanisms.

LECs	Fit-I	Fit-II
$d_8^r + d_9^r$	1.12 ± 0.01	1.12 ± 0.02
$d_8^r - d_9^r$	0.63 ± 0.15	0.64 ± 0.10
d_{20}^r	-0.29 ± 0.09	-0.29 ± 0.31
d_{21}^r	1.64 ± 0.06	1.64 ± 0.27
d_{22}^r	0.95 ± 0.13	0.95 ± 0.23
g_M	2.90 ± 0.01	$\mathbf{2.90 \pm 0.01}$
χ^2/dof	**2.7**	$\mathbf{2.7 \pm 1.1}$

As expected, the mean values of the fitting LECs with the bootstrap method (Fit-II) are in total agreement with those obtained by fixing the non-fitting parameters to their central values (Fit-I). On the other hand, the estimated uncertainties for all cases are somewhat larger than in the basic Fit-I, except for the combination $d_8^r - d_9^r$ which has a smaller uncertainty. [10]

Lastly, the calculation of the physical observables is obtained in a straightforward manner. As before, Eq. (5.9), the evaluation of the LECs in the ChPT amplitudes gives us a corresponding array of n-th values for each physical observable, $\mathcal{O}^{th}(a, c_{[n]}, x_{[n]})$ for any kinematical region $a = \{s, u, Q^2\}$. As they obey similar normal distributions as the input LECs, we can apply the same procedure as before in Eq. (5.11) to estimate the corresponding central and error values within the 1-σ confidence. In fact,

$$\overline{\mathcal{O}}^{th} = \sum_{n=1}^{1000} \frac{\mathcal{O}^{th}(c_{[n]}, x_{[n]})}{n}, \qquad \delta\mathcal{O}^{th} = \left(\sum_{n=1}^{1000} \frac{\left(\mathcal{O}^{th}(c_{[n]}, x_{[n]}) - \overline{\mathcal{O}}^{th}\right)^2}{n} \right)^{1/2} \tag{5.12}$$

The correlations between the LECs, which have to be taken into account when calculating errors in quantities, are already implicit in the low-energy constants arrays $c_{[n]}$ and $x_{[n]}$. Again, in the current scenario, we do not need to calculate neither the correlation matrix nor the variation of the observables over the LECs.

The results for the central values of the physical observables have been compared for the two fitting methods of Tab. 5.2. As we expected from the identical fitted LEC values obtained in both procedures, the central values for all the observables also coincide, showing the consistency between both approaches, with and without bootstrap, and testing the stability of the previous fit without bootstrap presented in Sec. 5.3.

Due to the larger errors of the fitted LECs in the bootstrap fit (Fit-II) as compared to Fit-I, we could expect that the corresponding errors for the observables follow the

[10] The parameter g_M was restricted within the range of the Fit-I due to an strong correlation with $d_8^r + d_9^r$. Otherwise, leaving g_M to move within the range 2.8 - 3.3, another local minimum was found for $d_8^r + d_9^r = 0.76 \pm 0.02\mathrm{GeV}^{-2}$ and $g_M = 3.3 \pm 0.01$ which corresponds to similar normal distributions, but appears less frequently in the random bins.

same proportion. Surprisingly, the error calculations for the pion photo- and electroproduction observables resulted quite similar for both fitting approaches.

In summary, the only differences among the theoretical calculations of observables with Fit-I and Fit-II are those regarding the barely noticeable changes in their corresponding uncertainties. Thus, we can use any of the two fitting approaches to show the observable results when they are compared to data. In the following Section, we show the results obtained directly from the Fit-I, (Full model fit in Tab. 5.1). Excepting only some particular cases for the charged channels where the error bars are larger with the inclusion of the uncertainties from fixed LECs, we will indicate them for each specific case.

It is worth mentioning that all the fitted d_i's from Tabs. 5.1 and 5.2 appear in the calculations of many other processes of interest like in the evaluation of neutrino induced pion production off nucleons. There, our results could be used to improve the corresponding predictions. This is specially important in the current precision era of neutrino physics, where an adequate modeling of cross sections and backgrounds is necessary for the investigation of neutrino masses, mixing angles and other properties [142]. For example, our results give support to the first ChPT calculations of these weak production processes [25,26], which assumed a natural size for these parameters to estimate the uncertainties of the theoretical predictions.

5.5 Results for the physical observables

In this section, I shall present the theoretical results for the $\gamma^{(*)} + N \longrightarrow \pi + N'$ observables obtained with the full theoretical model at $\mathcal{O}(p^3)$ and with Δ mechanisms. The fitted parameters correspond to the "Full model" column of Tab. 5.1. The results are displayed with the respective experimental data. First, I will show the electroproduction results for different invariant c.m. energies, W, c.m. pion angles, θ_π and momentum transfer Q^2, as well as for the virtual-photon polarization, ε, and the reaction plane azimuthal angle, ϕ_π. Finally, the photoproduction results are shown for several laboratory photon energies, E_γ^{lab}, and c.m. pion angles, θ_π.

5.5.1 Electroproduction observables

$\gamma^* + p \longrightarrow \pi^0 + p$ channel

Here, I show our results for the π electroproduction process compared to the experimental data. We start with the $\gamma^* p \to \pi^0 p$ channel, that represents the largest amount of data, in Figs. 5.3−5.7. As it was aforementioned, we have that, among the third order fitted LECs, this channel's amplitude depends only on the $(d_8^r + d_9^r)$ combination that is much constrained by neutral pion photoproduction. Actually, the current fit results for that LEC are fully consistent with a previous determination based just on the analysis of photoproduction [109]. Overall, the agreement with data is good for all the observables considered here.

In Fig. 5.3, we show the virtual photon cross section, $d\sigma_v/d\Omega_\pi^*$, at several energy bins close to threshold, $Q^2 = 0.10$ GeV^2 and for $\varepsilon = 0.67$, compared to the NIKHEF data from Ref. [114]. The angular dependence, on both θ_π and ϕ_π, and the energy dependence are well reproduced.

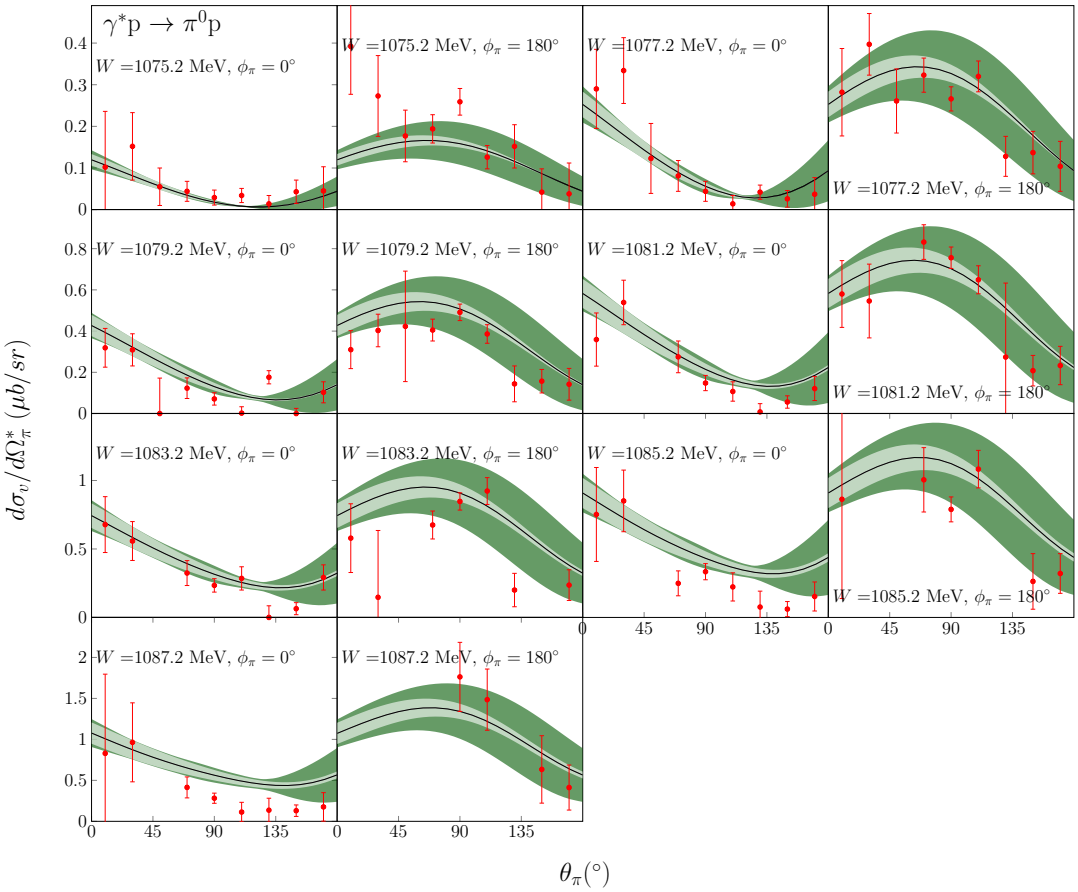

FIGURE 5.3: Angular distribution of the virtual cross section $d\sigma_v/d\Omega^*_\pi$ at different pion angles and for several photon energies. The transfer momentum is $Q^2 = 0.10$ GeV^2, and the virtual-photon polarization $\varepsilon = 0.670$. The solid line shows the theoretical results. The inner band depicts the statistical error, Eqs. (5.4) and (5.5), from the LECs variation within 1-σ given in Table 5.1. The outer band represents the total error including also the systematical error from the chiral truncation, Eq. (5.6), added to the statistical one in quadrature, Eq. (5.7). Data from Ref. [114].

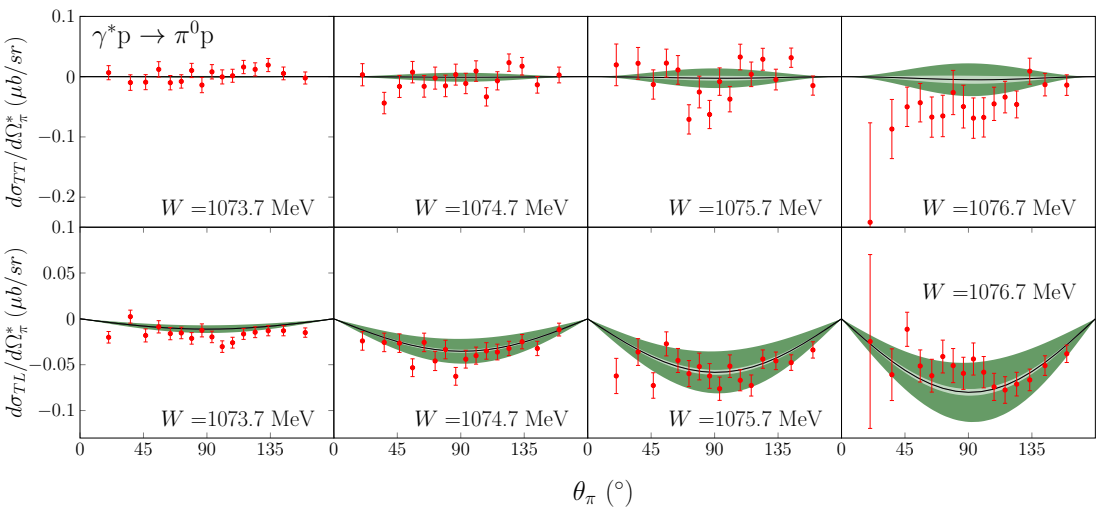

FIGURE 5.4: $d\sigma_{TT}/d\Omega^*_\pi$ and $d\sigma_{TL}/d\Omega^*_\pi$ at several energies as function of the c.m. pion angle θ_π for the $\gamma^* p \to \pi^0 p$ channel. Here, the momentum transfer is $Q^2 = 0.1$ GeV^2 and the virtual-photon polarization $\varepsilon = 0.713$. Data from Ref. [115]. Description of curves and bands as in Fig. 5.3.

The various pieces, related to the longitudinal and transverse responses and their interference, which contribute to the total cross section of Eq. (3.56), are explored next. In Fig. 5.4, we compare the model with the angular dependence of σ_{TT} and σ_{TL} measured by MAMI [115] at several energies very close to threshold. The two observables are very small. Both the size and the energy dependence are well accounted for by our calculation.

Much larger is the observable $d\sigma_T/d\Omega_\pi^* + \varepsilon d\sigma_L/d\Omega_\pi^*$ measured in a more recent MAMI experiment [116]. It is depicted in Fig. 5.5. These latter results show the Q^2 dependence, that at the low energies involved and for the relatively small examined Q^2 values is well described by the model.

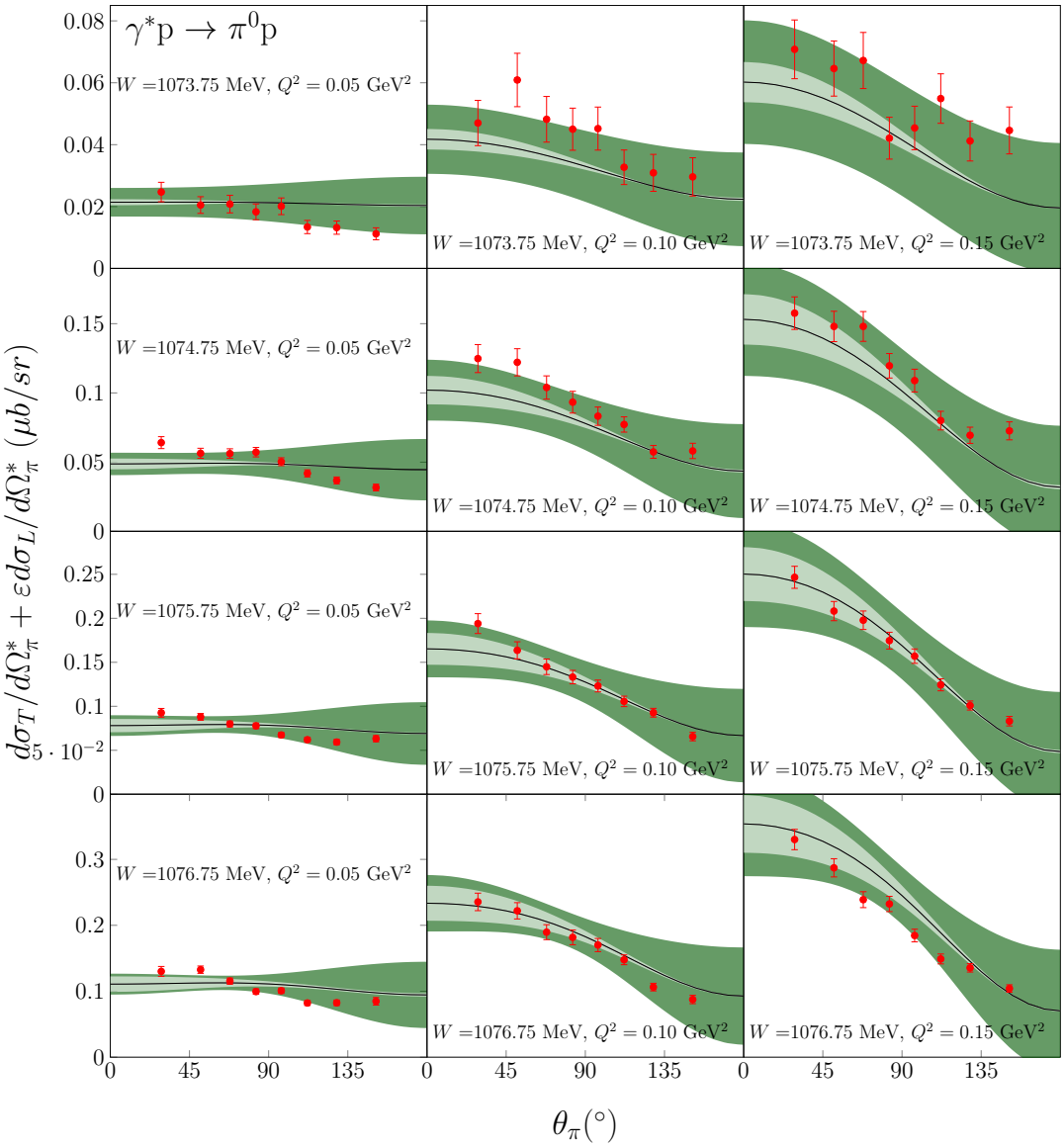

FIGURE 5.5: Angular distribution for $(d\sigma_T/d\Omega_\pi^* + \varepsilon\, d\sigma_L/d\Omega_\pi^*)$ at different c.m. energy values, W. The transfer momenta at $Q^2 = 0.05$ GeV^2 corresponds to polarization values of $\varepsilon = 0.932$, at $Q^2 = 0.10$ GeV^2 to $\varepsilon = 0.882$ and at $Q^2 = 0.15$ GeV^2 to $\varepsilon = 0.829$. Data from Ref. [116] and description as in Fig. 5.3.

The Q^2 dependence is further explored in the $d\sigma_{TL}/d\Omega_\pi^*$ cross section. The results, laid out in Fig. 5.6, also show a good agreement for the angular distribution at several

Q^2 values. We should remark that for neutral pions, apart from the well known fixed LECs, this dependence is only sensitive to $(d_8^r + d_9^r)$ and g_M, which are strongly constrained by the photoproduction ($Q^2 = 0$) data.

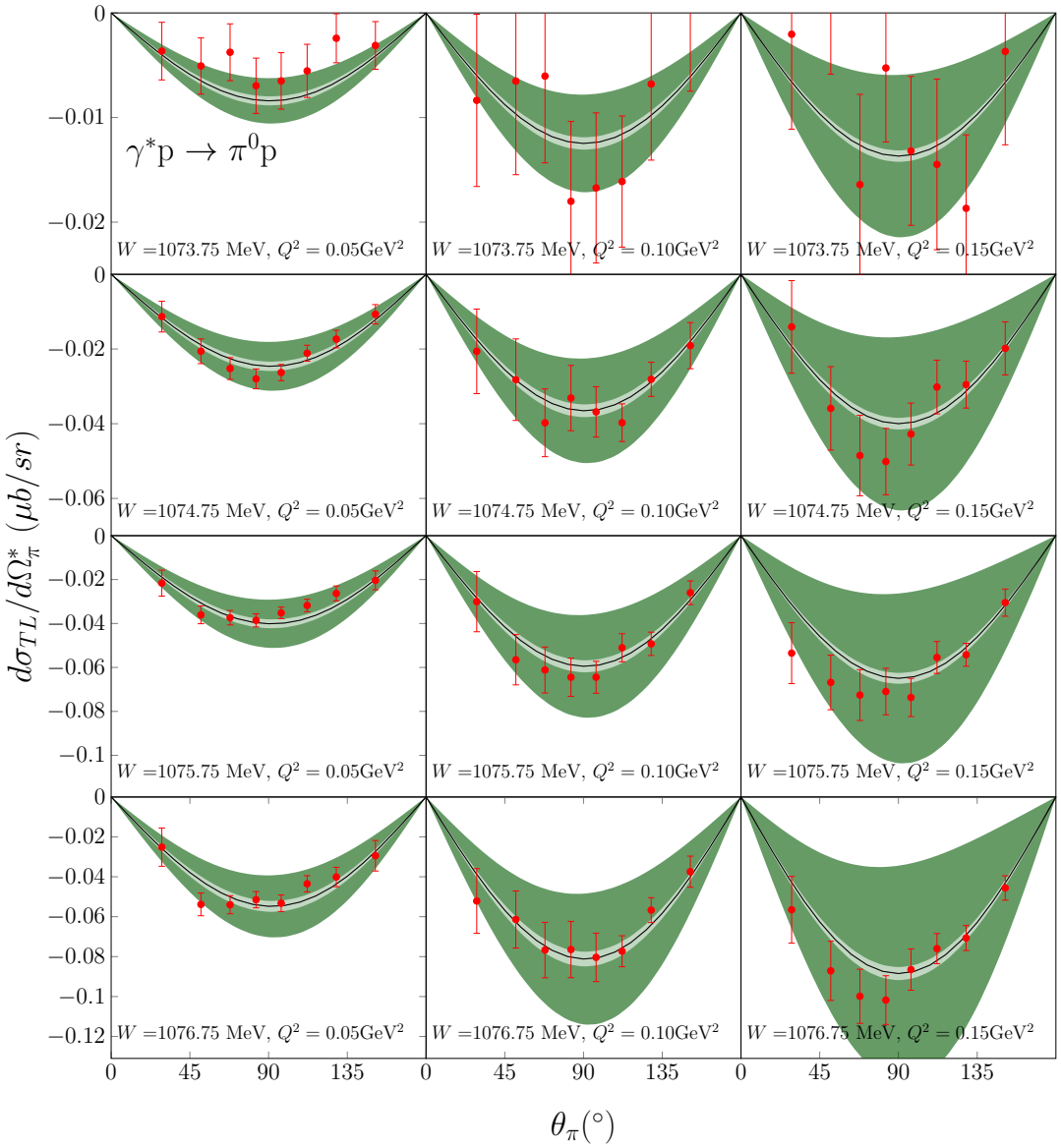

FIGURE 5.6: Angular distribution for $d\sigma_{TL}/d\Omega^*_\pi$ for different c.m. energy values, W. The transfer momenta at $Q^2 = 0.05$ GeV^2 corresponds to polarization values of $\varepsilon = 0.932$, $Q^2 = 0.10$ GeV^2 to $\varepsilon = 0.882$ and $Q^2 = 0.15$ GeV^2 to $\varepsilon = 0.829$. Data from [116] and description of curves and bands as in Fig. 5.3.

Finally, in Fig. 5.7, we compare our calculation with the very copious and precise data the A1 collaboration at MAMI, Ref. [95], where the energy dependence of $d\sigma_T/d\Omega^*_\pi$, $d\sigma_{TT}/d\Omega^*_\pi$, $d\sigma_{TL}/d\Omega^*_\pi$ and $A_{LT'}$ has been investigated at a transfer momentum $Q^2 = 0.05$ GeV^2 and a photon transverse polarization $\varepsilon = 0.933$. For $(d\sigma_T + \varepsilon d\sigma_L)/d\Omega^*_\pi$ and $d\sigma_{TL}/d\Omega^*_\pi$, the calculation agrees well up to a few MeV above threshold, what is consistent with the results shown in Figs. 5.5 and 5.6. However, we overestimate the absolute value of the observables $(d\sigma_T + \varepsilon\, d\sigma_L)/d\Omega^*_\pi$ and $d\sigma_{TT}/d\Omega^*_\pi$ at higher energies. In fact, our fit curve behaves as the HBChPT result of Ref. [143]

discussed in [95]. The agreement with $d\sigma_{TT}/d\Omega_\pi^*$ is good and with $d\sigma_{TL}/d\Omega_\pi^*$ excellent, in both cases improving the HBChPT prediction. In these three cases, the quality of the agreement of our $\mathcal{O}(p^3)$ model is very similar to that of the $\mathcal{O}(p^4)$ Δ-less covariant ChPT calculation of Ref. [77].

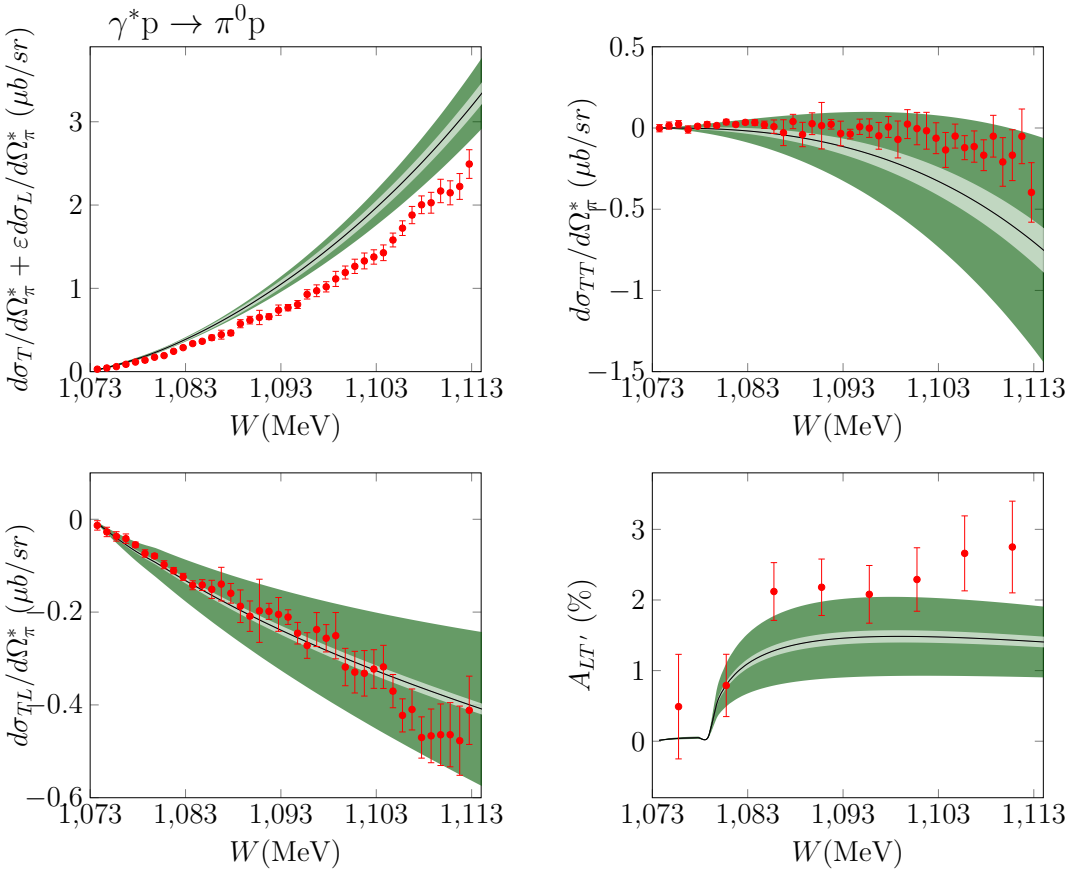

FIGURE 5.7: Energy dependence for $(d\sigma_T + \varepsilon d\sigma_L)/d\Omega_\pi^*$, $d\sigma_{TT}/d\Omega_\pi^*$, $d\sigma_{TL}/d\Omega_\pi^*$ and $A_{LT'}$ at $Q^2 = 0.05$ GeV^2, $\varepsilon = 0.933$, $\theta_\pi = 90°$. Data from [95].

Also well reproduced is the beam helicity asymmetry, $A_{LT'}$, a quite small effect, which shows the cusp related to the $n\pi^+$ threshold. The use of the physical masses in the loops, and the corresponding isospin symmetry breaking is essential for a proper reproduction of this shape.

Summarizing, the theoretical results for the π^0 channel are in accordance with data, describing properly the angular dependence and the Q^2 evolution. In regard to the energy, we obtain the best results very close to threshold. Nonetheless, the model starts to overestimate data for the observable $(d\sigma_T + \varepsilon d\sigma_L)/d\Omega_\pi^*$ at higher energies, see Fig. 5.7. Actually, this observable contributes strongly to the total χ^2. On the other hand, it is very sensitive to $(c_6 + c_7)$, $(2d_7^r + d_6^r)$ and g_M, which were restricted to the values allowed by the study of other processes. In our calculation, the only totally free parameter relevant for this channel has been the combination $(d_8^r + d_9^r)$, strongly constrained by the abundant photoproduction data.

$\gamma^* + p \to \pi^+ + n$ channel

For the channel $\gamma^* p \to \pi^+ n$, we present in Fig. 5.8 the results for $d\sigma_T/d\Omega_\pi^*$, $d\sigma_L/d\Omega_\pi^*$ and $d\sigma_{TL}/d\Omega_\pi^*$ as functions of Q^2 at various pion angles and from several experiments

[117–120] that are also well reproduced.

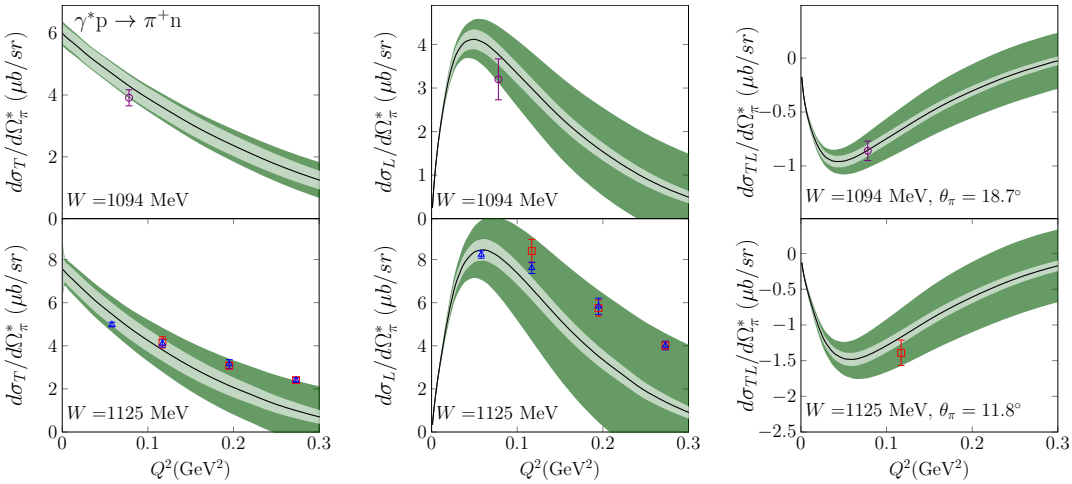

FIGURE 5.8: $d\sigma_T/d\Omega^*_\pi$, $d\sigma_L/d\Omega^*_\pi$ and $d\sigma_{TL}/d\Omega^*_\pi$ as functions of Q^2 for the $\gamma^* p \to \pi^+ n$ process. For $d\sigma_T$ and $d\sigma_L$, the pion angle is $\theta_\pi = 0°$. Magenta circles: data from [120]. Red squares: data from [117, 118]. Blue triangles: data from [119].

This channel depends on the $\mathcal{O}(p^3)$ LECs d^r_9, d^r_{20}, d^r_{21} and d^r_{22}, as well as the $\mathcal{O}(p^4)$ one l^r_6.[11] Thus, there are more fitting LECs than for the neutral pion channel. Furthermore, the data are scarce. For these reasons, there are less constrains on the relevant LECs and the statistical error is considerably wider.
Furthermore, for this electroproduction channel the Q^2 evolution of the cross sections is mostly driven by the LEC l^r_6. For this reason, the statistical errors are the mostly affected by the inclusion of the uncertainty from the fixed LEC $l^r_6 = (-1.34 \pm 0.12) \times 10^{-2}$, see Tab. 4.5. The largest increment in the statistical error is around a factor of 3.9, in absolute values, for $d\sigma_{TL}/d\Omega^*_\pi$ at $W = 1125\,\text{MeV}$ and $Q^2 = 0.117\,\text{GeV}^2$ as seen in Fig. 5.8. Besides, this error estimate for that cross section represents, in this case, a relative error change from 7.5 % to 28.6 %. Hence, the corresponding increased error is still smaller than the systematic error, such as is given by Eq. (5.6).

In summary, it was found that the few and scattered virtual photon cross section data [117, 118] agree well, within errors, with the theoretical model, and that the π^+ channel is more sensitive to the lower orders than to the $\mathcal{O}(p^3)$ contributions.

5.5.2 Photoproduction observables

$\gamma + p \longrightarrow \pi^0 + p$ **channel**

In Figs. 5.9, 5.10, 5.11 and 5.12, we compare the photoproduction results from the full model fit in Tab. 5.1 with data from the π^0 channel. Analogously to electroproduction, the only free third order LEC is the $(d^r_8 + d^r_9)$ combination.
The $\gamma p \to \pi^0 p$ channel is the most richly represented in the database, both in the amount and the precision of data. Thus, the relevant LECs combination $d^r_8 + d^r_9$ is strongly constrained and get a relatively small uncertainty in the fit.

[11] Other $\mathcal{O}(p^4)$ LECs appearing in the tree-level amplitudes for the $\gamma^* p \to \pi^+ n$ channel are l^r_3 and l^r_4. However, they are canceled in the amplitude expansion up to $\mathcal{O}(p^3)$ when, at the same time, we introduce the pion wave function renormalization, $\mathcal{Z}_\pi$, and the pion chiral mass, M, as a function of the pion physical mass, M_π. See App. Sec. 4.2.5 and Sec. 4.3.2.

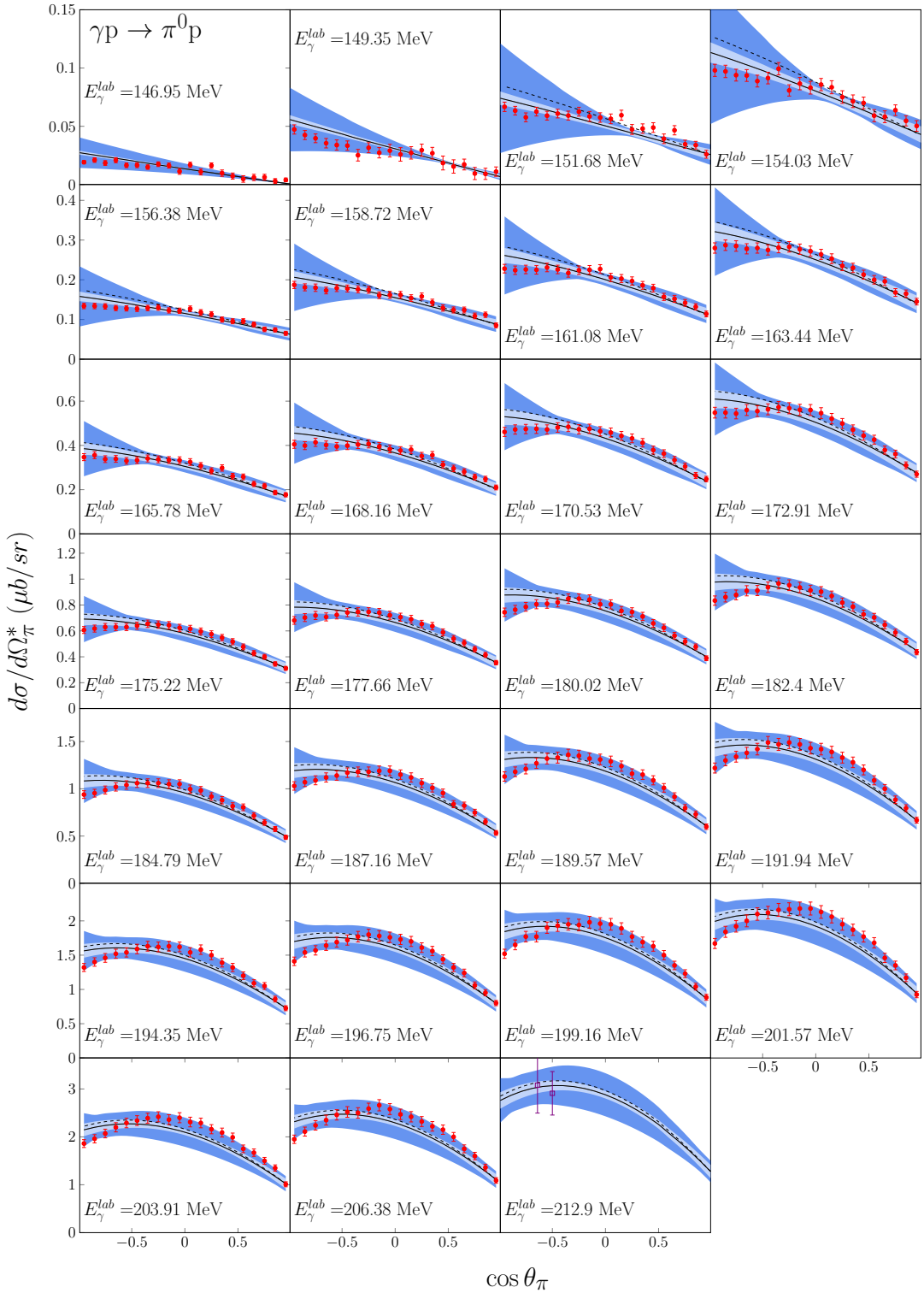

FIGURE 5.9: Angular cross section $d\sigma/d\Omega_\pi^*$ for the $\gamma p \to \pi^0 p$ channel at various energies. Solid line: theoretical model (full model fit from Tab. 5.1). The inner band represents the statistical errors as in Eq. (5.5). The outer band stands for the total errors where the theoretical uncertainties (due to the chiral truncation) are added to the statistical ones in quadrature, Eq. (5.7). Dashed line: results from photoproduction fit [109] in the full isospin symmetric case. Data from Ref. [125] marked as red points and from [126] as violet squares.

In Fig. 5.9, we show the results for the angular distribution of the cross section, $d\sigma/d\Omega_\pi^*$, from the threshold region and in Fig. 5.10 the integrated total cross section σ as function of the photon lab. energy.

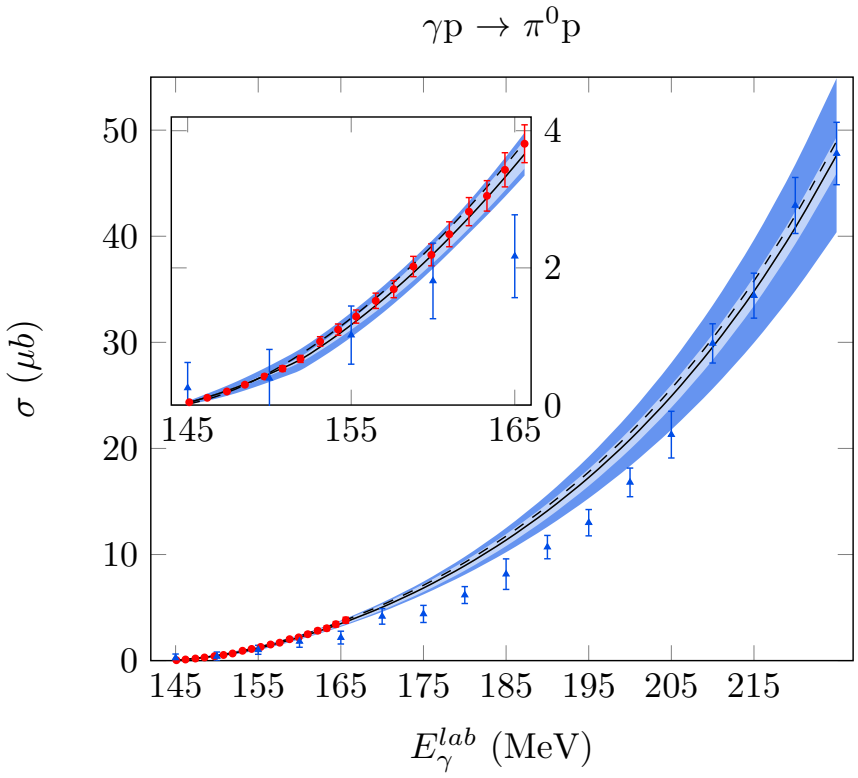

FIGURE 5.10: Cross section as a function of the lab. photon energy E_γ^{lab} for the $\gamma p \to \pi^0 p$ channel. Solid line: theoretical model, red circles: data from Ref. [124], blue triangles: data from Ref. [144], not included in the fit. Description same as Fig. 5.9.

The agreement is overall good for all cross sections in the full range of energies considered. Only the total cross sections from Ref. [144] are systematically below the calculation from 165 to 205 MeV, see Fig. 5.10. However, these data are incompatible with the differential cross sections measured at the same energies in Ref. [125]. Also, there is a slightly overestimation, within the error bands but systematic, of the angular distributions at backward angles. The uncertainties due to the truncation of the chiral expansion are considerable. This fact reflects the large size of the Δ contribution and the $O(p^3)$ mechanisms to this observable.

The use of physical masses in the loop propagators and, therefore, the breaking of the isospin symmetry is the main difference of this calculation with Refs. [22, 109] where only the photoproduction channels have been studied. It leads to a better description of the low energy region, where the effects of the different masses and thresholds are more relevant. Furthermore, in Refs. [22, 109], there was a systematic overestimation of the cross section at backward angles for the $\pi^0 p$ channel at all energies. The breaking of the isospin symmetry in the loops has now much improved the agreement with that cross section. As a consequence, the partial χ^2_γ, considering only photoproduction, has been reduced from 3.2 to 1.7. Also, without isospin breaking, the fit prefers values of d_{18} large and positive, which are inconsistent with πN scattering [14]. Now, the tension is much reduced and the χ^2 depends less strongly on

that parameter.

To compare the differences between the previous studies for the isospin symmetric amplitudes [109] and this latter work, I present both results in Figs. 5.9-5.12. I would like to emphasize that in the previous work from Ref. [109], additionally to the isospin symmetry imposed in the full amplitudes, the results corresponds to a fit with less photoproduction data than in present work. Here, it has been already included in the fit the target asymmetries dataset from [23] and the very close to threshold data below 150 MeV.

Our calculation still preserves the excellent energy dependence results for the beam asymmetry as previously obtained in [109]. We compare the results for this observable in Figure 5.11, where we can see the agreement with data by comparing the central value and the statistical error bands. On the other hand, the systematical errors are overestimated given the larger differences between the $\mathcal{O}(p^2)$ and the next $\mathcal{O}(p^{5/2})$ beam asymmetry calculations, see Eq. (5.6). In other words, the large systematical error is due to the significant contribution of the Δ mechanism in this observable.

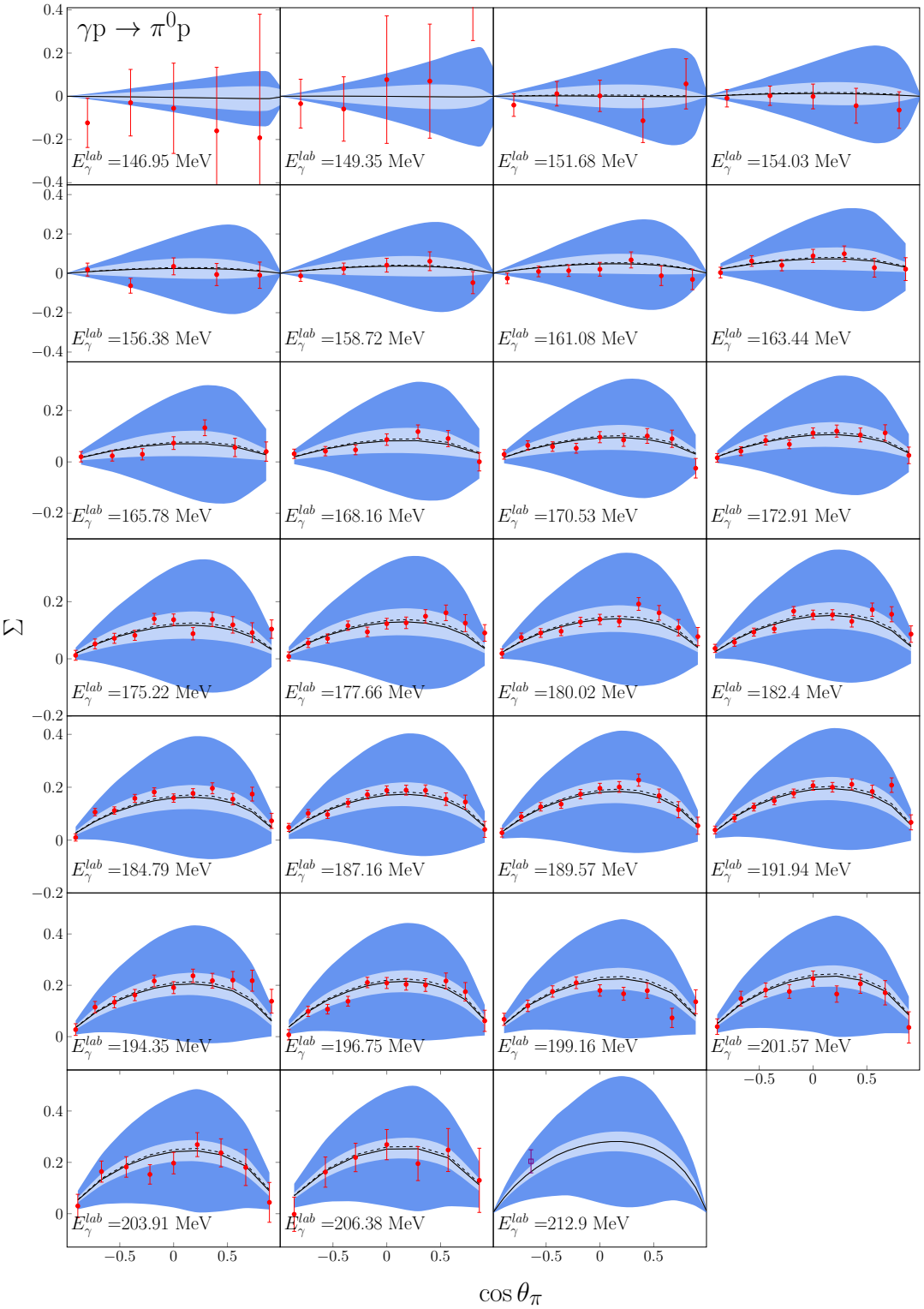

FIGURE 5.11: Beam asymmetry, Σ, for the $\gamma p \to \pi^0 p$ channel at various energies. Data from Ref. [125] marked as red points and from [126] as a violet square. Description same as in Fig. 5.9.

As mentioned before, we have analyzed the data from Ref. [23] studying the process occurring for transversely polarized protons. The observable $T d\sigma/d\Omega^*_\pi$, as in Eq. (3.95), is sensitive to the cusp effects due to the $n\pi^+$ threshold in loops. The

results are shown in Fig. 5.12 for the full range of energies. There is good agreement between T and the present results.

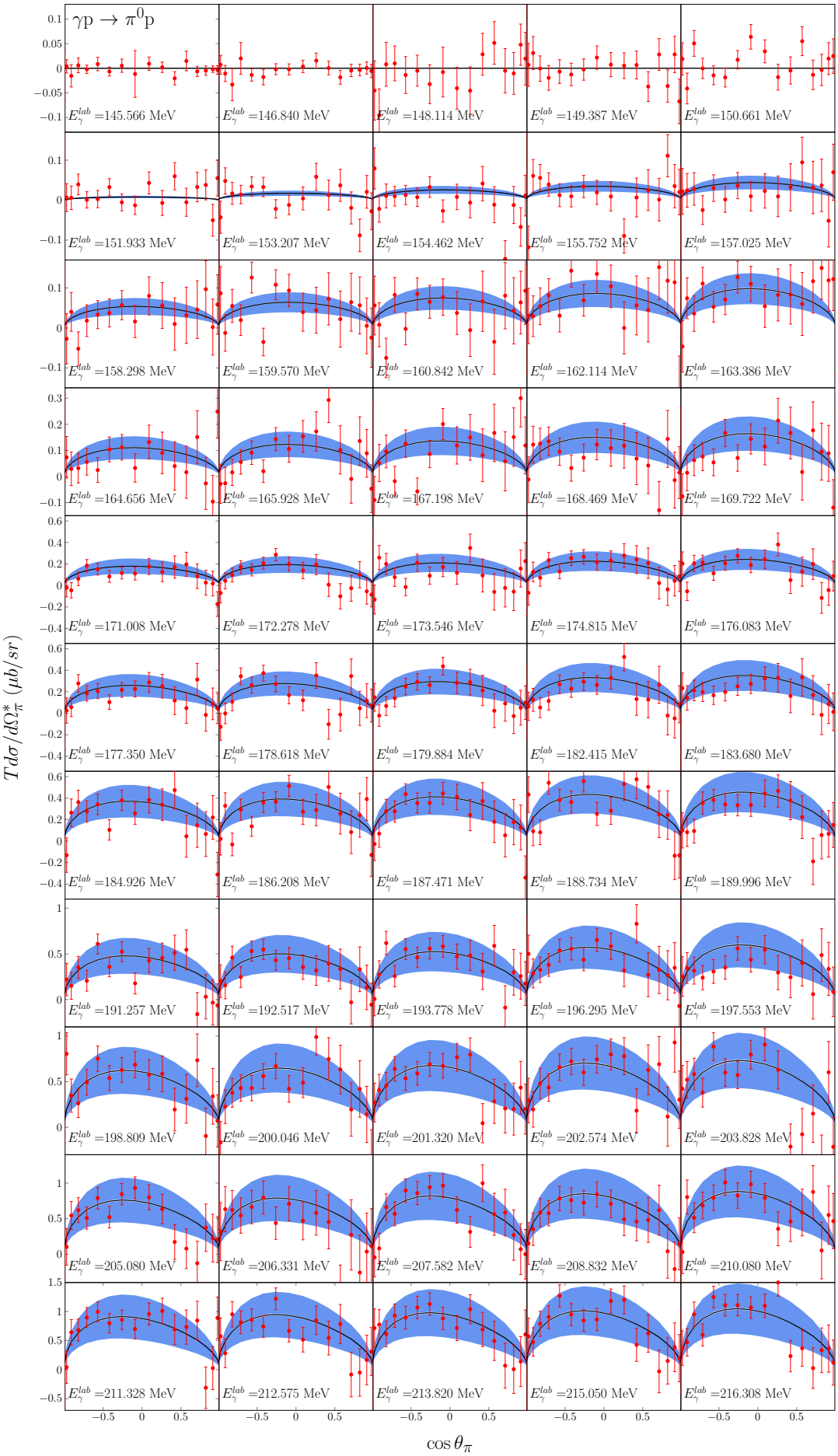

FIGURE 5.12: Angular distribution for the target asymmetry T, reported as the product $Td\sigma/d\Omega_\pi^*$, for the $\gamma p \to \pi^0 p$ channel. Data from [23]. Description same as Fig. 5.9.

$\gamma + p \longrightarrow \pi^+ + n$ channel

The channel $\gamma p \to \pi^+ n$ is sensitive to the LECs d_9^r, d_{20}^r, and the combination $(2d_{21}^r - d_{22}^r)$. As shown in Figs. 5.13, 5.14 and 5.15, the agreement is good for the cross sections, $d\sigma/d\Omega_\pi^*$ and σ, and for the few data available on the beam asymmetry, Σ.

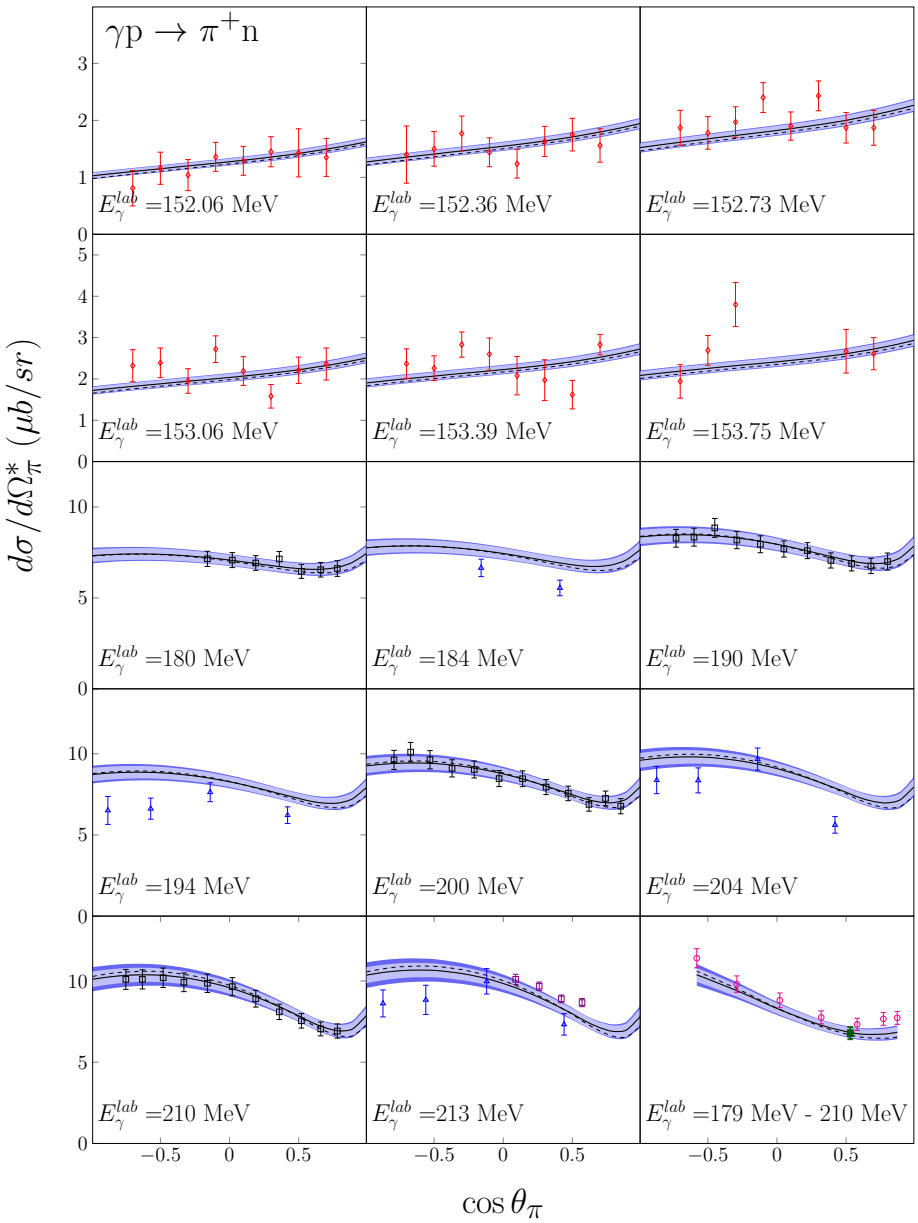

FIGURE 5.13: Angular cross section for the $\gamma p \to \pi^+ n$ channel at various energies. Going from low to high energy, the data from Ref. [145] are marked as red diamonds, [135] as black squares, [134] as blue triangles, [126] as violet squares. Finally, in the lowest right panel, data for different energies from Ref. [133] are marked as magenta circles and from [122] as dark-green squares. In this latter panel the theory has been calculated at precisely the energies and angles of the data points, and the lines and bands have been interpolated. Description same as Fig. 5.9.

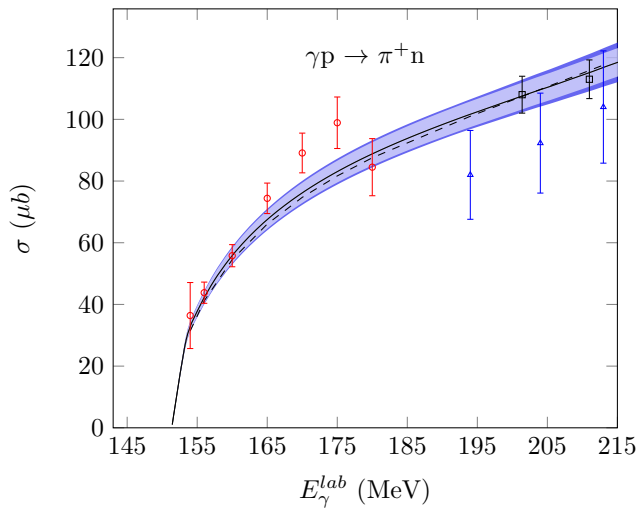

FIGURE 5.14: Cross section for the $\gamma p \to \pi^+ n$ channel at various energies. Data from Ref. [146] presented as red circles. In the same way as in Fig. 5.13, data from [134] as blue triangles and [135] as black squares. Description same as Fig. 5.10.

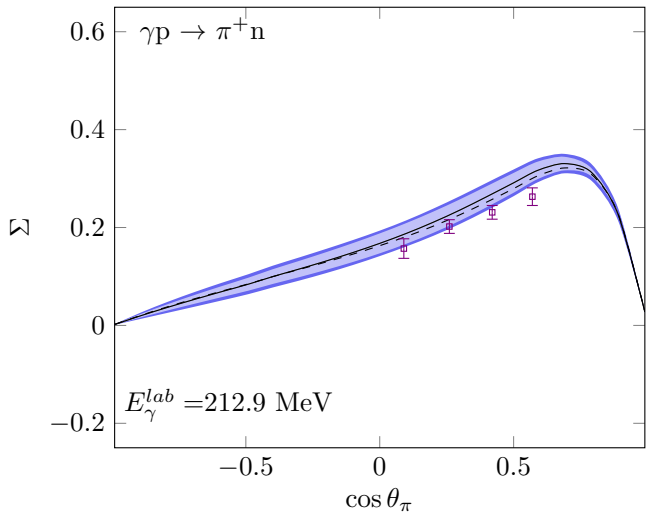

FIGURE 5.15: Beam asymmetry for the $\gamma p \to \pi^+ n$ channel at $E_\gamma^{lab} =$ 212.9 MeV. Data from Ref. [126]. Description same as Fig. 5.9.

As discussed before in Sec. 5.3.1, the combination $(d_8^r + d_9^r)$ is very precisely determined in our fits as compared to the other third order LECs and, in particular, to $(d_8^r - d_9^r)$. Using the correlation matrix and Eq. (5.4) or doing the fit with d_9^r instead, we estimate its individual values and uncertainty as $d_9^r = 0.25 \pm 0.08$ GeV^{-2} for the full model. The separate uncertainty is one order of magnitude larger than for the combination $(d_8^r + d_9^r)$ for the π^0 channel. Similarly to the electroproduction reaction, the propagated error in the observables, together with the errors from d_{20}^r and $(2d_{21}^r - d_{22}^r)$ produce larger statistical errors for all the cross sections. On the other hand, the systematical errors due to the chiral truncation are far smaller than the π^0 channel results which indicate the low dependence from the higher chiral orders.

$\gamma + n \longrightarrow \pi^- + p$ channel

The model also agrees well with the $\gamma n \to \pi^- p$ data as shown in Figs. 5.16 for $d\sigma/d\Omega^*_\pi$ and 5.17 for σ. This channel depends on the same third order LECs as the previous one. The measurements in this channel are scarce and the uncertainties are relatively large. However, it gets a larger contribution to χ^2 than the π^+ channel. This may come from some underestimation of the published experimental uncertainties. Actually, most of the contribution of this channel to the χ^2 function comes from regions with conflicting and incompatible measurements, such as the angular distribution at forward angles at $E_\gamma^{lab} = 211$ MeV (see Fig. 5.16). The accordance for the integrated cross section σ is still good for all the data up to $E_\gamma^{lab} = 215$ MeV, particularly from the most recent data results very close to threshold from Ref. [24], displayed in Fig. 5.17.

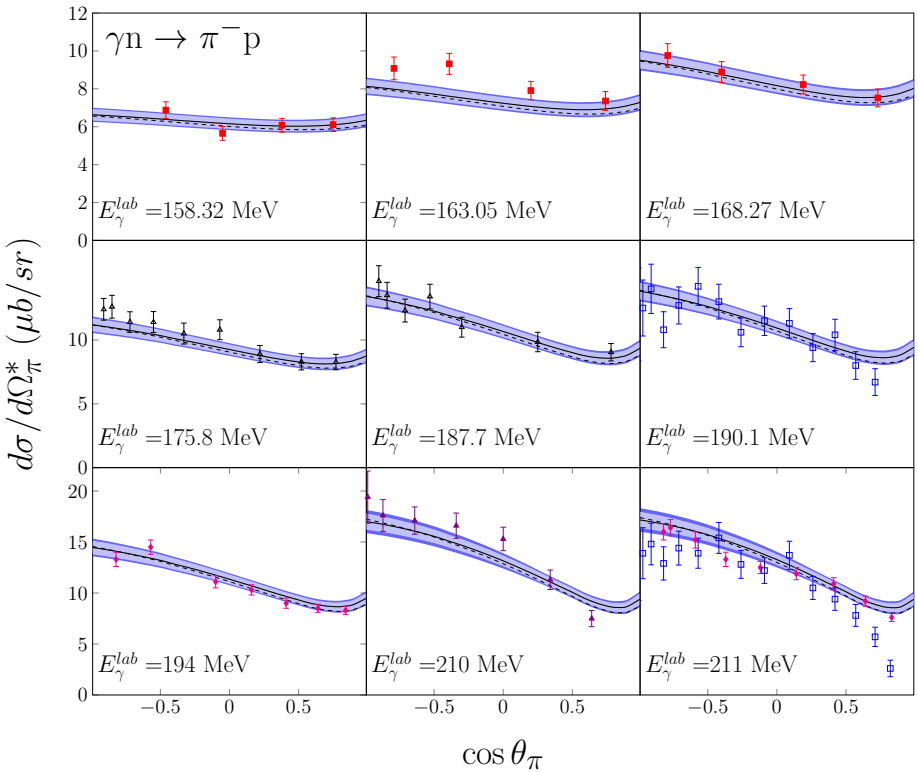

FIGURE 5.16: Angular cross section for the $\gamma n \to \pi^- p$ channel at various energies. Data from Ref. [147] are presented as red filled squares, [129] marked as black triangles, [127] as blue squares (corresponding to lab. frame energy of E_γ^{lab} =211.4 MeV in the lower-right plot), [128] as violet filled triangles and data from [130] as magenta filled diamonds. Description same as Fig. 5.10.

The quality of the agreement with the channels with charged pions has also improved upon the past photoproduction studies of Ref. [109], as can be seen comparing the partial χ^2_γ's. We would like to emphasize that the recent data for the $\gamma n \to \pi^- p$ process [24] have considerably enriched the database for this channel and therefore lead to a better determination of the LECs relevant for it, d^r_9, d^r_{20} and the combination $(2d^r_{21} - d^r_{22})$.

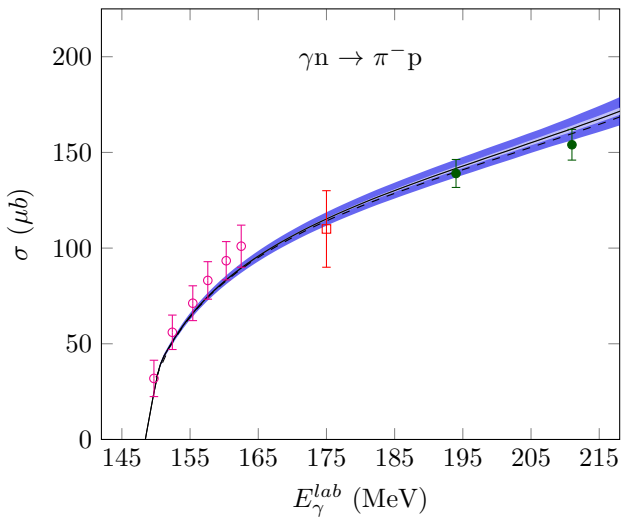

FIGURE 5.17: Cross section for the $\gamma n \rightarrow \pi^- p$ process. Data from [24] in magenta circles; red square, data from [148] and green dots, data from [149] (not included in the fit). Description same as Fig. 5.9.

Finally, the effect of the fixed LECs deviation from Tab. 4.5 has only increased a little the statistical uncertainties for the channel, $\gamma n \longrightarrow \pi^- p$. The maximum statistical error increment has been produced for the highest photon energy studied at $E_\gamma^{lab} = 211.4$ MeV for the differential cross section $d\sigma/d\Omega_\pi^*$. In particular, the inclusion of deviations from the LECs in Tab. 4.5 increase the statistical error by a factor 2.8 respect to the one obtained from Eq. 5.4. Although this change may be apparently big, the relative error respect to the mean value is only around 14%.
The results for the mean values of the observables were in all cases coincident to those obtained with central values of the LECs.

Chapter 6

Near threshold neutral pion photoproduction off the ^{12}C nucleus

6.1 Introduction

In the previous Chapter we presented the results for the study on the pion EM production on nucleons, where the numerical results for the relevant $\mathcal{O}(p^3)$ LECs in the ChPT Lagrangian have been shown. We have also established the relevance of the explicit inclusion of the Δ resonance. In this Chapter, we treat a complementary study on the near threshold π^0 photoproduction off the ^{12}C nucleus whose quite precise experimental data are of interest to further test the results obtained within the ChPT framework.

While there are only scarce data on the nuclear photoproduction of charged pions at low energies, see Refs. [134,150,151], the situation is different for the neutral pions. In this case, there has been a considerable experimental effort leading to very precise data [152–160], and also some theoretical studies [161–165]. There are several reasons for this situation, starting from the relatively high detection thresholds for charged pions. In the following, we will discuss mostly the theoretical considerations that make the neutral channel specially interesting.

From the elementary point of view, it was known that the threshold neutral pion photoproduction off the nucleon is one of the finest reactions to test the chiral QCD dynamics. In fact, one of the early achievements of BChPT was the discovery of the importance of the loop contributions for the π^0 channels [21, 64, 166]. On the other hand, for the theoretical study of pion photoproduction on complex nuclei, one must consider some issues related to the nuclear medium dynamics like pion distortion due to final state interactions, and nuclear structure. A full fledged investigation of the nuclear effects in the process is out of the scope of this work. Nonetheless, our study incorporates those medium effects with a similar level of sophistication to the available literature while improving the theoretical description of the elementary amplitude.

In particular, the pion photoproduction off ^{12}C reaction has been often studied using the Δ-hole model [167–169], which describes both the photoproduction process and the pion distortion assuming full Δ dominance. However, this model has limited success near threshold, so one often relies on the conventional plane wave impulse approximation (PWIA) or the distorted wave impulse approximation (DWIA) instead. See, *e.g.*, Refs. [155, 161, 170]. In both of them, one expresses the amplitude for the nuclear process in terms of the elementary one (on nucleons), but we must still account for the same subjects including Fermi motion, the nuclear structure and, in the case of DWIA, also pion distortion. However, in nuclei like ^{12}C, some of these difficulties can

be resolved by using information from other experimental studies. For example, pion distortion can be described in the DWIA by an optical potential deduced from pion nucleus scattering experiments, while the necessary nuclear structure information can be adopted directly from electron scattering form factors. Also, in a spin zero target nucleus such as ^{12}C, the elementary π photoproduction operator assumes a particularly simple form at low energy, which somehow eliminates the problem of Fermi motion. By taking these factors into account, we can straightforwardly deduce the nuclear photoproduction amplitudes from the corresponding free nucleon amplitudes and compare the results with the $^{12}\mathrm{C}(\gamma,\pi^0)$ cross section data.

In the context of ChPT, early results obtained for the π^0 photoproduction on the proton in HBChPT [171] have been later contrasted in the experimental analysis of pion photoproduction off ^{12}C in Ref. [157]. The theoretical calculations obtained a reasonable description of the experimental data but predicted a substantially slower rate of increase above threshold than observed.

Here, we will present a calculation for the nuclear reaction where we apply our results from the pion EM production on nucleons in our fully covariant ChPT approach. Then, we compare the predictions from the studied models with and without explicit Δ resonance with the $^{12}\mathrm{C}(\gamma,\pi^0)$ cross section data. Moreover, the high quality of the existing nuclear data could provide a stringent test for the theoretical model developed for the elementary process in ChPT and their parameters.

As studied previously, close to threshold the neutral pion photoproduction on nucleons ($\gamma+N\to\pi^0+N$) is highly dominated by the resonant $\Delta(1232)$, in contrast to the photoproduction of charged pions which are mainly governed by purely nucleonic Born terms, see diagrams of Fig. 4.1. Additionally, the near threshold survival of low energy pions is expected to be larger than in the Δ resonance region, due to the larger mean free path through the nucleus and thereby reducing the influence of final state interactions. Hence, the meson production near threshold could provide an interesting field to investigate in medium production, decay and propagation of the $\Delta(1232)$ resonance at its low energy tail.

An additional issue concerns to the fact that the $^{12}\mathrm{C}(\gamma,\pi^0)$ reaction can occur through coherent and incoherent (inelastic) transitions. The resonant production amplitude is of special importance for the coherent pion production from even-even nuclei, where the nucleus is left in its ground state such that the initial and final states of the nucleus are the same. In detail, the spin independent part of the amplitude for the elementary process of all nucleons adds up coherently, leading to an A^2 scaling of the cross section.

Besides the coherent process, π^0 photoproduction can also occur through an incoherent transition leaving the final nucleus in an excited state. These incoherent π production processes contribute to a vast part of the total cross section, especially in the resonance region. However, their inclusion for photon energies below 200 MeV has been studied in detail and could be relatively small. Experimentally, the incoherent part has been discriminated though quite crudely from the elastic coherent part by [152][1]. This stimulated theoretical studies to determine the strength of the incoherent production, see Ref. [168].

In the following, we detail briefly the theoretical formalism for the pion photoproduction off nuclei cross section within the DWIA approach. Then, we treat the calculation of elementary amplitudes in the context of the PWIA for both the coherent and the incoherent contributions. The extension of the nuclear cross section model to

[1]They used an active ^{12}C target where some energetic final particles can be detected, but could not separate from the coherent production the cases where the nuclear excitation energy was small.

the DWIA is considered by the inclusion of the final state interaction of the pion with the nuclear medium.

To obtain an estimate of the measured $^{12}\mathrm{C}(\gamma,\pi^0)$ cross section from the ChPT amplitudes, we adopt the DWIA method while considering the coherent part and the incoherent contribution where the final nucleus is in the first excited state, $J^P = 2^+$ (4.43 MeV). Finally we compare our theoretical predictions to the nuclear experimental data in [157] up to photon energies ~ 40 MeV above the threshold.

6.2 Formalism for pion photoproduction off nuclei

We closely follow the arguments presented in Refs. [155, 157, 161]. We detail here the construction of the model to describe the cross section for $\gamma + {}^{12}\mathrm{C} \to \pi^0 + {}^{12}\mathrm{C}$ at low energies. The model is founded on the usual impulse approximation in which free nucleon amplitudes describe the photoproduction from each bound nucleon. The model then evolves to incorporate the ^{12}C nucleus structure in a simple PWIA, assuming that photons and pions propagate in plane waves through a transparent nuclear medium, takes care of the transformation from the πN to the πA frame, and of the Fermi motion of the nucleons, all in various degrees of approximation. This approach is further extended with the DWIA by the consideration of the interaction of the outgoing pion particle through the nuclear medium.

Here we consider the pion photoproduction process on a nucleus A given by

$$\gamma(k) + A(P_A) \longrightarrow \pi^0(q) + A(P'_A). \tag{6.1}$$

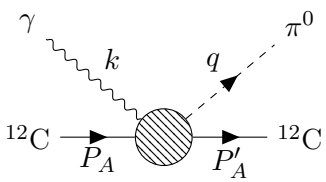

FIGURE 6.1: Diagram representation of the $^{12}\mathrm{C}(\gamma,\pi^0)$ process with k, q, P_A and P'_A the corresponding 4-momenta in the c.m. frame.

We use here the c.m. mass frame of the π-A system for the external 4-momenta, as depicted in Fig. 6.1. With the invariant energy of the πA system, W_A, defined by the Mandelstam variable $s = W_A^2 = (P_A + k)^2 = (P'_A + q)^2$, the 4-momenta in the π-A c.m. defined by $\vec{P}_A{}' = -\vec{q}$ are written as

$$|\vec{k}| = E_\gamma = \frac{1}{2W_A}\left(W_A^2 - m_A^2\right), \tag{6.2}$$

$$|\vec{q}| = \sqrt{E_\pi^2 - M_\pi^2}, \qquad E_\pi = \frac{1}{2W_A}\left(W_A^2 + M_\pi^2 - m_A^2\right), \tag{6.3}$$

$$|\vec{P}_A| = \sqrt{E_A^2 - m_A^2}, \qquad E_A = \frac{1}{2W_A}\left(W_A^2 + m_A^2\right), \tag{6.4}$$

$$|\vec{P}_A{}'| = \sqrt{E_{A'}^2 - m_A^2}, \qquad E_{A'} = \frac{1}{2W_A}\left(W_A^2 + m_A^2 - M_\pi^2\right), \tag{6.5}$$

with the conservation of four momenta $P_A + k = P_A{}' + q$ and the on-shell conditions $P_A^2 = P_A{}'^2 = m_A^2$, $q^2 = M_\pi^2$ and $k^2 = 0$.

Similarly to the single pion photoproduction on nucleons[2], the differential cross section for the nuclear process (6.1) in the π-A c.m. frame is given by

$$\frac{d\sigma}{d\Omega_\pi} = \frac{|\vec{q}|}{|\vec{k}|}\frac{1}{2(2J_i+1)}\sum_{\lambda M_i M_f}\left|\left\langle f\left|F^{(\lambda)}_{\pi\gamma}\right|i\right\rangle\right|^2. \tag{6.6}$$

Nuclear transition amplitudes $F^{(\lambda)}_{\pi\gamma}$ describe the transitions from the initial $|i\rangle = |J_i M_i\rangle$ to the final $|f\rangle = |J_f M_f\rangle$ nucleus states with total angular momenta $J_{i(f)}$ and projection $M_{i(f)}$, $\lambda = \pm 1$ is the photon polarization.

To approach the nuclear amplitude we follow the PWIA that relies on the *impulse approximation* and on the assumption that incident (photon) and outgoing (pion) particles do not interact with the nuclear medium and thus they propagate as free plane waves. In the *impulse approximation* one assumes that the interaction with the bound nucleons has the same form as with free ones, and that the amplitude for the nuclear process can be reduced to A independent elementary amplitudes (being A the number of bound nucleons). Further approximations on the Fermi motion are included for the amplitude transformation from the π-nucleus to the π-nucleon frames. A detailed treatment of those issues can be found in [161] and references therein.

This approach is further extended with the incorporation of the pion interaction with the nuclear medium in the DWIA. For our energy range, we consider the conventional DWIA treatment [155, 161] by including in the amplitude the pion distortion or final state interaction (FSI) effects as outlined below. In the momentum space coordinates the transition operator is given by the standard Lippman-Schwinger equation [155, 172],

$$F^{(\lambda)}_{\pi\gamma}(q,k) = V_{\pi\gamma}(q,k;\lambda) + D_{\pi\gamma}(q,k;\lambda), \tag{6.7}$$

where the first term $V_{\pi\gamma}(q,k;\lambda)$ corresponds to the plane wave part of the amplitude (PWIA). The second term, $D_{\pi\gamma}(q,k;\lambda)$, considers the interaction of the pion with the nucleus in the final state through the pion nucleus elastic scattering amplitude $F_{\pi\pi}$,

$$D_{\pi\gamma}(\vec{q},\vec{k};\lambda) = -\frac{a}{(2\pi)^2}\int\frac{d^3q'}{m(q)}\frac{F_{\pi\pi}(\vec{q}\,',\vec{q})V_{\pi\gamma}(\vec{q}\,',\vec{k};\lambda)}{W_A(\vec{q}) - W_A(\vec{q}\,') + i\varepsilon}, \tag{6.8}$$

where $m(q) = E_\pi(q)E_A(q)/W_A(q)$ is the relativistic reduced mass of the pion-nucleus system, $W_A(q) = E_\pi(q) + E'_A(q)$ is the π-nucleus invariant energy as in Eqs. (6.2)-(6.5). The factor $a = (A-1)/A$ eliminates the double counting in the re-scattering of pion on the nucleon and replaces A by $A-1$. The function $F_{\pi\pi}$ is constructed in the same fashion, as a solution of the Lippmann-Schwinger integral equation with an optical potential, [163, 173, 174]. Eq. (6.8) represents the expression in DWIA dealing with the pion wave distortion through its re-scattering with the nuclear medium.

6.2.1 Matrix elements and elementary amplitudes

First, we introduce the plane wave part $V^{(\lambda)}_{\pi\gamma}$ of the nuclear amplitude in (6.7), which also serves in the distorted wave calculation (6.8). Within the PWIA, it can be expressed in terms of the $\mathcal{T}$-matrix for pion photoproduction from nucleons as

[2]The cross section is given in the same form and conventions as the elementary cross section with nucleons in Eq. (3.87).

$$V_{\pi\gamma} = \sum_{j=1}^{A} \frac{m_N}{4\pi W_N} \left\langle p'_j; q \left| \mathcal{T}_j \right| p_j; k \right\rangle , \tag{6.9}$$

being $\mathcal{T}_j$ the amplitude of the elementary reaction $\gamma(k) + N(p_j) \to \pi^0(q) + N(p'_j)$ as evaluated in Eq. (3.60). W_N is the πN invariant energy. The index j runs over the number of the A bound nucleons, N, with initial(final) momentum $p_j(p'_j)$ and mass m_N, k and q are the photon and pion momenta [3]. In terms of the CGLN amplitude $\mathcal{F}$ (3.21), the matrix element (6.9) is reduced as

$$\frac{m_N}{4\pi W_N} \left\langle p'_j; q \left| \mathcal{T}_j \right| p_j; k \right\rangle = e^{i\vec{Q}\cdot\vec{r}_j} \mathcal{F}(\vec{k}, \vec{q}, \vec{p}_j\,'; \lambda), \tag{6.10}$$

where $\vec{Q} = \vec{k} - \vec{q}$ is the plane-wave momentum transfer to the nucleus [4]. As indicated before in Eq. (3.81), $\mathcal{F}$ corresponds to the elementary amplitude process (on the nucleon) written as

$$\mathcal{F} = i\,\vec{\sigma}\cdot\vec{\epsilon}_\lambda\,\mathcal{F}_1 + \vec{\sigma}\cdot\hat{q}\,\vec{\sigma}\cdot\hat{k}\times\vec{\epsilon}_\lambda\,\mathcal{F}_2 + i\,\vec{\sigma}\cdot\hat{k}\,\hat{q}\cdot\vec{\epsilon}_\lambda\,\mathcal{F}_3 + i\,\vec{\sigma}\cdot\hat{q}\,\hat{q}\cdot\vec{\epsilon}_\lambda\,\mathcal{F}_4, \tag{6.11}$$

with $\vec{\sigma} = (\sigma_1, \sigma_2, \sigma_3)$ the spin-1/2 Pauli matrices, $\hat{k}$, $\hat{q}$ the unitary 3-momentum for the initial photon and final pion respectively, and $\vec{\varepsilon}_\lambda$ the photon polarization vector. In the analysis of the nuclear amplitude is convenient to rearrange the different contributions as[5]

$$\mathcal{F} = i\vec{\sigma}\cdot\vec{K} + L\,, \qquad \text{with } \; L = \hat{q}\times\hat{k}\cdot\vec{\epsilon}_\lambda\,\mathcal{F}_2. \tag{6.12}$$

$\vec{\sigma}\cdot\vec{K}$ is the spin-flip (SF) part and the non-spin-flip (NSF) term is L.

In a spin saturated nucleus such as ^{12}C with equal proton and neutron numbers, only the spin independent term L can contribute in the sum over all the j-th elementary amplitude pieces of Eq. (6.9). Thus, the nuclear matrix element in (6.6) for the $^{12}C(\gamma, \pi^0)$ reduces to

$$\langle f \left| V_{\pi\gamma} \right| i \rangle = A \left\langle J_f M_f \left| e^{i\vec{Q}\cdot\vec{r}} L^{(+)} \right| J_i M_i \right\rangle , \tag{6.13}$$

being $\vec{r} = \{\vec{r}_1, \vec{r}_2, \ldots, \vec{r}_A\}$ the coordinates for each of the A=12 nucleons[6]. Given the isoscalar nature of the nucleus, the process is only sensitive to the isovector even part of L, $L^{(+)}$, given by

$$L^{(+)} = \frac{1}{2}\left(L^{(p)} + L^{(n)}\right) \tag{6.14}$$

where $L^{(p)}$ and $L^{(n)}$ are the amplitudes for the π^0 photoproduction on the proton and

[3]Note that all the nucleon, pion and photon momenta $\{p_j, p'_j, q, k\}$ are now defined in the πA frame. The boost transformation to the π-N c.m. frame is explained later.

[4]The complicated momentum dependence of the elementary amplitude in the nuclear frame is avoided by assuming several impulse approximations [161]. Among them, $p_j^0 = p'^0_j \approx m_N$.

[5]By using the identity $\vec{\sigma}\cdot\hat{q}\,\vec{\sigma}\cdot\hat{k}\times\vec{\epsilon} = \hat{q}\times\hat{k}\cdot\vec{\epsilon} + i\vec{\sigma}\cdot\left(\hat{k}\,\vec{\varepsilon}\cdot\hat{k} - \vec{\varepsilon}\,\hat{k}\cdot\hat{q}\right)$.

[6]Notice that in this approximation the position of the created pion is the same as that of the corresponding nucleon.

neutron respectively.
At this stage, from Eq. (6.10) all quantities appearing here are defined in the πA frame. As indicated in Chapter 4, the elementary photoproduction amplitude $\mathcal{F}$ is well known in ChPT at $\mathcal{O}(p^3)$ (see App. A) and can be easily evaluated in the πN frame, Eq. (3.28). However, we are now interested in the calculation of the corresponding amplitude in the πA frame. The relevant amplitude piece can be expressed in terms of the πN frame variables as

$$L(\vec{k},\vec{q}) = \mathcal{F}_2(\vec{k},\vec{q})\hat{q}\times\hat{k}\cdot\vec{\epsilon}_\lambda = \mathcal{W}_A\mathcal{F}_2(\vec{k}^*,\vec{q}^*)\hat{q}^*\times\hat{k}^*\cdot\vec{\epsilon}_\lambda. \tag{6.15}$$

The photon and pion momenta in the πN c.m. frame are denoted by k^* and q^* respectively. At low energies [155],

$$\mathcal{W}_A = \frac{W_N}{m_N}\frac{m_A}{W_A} \approx \frac{m_N+E_\gamma}{m_N+E_\gamma/A} \tag{6.16}$$

corresponds to the transformation factor which is necessary due to the convention of absorbing the phase space factor $m_N/4\pi W_N$ in the definition of the amplitude $\mathcal{F}$.

When passing the elementary amplitudes and momenta from the πN frame to the πA frame, the transformation for nucleon momenta cannot be decoupled from the consideration of the Fermi motion, *i.e.*, the dependence of the amplitudes on the bound nucleon's momentum in the nucleus frame. A good approximation to a proper averaging of the Fermi motion is the *factorization approximation* which assumes that $\vec{p}_i = -\vec{p}_f$ for the initial and final nucleon momenta in the nucleus rest frame. Then, together with the impulse approximation (spectator nucleons) $\vec{p}\,' = \vec{p}+\vec{Q}$ in the πA c.m. frame, the "effective" initial and final nucleon momenta are [175–178]

$$\vec{p}_j = -\frac{\vec{k}}{A} - \frac{A-1}{2A}\vec{Q}, \qquad \vec{p'}_j = -\frac{\vec{k}}{A} + \frac{A-1}{2A}\vec{Q}. \tag{6.17}$$

For further details see Ref. [155]. From there, the momenta transformation from πA to the πN frame in (6.15) is decoupled from Fermi motion and simplified as[7]

$$\vec{k^*}\times\vec{q^*} \approx \frac{1}{\mathcal{W}_A}\vec{q}\times\vec{k}. \tag{6.18}$$

On the other hand, a very convenient simplification in the study of nuclear systems at low energies is the analysis in multipoles. There, the complex momenta dependence of the $\mathcal{F}_2$ amplitude can be linearized in a low energy approximation. Multipolar expansions of $\mathcal{F}$ in terms of pion angular momentum, l, are made by including only the first terms, namely the s- and p-waves contributions. In detail, using the Eqs. (D.1), the multipolar expansion up to $l = 1$ in the angular momenta for the relevant $\mathcal{F}_2$ reads

$$\mathcal{F}_2 \approx (2M_{1+} + M_{1-}) \equiv P_3, \tag{6.19}$$

being $M_{1\pm}$ the multipole functions as defined in Eqs. (D.8). The multipole contribution to $\mathcal{F}_2$ starts at $l = 1$. Here, P_3 encodes the p-wave amplitude contribution for the NSF piece L. The term P_3 depends only on the invariant energy of the system, since

[7] Eq. (6.18) is a valid approximation to better than 1% for $E_\gamma^{lab} < 200$ MeV and $A = 12$.

the dependence on the pion angle θ_π has been integrated up to $l = 1$ [8]. The explicit angular dependence of $\mathcal{F}_2$ starts to appear with the d-wave contributions.
Finally, the transformation for the amplitude (6.15) to the πA frame is particularly straightforward if one adopts also the "Amaldi conjecture" for the πN amplitude [91], namely

$$P_3(k^*, q^*) = p_3 \left|\vec{k^*}\right| \left|\vec{q^*}\right| \tag{6.20}$$

where p_3 is assumed to be a constant close to threshold. In this prescription, we have that the elementary NSF amplitude L in the π-A c.m. frame (6.15) is

$$L(\vec{k}, \vec{q}) = \mathcal{W}_A \, p_3 \, \vec{k}^* \times \vec{q}^* \cdot \vec{\epsilon}_\lambda = p_3 \, \vec{k} \times \vec{q} \cdot \vec{\epsilon}_\lambda \tag{6.21}$$

in a very good approximation, where Fermi motion is not a relevant factor. See also Ref. [179]. The so called *reduced* amplitude p_3 is directly related to the free nucleon amplitude in the πN c.m. frame from Eq. (6.20).

6.2.2 Calculation of the PWIA cross sections

In the calculation of the cross section we adopt the conventions of Refs. [155, 157]. Assuming the coordinate system fixed by the photon momenta $\hat{z} = \hat{k} = \hat{\epsilon}_0$, then the photon polarization vector $\vec{\epsilon}_\lambda$ is given by (3.61) and the isovector even amplitude $L^{(+)}$ given by (6.14) and (6.21) takes the more convenient form

$$L^{(+)} = \frac{1}{\sqrt{2}} p_3^{(+)} |\vec{k}||\vec{q}| e^{i\lambda\phi_\pi} \sin\theta_\pi, \tag{6.22}$$

where θ_π and ϕ_π are the spherical angles describing the outgoing pion direction in the π-A c.m. frame. We introduce the isovector even combination $p_3^{(+)}$ for the reduced amplitudes in (6.20) as

$$p_3^{(+)} = \frac{1}{2}\left(p_3^{(p)} + p_3^{(n)}\right), \tag{6.23}$$

with the superindices (p) and (n) denoted as in Eq. (6.14). The particular form of $L^{(+)}$ allows it to be removed from the integrand in the transition nuclear matrix element in (6.13), *i.e.*,

$$\langle f \, |V_{\pi\gamma}| \, i\rangle = AL^{(+)} \left\langle J_f M_f \left| e^{i\vec{Q}\cdot\vec{r}} \right| J_i M_i \right\rangle = AL^{(+)} F_J(Q), \tag{6.24}$$

which greatly simplifies the PWIA amplitude expression. $F_J(Q)$ is the matter distribution form factor and it is shown explicitly in Ref. [155]. All the necessary structural information resides in the matrix element of $e^{i\vec{Q}\cdot\vec{r}}$. In the present work, we use the expressions for $F_J(Q)$ from Ref. [161] and they are given in Appendix E.

In the case of coherent transitions ($J = J_i = J_f = 0$), and performing the sum over M, M', λ in Eq. (6.6), the πA c.m. angular cross section for the ^{12}C(γ, π^0) reaction

[8] According to the P_3 definition in Eq. (6.19), since the multipoles $M_{1\pm}$ for $l = 1$ are written in terms of the CGLN basis $\mathcal{F}_i$ (D.8), the p-wave term P_3 reduces to (6.11) $P_3 = \int_1^1 \frac{dx}{2} \left[\mathscr{P}_0(x) - \mathscr{P}_2(x)\right] \mathcal{F}_2(x)$, with $x = \cos\theta_\pi$ and $\mathscr{P}_l$ the Legendre polynomials.

is thus described in PWIA as

$$\frac{d\sigma_{0+}}{d\Omega_\pi} = \frac{A^2}{2}\frac{|\vec{q}|}{|\vec{k}|}\left[p_3^{(+)}|\vec{k}||\vec{q}|\right]^2 F_0^2(Q)\sin^2\theta_\pi, \tag{6.25}$$

The momenta k, q and the pion-photon angle θ_π are given in the πA c.m. frame. Eq. (6.25) represents the coherent neutral pion photoproduction cross section on the nuclear ground state, $J^P = 0^+$, of a scalar and isoscalar nucleus, in a simple approximation in terms of the πN elementary amplitude through the $p_3^{(+)}$ parameter, (6.20) [9].

Incoherent photoproduction: $J^P = 2^+$(4.4 MeV) final state

In principle, when comparing with experimental data for the $^{12}C(\gamma,\pi^0)$ reaction where the final nucleus is not observed, the analysis of the cross section should include both coherent, with the final nucleus in the ground state, and incoherent contributions from all the possible final excited states of the nucleus. The coherent part in Eq. (6.25) is the most important contribution close to threshold, however as the energy increases the incoherent transitions become more sizable.
In the energy regime up to 40 MeV above threshold, it is known from electron [180] and pion inelastic scattering [181] that several excited states could have a sizable contribution, namely $J^P I = 2^+0$ (4.4 MeV), 0^+0 (7.65 MeV), 3^-0 (9.64 MeV), 1^+0 (12.7 MeV), etc. [168]. As a first correction to the coherent process, we restrict ourselves to the calculation of the reaction leading to the first excited state, 2^+ (4.4 MeV), and neglect the rest.

In contrast to the coherent process, the incoherent process may proceed through the spin dependent pieces of the amplitude, $\vec{\sigma}\cdot\vec{K}$ in Eq. (6.12). Nevertheless, electron scattering studies leading to the 2^+ (4.43 MeV) final state indicated that the spin dependent part of the (e,e') transition amplitude is very small. We expect, a similar behaviour for the pion photoproduction process and therefore, the spin dependent contributions are ignored. Hence, much of the formalism for the elastic reaction presented above may be adopted here, with the appropriate modifications for the final state. Also, the relative π-nucleus angular momenta are confined to s and p waves as before. The transition amplitude is again given by Eqs. (6.22) and (6.24).

In fact, the cross section from the 2^+ (4.43 MeV) contribution takes a very similar form to Eq. (6.25). In our calculation, we use the following expression for the PWIA angular cross section [157]

$$\frac{d\sigma_{2+}}{d\Omega_\pi} = \eta\frac{A^2}{2}\frac{|\vec{q}|}{|\vec{k}|}\left[p_3^{(+)}|\vec{k}||\vec{q}|\right]^2 F_2^2(Q)\sin^2\theta_\pi, \tag{6.26}$$

where $F_2(Q)$ is the corresponding transition form factor as can be found in Appendix E. The pion momentum $|\vec{q}|$ is adjusted to the energy shift of 4.43 MeV above threshold, and η represents a further normalization factor. The factor η governs the strength contribution of the 2^+ state to the $^{12}C(\gamma,\pi^0)$ cross section, since the 4.43 MeV state is unresolved in photoproduction studies. This η is fixed indirectly by analysis of the experimental data. The first estimate was provided by Koch et al. [154] from the angular dependence of the pion energies. They conclude that $\sigma_{2^+}/\sigma_{0+} \sim 0.06 - 0.1$, also confirmed by a separate experiment [182]. Then, it is inferred from the total cross

[9] Only s- and p-waves are included, but this is a very good approximation at the energies considered here [22].

section that $\eta \approx 1.5 - 2$, as reviewed in [155]. In the present work, we adopt the value

$$\eta = 1.77 \pm 0.20, \tag{6.27}$$

fixed with the later experimental data of Ref. [157] and analyzed with the same theoretical model used here. Finally, it is worth mentioning that the $F_2(Q)$ form factor is fully determined from electron scattering and no further ingredients should be necessary if the 2^+ transition is assumed to be driven by the NSF amplitude L.

6.2.3 DWIA cross section

In the PWIA approach, we have considered that the incoming photon and outgoing pion are propagated as plane waves by neglecting their interaction with the nuclear medium. In that picture, it is clear how nuclear targets can increase the size of the cross sections (scale as A^2). However, the nuclear medium introduces also considerable effects. They condition the magnitude of the cross sections and the angle and energy distributions of the observed final particles.

As introduced above in Eq. (6.7), in the DWIA approach one also considers the interaction of the produced pion with the nuclear medium. The distorted pion final state is taken into account with a quite standard procedure as shown in Eq. (6.8) . We consider an optical potential deduced from pion nucleus scattering, which modifies the pion wave function and the corresponding transition operator. In this way, the factor $F_{\pi\pi}(q, q')$ (6.8), accounting for the pion wave distortion from rescattering, modifies the total PWIA cross section in an energy dependent manner. To introduce those effects we rely on the method pioneered by Chumbalov et. al. in Ref. [161] and further implemented independently by J. C. Bergstrom [155]. There, a convenient measure of the pion wave distortion is given by the ratio

$$R = \frac{\sigma_D}{\sigma_P} \tag{6.28}$$

where σ_D corresponds to the angular integrated DWIA cross section given by the general Eq. (6.6) and the amplitude with distorted wave term Eq. (6.8), while σ_P is the PWIA cross section with only the plane wave amplitude term $V_{\pi\gamma}$ given in the previous subsections. This method simplifies the calculation of the DWIA cross sections by simply obtaining the energy dependence for the ratio R. Hence, in our particular case where the PWIA cross sections are driven by the coherent part and the incoherent contribution from the 2^+ (4.4 MeV) state, the DWIA cross section will be expressed as

$$\sigma_D = R\left(\sigma_{0+} + \sigma_{2+}\right), \tag{6.29}$$

with σ_{0+} and σ_{2+} the PWIA total cross section from Eqs. (6.25) and (6.26) respectively. In the DWIA treatment, one makes the tacit assumption that the distortion factor R is the same for the elastic and inelastic reactions, with due consideration for the different threshold energies. Any actual difference in distortion may be absorbed by the η normalization factor. The first estimations for R can be found in Figure 2 from Ref. [161] showing estimates of $R \approx 1.2 - 1.3$ for energies below the $E_\gamma^{lab} = 180$ MeV. Very similar results suggested the same estimates by independent calculations in Ref. [155]. In the present work we summarize the distortion ratio from these results using the value $R = 1.3$, for a maximum energy of $E_\gamma^{lab} = 180$ MeV.

6.3 Numerical results and comments

We use the model for the elementary process, $\gamma+N \to \pi^0+N$, derived in the previous Chap. 4. We remind here that the amplitude is based on a calculation at chiral $\mathcal{O}(p^3)$ within the δ power counting and using the EOMS approach for baryon ChPT. The LECs associated with the contact interactions are provided by the fit to charged and neutral pion EM production analysis of Chapter. 5. See Tabs. 4.5, 5.1 and 5.2. In particular, we need only the LECs relevant for the $(\gamma+p \to \pi^0+p)$ and $(\gamma+n \to \pi^0+n)$ channels. Namely, the required LECs are c_6, c_7 d_8, d_9, d_{18}, h_A and g_M. We stress that, since all of them have been determined from the nucleon data in the present study, there is not free parameter for the calculation of the amplitudes for the nuclear case.

As said above, we only need the spin independent part of the amplitude for the study of the $\gamma + {}^{12}\mathrm{C} \to \pi^0 + {}^{12}\mathrm{C}$ reaction. Furthermore, we only need the P_3 partial wave amplitude, Eq. (6.19), and uniquely the terms contributing to it will be evaluated here. Finally, dividing P_3 by $|\vec{k^*}||\vec{q^*}|$ we obtain the p_3 defined in Eq. (6.20). Indeed, we find that at low energies p_3 can be well approximated by a constant, giving support to the "Amaldi ansatz". In the present study, the values for the full model at chiral $\mathcal{O}(p^3)$ with explicit Δ contribution and in the Δ-less case approach lead to

$$\begin{aligned} p_3^{(+)} =&(11.20 \pm 0.14) \times 10^{-3}/M_{\pi^+}^3 \quad \text{(ChPT Full model)}, \\ p_3^{(+)} =&(12.92 \pm 0.22) \times 10^{-3}/M_{\pi^+}^3 \quad \text{(ChPT } \Delta\text{-less model)}, \end{aligned} \tag{6.30}$$

where the assigned uncertainties are estimated from the statistical errors of the fitted LECs. See Tabs. 4.5 and 5.2.

The value for the model with Δ contributions agrees well with the experimental results for the ${}^{12}\mathrm{C}(\gamma,\pi^0)$ reaction reported by [157]. They found that $p_3^{(+)} = (11.24 \pm 0.15) \times 10^{-3}/M_{\pi^+}^3$ in a fit to their data up to laboratory energies of 180 MeV within the DWIA approach for cross sections. Moreover, our result in EOMS ChPT with Δ is very similar to the value derived by *Bernard et al.* in a HBChPT calculation, $p_3^{(+)} = 11.4$ [171].

In Fig. 6.2, we show the ratio σ_{2+}/σ_{0+} of the incoherent and the coherent cross sections as a function of the photon energy[10] and without the η normalization factor. Our results agree well with the findings of [155].

For the calculation of the cross section, we use the ChPT predicted values for $p_3^{(+)}$, (6.30), and the cross section model as given in Eq. (6.29). Results for the $\gamma + {}^{12}\mathrm{C} \to \pi^0 + {}^{12}\mathrm{C}$ reaction cross section are displayed in Figure 6.3 as a function of the photon energy in the lab. frame, E_γ^{lab}, and compared with the experiments of Refs. [157, 183][11]. As we expected from the $p_3^{(+)}$ values in both the experimental and the ChPT analysis, the energy dependence of the ${}^{12}\mathrm{C}(\gamma,\pi^0)$ cross section is very well reproduced over the whole energy range up to 175 MeV. The differences between the full model and the Δ-less case are very clear and they reflect an overall scale factor of 1.33. We should remark here that the two models correspond to two totally independent global fits to electromagnetic pion production on nucleons. They are both of the same chiral order, $O(p^3)$, and use the same renormalization approach. Their only difference is the inclusion or not of the Δ as an explicit degree of freedom.

[10] Note that in the present PWIA the σ_{2+}/σ_{0+} ratio is independent of the elementary amplitude since it is common in both cross section expressions.

[11] We want to stress here that in the DWIA approach adopted here, the energy dependence for cross sections is influenced only by $p_3^{(+)}$ as a scaling parameter.

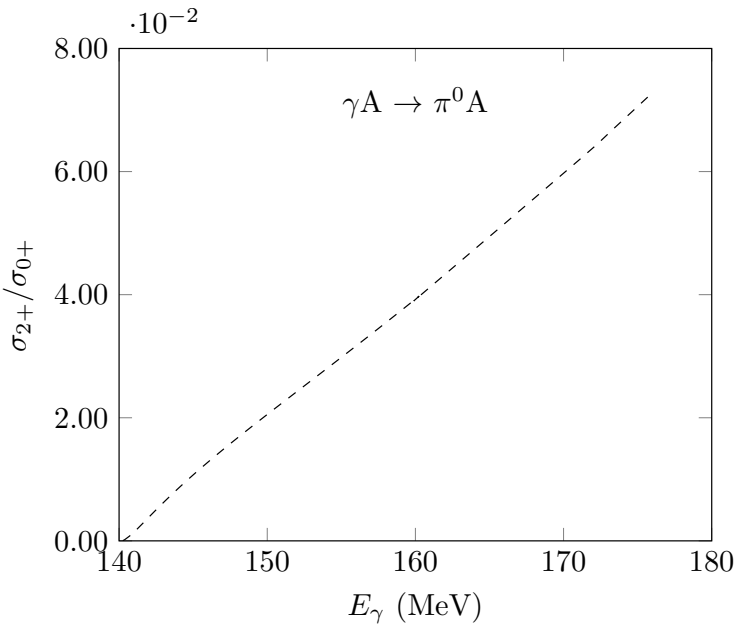

FIGURE 6.2: Ratio of the coherent and incoherent total cross sections as a function of E_γ, the lab photon energy. The normalization factor η in Eq. (6.26) is set to 1 as in Fig. 12 of Ref. [155].

The results here support, once more, the faster chiral convergence of the baryon ChPT models that include explicitly the Δ resonance.

The effects due to the incoherent transition to the $J^P = 2^+$ (4.4 MeV) excited state are exhibited in Fig. 6.3 by suppressing its contribution, as shown in the dashed curves. These curves reflect the rising importance of the nucleus excitation at higher energies, being this correction crucial to reproduce the experimental data. The low energy region close to threshold is more or less completely dominated by the coherent transitions and, of course, by an accurate inclusion of final state interactions (DWIA).

There are also data for differential cross sections as function of the π-nucleus c.m. angle and at photon energies from 137.4 MeV to 160.5 MeV in Ref. [157]. In Fig. 6.4, we display our results obtained from the full model ChPT amplitude with data. There, the agreement can be appreciated more closely for all the energies. On the other hand, we can observe the good accordance for the angular distribution with data. The dependence of the angular distributions is not carried by our ChPT prediction, but driven completely by the PWIA expressions for the differential cross sections, Eqs. (6.25) and (6.26). In particular, at these energies the coherent contributions $d\sigma_{0+}/d\Omega_\pi$ amounts to almost the total contribution, hence it leads mainly the angular distribution as $F_0^2(Q)\sin^2\theta_\pi$. We want to emphasize that the angular distributions are genuine predictions since the ground state form factor $F_0(Q)$ is completely fixed by the properties of the final pion state interactions (FSI) and the ^{12}C(e,e') data [161]. The explicit $\sin\theta_\pi$ dependence is derived by considering only the p-wave contribution in the NSF elementary amplitude (6.12) and the impulse approximation.

Finally, at high enough energies, the intrinsic momentum dependence of the elementary mechanism can make that $p_3^{(+)}$, in cross sections (6.25) and (6.26), carries itself a significant energy dependence and the assumption that $p_3^{(+)}$ is a constant may no longer be valid. Then, it would be necessary to include further energy and angular dependence by going beyond the p-wave multipole approximation.

On the other hand, the strong effect of the $\Delta(1232)$ in the π^0 photoproduction

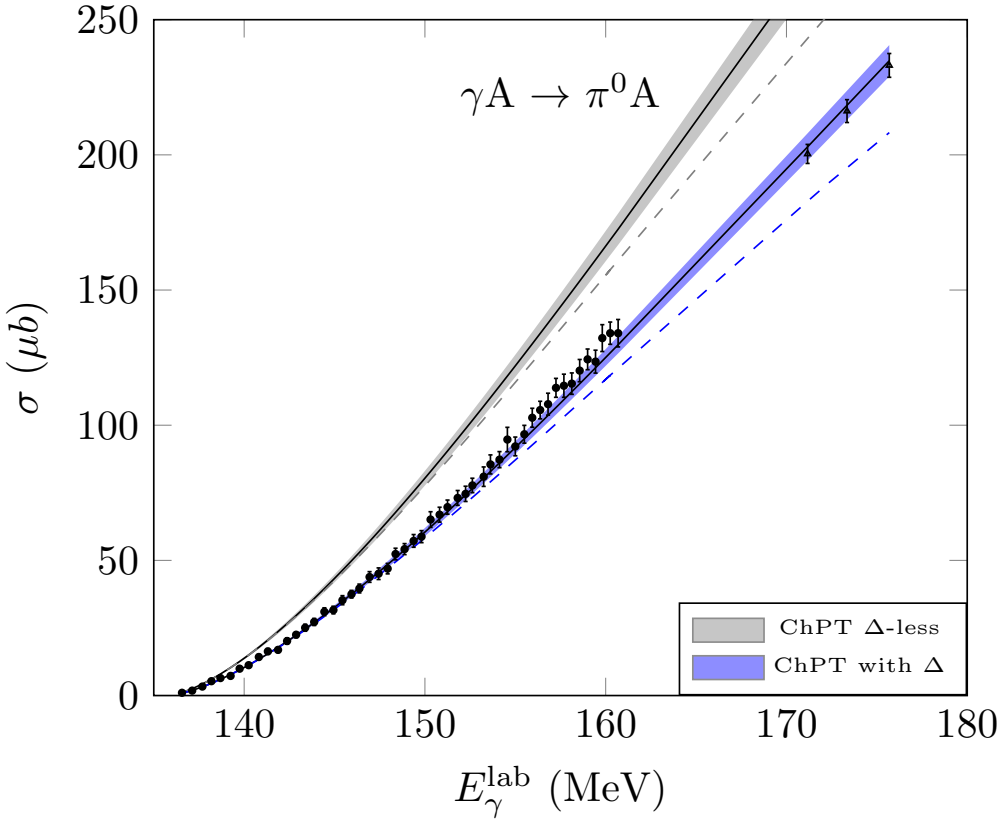

FIGURE 6.3: Cross section of the $^{12}C(\gamma, \pi^0)$ reaction as a function of the photon energy in the lab. frame. The blue/gray bands show the results of the full model, Eq. (6.29), with contribution of both coherent and the incoherent transition to the 2^+(4.4 MeV) state. Band widths correspond to the statistical error propagated from the LEC uncertainties, Tab. 4.5 and 5.2. The respective dashed curves show the effect of removing the incoherent contribution from the central values. Data below 161 MeV from [157] and the tree points at the higher energies from [183].

amplitudes introduces an important energy dependence, see Fig. 6.5. Given its importance, to accurately estimate the role of the Δ-resonance in π^0 production from complex nuclei, more detailed and appropriate treatments of the Δ degree of freedom in nuclear media are needed.

6.4 Summary and Outlook

We have analyzed the nuclear reaction $\gamma + {}^{12}C \longrightarrow \pi^0 + {}^{12}C$ in the near threshold region. The impulse approximation provides us a simple approach for a straightforward calculation of the nuclear process in terms of the elementary amplitudes on nucleons.

The study of the elementary reaction mechanism for free nucleons is based on the covariant ChPT from Chapter 2. Therefore, we were able to apply the previous results in pion production on nucleons for determining the relevant LECs utilized in the evaluation of the elementary amplitudes.

It is worth to mention that the lack of experimental data for the $\gamma + n \to \pi^0 + n$ process had hindered the determination of some relevant LECS. Some of those LECs that remained undetermined, namely, d_8 and d_9, have been fixed in the present work with

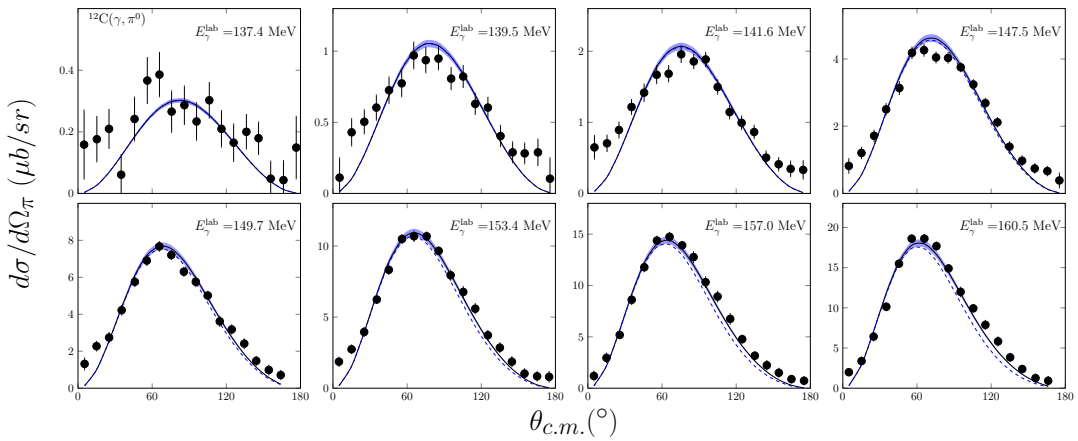

FIGURE 6.4: Differential cross sections of the $^{12}C(\gamma,\pi^0)$ reaction in the π-nucleus c.m. frame for various lab. energies E_γ^{lab}. The solid/dashed curves show the results of the DWIA calculation with the ChPT amplitude. The solid curve correspond to the total contribution from the coherent and incoherent transitions, whilst the dashed curve removes the incoherent part. The error bands are propagated from the LECs errors. Data points are from [157].

our global analysis including other photo- and electroproduction channels: $\gamma^{(*)}+p\to\pi^0+p$, $\gamma^{(*)}+p\to\pi^++n$ and $\gamma^{(*)}+n\to\pi^-+p$, see Chapter. 5.

We have obtained the corresponding $^{12}C(\gamma,\pi^0)$ cross sections in a PWIA calculation where we have considered the contributions from elastic coherent and incoherent transitions. Moreover, we have taken into account the effects of the pion-nucleus interaction or FSI. For the latter, we introduced the distorted wave correction obtained in previous DWIA studies [155,161] which model the rescattering of the outgoing pion in the nuclear medium by a phenomenological optical potential.

Our results reproduce satisfactorily the total and angular cross section data from [157, 183] up to 40 MeV above threshold. The model for cross section calculations relies only on the spin independent part in elementary amplitude (6.12) and the low energy conjecture for p-wave amplitudes being proportional to a constant $p_3^{(+)}$ as in Eq. (6.20). The predictions for the total cross sections have been derived from an estimate of that reduced p-wave term, $p_3^{(+)}$, based on our ChPT calculations at $\mathcal{O}(p^3)$. The ChPT models with and without $\Delta(1232)$ contributions show different tendencies as energy increases. Only those results including the Δ effects are observed to agree well with data and other studies [155, 161, 171].

Although cross sections data are not separated for elastic and inelastic processes, the quality of experimental data allow us to distinguish the theoretical estimations between the different ground and excited contribution. The process is completely coherent within the first 4.43 MeV above threshold. Above this energy, the reported experimental cross sections are interpreted as the sum of coherent and incoherent contributions.

Our elementary ChPT amplitudes are well applicable to an energy range of almost 70 MeV above threshold, however the extended dynamics due to excited nucleus transitions introduce additional contributions for increasing energies. The contribution of the 2^+ (4.4 MeV) final state is of nearly an additional 10% in the cross section with respect to the coherent nuclear transitions at around 40 MeV above the threshold. This is shown to improve the agreement with data. Furthermore, the underlying $\Delta(1232)$ mechanism is in fact crucial for the accordance with data in the overall energy range.

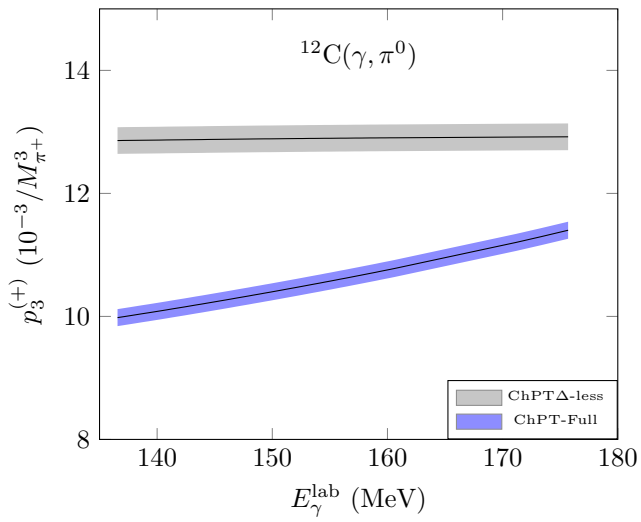

FIGURE 6.5: Dependence of the function $p_3^{(+)}$ on the laboratory photon energy, comparing the full and the Δ-less model.

Otherwise, none of the different contributions would reproduce the evolution of cross sections. Thus, we confirm the importance of Δ mechanism for π^0 photoproduction on ^{12}C. Notwithstanding the limitations imposed by the simple approach used to deal with the complex dynamics of the process in a nucleus, the high quality of the experimental data may suffice to further constrain the theoretical models for the elementary process.

Chapter 7

Conclusions

In this thesis, we have studied the pion production with electromagnetic probes on nucleons and nuclei. For each of the studies made here, our approach was Chiral Perturbation Theory for light hadrons: nucleons, pions, and Δs as degrees of freedom. To preserve the covariance of the theory, the renormalization method was implemented in the Extended On Mass Shell scheme. There, divergences and power-counting breaking terms are absorbed into the low-energy constants in the effective Lagrangian.

The present work is developed within three main studies related to the single pion production through different processes. In detail, we investigate the pion photoproduction on nucleons, where the four physical channels and their observables are treated. Analogously, the charged and neutral pion electroproduction on nucleons was investigated and approached as an extension to the photoproduction with virtual photons. Lastly, the pion photoproduction on the ^{12}C nucleus was studied as an application of our results from the elementary processes (on nucleons). These studies are distributed through the chapters 4, 5, and 6. We aimed to make a global analysis of the elementary processes and constrain the relevant LECs in the ChPT Lagrangian with current data.

Chapter 4 was dedicated to the amplitude calculation for the pion electromagnetic production on nucleons. The photoproduction process was presented as a particular case of the electroproduction reaction by considering the real photon as a particular case of the virtual one. Then, the corresponding observables were computed separately for each reaction and channel.
In Chapter 5 we have presented the corresponding results for the LECs and the various observables for both the pion electro- and photoproduction on nucleons. We have fitted the relevant LECs that remained unknown by comparing our theoretical calculations with data corresponding to the measured observables up to a πN c.m. energy $W = 60$ MeV above the threshold. The fitting procedure to determine the best LEC values has been implemented numerically for two different models: One model with the explicit contribution of the $\Delta(1232)$ degree of freedom and the other one for the Δ-less case. In this context, this study has represented a comprehensive exploration of the relevant degrees of freedom in the single pion EM production on the nucleon in a fully covariant ChPT.
Finally in Chapter 6, as an application of the obtained results, we computed the effects of the $\Delta(1232)$ in a simple model at low energies for π^0 photoproduction off the ^{12}C nucleus. We gave here an estimate for the corresponding coherent and incoherent cross sections at various laboratory photon energies up to ~ 175 MeV. In this study, we incorporated the elementary processes based on the calculations within the ChPT approach, namely the π^0 photoproduction on the proton and the neutron. There we have evaluated the elementary amplitudes with the relevant LECs previously fitted in this work. In consequence, the resulting cross sections are completely predictive, although dependent on the nuclear model.

Throughout the Chapters 4 and 5 the investigation of the charged pion photoproduction on nucleon targets was studied as a natural extension of previous works on neutral pion photoproduction off the proton within the same ChPT approach at $\mathcal{O}(p^3)$ in the chiral expansion. The results from this production channel have shown that the $\Delta(1232)$ plays a particularly important role in improving the agreement with data up to 60 MeV above the threshold. Other past studies within the same covariant ChPT approach but at a higher $\mathcal{O}(p^4)$ and without the Δ degree of freedom have shown good accordance with data but at only near 20 MeV from the threshold. The situation turned out that the inclusion of $\Delta(1232)$ as an additional degree of freedom at low energies is more relevant than higher chiral order contributions in approaches without explicit Δ's. Even more, this ChPT model up to only $\mathcal{O}(p^3)$ preserves the predictive power that otherwise would be hindered with the inclusion of too many LECs involved in an $\mathcal{O}(p^4)$ calculation.

In addition to the study on neutral pion photoproduction off the proton including the Δ mechanism within the relativistic ChPT, we have extended the previous work by considering the four possible channels of charged and neutral pion production. Several unexplored aspects of this reaction motivated the extension of the previous study through further physical mechanisms. This extension made the analysis sensitive to additional processes in which charged pions are also produced. We begin with the investigation of the near-threshold pion photoproduction on nucleons, including all the physical channels with the SU(2) covariant ChPT framework. We emphasize the importance of the explicit $\Delta(1232)$ degree of freedom for these processes. We have performed a full $\mathcal{O}(p^3)$ calculation within the aforementioned approach with the EOMS renormalization scheme.
In the amplitude calculation, the inclusion of the charged channels requires the addition of a more extensive set of Feynman diagram topologies and therefore some extra pieces of the chiral Lagrangian with the corresponding LECs.
We proceeded by first calculating the tree-level and one-loop amplitudes for all the charge channels from the lowest-order up to $\mathcal{O}(p^3)$, including pions, nucleons and the resonance Δ by means of the Feynman rules derived from the chiral Lagrangian.

We included the explicit contribution of the $\Delta(1232)$ resonance through its couplings to nucleons, pions and the photon. Since we followed the δ-power counting scheme, the resonant diagrams contributed only at tree-level and the corresponding amplitudes were counted as of 3/2-order. The next orders in the resonant amplitudes include trees and loops with Δ but they were discarded because they start contributing at higher-order than the $\mathcal{O}(p^3)$, namely at $\mathcal{O}(p^{7/2})$.

Besides the global analysis for the single pion electromagnetic production off nucleons, an interesting aspect is related to the isospin-breaking effects due to the mass gaps between the charged and neutral pions, and between protons and neutrons. This mechanism is particularly relevant in the $\pi^0 + p$ production channel where the observation of the cusp effect close to the threshold is reproduced only if the mass splittings are introduced in the amplitude calculations. In the context of the ChPT, the cusps effect is a consequence of different opening channels for charged and neutral pion loops. This effect is exclusively produced by loop amplitudes given the different imaginary contribution for different energies near the threshold region. Otherwise, in the isospin symmetric case, the loops contribution is uniform in the full energy domain. As expected from this mechanism in ChPT, cusp effects do not appear in charged pion production channels, since the physical threshold for these channels occurs at

higher energies than the loop opening-channel mechanism and hence it is suppressed by phase space. Even so, the isospin-breaking effects are shown to have non-negligible contributions above the threshold which remain important for reproducing much of the low energy data.

Finally, we perform a global study of all the data currently available in the low energy region. This amounts to measurements of angular and total cross sections, as well as beam and target asymmetries that measure spin observables. We have compared our theoretical results with data and determined as a first step the numerical values for the relevant LECs.

Parallel to the studies on pion photoproduction, single pion electroproduction on nucleons $e + N \to e + \pi + N'$ is presented in Chapter 4 as a more general treatment of pion photoproduction by considering the virtuality of the photon.

Since the electron-photon coupling is considerably weaker than hadron couplings in the low energy regime of QCD, the one-photon exchange approximation allows us to compute the electroproduction amplitude in terms of an photoproduction process but with virtual photons. This approximation provides a direct calculation of the electroproduction amplitudes in a simple task.

In this sense, this study represents a kinematical extension of the processes considered in photoproduction. We approached this reaction in the same covariant ChPT at $\mathcal{O}(p^3)$ in EOMS and with explicit Δ resonances, for neutral and charged pion channels and with isospin-breaking effects.

The inclusion of electroproduction in a broader analysis allows for the exploration of the interaction of nucleons with virtual photons, and thus to investigate some additional pieces of the chiral Lagrangian.

Specifically, this study was first motivated by finding more constraints for the LECs, given that the single pion electroproduction process provides access to a wide range of data for various observables including scattering angles, energies, polarizations and transfer momenta from a virtual photon.

We have compared our model to the available experimental data for photo- and electroproduction observables, this time with kinematical limits for virtual photons to ensure the small external momenta condition. We have considered a constrained kinematical region with $\sqrt{s} < 1.13$ GeV and $Q^2 < 0.15\,\mathrm{GeV}^2$, where we expected our model to be reliable and still well below the $\Delta(1232)$ peak.

The values obtained for the fitted LECs resulted in all of them being of natural size, which is satisfactory from the point of view of chiral convergence. This gives support to the uncertainty estimates of recent chiral calculations of neutrino-induced pion production. The comprehensive investigation of all single pion electromagnetic production channels, including all the available observables, has allowed us disentangling all the relevant third-order LECs involved, which appeared correlated in the photoproduction case.

We have confirmed the importance of the loop terms. The imaginary parts of the scattering amplitude and the cusp effects, coming from the opening of the various charge channels, are crucial in the description of some low-energy electroproduction observables. Also, the inclusion of the isospin-breaking mechanism in loops is shown to solve the inconsistency with the parameter related to πN scattering through the Goldberger–Treiman relation.

With the model approached in this work, only 5 fitting parameters were sufficient to describe well all the experimental data used, consisting of near 2700 data points, for angular and energy dependence in cross sections and numerous polarization observables.
In summary, the inclusion of the Δ mechanism in ChPT calculations at $\mathcal{O}(p^3)$ is better than the extension to higher orders that do not include the Δ resonance. Without Δ, our model is only able to reproduce data a few MeV above the threshold. In particular, neutral pion photoproduction is the most sensitive channel to this resonance due to the smaller size of its lowest order contributions.

The results from the covariant ChPT at third order calculation and with explicit Δ are found to reproduce the high-precision data of cross sections and polarization asymmetries remarkably well up to 70 MeV above threshold. On the other hand, the Δ-less calculation performed within the same approach demonstrates a much worse description of the data.

The final study within the present thesis is described in Chapter 6, where we treat the near threshold single pion photoproduction off ^{12}C nucleus. Our purpose here was twofold: to apply and test the fitted LECs resulting from the analysis on pion electromagnetic production in the nucleon within the ChPT framework, and to estimate the contribution of the Δ-mechanism in the $^{12}\mathrm{C}(\gamma, \pi^0)$ nuclear cross section.

The model to study the $^{12}\mathrm{C}(\gamma, \pi^0)$ reaction relied on the usual impulse approximation in which the free-nucleon amplitudes describe the pion photoproduction on the nucleus at low energies from each bound nucleon. In this approximation is, therefore, possible to express the nuclear reaction amplitude in terms of the elementary amplitudes with nucleons. In our case, this approach allowed us to calculate the nuclear cross section in terms of the π^0 photoproduction on the proton and the neutron amplitudes with the covariant ChPT framework as before. In particular, only the spin-independent part in the amplitude was relevant for the process on the ^{12}C nucleus. Further nuclear medium effects were introduced systematically. First, the nuclear structure of the ^{12}C nucleus was taken into account in the usual plane-wave impulse-approximation (PWIA) by assuming that incoming and outgoing particles, here the photon and the observed pion, were propagated as plane waves through an approximately transparent nuclear medium. In addition, the pion photoproduction process may include the contribution of inelastic transitions due to the excited final nucleus states. This kind of mechanism is typically considered when the final nucleus is not observed, as in the data we compare our model with. Then, within PWIA we obtain the corresponding nuclear cross section contributions from the coherent and incoherent transitions from the first excited state 2^+ (4.43 MeV) as a good approximation. In particular, the coherent and incoherent are mainly driven by the same spin-independent amplitude.

Moreover, an important correction to the $^{12}\mathrm{C}(\gamma, \pi^0)$ cross section calculation was included by means of the the pion-nucleus interaction in the distorted-wave impulse-approximation (DWIA). This effect produces a distortion for the outgoing pions off the nucleus by the re-scattering with nuclear medium and their inclusion is standard at energies close to the threshold where it reduces to an approximate scale factor. We assumed that coherent and incoherent contributions were equally corrected by pion distortion effects.

Our calculations, based on the amplitudes obtained in the framework of ChPT and applied to a simple nuclear model at low energies, successfully reproduced the energy dependence of the cross section for the $^{12}\mathrm{C}(\gamma, \pi^0)$ reaction. We have compared the predicted results for energies up to 40 MeV above the threshold. The contribution

from the elementary process was evaluated by taking the numerical values of the relevant LECs fitted in this work with data from the pion electromagnetic production on nucleons.

We have observed that the ChPT calculations at $\mathcal{O}(p^3)$ with and without $\Delta(1232)$ contributions reproduce a different energy dependence. Only the cross section estimations including the Δ resonance together with the coherent, incoherent, and an adequate inclusion of FSI for distorted pions, were in agreement with the experimental measurements.

As a final remark, we can say that some of the most successful approaches have been the ChPT calculations within the fully covariant formalism. There, the expansion of the chiral series is under control at the lower energies, and then higher-order contributions usually help to reproduce the precise data measurements. However, the extension to higher orders is limited given the arising number of unknown parameters (LECs). The consideration of suitable degrees of freedom, in pion photoproduction, as the spin-3/2 Δ resonance, results in more convenient than a higher order calculation without their explicit inclusion. Apart from the added technical complications, the model would lose its predictive power because of the new set of undetermined LECs appearing in the Lagrangian. Moreover, Δ resonance contributions help to reproduce the data in a wider range of energies in pion electromagnetic production processes.

Finally, we discuss some questions that may be treated in follow-up studies to this thesis.

Our results consisted of the determination of some relevant LECs in the processes studied here. As it was shown in the study of the $^{12}\mathrm{C}(\gamma, \pi^0)$ reaction, the numerical values of the LECs can be further applied to other low energy processes approached within the same framework.

Specifically, all the fitted LECs in this work appear also in the evaluation of neutrino-induced pion production off nucleons. These LEC values could be used to improve the corresponding predictions of the low energy neutrino nucleon cross sections of relevance to achieve the precision goals of modern neutrino experiments.

In addition, our results give support to the first ChPT calculations of these weak production processes, which assumed a natural size for these parameters to estimate the uncertainties of the theoretical predictions. The examination of the vector couplings of the nucleons might reduce the large uncertainties that currently hinder our efforts to provide a theoretically well-founded prediction of the neutrino-induced pion production.

This is especially important in the current precision era of neutrino physics, where adequate modeling of cross sections and backgrounds is necessary for the investigation of neutrino masses, mixing angles, and other properties. Finally, the extension to the description of electro- and weak production data will advance these studies even further, while offering the possibility of making reliable and accurate predictions for weak processes where data are more scarce.

On the other hand, the framework used to extract the results in pion electromagnetic production on nucleons can be extended from the SU(2) to the SU(3) flavour symmetry and therefore be applied to the extraction of other light baryon properties related to other low energy processes including strangeness.

Finally, the theoretical framework used to obtain the cross section results for the $^{12}\mathrm{C}(\gamma, \pi^0)$ reaction can be applied to other similar low energy nuclear processes in which the elementary amplitudes take place in the calculations. For instance, the same procedure presented here is also applicable for predictive results of pion photoproduction off ^{2}H or ^{6}Li nuclei.

Chapter 8

Resumen en español

8.1 Motivación

Desde que se descubrió a principios de los 1950 que los piones podían ser producidos mediante haces de fotones [1], las pruebas electromagnéticas sobre hadrones se han convertido en una muy importante fuente de información en el estudio de las interacciones hadrónicas, siendo además cruciales en la investigación de los bariones y sus resonancias. Más aún, las interacciones entre hadrones son de un gran interés para la comprensión de la interacción nuclear fuerte a bajas energías. Estas interacciones son descritas por la cromodinámica cuántica (QCD), una teoría no abeliana de campos *gauge* desarrollada en los 1970 en términos de quarks y gluones, los constituyentes básicos de la materia hadrónica.

Han sido varios los esfuerzos llevados a cabo, tanto teóricos como experimentales, para el estudio de la fotoproducción de piones a energías intermedias, desde el umbral hasta regiones donde las resonancias juegan un papel importante. En este trabajo, me enfoco en el estudio de la producción electromagnética de piones sobre nucleones. En detalle, en el efecto que puede tener la resonancia $\Delta(1232)$ en los diferentes canales de carga para los procesos de foto- y electroproducción de piones en nucleones, calculando para ellos las secciones eficaces, sus distribuciones angulares y la dependencia en energía con el objetivo de comparar los resultados teóricos con los datos experimentales actuales. Subsecuentemente, los resultados obtenidos a partir de esos estudios son aplicados como ejemplo al estudio de una reacción nuclear, en particular a la fotoproducción de piones sobre núcleos de ^{12}C, en donde los efectos de la Δ pueden ser tratados en términos de la amplitud elemental (fotoproducción de piones en nucleones).

Aunque la teoría de QCD describe con éxito los procesos de la interacción fuerte a altas energías, esta no puede aplicarse de forma directa en la región de bajas energías para procesos hadrónicos. Esto es debido a la dependencia en energía de la constante de acoplamiento fuerte, α_S, cuya magnitud es pequeña para energías altas. Este fenómeno es lo que conocemos como *libertad asintótica* de los quarks. En consecuencia QCD puede ser tratada como una teoría perturbativa cuántica de campos (QFT perturbativa) en el régimen de altas energías. Por el otro lado, el acoplamiento α_S es considerablemente grande para energías bajas y por lo tanto QCD es una teoría no-perturbativa. Esto hace que las técnicas típicas de perturbaciones en QFT sean prácticamente inútiles. Por lo tanto, la aplicabilidad de la QCD se divide en diferentes partes dependiendo de las región de energía, típicamente separadas por la escala energética $\Lambda = 1$ GeV. Esta escala determina el límite inferior en el cual las series perturbativas de QCD dejan de ser válidas.

En efecto, las energías de los procesos investigados aquí pertenecen a la región no perturbativa de QCD, puesto que estas se encuentran muy por debajo de las escala Λ. Es bueno notar aquí que esta escala puede además entenderse como el límite superior

en donde los quarks interactúan lo suficientemente fuerte como para configurarse en estados confinados, es decir, para formar los llamados hadrones y que son los grados de libertad efectivos a bajas energías. En consecuencia, consideramos aquí una teoría efectiva de campos (EFT) como enfoque para describir la dinámica a bajas energías de la interacción fuerte de QCD pero en términos de hadrones.

Los primeras formulaciones teóricas dirigidas al estudio de los procesos electromagnéticos en hadrones fueron construidas a partir de modelos puramente fenomenológicos que en ocasiones sólo requerían invariancia bajo transformaciones de Lorentz y en campos de gauge. Algunos otros modelos requerían también la conservación de corrientes (en álgebra de corrientes) y la conservación parcial de la corriente axial (PCAC). No obstante, estos modelos carecían de un procedimiento sistemático para describir los diferentes procesos y fallaban al reproducir resultados en algunos casos como la fotoproducción de piones neutros a baja energía.

8.2 Metodología

En este trabajo hacemos uso de la Teoría Quiral de Perturbaciones (ChPT), una EFT desarrollada durante los últimos 40 años. Esta representa una potente herramienta teórica para describir la dinámica a bajas energías de procesos ocurridos mediante la interacción fuerte y en términos de estados efectivos de hadrones. ChPT fue formulada como una EFT sistemática tal que satisface la simetría quiral, su rompimiento y todas las demás propiedades fundamentales de QCD. Esta EFT está construida para ser aplicada en la región energética no perturbativa de QCD, es decir, para energías suficientemente menores que 1 GeV. Más aún, ChPT ha demostrado ser una teoría muy útil al reproducir satisfactoriamente los resultados experimentales para la fotoproducción de piones cargados y neutros en nucleones muy cerca del umbral.

El Lagrangiano en ChPT está escrito en términos de campos de bariones y mesones como los grados de libertad relevantes, en vez de los quarks y gluones. Aquí nos enfocaremos en el espectro de bariones más ligeros y en los mesones pseudoescalares en el límite de isoespín: piones, nucleones y las resonancias Δ, que siguen la simetría aproximada de isoespín $SU(2)$. Adicionalmente, desde el punto de vista de la QCD, estos bariones y mesones son estados compuestos de quarks de sabores u y d organizados en un grupo de simetría de sabor, $SU(2)$. Los campos de quarks pueden ser descompuestos en componentes quirales, izquierdos q_L y derechos q_R que en el límite relativista donde las masas de los quarks se desvanecen, las componentes quirales están desacopladas en el Lagrangiano de QCD, produciendo globalmente una simetría quiral.

Sin embargo, la observación fenomenológica indica que los mesones ligeros poseen masa lo que sugiere que la simetría quiral está rota. Las masas del espectro de bariones y mesones son interpretadas como una consecuencia de las masas de los quarks produciendo un rompimiento explícito de la simetría quiral. En adición, dado que las masas de los mesones ligeros son pequeñas en comparación con la escala Λ, los mesones pseudoescalares son asociados a bosones de Goldstone correspondientes al rompimiento espontáneo de simetría (SSB). Además, dentro del espectro bariónico el rompimiento espontáneo de la simetría puede confirmarse por la inexistencia de bariones asociados de la misma masa pero con paridad negativa.

El rompimiento de la simetría, tanto espontáneo como explícito, es una de las propiedades básicas en la construcción del Lagrangiano efectivo de la ChPT. Al igual que en cualquier teoría de campos efectiva adecuada, el Lagrangiano de la ChPT está ordenado según una expansión en términos de potencias de pequeños parámetros. Los

parámetros de expansión en este caso, comparados con la escala $\Lambda_\chi \approx 1$ GeV, tienen que ver con los momentos p/Λ_χ y las pequeñas masas de los bosones de Goldstone M_π/Λ_χ. Este es un método de aproximación adecuado para energías muy por debajo de la Λ_χ, en lugar de la constante de acoplamiento fuerte α_S. Además, los grados de libertad relevantes en la expansión de pequeños momentos (a distancias largas) son los de los hadrones observados asintóticamente, ya que son los estados confinados producidos por la interacción fuerte.

Aunque la idea de una aproximación en una serie de parámetros de expansión parece inexacta, ya que no podemos calcular infinitos términos, la convergencia de la serie está bajo control y no necesariamente significa una falta de precisión. La calidad de la convergencia depende del pequeño tamaño de las masas de los bosones de Goldstone, que en el caso de la simetría de sabor $SU(2)$ se considera una buena suposición ya que $M_\pi << 1$ GeV. Por lo tanto, el enfoque de la ChPT es suficientemente preciso para el multiplete en $SU(2)$ de piones pseudoescalares a baja energía. La inclusión de campos de nucleón en la ChPT como grados de libertad también es posible en el límite de pequeños momentos, pero esto introduce una nueva escala, la masa del nucleón, que es de tamaño similar a la escala donde la expansión quiral es inválida, $m \approx \Lambda_\chi$.

Dentro del marco de ChPT, las amplitudes de un *loop* también pueden contribuir en los cálculos de amplitud a un orden quiral dado. Las amplitudes de *loops* pueden contener divergencias ultravioletas (UV) que se pueden renormalizar con la inclusión de contra-términos en el Lagrangiano de ChPT. Por lo tanto, ChPT se puede renormalizar sistemáticamente orden por orden en la expansión quiral. Además, cada uno de los términos de la serie infinita del Lagrangiano de ChPT es proporcional a una constante de baja energía (LEC). Estas LEC, careciendo de una extracción directa desde la dinámica de QCD a bajas energías, se pueden fijar mediante un ajuste a datos experimentales. Luego, el Lagrangiano resultante se puede usar directamente para hacer más predicciones.

Es sabido que la inclusión de amplitudes que contienen *loops* con bariones pueden estropear la regla del conteo de potencias en la expansión quiral en términos de p y M_π. En particular, los *loops* de nucleones pueden dar contribuciones de gran tamaño del tipo m_N/Λ_χ dadas por el tamaño parecido de la masa del nucleón a la escala Λ_χ.

Este conflicto se resolvió primero en la aproximación para bariones pesados en ChPT (HBChPT por sus siglas en inglés) a expensas de perder la invariancia en Lorentz, mientras que la formulación covariante ChPT original se dejó de lado. Así entonces, HBChPT se convirtió en un enfoque estándar para el análisis de procesos de hadrones como la electroproducción y fotoproducción de piones.

Mientras que en el enfoque no-relativista de HB se restauraba el conteo de potencias en los *loops* de nucleones, el hecho de que las correcciones relativistas pueden ser grandes en algunos procesos cuestionó la aplicabilidad de este marco. El interés en los métodos relativistas se renovó y, eventualmente, la conciliación de un conteo de potencias consistente con los *loops* bariónicos fue posible en la formulación relativista original de ChPT mediante nuevos esquemas de regularización, a saber, el esquema de infrarrojo (IR) [2] y extendido en la capa de masa (EOMS) [3, 4].

Los dos métodos, IR y EOMS, extraen los términos que rompen el conteo de potencias (PCBT) conflictivos de las contribuciones del *loop*-nucleónico y los reabsorben en las LECs, además de los términos de renormalización UV. La principal diferencia del esquema EOMS con el esquema IR es que en el EOMS se restan únicamente los términos conflictivos en órdenes inferiores, mientras que en la renormalización IR

también se incluyen en la resta términos de órdenes superiores.

En esta tesis, implementamos la renormalización con el esquema EOMS en nuestros cálculos. Son dos las razones principales. En primer lugar, EOMS suele converger más rápido que HB y (IR) ChPT. Como consecuencia, este marco se ha vuelto popular y ha sido utilizado con éxito para describir muchos observables que involucran a los bariones [5–22]. Por otro lado, tanto HBChPT como IRChPT mostraron una buena concordancia con la producción de piones EM en los núcleos pero únicamente a muy bajas energías.

Las extensiones a los órdenes quiral más altos en IRChPT mostraron una mejor concordancia para estos procesos. Sin embargo, como en el caso de HBChPT, el acuerdo fue aceptable solo para un rango de energías aún limitado [20]. Además, la situación era técnicamente más complicada debido al gran número de LECs todavía desconocidas involucradas en esos órdenes más altos.

Recientes estudios han demostrado que, en algunos casos, una forma sencilla de mejorar la convergencia de las series en cálculos de amplitudes en ChPT relativista es incluir a la resonancia de espín 3/2 Δ como un grado de libertad adicional. De hecho, la calidad y convergencia de un cálculo de amplitud dado a energías más altas depende también de los grados de libertad tomados en cuenta. Más aún, es bien sabido que, además de los piones y nucleones, la contribución de la $\Delta(1232)$ juega un papel importante en el proceso de producción de piones neutros en nucleones debido a su proximidad con el umbral de producción πN.

Dentro de la simetría de isospín de SU(2), los campos Δ forman un cuadruplete con valores propios de isospín $I = 3/2$. Estas resonancias $\Delta(1232)$, que se acoplan fuertemente a nucleones y piones, se incorporan fácilmente en nuestro marco teórico. Esto significa que la Δ se propaga explícitamente como un estado intermedio en los procesos estudiados aquí. Este grado de libertad en particular implica un parámetro adicional en la serie quiral dado por la diferencia entre las masas del nucleón y la Δ, $\delta = m_\Delta - m_N \approx 300$ MeV. Este parámetro induce una extensión a las reglas de conteo de potencias de la serie quiral con sólo nucleones y piones como grados de libertad.

Nuestro propósito aquí es hacer un análisis más completo y exhaustivo dentro del marco antes mencionado de la fotoproducción y la electroproducción de piones en nucleones y estudiar los efectos de la resonancia $\Delta(1232)$ en ellos. El canal de fotoproducción de piones neutros ya se ha investigado en la ChPT covariante en EOMS y con contribuciones de Δ [21, 22].
Aquí, extendemos el estudio anterior agregando la fotoproducción de piones cargados e incluyendo el proceso de electroproducción de piones para todos los canales de piones neutros y cargados. Esto permite explorar más vértices de interacción con fotones reales y virtuales y, por lo tanto, examinar algunas otras piezas del Lagrangiano quiral. De esta manera, se puede hacer una determinación más completa y mejor de las LEC relevantes comparando nuestros resultados teóricos con un conjunto más completo de datos experimentales.
Además, incorporamos algunos datos recientes para la fotoproducción de piones neutros [23] y cargados [24], y consideramos el cálculo de los *loops* con rompimiento explícito del isospín. Este último punto mejora considerablemente el acuerdo con los datos a bajas energías.
Finalmente, una mejor determinación de un conjunto más completo de LECs podría usarse para hacer predicciones como en la producción débil de piones y muchos otros procesos. En particular, el examen de los acoplamientos vectoriales de los nucleones con fotones tanto reales como virtuales podría reducir las grandes incertidumbres que

actualmente dificultan los esfuerzos para proporcionar una predicción teóricamente bien fundamentada de la producción de piones inducida por neutrinos [25, 26], un proceso muy importante en muchos de los experimentos de neutrinos.

La presente tesis incluye tres estudios principales: la fotoproducción y electroproducción de piones en nucleones, así como la fotoproducción de piones en el núcleo ^{12}C. Se desarrollan a través de los siguientes capítulos:
En el capítulo 2, se introducen los fundamentos de las interacciones de hadrones en el marco de la ChPT relativista para su uso en los cálculos de amplitudes. En el capítulo 3, se presenta el formalismo general para la producción electromagnética de piones en nucleones, que incluye las parametrizaciones de los elementos de matriz y sus propiedades generales. También se muestran las expresiones teóricas para calcular las observables relevantes que deben compararse con los datos experimentales. El capítulo 4 está dedicado a los cálculos de amplitudes de tipo árbol y *loop* dentro del enfoque ChPT y el procedimiento seguido en el límite de la simetría de sabor SU(2). A continuación, se muestran los resultados obtenidos del ajuste de las LEC relevantes con los datos experimentales en el capítulo 5. También se presenta aquí la comparación de los observables teóricos en ChPT con los datos. En este trabajo, comparamos dos modelos: uno con la inclusión de la resonancia $\Delta(1232)$ y el otro en el caso sin Δ. Muestro los resultados obtenidos para los canales cargados y neutros de fotoproducción y electroproducción de piones en nucleones. Luego, en el capítulo 6 se presenta un estudio para la fotoproducción de piones neutros en núcleos de ^{12}C como una aplicación ejemplificada de los estudios de los capítulos anteriores. Finalmente, discuto los resultados finales y conclusiones en el Capítulo 7.

8.3 Resultados

En esta tesis, hemos estudiado la producción de piones mediante pruebas electromagnéticas en nucleones. Para cada uno de los estudios realizados aquí, nos enfocamos en la Teoría Quiral de Perturbaciones relativista para hadrones ligeros: nucleones, piones y los grados de libertad explícitos Δ. Para preservar la covariancia de la teoría, se implementó el método de renormalización en el esquema *Extended On Mass Shell* (EOMS). En este caso, las divergencias y los términos que violan el conteo de potencias se absorben en las constantes de baja energía (LECs) del Lagrangiano efectivo.

El presente trabajo se desarrolló dentro de tres estudios principales relacionados con la producción de piones a través de diferentes procesos. En detalle, se estudió la fotoproducción de piones en nucleones, donde se trataron los cuatro canales de carga físicos y sus observables. De manera análoga, se investigó una extensión a fotones virtuales con la electroproducción de piones en nucleones. Por último, se estudió la fotoproducción de piones en el núcleo ^{12}C como una aplicación de nuestros resultados de los procesos elementales (en nucleones). Estos estudios se distribuyen a través de los capítulos 4, 5, y 6. Nuestro objetivo era hacer un análisis global de los procesos elementales y determinar los valores de las LECs relevantes en el Lagrangiano de ChPT. El capítulo 4 estuvo dedicado al cálculo de la amplitud para la fotoproducción y electroproducción de piones en nucleones. El estudio de la fotoproducción se presenta como un caso particular de la electroproducción al considerar simplemente en el proceso el fotón real como un caso particular del virtual. A continuación, se calcularon los observables correspondientes por separado para cada reaccion.

En el capítulo 5 se presentan los resultados correspondientes para las LECs y los diversos observables en la producción electromagnética de piones cargados y neutros

sobre nucleones. Hemos comparado nuestras estimaciones teóricas con los observables correspondientes medidos para energías del centro de masa de hasta 60 MeV por encima del umbral. En este contexto, se ha implementado el procedimiento de ajuste de las LECs y se presenta el mejor ajuste numérico para dos modelos diferentes: uno con la contribución del grado de libertad $\Delta(1232)$ y el segundo para el caso sin Δ. Esto representa una exploración exhaustiva de los parámetros relevantes.

Por último, en el capítulo 6 como un ejemplo de aplicación de los resultados obtenidos, calculamos los efectos de la $\Delta(1232)$ en un modelo simple a bajas energías para la fotoproducción de π^0 en el núcleo ^{12}C. Aquí damos una estimación de las secciones eficaces coherentes e incoherentes en diversas energías del fotón en laboratorio hasta un máximo de $\sim$ 175 MeV. En este cálculo, se incorporaron los procesos elementales basados en los estudios con ChPT, es decir, la fotoproducción de π^0 en el protón y el neutrón con la inclusión de las LECs relevantes y previamente ajustadas. Por lo tanto, los resultados en este trabajo son predictivos, aunque dependientes del modelo nuclear usado y de sus propias renormalizaciones.

A lo largo de los capítulos 4 y 5 el estudio de la fotoproducción de piones cargados en blancos de nucleones se motivó como una extensión natural de los trabajos anteriores sobre la fotoproducción de piones neutrales en el protón dentro del mismo enfoque de ChPT a $\mathcal{O}(p^3)$. Los resultados recientes de este canal en particular han demostrado que la $\Delta(1232)$ juega un papel particularmente importante en mejorar el acuerdo con los datos en al menos 55 MeV por encima del umbral. Otros estudios anteriores dentro del mismo enfoque de ChPT covariante pero a $\mathcal{O}(p^4)$ y sin la presencia de la Δ como grado de libertad han mostrado un buen acuerdo con los datos solo a unos 20 MeV del umbral. La situación resultó ser que la inclusión de la $\Delta(1232)$ como un grado de libertad adicional a bajas energías es más relevante que las contribuciones de orden más alto. Más aún, el modelo en ChPT hasta $\mathcal{O}(p^3)$ mantiene el poder predictivo que de lo contrario se vería afectado con la inclusión de demasiadas LEC involucradas en un cálculo a $\mathcal{O}(p^4)$.

Además del estudio anterior sobre la fotoproducción de piones neutrales en el protón que incluye el mecanismo Δ en la ChPT relativista, varios aspectos inexplorados de esta reacción motivaron la extensión de ese estudio a través de otros mecanismos físicos. Entre ellos, hemos extendido el trabajo anterior al incluir los diversos canales de producción de piones. Esto se motivó por la sensibilidad del análisis a otros procesos en los que también se producen piones cargados.

Comenzamos con la investigación de la fotoproducción de piones cerca del umbral en nucleones, incluyendo los cuatro canales físicos para los piones cargados y neutros producidos. Hacemos hincapié en la importancia de la inclusión explícita de la $\Delta(1232)$ en estos procesos. Hemos realizado un cálculo completo a $\mathcal{O}(p^3)$ dentro del enfoque antes mencionado, ChPT covariante en el esquema de renormalización EOMS.

La inclusión de los canales cargados requiere la adición de un conjunto más amplio de topologías de diagramas de Feynman y por lo tanto algunas piezas adicionales del Lagrangiano quiral con las constantes de baja energía correspondientes, LECs.

Procedimos derivando primero las amplitudes a nivel de árbol y de un *loop* para todos los canales de carga de orden por orden hasta $\mathcal{O}(p^3)$. Además, incluimos la contribución explícita de la resonancia $\Delta(1232)$ a través del acoplamiento a los nucleones y piones (o fotones). Estos últimos diagramas sólo contribuyen al nivel de árbol, ya que las amplitudes correspondientes se cuentan como de orden 3/2 en nuestro conteo de

potencias con Δ. Los siguientes ordenes incluyen términos de árbol de *loop* con Δ pero se han descartado porque introducen contribuciones de orden superior a $\mathcal{O}(p^3)$, a saber a orden $\mathcal{O}(p^{7/2})$.

Además de la extensión a un análisis global para la fotoproducción de piones, un aspecto interesante está relacionado con los efectos del rompimiento de isospín debido a las diferencias de masa entre los piones cargados y neutros, y entre protones y neutrones. Este mecanismo es particularmente relevante para el canal $\gamma + p \to \pi^0 + p$, donde la observación del efecto de cúspide cerca del umbral se reproduce solo si se introducen las diferencias de masa en los cálculos de amplitud. En particular, encontramos que dentro del marco de la ChPT, los efectos de cúspide son consecuencia de diferentes canales de apertura para los *loops* de piones cargados y neutros. Este efecto es producido exclusivamente por amplitudes de *loop* dadas las diferentes contribuciones reales e imaginarias en la amplitud de algunos diagramas de *loop*. Como se esperaba de este mecanismo en ChPT, los efectos de cúspide no aparecen en los canales de fotoproducción de piones cargados, ya que el umbral físico del pion cargado ocurre a energías más altas que los *loops* con piones neutros y estos se encuentran suprimido por el espacio fase. Sin embargo, los efectos de rompimiento de isospín muestran tener contribuciones no nulas por encima del umbral y que son importantes para reproducir muchos de los datos a baja energía.

Finalmente, realizamos un estudio global de todos los datos disponibles actualmente en la región de baja energía. Esto equivale a medidas de secciones eficaces diferenciales y totales, así como asimetrías de haz y del blanco que miden observables de espín. Hemos comparado nuestros resultados teóricos con los datos y determinado como un primer paso los valores numéricos de las LECs relevantes.

Paralelamente a los estudios de fotoproducción de piones, la producción de piones por electrones $e + N \to e + \pi + N'$ se presenta en el capítulo 4 como un tratamiento más general de la fotoproducción de piones al considerar la virtualidad del fotón.

Dado que la interacción electrón-fotón es considerablemente más débil en comparación con las interacciones hadrónicas en el régimen de baja energía de QCD, la aproximación de un solo intercambio de fotón nos permite reducir fácilmente la amplitud del proceso de electroproducción a la fotoproducción pero con fotones virtuales. Este método permite calcular las amplitudes de electroproducción de una manera sencilla.

En este sentido, este estudio representa una extensión en la cinemática de los procesos considerados en la fotoproducción. Abordamos esta reacción de la misma forma en ChPT covariante a $\mathcal{O}(p^3)$ en EOMS y con la inclusión explícita de resonancias Δ, para los canales de piones neutros y cargados y con efectos de rompimiento de isospín.

La inclusión de la electroproducción en un análisis más amplio permite explorar la interacción de los nucleones con fotones virtuales, y por lo tanto investigar algunas piezas adicionales del Lagrangiano quiral.

Este estudio se motivó principalmente por encontrar más restricciones para las LECs. El proceso de electroproducción de piones permite el acceso a una amplia gama de datos para diversos observables, incluyendo ángulos de dispersión, energías, polarizaciones y momentos transferidos de un fotón virtual.

Hemos comparado nuestro modelo con los datos experimentales disponibles, esta vez para observables de fotoproducción y electroproducción juntos, con algunos límites cinemáticos para garantizar que los momentos externos fueran lo suficientemente pequeños. Hemos considerado una región cinemática restringida con $\sqrt{s} < 1.13$ GeV y

$Q^2 < 0.15\,\mathrm{GeV}^2$, donde esperábamos que nuestro modelo fuera confiable y aún estuviera por debajo del pico $\Delta(1232)$.

Los valores obtenidos para los LEC ajustados resultaron todos ser de tamaño natural, lo cual es satisfactorio desde el punto de vista de la convergencia quiral. Esto da respaldo a las estimaciones de incertidumbre de los cálculos recientes de producción de piones inducidos por neutrinos. La investigación exhaustiva de todos los canales de producción electromagnética de piones, incluyendo todos los observables disponibles, ha permitido desacoplar todas las LEC relevantes de tercer orden involucradas, y que aparecieron correlacionados en el caso de la fotoproducción.

Hemos confirmado la importancia de los términos de *loops*. Las partes imaginarias de la amplitud de dispersión y los efectos de cúspide, que provienen de la apertura de los diferentes canales de carga, son cruciales en la descripción de algunos observables de electroproducción a baja energía. También se muestra que la inclusión del mecanismo de rompimiento de isospín en los *loops* resuelve la inconsistencia con el parámetro relacionado con la dispersión πN a través de la relación de Goldberger–Treiman.

Con el modelo abordado en este trabajo, sólo 5 parámetros de ajuste fueron suficientes para describir bien todos los datos experimentales, consistiendo de aproximadamente 2700 puntos, para la dependencia angular y energética en las secciones eficaces y numerosos observables de polarización.

En resumen, la inclusión del mecanismo Δ en cálculos dentro de ChPT a $\mathcal{O}(p^3)$ es mejor que la extensión a cálculos de orden más altos que no incluyen la resonancia Δ. Sin Δ, nuestro modelo solo puede reproducir datos unos pocos MeV por encima del umbral. En particular, la fotoproducción de piones neutros es el canal más sensible a esta resonancia debido a la pequeñez de las contribuciones de orden inferior.

Los resultados del cálculo en la ChPT covariante a tercer orden y con la inclusión explícita de la Δ reproducen los datos de las secciones eficaces y las asimetrías de polarización de alta precisión de manera sorprendente. Por otro lado, el cálculo sin Δ realizado dentro del mismo enfoque demuestra una descripción mucho peor de los datos.

El estudio final dentro de la presente tesis se describe en el capítulo 6, en donde tratamos la fotoproducción del pion cercana al umbral en el núcleo ^{12}C. Nuestro propósito aquí se dividió en dos vías, a saber, aplicar y probar las LEC ajustadas que resultan del análisis en la producción electromagnética de piones en el marco de la ChPT, y estimar la contribución del mecanismo Δ en la sección eficaz nuclear.

El modelo para estudiar la reacción $^{12}\mathrm{C}(\gamma, \pi^0)$ se basó en la aproximación de impulso habitual en la que las amplitudes de nucleón libre describen la fotoproducción de piones en el núcleo a bajas energías desde cada nucleón ligado. En esta aproximación, es, por lo tanto, posible expresar la amplitud de la reacción nuclear en términos de las amplitudes elementales con nucleones. En nuestro caso, esta aproximación nos permitió calcular las secciones eficaces correspondientes en términos de las amplitudes de fotoproducción de π^0 en el protón y el neutrón dentro del enfoque de ChPT covariante, como antes. En particular, solo la parte de isovector independiente de espín fue relevante para el proceso en el núcleo de ^{12}C.

Efectos nucleares adicionales se introdujeron sistemáticamente. En primer lugar, la estructura nuclear para el núcleo ^{12}C se tomó en cuenta en la aproximación de impulso de onda plana (PWIA), suponiendo que las partículas entrantes y salientes, aquí el fotón y el pion observado, se propagaban como ondas planas a través de un medio nuclear.

El proceso de fotoproducción de piones puede incluir la contribución de transiciones inelásticas debido a los estados finales del núcleo excitado. Este tipo de mecanismo se considera típicamente cuando el núcleo final no se observa, como en los datos con los que comparamos nuestro modelo.

A continuación, dentro de la PWIA, obtenemos las contribuciones de sección eficaz nuclear de las transiciones coherentes e incoherentes al primer estado excitado 2^+ (4.43 MeV) como una buena aproximación. Esas transiciones coherentes e incoherentes particulares están principalmente descritas por la misma amplitud elemental.

Además, se ha incluido una contribución importante a la sección eficaz $^{12}\mathrm{C}(\gamma, \pi^0)$ mediante la interacción pion-núcleo en la aproximación de onda distorsionada por el impulso (DWIA, por sus siglas en inglés). Este efecto produce una distorsión de los piones que salen del núcleo debido a la re-dispersión con la materia nuclear, y su inclusión es estándar a energías cercanas al umbral, donde se reduce a un factor de escala aproximado. Se asumió que las contribuciones coherentes e incoherentes se corrigieron por igual mediante los efectos de distorsión del pion.

Nuestros cálculos, basados en las amplitudes obtenidas en el marco de ChPT aplicada a un modelo nuclear simple a bajas energías, reprodujeron satisfactoriamente la dependencia energética de la sección eficaz de la reacción $^{12}\mathrm{C}(\gamma, \pi^0)$. Hemos comparado los resultados predichos para energías hasta 40 MeV por encima del umbral. La contribución del proceso elemental se derivó tomando los valores numéricos de las LEC relevantes ya ajustados en este trabajo por datos de la producción electromagnética de piones en núcleos. La contribución de la re-dispersión de los piones en la materia nuclear se incluyó mediante el DWIA.

Hemos observado que los cálculos de ChPT a $\mathcal{O}(p^3)$ con y sin contribuciones de $\Delta(1232)$ reproducen una diferente dependencia en la energía. Sólo las estimaciones de la sección eficaz que incluyen la resonancia Δ junto con la consideración del scattering coherente e incoherente, y una adecuada inclusión de las interacciones del estado final (FSI) para piones distorsionados, estuvieron de acuerdo con las medidas experimentales.

A modo de conclusión, podemos decir que algunos de los enfoques más exitosos han sido los cálculos de ChPT dentro de la formalidad covariante completa. Allí, la expansión de la serie quiral está bajo control a bajas energías, y luego las contribuciones de mayor orden suelen ayudar a reproducir los datos medidos experimentalmente de mayor precisión. Sin embargo, la extensión hacia los órdenes superiores está limitada dada la cantidad de parámetros desconocidos (constantes de baja energía o LECs) que surgen. La consideración de grados de libertad adecuados, en la fotoproducción de piones como la resonancia de espín-3/2 Δ, resulta más conveniente que un cálculo de mayor orden sin su inclusión explícita. Aparte de las complicaciones técnicas añadidas, el modelo perdería su poder predictivo debido a la nueva serie de LECs indeterminadas que aparecen en el Lagrangiano. Además, las contribuciones de la resonancia Δ pueden reproducir datos en un rango más amplio de energías en los procesos de producción electromagnética de piones.

Finalmente, discutimos algunas cuestiones que pueden ser tratadas en estudios posteriores a esta tesis.

Nuestros resultados consistieron en la determinación de algunos parámetros relevantes en los procesos estudiados aquí. Como se muestra en el estudio de $^{12}\mathrm{C}(\gamma, \pi^0)$, los valores numéricos de las LECs pueden aplicarse a otros procesos de baja energía abordados dentro del mismo marco.

En concreto, todos los parámetros ajustados en este trabajo también aparecen en la evaluación de la producción de piones inducida por neutrinos en núcleos. Estos valores de parámetros podrían usarse para mejorar las predicciones correspondientes

de las secciones eficaces de neutrinos de baja energía en el núcleo, que son relevantes para lograr los objetivos de precisión de los experimentos de neutrinos modernos.

Además, nuestros resultados respaldan los primeros cálculos en ChPT de estos procesos de producción débil, que asumieron un tamaño natural para estos parámetros para estimar las incertidumbres de las predicciones teóricas. El examen de los acoplamientos vectoriales de los nucleones podría reducir las grandes incertidumbres que actualmente dificultan nuestros esfuerzos por proporcionar una predicción teóricamente bien fundamentada de la producción de piones inducida por neutrinos.

Esto es especialmente importante en la era de precisión actual de la física de neutrinos, donde un adecuado modelado de las secciones eficaces y de los fondos es necesario para la investigación de las masas de neutrinos, los ángulos de mezcla y otras propiedades. Finalmente, la extensión a la descripción de los datos de producción electrodébil avanzará aún más estos estudios, ofreciendo la posibilidad de hacer predicciones fiables y precisas para los procesos débiles donde los datos son más escasos.

Por otro lado, el marco utilizado para extraer los resultados en la producción electromagnética de piones en nucleones se puede extender de la simetría de sabor SU(2) a la simetría de sabor SU(3) y, por lo tanto, se puede aplicar a la extracción de otras propiedades de los bariones ligeros relacionadas con otros procesos de baja energía, incluida la extrañeza.

Finalmente, el marco teórico utilizado para obtener los resultados de la sección eficaz para la reacción $^{12}\mathrm{C}(\gamma, \pi^0)$ puede aplicarse a otros procesos nucleares similares de baja energía en los cuales las amplitudes elementales tienen lugar en los cálculos. Por ejemplo, el mismo procedimiento presentado aquí también es aplicable para resultados predictivos de la fotoproducción de piones en núcleos de $^{2}\mathrm{H}$ o $^{6}\mathrm{Li}$.

Appendix A

Feynman diagram amplitudes

Here, I detail the basic elements in building the amplitudes for the pion electromagnetic production on nucleons. A brief derivation of the relevant Feynman rules from the ChPT Lagrangian is illustrated below. Subsequently, the corresponding Feynman rules expressions for the vertices are given order by order.
Last, I present the explicit expressions for the tree and one-loop amplitudes for the four π-nucleon channels and for the two reactions, electro- and photoproduction respectively.

Feynman rules for vertices at LO

First, I will detail some representative examples in the derivation of the Feynman rules for vertices involved in the $\mathcal{O}(p^1)$ tree diagrams shown in Fig. 4.1 (a)-(d). For all the higher order $\mathcal{O}(p^{n>1})$ diagrams, the Feynman rules and amplitudes are obtained in the same way. The respective vertices for each order are pointed out in Fig.4.1 derived from the corresponding higher order Lagrangian pieces in Eq. (4.3).
As we see in the $\mathcal{O}(p^1)$ diagrams in Figures 4.1 (a)-(c), they only involve vertices at $\mathcal{O}(p^1)$ from the interacting terms in the nucleon Lagrangian $\mathcal{L}_N^{(1)}$ (2.61). The $\mathcal{O}(p^1)$ pion-exchange diagram in Figure 4.1 (d) involves a second-order $\mathcal{O}(p^2)$ vertex coming from the lowest-order pion Lagrangian $\mathcal{L}_{\pi\pi}^{(2)}$ (2.38). To begin, one derives the Feynman rules vertices at $\mathcal{O}(p^1)$ from the LO Lagrangian (2.61),

$$\mathcal{L}_N^{(1)} = \overline{N}\Bigg(\underbrace{i\gamma^\mu\partial_\mu - m}_{\mathcal{L}_N^{(1)\,\mathrm{free}}} + \underbrace{i\gamma^\mu\Gamma_\mu}_{\mathcal{L}_N^{(1)\,\mathrm{S}}} + \underbrace{\frac{g}{2}\gamma^\mu\gamma^5 u_\mu}_{\mathcal{L}_N^{(1)\,\mathrm{PS}}}\Bigg)N\,, \tag{A.1}$$

the nucleon isospin doublet is $N = (p, n)^T$, the different terms are signaled for the free nucleon interaction term $\mathcal{L}_N^{(1)\,\mathrm{free}}$, a scalar, $\mathcal{L}_N^{(1)\,\mathrm{S}}$, and pseudoscalar-vector couplings, $\mathcal{L}_N^{(1)\,\mathrm{PS}}$. As pointed in Eqs. (2.53) and (2.62) the tensors u_μ and Γ_μ with external electromagnetic field sources $\mathscr{A}_\mu$ are

$$\Gamma_\mu = \frac{1}{2}\left\{u^\dagger\left(\partial_\mu - ie\mathscr{A}_\mu Q\right)u + u\left(\partial_\mu - ie\mathscr{A}_\mu Q\right)u^\dagger\right\}, \tag{A.2}$$

$$u_\mu = iu^\dagger\left(\partial_\mu - ie\mathscr{A}_\mu[Q, u^2]\right)u^\dagger, \tag{A.3}$$

with the isospin charge matrix $Q = \frac{1}{2}(\mathbf{1} + \tau^3)$. In the above expressions, the pion coset u expands as

$$u = U^{1/2} = \exp i\Phi/2F = \mathbf{1} + i\frac{\Phi}{2F} - \frac{\Phi^2}{8F^2} + \cdots , \tag{A.4}$$

with

$$\Phi = \vec{\tau}\cdot\vec{\pi} = \begin{pmatrix} \pi_3 & \pi_1 - i\pi_2 \\ \pi_1 + i\pi_2 & -\pi_3 \end{pmatrix} = \begin{pmatrix} \pi^0 & \sqrt{2}\pi^+ \\ \sqrt{2}\pi^- & -\pi^0 \end{pmatrix} . \tag{A.5}$$

where the pion fields, π^a, entering in Φ are represented in the cartesian and isospin basis through the Pauli matrices Eq. (3.99). Then, the scalar $\mathcal{L}_N^{(1)\,\mathrm{S}}$ and pseudoscalar $\mathcal{L}_N^{(1)\,\mathrm{PS}}$ Lagrangian terms in (A.1) expands in the isospin basis as

$$\mathcal{L}_N^{(1)S} = e\,\overline{p}\gamma^\mu \mathscr{A}_\mu p + \frac{i}{4F^2}\left(\overline{n}\pi^-\partial_\mu\pi^+\gamma^\mu n - \overline{n}\pi^+\partial_\mu\pi^-\gamma^\mu n + \cdots\right. \tag{A.6}$$

$$\begin{aligned}\mathcal{L}_N^{(1)PS} =& i\frac{e\,g}{\sqrt{2}F}\left(\overline{p}\pi^+\gamma^\mu\mathscr{A}_\mu\gamma^5 n - \overline{n}\pi^-\gamma^\mu\mathscr{A}_\mu\gamma^5 p\right) \\ &- \frac{g}{2F}\left(\overline{p}\partial\!\!\!/\pi^0\gamma^5 p + \sqrt{2}\,\overline{p}\partial\!\!\!/\pi^+\gamma^5 n + \sqrt{2}\,\overline{n}\partial\!\!\!/\pi^-\gamma^5 p - \overline{n}\partial\!\!\!/\pi^0\gamma^5 n\right) + \cdots ,\end{aligned} \tag{A.7}$$

The first term in $\mathcal{L}_N^{(1)S}$ from (A.6) corresponds to the LO interaction vertex γpp, and the following terms proportional to $1/F^2$ lead the $\pi\pi NN$ interaction vertices used afterwards for the pion-loop diagrams. The expansion of the pseudoscalar term $\mathcal{L}_N^{(1)PS}$ (A.7) includes *e.g.* the interaction terms for the $\gamma\pi NN$ and πNN coupling vertices. Thus, the different interaction terms appearing in the previous expressions can be grouped as follows

$$\mathcal{L}_{\gamma NN}^{(1)} = e\,\overline{p}\gamma^\mu\mathscr{A}_\mu p, \tag{A.8}$$

$$\mathcal{L}_{\gamma\pi NN}^{(1)} = i\frac{e\,g}{\sqrt{2}F}\left(\overline{p}\pi^+\gamma^\mu\mathscr{A}_\mu\gamma^5 n - \overline{n}\pi^-\gamma^\mu\mathscr{A}_\mu\gamma^5 p\right), \tag{A.9}$$

$$\mathcal{L}_{\pi NN}^{(1)} = \frac{g}{2F}\left(\overline{n}\partial\!\!\!/\pi^0\gamma^5 n - \sqrt{2}\,\overline{p}\partial\!\!\!/\pi^+\gamma^5 n - \sqrt{2}\,\overline{n}\partial\!\!\!/\pi^-\gamma^5 p - \overline{p}\partial\!\!\!/\pi^0\gamma^5 p\right). \tag{A.10}$$

where the subscripts in the Lagrangian terms indicates the associated interacting vertices. From the above terms, we get the corresponding amplitudes for the vertices depicted in Fig. A.1 with diagrams.

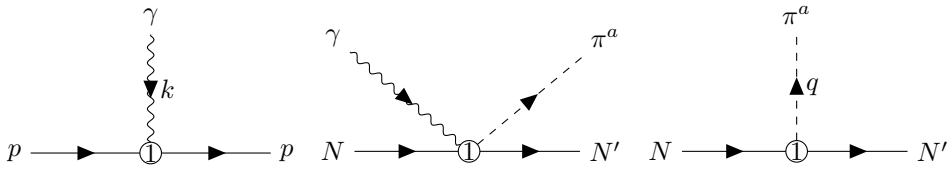

FIGURE A.1: Feynman diagrams for the $\gamma NN'$, $\gamma N\pi N'$ and $NN'\pi$ vertices and corresponding to the amplitudes in Eqs. (A.11), (A.12) and (A.13) respectively.

In detail, the $\mathcal{O}(p^n)$ vertex Feynman rules, here denoted by $\mathcal{V}_{\mathrm{vertex}}^{(n)}$, can be obtained for each vertex through the following amplitudes

$$\left\langle N'(p')\left|i\mathcal{L}^{(1)}_{\gamma NN}\right|\gamma(k),N(p)\right\rangle = \epsilon_\mu \overline{u}_{N'}(p')\mathcal{V}^{\mu\,(1)}_{\gamma N;N'}u_N(p), \tag{A.11}$$

$$\left\langle \pi^a(q),N'(p')\left|i\mathcal{L}^{(1)}_{\gamma\pi NN}\right|\gamma(k),N(p)\right\rangle = \epsilon_\mu \overline{u}_{N'}(p')\mathcal{V}^{\mu\,(1)}_{\gamma N;\pi N'}u_N(p), \tag{A.12}$$

$$\left\langle \pi^a(q),N'(p')\left|i\mathcal{L}^{(1)}_{\pi NN}\right|N(p)\right\rangle = \overline{u}_{N'}(p')\mathcal{V}^{(1)}_{N;\pi N'}u_N(p), \tag{A.13}$$

where $\mathcal{V}^{\mu\,(1)}_{\gamma N;N'}$, $\mathcal{V}^{\mu\,(1)}_{\gamma N;\pi N'}$, $\mathcal{V}^{(1)}_{N;\pi N'}$ indicates the Feynman rules expressions for the $\gamma NN'$, $\gamma N\pi N'$ and $NN'\pi$ vertices respectively. The 4-momenta conservation is included by taking the photon and the initial nucleon with incoming momenta, and the pion and final nucleon with outgoing momenta [1]. Explicitly, the Feynman rules for the vertices in Fig. A.1 are extracted from (A.11)-(A.13) in the physical basis by just specifying the isospin of nucleons and pions $\pi^a = \{\pi^+,\pi^-,\pi^0\}$:

$$\mathcal{V}^{\mu\,(1)}_{\gamma N;N'} = \begin{cases} ie\gamma^\mu, & \text{for } \gamma p \to p, \\ 0, & \text{otherwise} \end{cases} \tag{A.14}$$

$$\mathcal{V}^{\mu\,(1)}_{\gamma N;\pi N'} = \begin{cases} \dfrac{e\,g}{\sqrt{2}F}\gamma^\mu\gamma^5, & \text{for } \gamma p \to \pi^+ n, \\ -\dfrac{e\,g}{\sqrt{2}F}\gamma^\mu\gamma^5, & \text{for } \gamma n \to \pi^- p, \\ 0, & \text{otherwise} \end{cases} \tag{A.15}$$

$$\mathcal{V}^{(1)}_{N;\pi N'} = \begin{cases} \dfrac{g}{2F}\not{q}\gamma^5, & \text{for } p \to \pi^0 p, \\ -\dfrac{g}{2F}\not{q}\gamma^5, & \text{for } n \to \pi^0 n, \\ \dfrac{g}{\sqrt{2}F}\not{q}\gamma^5, & \text{for } p \to \pi^+ n,\ n \to \pi^- p. \end{cases} \tag{A.16}$$

Anagously, for the LO pion Lagrangian at $\mathcal{O}(p^2)$ (2.38) with external EM sources

$$\mathcal{L}^{(2)}_{\pi\pi} = \frac{F^2}{4}\mathrm{Tr}\left\{\left(\partial^\mu U - ie\mathscr{A}^\mu[Q,U]\right)\left(\partial_\mu U - ie\mathscr{A}_\mu[Q,U]\right)^\dagger + \chi U^\dagger + U\chi^\dagger\right\} \tag{A.17}$$

the Feynman rules can be derived by expanding $U = u^2$ as in Eq. (A.4). The Feynman rule for the $\pi\pi\gamma$ vertex involved in the diagram amplitude 4.1-(d) and depicted in Fig. A.2, corresponds to the term in the expansion

$$\mathcal{L}^{(2)}_{\pi\pi} = ie\mathscr{A}^\mu\left(\pi^+\partial_\mu\pi^- - \pi^-\partial_\mu\pi^+\right) + \cdots, \tag{A.18}$$

which results in the amplitude for the $\gamma\pi\pi$ vertex

$$\left\langle \pi^b(q_b)\left|i\mathcal{L}^{(2)}_{\pi\pi}\right|\gamma(k),\pi^a(q_a)\right\rangle = \epsilon_\mu \mathcal{V}^{\mu\,(2)}_{\gamma\pi;\pi}. \tag{A.19}$$

$\mathcal{V}^{\mu\,(2)}_{\gamma\pi;\pi}$ stands for the interacting vertex $\gamma\pi\pi$ Feynman rule, for incoming pion and photon fields and an outgoing pion. Due to the charge and 4-momenta conservation, the incoming and outgoing pion are of the same charge, or with opposite charge when both pions are incoming.

[1] In the momentum space amplitudes the space integral $\int d^4x\langle f(p'+q)|i\mathcal{L}|i(p+k)\rangle = (2\pi)^4\delta^4(p'+q-p-k)\langle f(p'+q)|i\mathcal{L}|i(p+k)\rangle$ understood when applying momenta conservation.

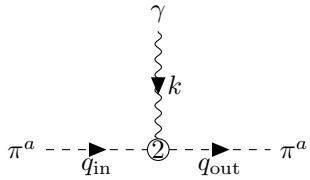

FIGURE A.2: Feynman diagram for the $\gamma\pi\pi$ vertex corresponding to the amplitude in (A.19).

The resulting Feynman vertex rule is written as

$$\mathcal{V}^{\mu\,(2)}_{\gamma\pi;\pi} = \begin{cases} ie\left(q^\mu_{\rm in} + q^\mu_{\rm out}\right), & \text{for } \gamma\pi^+ \to \pi^+, \\ -ie\left(q^\mu_{\rm in} + q^\mu_{\rm out}\right), & \text{for } \gamma\pi^- \to \pi^-, \\ 0, & \text{otherwise} \end{cases} \tag{A.20}$$

with the 4-momenta conservation $q^\mu_{\rm in} = q^\mu_{\rm out} - k^\mu$. The rest of Feynman rules for the other vertices at $\mathcal{O}(p^2)$, $\mathcal{O}(p^3)$ and $\mathcal{O}(p^4)$ are obtained in the same way and are displayed explicitly in App. A.1.

Feynman rules for propagators

The corresponding rules for the internal lines in the diagrams 4.1 are given by the on-mass-shell propagators. For the pseudoscalar pion multiplet with 4-momentum q and invariant mass M, the corresponding propagator in the momentum space reads

$$iS_\pi(q) = \frac{i}{q^2 - M^2 + i\epsilon} \tag{A.21}$$

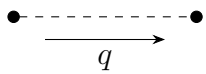

For the fermionic nucleon multiplet with 4-momentum p and mass m, the propagator is

$$iS_N(p) = i\frac{\not{p} + m}{p^2 - m^2 + i\epsilon} \tag{A.22}$$

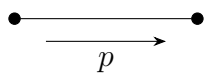

The diagrams with the explicit contribution of the Δ-resonance, Fig. 4.3, are calculated with the corresponding Rarita-Schwinger propagator

$$iS^{\mu\nu}_\Delta(P) \tag{A.23}$$

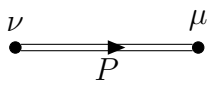

where

$$S^{\mu\nu}_\Delta(P) = \frac{\not{P} + m_\Delta}{P^2 - m^2_\Delta + i\epsilon}\left[-g^{\mu\nu} + \frac{1}{D-1}\gamma^\mu\gamma^\nu + \frac{(\gamma^\mu P^\nu - \gamma^\nu P^\mu)}{(D-1)m_\Delta} + \frac{(D-2)}{(D-1)m^2_\Delta}P^\mu P^\nu\right] \tag{A.24}$$

which is a 2nd-rank tensor. The number D indicates the space-time dimension, in

this case $D = 4$ is enough for the tree level Feynman amplitudes. From the Δ ChPT Lagrangian this propagator couples to the vertices $N\Delta\gamma$ and $N\Delta\pi$, given in App. A.1.

A.1 Vertex Feynman-rules

A.1.1 $\mathcal{O}(p^1)$ vertices

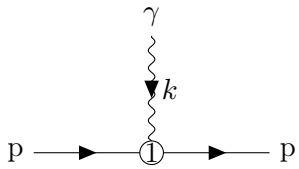

$$\mathcal{V}^{\mu\,(1)}_{\gamma p;p} = ie\gamma^\mu \tag{A.25}$$

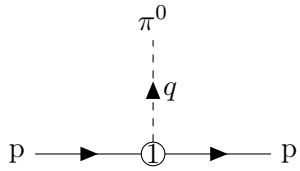

$$\mathcal{V}^{(1)}_{p;p\pi^0} = \frac{g}{2F}\not{q}\gamma^5 \tag{A.26}$$

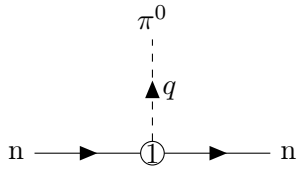

$$\mathcal{V}^{(1)}_{n;n\pi^0} = -\frac{g}{2F}\not{q}\gamma^5 \tag{A.27}$$

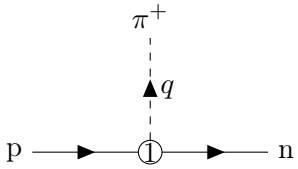

$$\mathcal{V}^{(1)}_{p;n\pi^+} = \frac{g}{\sqrt{2}F}\not{q}\gamma^5 \tag{A.28}$$

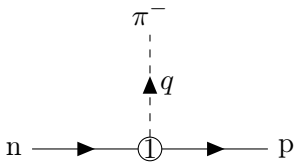

$$\mathcal{V}^{(1)}_{n;p\pi^-} = \frac{g}{\sqrt{2}F}\not{q}\gamma^5 \tag{A.29}$$

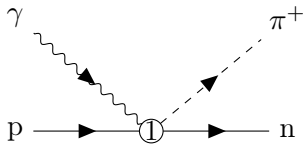

$$\mathcal{V}^{\mu\,(1)}_{\gamma p;n\pi^+} = \frac{e\,g}{\sqrt{2}F}\gamma^\mu\gamma^5 \tag{A.30}$$

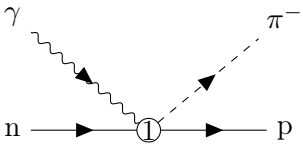

$$\mathcal{V}^{\mu\,(1)}_{\gamma n;p\pi^-} = -\frac{e\,g}{\sqrt{2}F}\gamma^\mu\gamma^5 \tag{A.31}$$

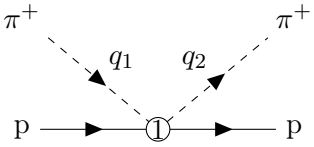

$$\mathcal{V}^{(1)}_{p\pi^+;p\pi^+} = -\frac{i}{4F^2}\left(\not{q}_1 + \not{q}_2\right) \tag{A.32}$$

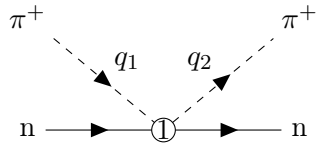

$$\mathcal{V}^{(1)}_{n\pi^+;n\pi^+} = \frac{i}{4F^2}\left(\not{q}_1 + \not{q}_2\right) \tag{A.33}$$

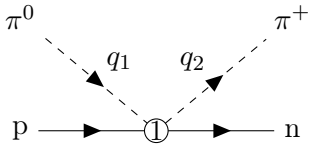

$$\mathcal{V}^{(1)}_{p\pi^0;n\pi^+} = \frac{i}{2\sqrt{2}F^2}\left(\not{q}_1 + \not{q}_2\right) \tag{A.34}$$

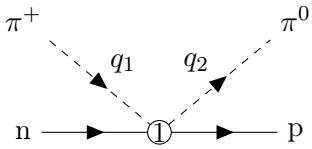

$$\mathcal{V}^{(1)}_{n\pi^+;p\pi^0} = \frac{i}{2\sqrt{2}F^2}\left(\not{q}_1 + \not{q}_2\right) \tag{A.35}$$

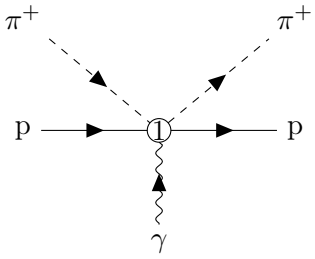

$$\mathcal{V}^{\mu\,(1)}_{\gamma p\pi^+;p\pi^+} = -\frac{ie}{2F^2}\gamma^\mu \tag{A.36}$$

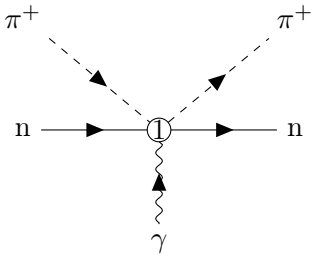

$$\mathcal{V}^{\mu\,(1)}_{\gamma n\pi^+;n\pi^+} = \frac{ie}{2F^2}\gamma^\mu \tag{A.37}$$

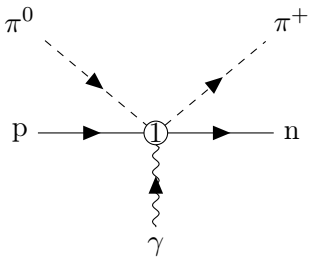

$$\mathcal{V}^{\mu\,(1)}_{\gamma p\pi^0;n\pi^+} = \frac{ie}{2\sqrt{2}F^2}\gamma^\mu \tag{A.38}$$

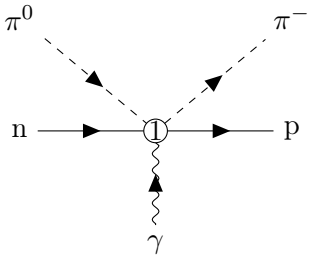

$$\mathcal{V}^{\mu\,(1)}_{\gamma n\pi^0;p\pi^-} = \frac{ie}{2\sqrt{2}F^2}\gamma^\mu \tag{A.39}$$

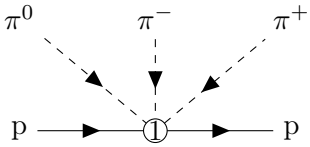

$$\mathcal{V}^{(1)}_{p\pi^+\pi^-\pi^0;p} = \frac{g}{12F^3}\left(2\not{q}^0 - \not{q}^- - \not{q}^+\right)\gamma^5 \tag{A.40}$$

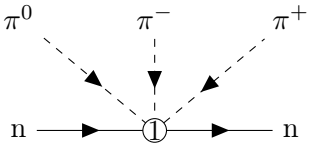

$$\mathcal{V}^{(1)}_{n\pi^+\pi^-\pi^0;n} = -\frac{g}{12F^3}\left(2\not{q}^0 - \not{q}^- - \not{q}^+\right)\gamma^5 \tag{A.41}$$

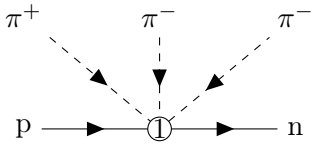

$$\mathcal{V}^{(1)}_{p\pi^-\pi^-\pi^+;n} = \frac{g}{F^3}\left(-\frac{\sqrt{2}}{6}\not{q}^+ + \frac{1}{6\sqrt{2}}\left[\not{q}_1^- + \not{q}_2^-\right]\right)\gamma^5 \tag{A.42}$$

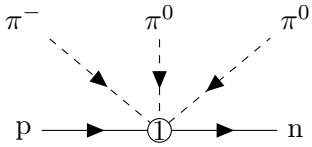

$$\mathcal{V}^{(1)}_{p\pi^0\pi^0\pi^-;n} = \frac{g}{F^3}\left(\frac{\sqrt{2}}{6}\not{q}^- - \frac{1}{6\sqrt{2}}\left[\not{q}_1^0 + \not{q}_2^0\right]\right)\gamma^5 \tag{A.43}$$

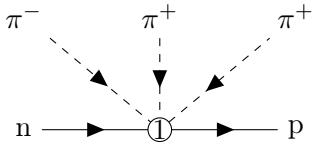

$$\mathcal{V}^{(1)}_{n\pi^+\pi^+\pi^-;p} = \frac{g}{F^3}\left(-\frac{\sqrt{2}}{6}\not{q}^- + \frac{1}{6\sqrt{2}}\left[\not{q}_1^+ + \not{q}_2^+\right]\right)\gamma^5 \tag{A.44}$$

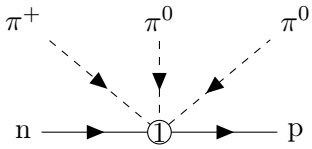

$$\mathcal{V}^{(1)}_{n\pi^0\pi^0\pi^+;p} = \frac{g}{F^3}\left(-\frac{\sqrt{2}}{6}\not{q}^+ - \frac{1}{6\sqrt{2}}\left[\not{q}_1^0 + \not{q}_2^0\right]\right)\gamma^5 \tag{A.45}$$

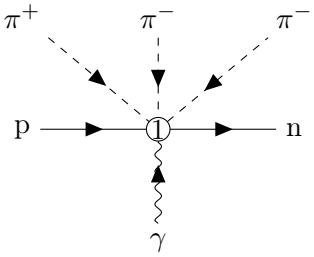

$$\mathcal{V}^{\mu\,(1)}_{\gamma p\pi^-\pi^-\pi^+;n} = -\frac{\sqrt{2}e\,g}{3F^3}\gamma^\mu\gamma^5 \tag{A.46}$$

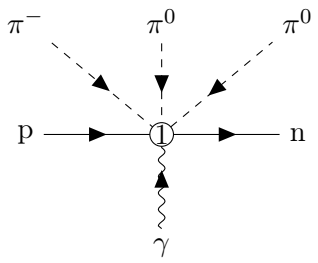

$$\mathcal{V}^{\mu\,(1)}_{\gamma p\pi^0\pi^0\pi^-;n} = -\frac{\sqrt{2}e\,g}{6F^3}\gamma^\mu\gamma^5 \tag{A.47}$$

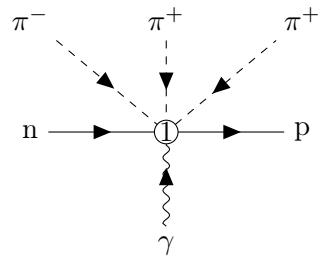

$$\mathcal{V}^{\mu\,(1)}_{\gamma n\pi^+\pi^+\pi^-;p} = \frac{\sqrt{2}e\,g}{3F^3}\gamma^\mu\gamma^5 \tag{A.48}$$

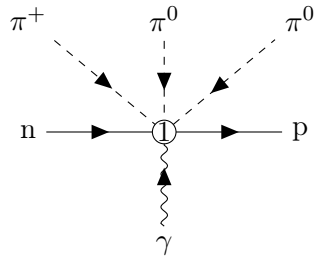

$$\mathcal{V}^{\mu\,(1)}_{\gamma n\pi^0\pi^0\pi^+;p} = \frac{\sqrt{2}e\,g}{6F^3}\gamma^\mu\gamma^5 \tag{A.49}$$

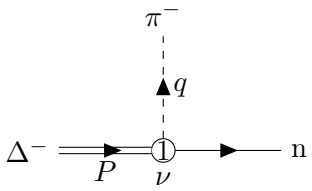

$$\mathcal{V}^{\nu\,(1)}_{\Delta^-;n\pi^-} = -\frac{h_A}{2Fm_\Delta}\gamma^{\mu\nu\lambda}P_\mu q_\lambda = -\text{H.c.} \tag{A.50}$$

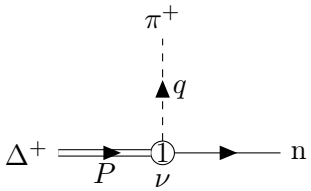

$$\mathcal{V}^{\nu\,(1)}_{\Delta^+;n\pi^+} = \frac{h_A}{2\sqrt{3}Fm_\Delta}\gamma^{\mu\nu\lambda}P_\mu q_\lambda = -\text{H.c.} \tag{A.51}$$

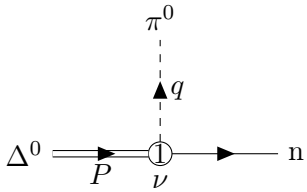

$$\mathcal{V}^{\nu\,(1)}_{\Delta^0;n\pi^0} = -\frac{h_A}{\sqrt{6}Fm_\Delta}\gamma^{\mu\nu\lambda}P_\mu q_\lambda = -\text{H.c.} \tag{A.52}$$

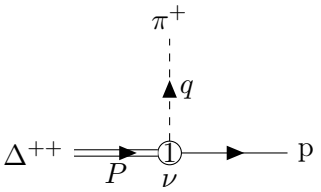

$$\mathcal{V}^{\nu\,(1)}_{\Delta^{++};p\pi^+} = \frac{h_A}{2Fm_\Delta}\gamma^{\mu\nu\lambda}P_\mu q_\lambda = -\text{H.c.} \tag{A.53}$$

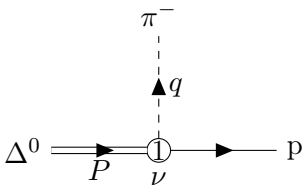

$$\mathcal{V}^{\nu\,(1)}_{\Delta^0;p\pi^-} = -\frac{h_A}{2\sqrt{3}Fm_\Delta}\gamma^{\mu\nu\lambda}P_\mu q_\lambda = -\text{H.c.} \tag{A.54}$$

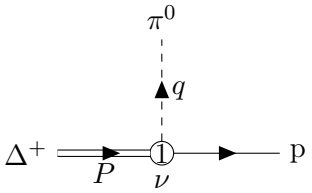

$$\mathcal{V}^{\nu\,(1)}_{\Delta^+;p\pi^0} = -\frac{h_A}{\sqrt{6}Fm_\Delta}\gamma^{\mu\nu\lambda}P_\mu q_\lambda = -\text{H.c.} \tag{A.55}$$

A.1.2 $\mathcal{O}(p^2)$ vertices

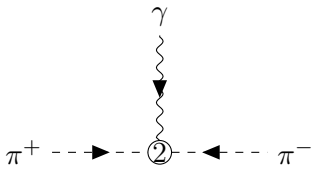

$$\mathcal{V}^{\mu\,(2)}_{\gamma\pi^+\pi^-;} = ie(q_+ - q_-)^\mu \tag{A.56}$$

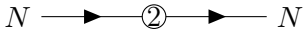

$$\mathcal{V}^{(2)}_{N;N} = i\,4M^2c_1 \tag{A.57}$$

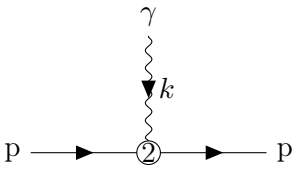

$$\mathcal{V}^{\mu\,(2)}_{\gamma p;p} = \frac{e}{2m}k_\nu\sigma^{\nu\mu}(c_6 + c_7) \tag{A.58}$$

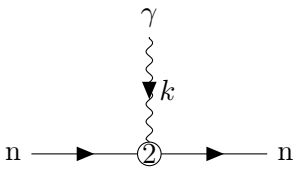

$$\mathcal{V}^{\mu\,(2)}_{\gamma n;n} = \frac{e}{2m}k_\nu\sigma^{\nu\mu}c_7 \tag{A.59}$$

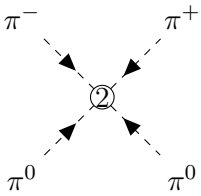

$$\mathcal{V}^{(2)}_{\pi^+\pi^-\pi^0\pi^0;} = \frac{i}{3F^2}\Big(M^2 + 2q_1^0\cdot q_2^0 + 2q^+\cdot q^- - (q^+ + q^-)\cdot(q_1^0 + q_2^0)\Big) \tag{A.60}$$

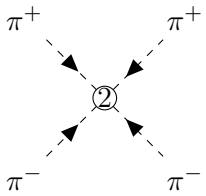

$$\mathcal{V}^{(2)}_{\pi^+\pi^+\pi^-\pi^-;} = \frac{i}{3F^2}\Big(2M^2 - 2q_1^- \cdot q_2^- - 2q_1^+ \cdot q_2^+ + (q_1^- + q_2^-)\cdot(q_1^+ + q_2^+)\Big) \tag{A.61}$$

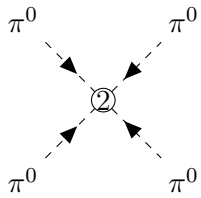

$$\mathcal{V}^{(2)}_{\pi^0\pi^0\pi^0\pi^0;} = i\frac{M^2}{F^2} \tag{A.62}$$

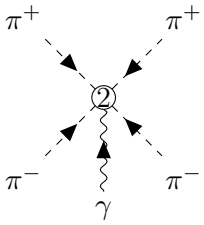

$$\mathcal{V}^{\mu\,(2)}_{\gamma\pi^+\pi^+\pi^-\pi^-;} = i\frac{4e}{3F^2}\left[(q_1^- + q_2^-) - (q_1^+ + q_2^+)\right]^\mu \tag{A.63}$$

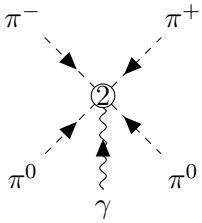

$$\mathcal{V}^{\mu\,(2)}_{\gamma\pi^+\pi^-\pi^0\pi^0;} = i\frac{2e}{3F^2}(q^- - q^+)^\mu \tag{A.64}$$

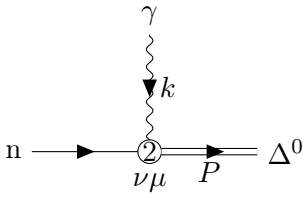

$$\mathcal{V}^{\nu\mu\,(2)}_{\gamma n;\Delta^0} = \sqrt{\frac{3}{2}}\frac{e\,g_M}{2m(m+m_\Delta)}2\varepsilon^{\alpha\nu\beta\mu}P_\alpha k_\beta = \text{H.c.} \tag{A.65}$$

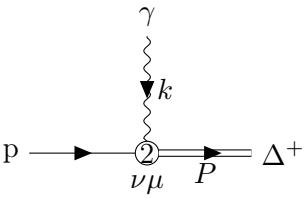

$$\mathcal{V}^{\nu\mu\,(2)}_{\gamma p;\Delta^+} = \sqrt{\frac{3}{2}}\frac{e g_M}{2m(m+m_\Delta)}2\varepsilon^{\alpha\nu\beta\mu}P_\alpha k_\beta = \text{H.c.} \tag{A.66}$$

A.1.3 $\mathcal{O}(p^3)$ vertices

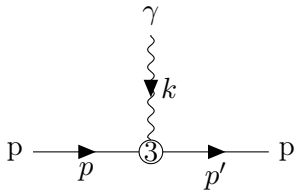

$$\mathcal{V}^{\mu\,(3)}_{\gamma p;p} = i\frac{e}{2m}k_\nu\left[k^\mu\left(p+p'\right)^\nu - k^\nu\left(p+p'\right)^\mu\right](2d_7+d_6) \tag{A.67}$$

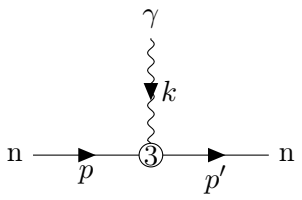

$$\mathcal{V}^{\mu\,(3)}_{\gamma n;n} = i\frac{e}{2m}k_\nu\left[k^\mu\left(p+p'\right)^\nu - k^\nu\left(p+p'\right)^\mu\right](2d_7-d_6) \tag{A.68}$$

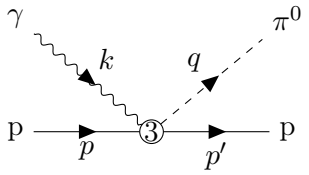

$$\mathcal{V}^{\mu\,(3)}_{\gamma p;p\pi^0} = i\frac{e}{mF}2\varepsilon^{\mu\nu\alpha\beta}k_\nu(p_\beta+p'_\beta)q_\alpha(d_8+d_9) \tag{A.69}$$

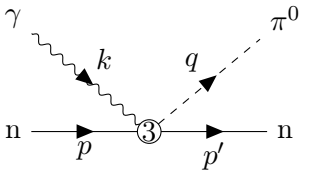

$$\mathcal{V}^{\mu\,(3)}_{\gamma n;n\pi^0} = i\frac{e}{mF}2\varepsilon^{\mu\nu\alpha\beta}k_\nu(p_\beta+p'_\beta)q_\alpha(d_8-d_9) \tag{A.70}$$

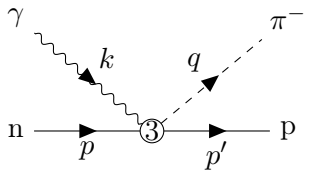

$$\mathcal{V}^{\mu\,(3)}_{\gamma n;p\pi^-} = i\frac{\sqrt{2}e}{mF}2\varepsilon^{\mu\nu\alpha\beta}k_\nu(p_\beta+p'_\beta)q_\alpha d_9 \tag{A.71}$$

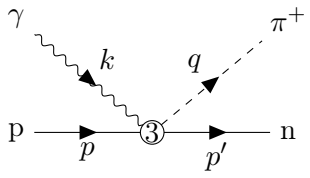

$$\mathcal{V}^{\mu\,(3)}_{\gamma p;n\pi^+} = i\frac{\sqrt{2}e}{mF}2\varepsilon^{\mu\nu\alpha\beta}k_\nu(p_\beta+p'_\beta)q_\alpha d_9 \tag{A.72}$$

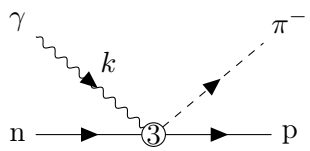

$$\mathcal{V}^{\mu\,(3)}_{\gamma n;p\pi^-} = \frac{\sqrt{2}eM^2}{F}\gamma^\mu\gamma^5(d_{18}-2d_{16}) \tag{A.73}$$

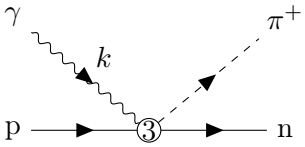

$$\mathcal{V}^{\mu\,(3)}_{\gamma p;n\pi^+} = -\frac{\sqrt{2}eM^2}{F}\gamma^\mu\gamma^5(d_{18}-2d_{16}) \tag{A.74}$$

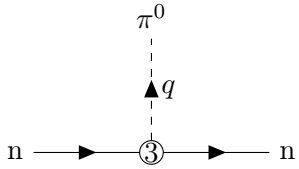

$$\mathcal{V}^{(3)}_{n;n\pi^0} = \frac{M^2}{F}\not{q}\gamma^5(d_{18}-2d_{16}) \tag{A.75}$$

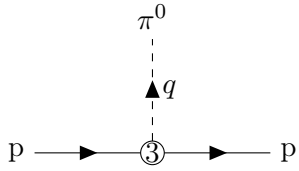

$$\mathcal{V}^{(3)}_{p;p\pi^0} = -\frac{M^2}{F}\not{q}\gamma^5(d_{18}-2d_{16}) \tag{A.76}$$

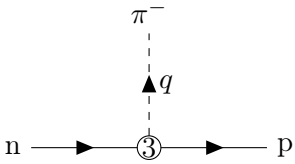

$$\mathcal{V}^{(3)}_{n;p\pi^-} = -\frac{\sqrt{2}M^2}{F}\not{q}\gamma^5(d_{18}-2d_{16}) \tag{A.77}$$

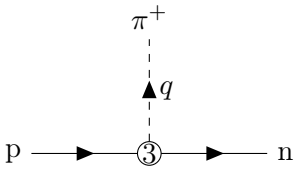

$$\mathcal{V}^{(3)}_{p;n\pi^+} = -\frac{\sqrt{2}M^2}{F}\not{q}\gamma^5(d_{18}-2d_{16}) \tag{A.78}$$

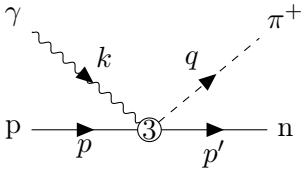

$$\begin{aligned}\mathcal{V}^{\mu\,(3)}_{\gamma p;n\pi^+} =& \frac{e}{\sqrt{2}m^2F}k_\nu\Big[\gamma^\mu\gamma^5(p\cdot qp^\nu + p'\cdot qp'^\nu)\\ &-\gamma^\nu\gamma^5(p\cdot qp^\mu + p'\cdot qp'^\mu)\Big]d_{20}\end{aligned} \tag{A.79}$$

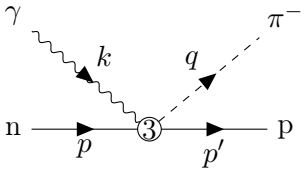

$$\begin{aligned}\mathcal{V}^{\mu\,(3)}_{\gamma n;p\pi^-} =& -\frac{e}{\sqrt{2}m^2F}k_\nu\Big[\gamma^\mu\gamma^5(p\cdot qp^\nu + p'\cdot qp'^\nu)\\ &-\gamma^\nu\gamma^5(p\cdot qp^\mu + p'\cdot qp'^\mu)\Big]d_{20}\end{aligned} \tag{A.80}$$

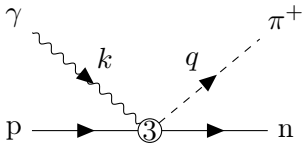

$$\mathcal{V}^{\mu\,(3)}_{\gamma p;n\pi^+} = \frac{2e}{\sqrt{2}F}k_\nu\left(\gamma^\mu\gamma^5q^\nu - \gamma^\nu\gamma^5q^\mu\right)d_{21} \tag{A.81}$$

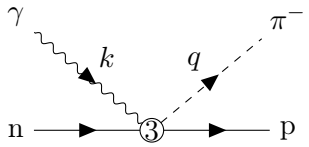

$$\mathcal{V}^{\mu\,(3)}_{\gamma n;p\pi^-} = -\frac{2e}{\sqrt{2}F} k_\nu \left(\gamma^\mu\gamma^5 q^\nu - \gamma^\nu\gamma^5 q^\mu\right) d_{21} \tag{A.82}$$

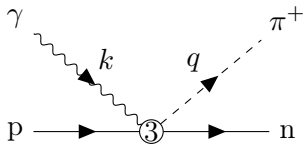

$$\mathcal{V}^{\mu\,(3)}_{\gamma p;n\pi^+} = -\frac{e}{\sqrt{2}F} k_\nu \left(\gamma^\mu\gamma^5 (q-k)^\nu - \gamma^\nu\gamma^5 (q-k)^\mu\right) d_{22} \tag{A.83}$$

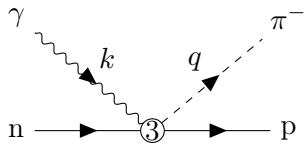

$$\mathcal{V}^{\mu\,(3)}_{\gamma n;p\pi^-} = \frac{e}{\sqrt{2}F} k_\nu \left(\gamma^\mu\gamma^5 (q-k)^\nu - \gamma^\nu\gamma^5 (q-k)^\mu\right) d_{22} \tag{A.84}$$

A.1.4 $\mathcal{O}(p^4)$ vertices

Using pion Lagrangian at $\mathcal{O}(q^4)$ of Gasser, Sainio and Svarc, Eq. (2.44), we have the following Feynman rules

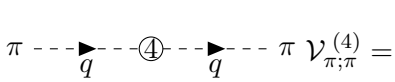

$$\mathcal{V}^{(4)}_{\pi;\pi} = -i\frac{2M^2}{F^2}\left(M^2 l_3 + \left[M^2 - q^2\right] l_4\right) \tag{A.85}$$

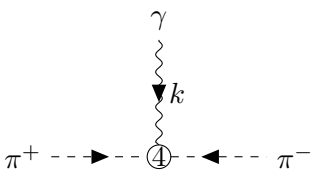

$$\mathcal{V}^{\mu\,(4)}_{\gamma\pi^+\pi^-;} = i\frac{2e}{F^2} M^2 (q_+ - q_-)^\mu l_4 \tag{A.86}$$

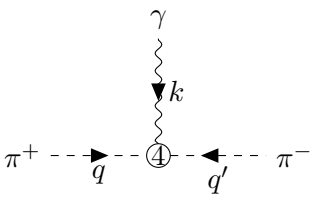

$$\mathcal{V}^{\mu\,(4)}_{\gamma\pi^+\pi^-;} = i\frac{2e}{F^2} k_\nu \left(q^\mu q'^\nu - q^\nu q'^\mu\right) l_6 \tag{A.87}$$

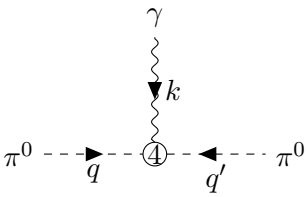

$$\mathcal{V}^{\mu\,(4)}_{\gamma\pi^0\pi^0;} = i\frac{e}{F^2}\left(q^\mu q'^\nu + q'^\mu q^\nu\right)(\epsilon_\mu k_\nu - \epsilon_\nu k_\mu) l_6 = 0 \tag{A.88}$$

A.2 Tree level amplitudes

A.2.1 Electroproduction

$\mathcal{O}(p^1)$ amplitudes

The $O(p^1)$ Feynman amplitudes, after operating with the external nucleon spinors $\bar{u}_{N'}(p')\mathcal{M}^{\mu\,(1)}_{\text{tree}}u_N(p)$ and simplifying, one can express them in the Ball parametrization, Eq. (3.13), and in terms of the Mandelstam representation Eq. (3.6). We have for the pion electroproduction case the following expressions

$$\mathcal{M}^{\mu\,(1)}_{(a)} = C^{(1)}_{I}\frac{eg}{F}V^{\mu}_{1}, \tag{A.89}$$

$$\mathcal{M}^{\mu\,(1)}_{(b)} = C^{(1)}_{II}\frac{eg}{F}\left(\frac{\left(m_N^2-s\right)V^{\mu}_{1}}{s-m^2}-\frac{(m_N+m)\left(2V^{\mu}_{2}+V^{\mu}_{3}+V^{\mu}_{4}-V^{\mu}_{5}\right)}{m^2-s}\right), \tag{A.90}$$

$$\mathcal{M}^{\mu\,(1)}_{(c)} = C^{(1)}_{III}\frac{eg}{F}\left(\frac{\left(u-m_N^2\right)V^{\mu}_{1}}{u-m^2}-\frac{(m_N+m)\left(2V^{\mu}_{2}-V^{\mu}_{3}+V^{\mu}_{4}-V^{\mu}_{5}\right)}{m^2-u}\right), \tag{A.91}$$

$$\mathcal{M}^{\mu\,(1)}_{(d)} = C^{(1)}_{IV}\frac{\sqrt{2}em_N g\left(2V^{\mu}_{3}-V^{\mu}_{4}\right)}{F\left(-2m_N^2+Q^2+s+u\right)}. \tag{A.92}$$

Here, m is the nucleon mass in the chiral limit which appear in the corresponding propagator, while m_N is the physical nucleon mass from the external nucleon momenta. The coefficients $C^{(1)}_{I}$, $C^{(1)}_{II}$, $C^{(1)}_{III}$, $C^{(1)}_{IV}$ are those given in Table 4.1 for each production channel.

$\mathcal{O}(p^2)$ amplitudes

As before, we operate the corresponding $\mathcal{O}(p^2)$ amplitudes with the external nucleon spinors, *i.e.* $\bar{u}_{N'}(p')\mathcal{M}^{\mu\,(2)}_{\text{tree}}u_N(p)$ and apply the Dirac equation.

$$\mathcal{M}^{\mu\,(2)}_{(e)} = C^{(2)}_{II}\frac{eg_A}{F_\pi}\left(-\frac{2V^{\mu}_{6}+V^{\mu}_{7}}{m_N^2-s}-\frac{\left(3m_N^2+s\right)\left(V^{\mu}_{4}-V^{\mu}_{5}\right)}{2m_N(m_N^2-s)}-V^{\mu}_{1}\right), \tag{A.93}$$

$$\mathcal{M}^{\mu\,(2)}_{(f)} = C^{(2)}_{III}\frac{eg_A}{F_\pi}\left(\frac{V^{\mu}_{7}-2V^{\mu}_{6}}{m_N^2-u}-\frac{\left(3m_N^2+u\right)\left(V^{\mu}_{4}-V^{\mu}_{5}\right)}{2m_N(m_N^2-u)}+V^{\mu}_{1}\right). \tag{A.94}$$

The constants $C^{(2)}_{II}$ and $C^{(2)}_{III}$ are given in Table 4.2 for each channel. As explained in the Sec. 4.3.1, the other amplitudes $\mathcal{M}^{\mu\,(2)}_{(g)}$ and $\mathcal{M}^{\mu\,(2)}_{(f)}$ corresponding to the Feynman diagrams (g) and (h) in Fig. 4.1 are already included in the above $\mathcal{O}(p)$ amplitudes by making the substitution

$$m \to m_2 = m - 4c_1M_\pi^2 \tag{A.95}$$

In fact, the $\mathcal{O}(p^2)$ and also other relevant higher order amplitudes can be generated [2]. Expanding in series of the pion mass, we have that

[2] As we can see in Eq. (4.107), this technique is independent of the renormalization scheme.

$$\mathcal{M}^{\mu\,(1)}_{(b)}\{m\to m_2\} = \mathcal{M}^{\mu\,(1)}_{(b)} + \mathcal{M}^{\mu\,(2)}_{(g)} + \mathcal{M}^{\mu\,(3)}_{(q)} + \mathcal{O}(p^4) \tag{A.96}$$

$$\mathcal{M}^{\mu\,(1)}_{(c)}\{m\to m_2\} = \mathcal{M}^{\mu\,(1)}_{(c)} + \mathcal{M}^{\mu\,(2)}_{(h)} + \mathcal{M}^{\mu\,(3)}_{(r)} + \mathcal{O}(p^4) \tag{A.97}$$

where $\mathcal{M}^{\mu\,(3)}_{(q)}$ and $\mathcal{M}^{\mu\,(3)}_{(r)}$ are the $\mathcal{O}(p^3)$ amplitudes corresponding to the diagrams (q) and (r) in Fig. 4.1.

$\mathcal{O}(p^3)$ amplitudes

The rest of the tree level $\mathcal{O}(p^3)$ amplitudes, as depicted in Fig. 4.1, are given as follows,

$$\begin{aligned}
\mathcal{M}^{\mu\,(3)}_{(i)} =& C^{(3)}_{Ia}\frac{e}{F_\pi m_N}\Bigg[V_4^\mu\left(2M_\pi^2-4m_N^2-2Q^2-3s-u\right)+2V_5^\mu\left(2m_N^2-M_\pi^2+Q^2+s+u\right)\\
&+V_2^\mu\left(4m_N^2-2\left(2Q^2+s+u\right)\right)+2m_N(s-u)V_1^\mu-8m_NV_6^\mu+(s-u)V_3^\mu\Bigg]\\
&+C^{(3)}_{Ib}\frac{e}{F_\pi}\Bigg[\sqrt{2}\left(d_{18}-2d_{16}\right)M_\pi^2V_1^\mu\\
&+\frac{d_{20}}{\sqrt{2}m_N^2}\Bigg(\frac{1}{4}(V_7^\mu-V_8^\mu)\left(2m_N^2+2M_\pi^2-s-u\right)+\frac{1}{2}(s-u)V_6^\mu\\
&+\frac{1}{4}V_1^\mu\left(2m_N^4+Q^2\left(s+u-2m_N^2-2M_\pi^2\right)+2m_N^2\left(M_\pi^2-s-u\right)-M_\pi^2(s+u)+2su\right)\Bigg)\\
&+d_{21}\left(\frac{\left(2m_N^2-s-u\right)}{\sqrt{2}}V_1^\mu+\sqrt{2}V_7^\mu\right)\\
&+d_{22}\left(\frac{V_1^\mu\left(-2m_N^2+2Q^2+s+u\right)}{2\sqrt{2}}+\frac{V_8^\mu-V_7^\mu}{\sqrt{2}}\right)\Bigg],
\end{aligned} \tag{A.98}$$

$$\mathcal{M}^{\mu\,(3)}_{(j)} = C^{(3)}_{IIa}\frac{\left(d_{18}-2d_{16}\right)eM_\pi^2}{F_\pi}\left[V_1^\mu+\frac{2m_N\left(2V_2^\mu+V_3^\mu+V_4^\mu-V_5^\mu\right)}{m_N^2-s}\right], \tag{A.99}$$

$$\begin{aligned}
\mathcal{M}^{\mu\,(3)}_{(m)} =& C^{(3)}_{IIb}\frac{eg_A}{4F_\pi}\Bigg[Q^2\left(\frac{2\left(2V_6^\mu+V_7^\mu\right)}{m_N^2-s}-\frac{\left(3m_N^2+s\right)\left(2V_2^\mu+V_3^\mu\right)}{m_N(m_N^2-s)}\right)\\
&+\left(\frac{s}{m_N}+3m_N\right)V_4^\mu-2V_8^\mu\Bigg],
\end{aligned} \tag{A.100}$$

$$\mathcal{M}^{\mu\,(3)}_{(k)} = C^{(3)}_{IIIa}\frac{\left(d_{18}-2d_{16}\right)eM_\pi^2}{F_\pi}\left[-V_1^\mu+\frac{2m_N\left(2V_2^\mu-V_3^\mu+V_4^\mu-V_5^\mu\right)}{m_N^2-u}\right], \tag{A.101}$$

$$\begin{aligned}
\mathcal{M}^{\mu\,(3)}_{(n)} =& C^{(3)}_{IIIb}\frac{eg_A}{4F_\pi}\Bigg[Q^2\left(\frac{2(2V_6^\mu-V_7^\mu)}{m_N^2-u}-\frac{\left(3m_N^2+u\right)\left(2V_2^\mu-V_3^\mu\right)}{m_N(m_N^2-u)}\right)\\
&-\left(\frac{u}{m_N}+3m_N\right)V_4^\mu+2V_8^\mu\Bigg],
\end{aligned} \tag{A.102}$$

$$\mathcal{M}^{\mu\,(3)}_{(o)} = C^{(3)}_{IV}\frac{2\sqrt{2}\left(d_{18}-2d_{16}\right)em_NM_\pi^2\left(2V_3^\mu-V_4^\mu\right)}{F_\pi\left(-2m_N^2+Q^2+s+u\right)}, \tag{A.103}$$

$$\mathcal{M}^{\mu\,(3)}_{(l)} = C^{(3)}_{IV}\frac{eg_A}{F_\pi^3}\Bigg[-\frac{2\sqrt{2}l_4 m_N M_\pi^2\left(2V_3^\mu - V_4^\mu\right)}{-2m_N^2+Q^2+s+u} - \frac{\sqrt{2}l_6 m_N\left(V_4^\mu\left(-2m_N^2+s+u\right)+2Q^2V_3^\mu\right)}{-2m_N^2+Q^2+s+u}\Bigg], \tag{A.104}$$

$$\mathcal{M}^{\mu\,(3)}_{(p)} = C^{(1)}_{IV}\frac{\sqrt{2}em_N g_A\left(2V_3^\mu - V_4^\mu\right)}{F_\pi\left(-2m_N^2+Q^2+s+u\right)}\xi. \tag{A.105}$$

The coefficcients $C^{(3)}_{Ia},\cdots,C^{(3)}_{IV}$ are given in Tab. 4.3 and $C^{(1)}_{IV}$ in Tab. 4.1 for all production channels.

$\mathcal{O}(p^{5/2})$ amplitudes

$$\begin{aligned}
\mathcal{M}^{\mu\,(5/2)}_{(a)} =& D_{II}\frac{eh_A g_M}{24F_\pi m_N m_\Delta\left(m_\Delta+m_N\right)\left(m_\Delta^2-s-i\Gamma_\Delta m_\Delta\right)}\Bigg[\\
&\left\{m_N\left(m_N^4+m_N^2\left(-M_\pi^2+Q^2+2s\right)+M_\pi^2\left(s-Q^2\right)+s\left(-Q^2+3s-6u\right)\right)\right.\\
&\left.-m_\Delta\left(3m_N^4+m_N^2\left(M_\pi^2-Q^2-10s\right)+M_\pi^2\left(5Q^2-s\right)+s\left(Q^2+s+6u\right)\right)\right\}V_1^\mu\\
&+\left\{2Q^2\left(m_N^2-4m_Nm_\Delta-M_\pi^2-5s\right)+6\left(m_Nm_\Delta+s\right)\left(2m_N^2-s-u\right)\right\}V_2^\mu\\
&+\left\{Q^2\left(m_N^2-10m_Nm_\Delta-M_\pi^2+s\right)+3(s-u)\left(m_Nm_\Delta+s\right)\right\}V_3^\mu\\
&+\left\{Q^2\left(m_N^2-4m_Nm_\Delta-M_\pi^2-5s\right)+m_Nm_\Delta\left(2m_N^2+4M_\pi^2-3(5s+u)\right)\right.\\
&\left.-s\left(6m_N^2-4M_\pi^2+7s+3u\right)\right\}V_4^\mu\\
&+\left\{-m_N^4+m_\Delta\left(8m_N^3-4m_NM_\pi^2+8m_Ns\right)+Q^2\left(-m_N^2+4m_Nm_\Delta+M_\pi^2+5s\right)\right.\\
&\left.+m_N^2\left(M_\pi^2+6s\right)+s\left(-5M_\pi^2+5s+6u\right)\right\}V_5^\mu\\
&+\left\{2m_N\left(m_N^2-M_\pi^2-9s\right)-2m_\Delta\left(9m_N^2+M_\pi^2+2s-3u\right)\right\}V_6^\mu\\
&+\left\{-m_\Delta\left(3m_N^2+M_\pi^2-4s-3u\right)+m_N\left(m_N^2-M_\pi^2+3s\right)+6Q^2m_\Delta\right\}V_7^\mu\\
&+\left\{m_\Delta\left(-5m_N^2-5M_\pi^2+2s+3u\right)+m_N\left(m_N^2-M_\pi^2-s\right)\right\}V_8^\mu\Bigg],
\end{aligned} \tag{A.106}$$

$$
\begin{aligned}
\mathcal{M}^{\mu\,(5/2)}_{(b)} =& D_{III}\frac{e h_A g_M}{24F_\pi m_N m_\Delta\left(m_\Delta+m_N\right)\left(m_\Delta^2-u\right)}\Bigg[\\
&\left\{m_N\left(u\left(2m_N^2+M_\pi^2-Q^2-6s\right)+(m_N-M_\pi)(m_N+M_\pi)\left(m_N^2+Q^2\right)+3u^2\right)\right. \\
&\left.-m_\Delta\left(3m_N^4+m_N^2\left(M_\pi^2-Q^2-10u\right)+M_\pi^2\left(5Q^2-u\right)+u\left(Q^2+6s+u\right)\right)\right\}V_1^\mu \\
&+\left\{2Q^2\left(-m_N^2+4m_Nm_\Delta+M_\pi^2+5u\right)-6\left(2m_N^2-s-u\right)\left(m_Nm_\Delta+u\right)\right\}V_2^\mu \\
&+\left\{Q^2\left(m_N^2-10m_Nm_\Delta-M_\pi^2+u\right)-3(s-u)\left(m_Nm_\Delta+u\right)\right\}V_3^\mu \\
&+\left\{-2m_N^4+Q^2\left(-m_N^2+4m_Nm_\Delta+M_\pi^2+5u\right)+2m_N^2\left(M_\pi^2+3u\right)\right. \\
&\left.+m_Nm_\Delta\left(18m_N^2-4M_\pi^2-3s+u\right)+3u\left(-2M_\pi^2+3s+u\right)\right\}V_4^\mu \\
&+\left\{m_N^4+Q^2\left(m_N^2-4m_Nm_\Delta-M_\pi^2-5u\right)+4m_Nm_\Delta\left(-2m_N^2+M_\pi^2-2u\right)\right. \\
&\left.-m_N^2\left(M_\pi^2+6u\right)+u\left(5M_\pi^2-6s-5u\right)\right\}V_5^\mu \\
&+\left\{2m_\Delta\left(9m_N^2+M_\pi^2-3s+2u\right)+2m_N\left(-m_N^2+M_\pi^2+9u\right)\right\}V_6^\mu \\
&+\left\{-m_\Delta\left(3m_N^2+M_\pi^2-3s-4u\right)+m_N\left(m_N^2-M_\pi^2+3u\right)+6Q^2m_\Delta\right\}V_7^\mu \\
&+\left\{m_\Delta\left(-5m_N^2-5M_\pi^2+3s+2u\right)+m_N\left(m_N^2-M_\pi^2-u\right)\right\}V_8^\mu\Bigg],
\end{aligned}
\tag{A.107}
$$

with $\Gamma_\Delta(s)$ is the energy-dependent width, Eq. (4.57). The constants D_{II} and D_{III} are presented in Table 4.4.

A.2.2 Photoproduction

$\mathcal{O}(p^1)$ amplitudes

Similarly to the electroproduction amplitudes, pion photoproduction amplitudes are obtained in the same way but for $Q=0$. Therefore, they are written in the basis of Eq. (3.73) by including the photon polarization vector ϵ_μ. We have that the $\mathcal{O}(p)$ tree amplitudes terms are

$$\epsilon_\mu\mathcal{M}^{\mu\,(1)}_{(a)} = C_I^{(1)}\frac{eg}{F}V_E \tag{A.108}$$

$$\epsilon_\mu\mathcal{M}^{\mu\,(1)}_{(b)} = C_{II}^{(1)}\frac{eg}{F}\left[\frac{\left(s-m^2\right)}{\left(m_2^2-s\right)}V_E+\frac{(m_N+m_2)}{\left(m_2^2-s\right)}V_{EK}\right] \tag{A.109}$$

$$\epsilon_\mu\mathcal{M}^{\mu\,(1)}_{(c)} = C_{III}^{(1)}\frac{eg}{F}\left[\frac{\left(m_N^2-u\right)}{\left(m_2^2-u\right)}V_E+\frac{2(m_N+m_2)}{\left(m_2^2-u\right)}q\cdot\epsilon\,V_N+\frac{(m_N+m_2)}{\left(m_2^2-u\right)}V_{EK}\right] \tag{A.110}$$

$$\epsilon_\mu\mathcal{M}^{\mu\,(1)}_{(d)} = C_{IV}^{(1)}\frac{eg}{F}\frac{2\sqrt{2}m_N}{\left(-2m^2+s+u\right)}q\cdot\epsilon\,V_N \tag{A.111}$$

$\mathcal{O}(p^2)$ amplitudes

Analogously to the electroproduction amplitudes presented above, the relevant amplitudes are

$$\epsilon_\mu \mathcal{M}^{\mu\,(2)}_{(e)} = C^{(2)}_{II} \frac{e g_A}{F_\pi} \left[\frac{\left(3m^2+s\right)}{2m\left(m^2-s\right)} V_{EK} - V_E \right] \tag{A.112}$$

$$\epsilon_\mu \mathcal{M}^{\mu\,(2)}_{(f)} = C^{(2)}_{III} \frac{e g_A}{F_\pi} \left[\frac{2}{\left(m^2-u\right)} q\cdot\epsilon\, V_K + \frac{\left(3m^2+u\right)}{2m\left(m^2-u\right)} V_{EK} + V_E \right] \tag{A.113}$$

$\mathcal{O}(p^3)$ amplitudes

The relevant $\mathcal{O}(p^3)$ tree-level amplitudes in photoproduction are

$$\begin{aligned}\epsilon_\mu \mathcal{M}^{\mu\,(3)}_{(i)} =& C^{(3)}_{Ia} \frac{e}{F_\pi} \left[\frac{2\left(s-m_N^2\right)}{m_N} q\cdot\epsilon\, V_N + 4q\cdot\epsilon\, V_K + 2(s-u)\, V_E \right.\\ &\left. + \frac{2\left(2m_N^2 - M_\pi^2 + s + u\right)}{m_N} V_{EK} \right]\\ &+ C^{(3)}_{Ib} \frac{e}{4\sqrt{2}F_\pi m_N^2} \left[2\left(2d_{212}m_N^2 - d_{20}\left(m_N^2 + M_\pi^2 - s\right)\right) q\cdot\epsilon\, V_K \right.\\ &\left. + \left(M_\pi^2\left(d_{20}(u-s) - 8d_{168}m_N^2\right) + 2d_{212}m_N^2\left(2m_N^2 - s - u\right)\right) V_E \right]\end{aligned} \tag{A.114}$$

$$\epsilon_\mu \mathcal{M}^{\mu\,(3)}_{(j)} = C^{(3)}_{II} \frac{e}{F_\pi} d_{168} \left[\frac{2m_N M_\pi^2}{m_N^2 - s} V_{EK} - M_\pi^2 V_E \right] \tag{A.115}$$

$$\epsilon_\mu \mathcal{M}^{\mu\,(3)}_{(k)} = C^{(3)}_{III} \frac{e}{F_\pi} d_{168} \left[\frac{4m_N M_\pi^2}{m_N^2 - u} q\cdot\epsilon\, V_N + \frac{2m_N M_\pi^2}{m_N^2 - u} V_{EK} + M_\pi^2 V_E \right] \tag{A.116}$$

$$\epsilon_\mu \mathcal{M}^{\mu\,(3)}_{(l)} = C^{(3)}_{IV} \frac{e}{F_\pi} d_{168} \frac{4\sqrt{2}m_N M_\pi^2}{\left(2m_N^2 - s - u\right)} q\cdot\epsilon\, V_N \tag{A.117}$$

where $d_{168} = 2d_{16} - d_{18}$ and $d_{212} = 2d_{21} - d_{22}$.

$\mathcal{O}(p^{5/2})$ amplitudes

The following amplitudes correspond to the Δ contribution in the photoproduction process $\gamma N \longrightarrow \pi N'$

$$\begin{aligned}\epsilon_\mu \mathcal{M}^{\mu\,(5/2)}_{(a)} =& D_{II} \frac{e g_M h_A}{4Fm\, m_\Delta (m+m_\Delta)} \left[\frac{\left(m^2-s\right)\left(m\, m_\Delta + s\right)}{\left(-i\Gamma_\Delta(s) m_\Delta + m_\Delta^2 - s\right)} q\cdot\epsilon\, V_N \right.\\ &- \frac{\left(m^2 m_\Delta + 2ms + m_\Delta s\right)}{\left(-i\Gamma_\Delta(s) m_\Delta + m_\Delta^2 - s\right)} q\cdot\epsilon\, V_K\\ &+ \frac{\left(m^4 - 8m^3 m_\Delta - m^2\left(M_\pi^2 + 6s\right) + 4m\, m_\Delta\left(M_\pi^2 - 2s\right) + s\left(5M_\pi^2 - 5s - 6u\right)\right)}{6\left(-i\Gamma_\Delta(s) m_\Delta + m_\Delta^2 - s\right)} V_{EK}\\ &+ \frac{1}{6\left(-i\Gamma_\Delta(s) m_\Delta + m_\Delta^2 - s\right)} \left\{ -m^5 + 3m^4 m_\Delta + m^3\left(M_\pi^2 - 2s\right) + m^2 m_\Delta\left(M_\pi^2 - 10s\right) \right.\\ &\left.\left. - ms\left(M_\pi^2 + 3s - 6u\right) + m_\Delta s\left(s + 6u - M_\pi^2\right) \right\} V_E \right],\end{aligned} \tag{A.118}$$

$$\epsilon_\mu \mathcal{M}^{\mu\,(5/2)}_{(b)} = D_{III}\frac{e g_M h_A}{4Fm\,m_\Delta(m+m_\Delta)}\Bigg[-\frac{\left(m^2-s\right)\left(m\,m_\Delta+u\right)}{\left(m_\Delta^2-u\right)}q\cdot\epsilon\,V_N$$
$$+\frac{\left(-m^3+6m^2m_\Delta+m\left(M_\pi^2+3u\right)+m_\Delta\left(M_\pi^2-3s-u\right)\right)}{3\left(m_\Delta^2-u\right)}q\cdot\epsilon\,V_K$$
$$+\frac{\left(-m^4+8m^3m_\Delta+m^2\left(M_\pi^2+6u\right)-4m\,m_\Delta\left(M_\pi^2-2u\right)+u\left(-5M_\pi^2+6s+5u\right)\right)}{6\left(m_\Delta^2-u\right)}V_{EK}$$
$$+\frac{1}{6\left(m_\Delta^2-u\right)}\Big\{-m^5+3m^4m_\Delta+m^3\left(M_\pi^2-2u\right)+m^2m_\Delta\left(M_\pi^2-10u\right)$$
$$-mu\left(M_\pi^2-6s+3u\right)+m_\Delta u\left(6s+u-M_\pi^2\right)\Big\}V_E\Bigg], \tag{A.119}$$

A.3 One-loop level $\mathcal{O}(p^3)$ amplitudes

Here, I detail the amplitudes explicitly obtained from the corresponding Feynman diagrams generated for each topology in Fig. 4.2 and for the four physical channels $\gamma^{(*)}p \longrightarrow \pi^0 p$, $\gamma^{(*)}p \longrightarrow \pi^+ n$, $\gamma^{(*)}n \longrightarrow \pi^- p$, $\gamma^{(*)}n \longrightarrow \pi^0 n$. The expressions depicted below correspond to the integrand part $f^\mu_{topo}(p,p',k,q,z)$ for the particular amplitude

$$\mathcal{M}^{\mu\,(3)}_{(topo)} = \int \frac{d^4z}{(2\pi)^4} f^\mu_{topo}(p,p',k,q,z) \tag{A.120}$$

where $topo = \{a1, a2, \ldots, i3\}$ indicates the specific one-loop Feynman diagram from Fig. 4.2. z denotes the inner loop momentum [see example from Fig. 4.5 for the diagram (g7)]. The following integrand expressions are written with the propagators with the explicit nucleon and pion mass depending on their charge. That is, we specify the mass for the proton m_p, neutron m_n, neutral pion $M = M_{\pi^0}$ and the charged pions $Mc = M_{\pi^\pm}$ as they appear in the loops. This distinction provides us the isospin breaking effects. As always, in the isospin limit the amplitudes are reduced by doing $m_p = m_n = m$ and $Mc = M$.

Channel $\gamma^{(*)}p \longrightarrow \pi^0 p$

Topology	Integrand $f^{\mu}_{topo}(p,p',k,q,z)$
a1	$\frac{ieg_A\gamma^\mu.(m_p+\gamma\cdot(p-q)).(\gamma\cdot q).\gamma^5}{4F^3(z^2-Mc^2)\left((p-q)^2-m_p^2\right)}$
a2	0
a3	$\frac{1}{2}\Bigg[-\frac{ieg_A(-k-2z)^\mu(\gamma\cdot(-k-z)-\gamma\cdot z).(m_p+\gamma\cdot(p-q)).(\gamma\cdot q).\gamma^5}{8F^3(z^2-Mc^2)((k+z)^2-Mc^2)\left((p-q)^2-m_p^2\right)}$ $-\frac{ieg_A(k+2z)^\mu(\gamma\cdot(k+z)+\gamma\cdot z).(m_p+\gamma\cdot(p-q)).(\gamma\cdot q).\gamma^5}{8F^3(z^2-Mc^2)((k+z)^2-Mc^2)\left((p-q)^2-m_p^2\right)}\Bigg]$
b1	$\frac{ieg_A(\gamma\cdot q).\gamma^5.(\gamma\cdot(k+p)+m_p).\gamma^\mu}{6F^3(z^2-Mc^2)\left((k+p)^2-m_p^2\right)}$
b2	0
b3	$\frac{ieg_A\gamma^\mu.(m_p+\gamma\cdot(p-q)).(\gamma\cdot q).\gamma^5}{6F^3(z^2-Mc^2)\left((p-q)^2-m_p^2\right)}$
b4	0
b5	$\frac{1}{2}\Bigg[-\frac{ieg_A(-k-2z)^\mu(-\gamma\cdot(-k-z)-2\gamma\cdot q-\gamma\cdot z).\gamma^5}{12F^3(z^2-Mc^2)((k+z)^2-Mc^2)}$ $-\frac{ieg_A(k+2z)^\mu(-\gamma\cdot(k+z)-2\gamma\cdot q+\gamma\cdot z).\gamma^5}{12F^3(z^2-Mc^2)((k+z)^2-Mc^2)}\Bigg]$
c1	0
c2	$\frac{ieg_A(\gamma\cdot q).\gamma^5.(\gamma\cdot(k+p)+m_p).\gamma^\mu}{4F^3(z^2-Mc^2)\left((k+p)^2-m_p^2\right)}$
c3	$\frac{1}{2}\Bigg[-\frac{ieg_A(-k-2z)^\mu(\gamma\cdot q).\gamma^5.(\gamma\cdot(k+p)+m_p).(\gamma\cdot(-k-z)-\gamma\cdot z)}{8F^3(z^2-Mc^2)\left((k+p)^2-m_p^2\right)((k+z)^2-Mc^2)}$ $-\frac{ieg_A(k+2z)^\mu(\gamma\cdot q).\gamma^5.(\gamma\cdot(k+p)+m_p).(\gamma\cdot(k+z)+\gamma\cdot z)}{8F^3(z^2-Mc^2)\left((k+p)^2-m_p^2\right)((k+z)^2-Mc^2)}\Bigg]$
d1	$\frac{ieg_A^3(\gamma\cdot z).\gamma^5.(m_n+\gamma\cdot(p'-z)).\gamma^\mu.\gamma^5.(m_p+\gamma\cdot(p-q)).(\gamma\cdot q).\gamma^5}{4F^3(z^2-Mc^2)\left((p-q)^2-m_p^2\right)\left((p'-z)^2-m_n^2\right)}$
d2	$-\frac{ieg_A^3(\gamma\cdot z).\gamma^5.(m_p+\gamma\cdot(p'-z)).\gamma^\mu.(\gamma\cdot(-k+p'-z)+m_p).(\gamma\cdot z).\gamma^5.(m_p+\gamma\cdot(p-q)).(\gamma\cdot q).\gamma^5}{8F^3(z^2-M^2)\left((p-q)^2-m_p^2\right)\left((p'-z)^2-m_p^2\right)\left((-k+p'-z)^2-m_p^2\right)}$
d3	$\frac{ieg_A^3\gamma^\mu.\gamma^5.(m_n+\gamma\cdot(p-q-z)).(\gamma\cdot z).\gamma^5.(m_p+\gamma\cdot(p-q)).(\gamma\cdot q).\gamma^5}{4F^3(z^2-Mc^2)\left((p-q)^2-m_p^2\right)((p-q-z)^2-m_n^2)}$
d4	$-\frac{ieg_A^3\gamma^\mu.(\gamma\cdot(p'-k)+m_p).(\gamma\cdot z).\gamma^5.(m_p+\gamma\cdot(p-q-z)).(\gamma\cdot z).\gamma^5.(m_p+\gamma\cdot(p-q)).(\gamma\cdot q).\gamma^5}{8F^3(z^2-M^2)\left((p-q)^2-m_p^2\right)\left((p'-k)^2-m_p^2\right)\left((p-q-z)^2-m_p^2\right)}$ $-\frac{ieg_A^3\gamma^\mu.(\gamma\cdot(p'-k)+m_p).(\gamma\cdot z).\gamma^5.(m_n+\gamma\cdot(p-q-z)).(\gamma\cdot z).\gamma^5.(m_p+\gamma\cdot(p-q)).(\gamma\cdot q).\gamma^5}{4F^3(z^2-Mc^2)\left((p-q)^2-m_p^2\right)\left((p'-k)^2-m_p^2\right)((p-q-z)^2-m_n^2)}$
d5	$\frac{ieg_A^3(k+2z)^\mu(\gamma\cdot(-k-z)).\gamma^5.(m_n+\gamma\cdot(p-q-z)).(\gamma\cdot z).\gamma^5.(m_p+\gamma\cdot(p-q)).(\gamma\cdot q).\gamma^5}{4F^3(z^2-Mc^2)((k+z)^2-Mc^2)\left((p-q)^2-m_p^2\right)((p-q-z)^2-m_n^2)}$
e1	$-\frac{ieg_A(\gamma\cdot z).\gamma^5.(m_n+\gamma\cdot(p'-z)).(\gamma\cdot z-\gamma\cdot q).(\gamma\cdot(k+p)+m_p).\gamma^\mu}{4F^3(z^2-Mc^2)\left((k+p)^2-m_p^2\right)\left((p'-z)^2-m_n^2\right)}$
e2	$\frac{ieg_A(\gamma\cdot z).\gamma^5.(m_n+\gamma\cdot(p'-z)).\gamma^\mu}{4F^3(z^2-Mc^2)\left((p'-z)^2-m_n^2\right)}$
e3	0
e4	$\frac{ieg_A\gamma^\mu.\gamma^5.(\gamma\cdot(-k+p'-z)+m_n).(\gamma\cdot z-\gamma\cdot q)}{4F^3(z^2-Mc^2)\left((-k+p'-z)^2-m_n^2\right)}$
e5	$-\frac{ieg_A\gamma^\mu.(\gamma\cdot(p'-k)+m_p).(\gamma\cdot z).\gamma^5.(m_n+\gamma\cdot(p-q-z)).(\gamma\cdot z-\gamma\cdot q)}{4F^3(z^2-Mc^2)\left((p'-k)^2-m_p^2\right)((p-q-z)^2-m_n^2)}$
e6	0
e7	$\frac{ieg_A(k+2z)^\mu(\gamma\cdot(-k-z)).\gamma^5.(m_n+\gamma\cdot(p-q-z)).(\gamma\cdot z-\gamma\cdot q)}{4F^3(z^2-Mc^2)((k+z)^2-Mc^2)((p-q-z)^2-m_n^2)}$
f1	$\frac{ieg_A^3(\gamma\cdot z).\gamma^5.(m_n+\gamma\cdot(p'-z)).(\gamma\cdot q).\gamma^5.(\gamma\cdot(k+p-z)+m_n).(\gamma\cdot z).\gamma^5.(\gamma\cdot(k+p)+m_p).\gamma^\mu}{4F^3(z^2-Mc^2)\left((k+p)^2-m_p^2\right)((k+p-z)^2-m_n^2)\left((p'-z)^2-m_n^2\right)}$ $-\frac{ieg_A^3(\gamma\cdot z).\gamma^5.(m_p+\gamma\cdot(p'-z)).(\gamma\cdot q).\gamma^5.(\gamma\cdot(k+p-z)+m_p).(\gamma\cdot z).\gamma^5.(\gamma\cdot(k+p)+m_p).\gamma^\mu}{8F^3(z^2-M^2)\left((k+p)^2-m_p^2\right)\left((k+p-z)^2-m_p^2\right)\left((p'-z)^2-m_p^2\right)}$

f2 $$-\frac{ieg_A^3(\gamma\cdot z).\gamma^5.(m_n+\gamma\cdot(p'-z)).(\gamma\cdot q).\gamma^5.(\gamma\cdot(k+p-z)+m_n).\gamma^\mu.\gamma^5}{4F^3(z^2-Mc^2)((k+p-z)^2-m_n^2)\big((p'-z)^2-m_n^2\big)}$$

f3 $$-\frac{ieg_A^3(\gamma\cdot z).\gamma^5.(m_p+\gamma\cdot(p'-z)).(\gamma\cdot q).\gamma^5.(\gamma\cdot(k+p-z)+m_p).\gamma^\mu.(m_p+\gamma\cdot(p-z)).(\gamma\cdot z).\gamma^5}{8F^3(z^2-M^2)\big((p-z)^2-m_p^2\big)\big((k+p-z)^2-m_p^2\big)\big((p'-z)^2-m_p^2\big)}$$

f4 $$0$$

f5 $$-\frac{ieg_A^3(\gamma\cdot z).\gamma^5.(m_p+\gamma\cdot(p'-z)).\gamma^\mu.(\gamma\cdot(-k+p'-z)+m_p).(\gamma\cdot q).\gamma^5.(m_p+\gamma\cdot(p-z)).(\gamma\cdot z).\gamma^5}{8F^3(z^2-M^2)\big((p-z)^2-m_p^2\big)\big((p'-z)^2-m_p^2\big)\big((-k+p'-z)^2-m_p^2\big)}$$

f6 $$-\frac{ieg_A^3\gamma^\mu.\gamma^5.(m_n+\gamma\cdot(p-q-z)).(\gamma\cdot q).\gamma^5.(m_n+\gamma\cdot(p-z)).(\gamma\cdot z).\gamma^5}{4F^3(z^2-Mc^2)((p-z)^2-m_n^2)((p-q-z)^2-m_n^2)}$$

f7 $$\frac{ieg_A^3\gamma^\mu.(\gamma\cdot(p'-k)+m_p).(\gamma\cdot z).\gamma^5.(m_n+\gamma\cdot(p-q-z)).(\gamma\cdot q).\gamma^5.(m_n+\gamma\cdot(p-z)).(\gamma\cdot z).\gamma^5}{4F^3(z^2-Mc^2)\big((p'-k)^2-m_p^2\big)((p-z)^2-m_n^2)((p-q-z)^2-m_n^2)}$$
$$-\frac{ieg_A^3\gamma^\mu.(\gamma\cdot(p'-k)+m_p).(\gamma\cdot z).\gamma^5.(m_p+\gamma\cdot(p-q-z)).(\gamma\cdot q).\gamma^5.(m_p+\gamma\cdot(p-z)).(\gamma\cdot z).\gamma^5}{8F^3(z^2-M^2)\big((p-z)^2-m_p^2\big)\big((p'-k)^2-m_p^2\big)\big((p-q-z)^2-m_p^2\big)}$$

f8 $$0$$

f9 $$-\frac{ieg_A^3(k+2z)^\mu(\gamma\cdot(-k-z)).\gamma^5.(m_n+\gamma\cdot(p-q-z)).(\gamma\cdot q).\gamma^5.(m_n+\gamma\cdot(p-z)).(\gamma\cdot z).\gamma^5}{4F^3(z^2-Mc^2)((k+z)^2-Mc^2)((p-z)^2-m_n^2)((p-q-z)^2-m_n^2)}$$

g1 $$\frac{ieg_A(\gamma\cdot q+\gamma\cdot z).(\gamma\cdot(k+p-z)+m_n).(\gamma\cdot z).\gamma^5.(\gamma\cdot(k+p)+m_p).\gamma^\mu}{4F^3(z^2-Mc^2)\big((k+p)^2-m_p^2\big)((k+p-z)^2-m_n^2)}$$

g2 $$-\frac{ieg_A(\gamma\cdot q+\gamma\cdot z).(\gamma\cdot(k+p-z)+m_n).\gamma^\mu.\gamma^5}{4F^3(z^2-Mc^2)((k+p-z)^2-m_n^2)}$$

g3 $$0$$

g4 $$-\frac{ieg_A\gamma^\mu.(m_n+\gamma\cdot(p-z)).(\gamma\cdot z).\gamma^5}{4F^3(z^2-Mc^2)((p-z)^2-m_n^2)}$$

g5 $$\frac{ieg_A\gamma^\mu.(\gamma\cdot(p'-k)+m_p).(\gamma\cdot q+\gamma\cdot z).(m_n+\gamma\cdot(p-z)).(\gamma\cdot z).\gamma^5}{4F^3(z^2-Mc^2)\big((p'-k)^2-m_p^2\big)((p-z)^2-m_n^2)}$$

g6 $$0$$

g7 $$\frac{ieg_A(k+2z)^\mu(\gamma\cdot(k+z)+\gamma\cdot q).(m_n+\gamma\cdot(p-z)).(\gamma\cdot z).\gamma^5}{4F^3(z^2-Mc^2)((-k-z)^2-Mc^2)((p-z)^2-m_n^2)}$$

h1 $$-\frac{ieg_A^3(\gamma\cdot q).\gamma^5.(m_p+\gamma\cdot(p'+q)).(\gamma\cdot z).\gamma^5.(\gamma\cdot(k+p-z)+m_p).(\gamma\cdot z).\gamma^5.(\gamma\cdot(k+p)+m_p).\gamma^\mu}{8F^3(z^2-M^2)\big((k+p)^2-m_p^2\big)\big((k+p-z)^2-m_p^2\big)\big((p'+q)^2-m_p^2\big)}$$
$$-\frac{ieg_A^3(\gamma\cdot q).\gamma^5.(m_p+\gamma\cdot(p'+q)).(\gamma\cdot z).\gamma^5.(\gamma\cdot(k+p-z)+m_n).(\gamma\cdot z).\gamma^5.(\gamma\cdot(k+p)+m_p).\gamma^\mu}{4F^3(z^2-Mc^2)\big((k+p)^2-m_p^2\big)\big((p'+q)^2-m_p^2\big)((k+p-z)^2-m_n^2)}$$

h2 $$\frac{ieg_A^3(\gamma\cdot q).\gamma^5.(m_p+\gamma\cdot(p'+q)).(\gamma\cdot z).\gamma^5.(\gamma\cdot(k+p-z)+m_n).\gamma^\mu.\gamma^5}{4F^3(z^2-Mc^2)\big((p'+q)^2-m_p^2\big)((k+p-z)^2-m_n^2)}$$

h3 $$-\frac{ieg_A^3(\gamma\cdot q).\gamma^5.(m_p+\gamma\cdot(p'+q)).(\gamma\cdot z).\gamma^5.(\gamma\cdot(k+p-z)+m_p).\gamma^\mu.(m_p+\gamma\cdot(p-z)).(\gamma\cdot z).\gamma^5}{8F^3(z^2-M^2)\big((p-z)^2-m_p^2\big)\big((k+p-z)^2-m_p^2\big)\big((p'+q)^2-m_p^2\big)}$$

h4 $$\frac{ieg_A^3(\gamma\cdot q).\gamma^5.(m_p+\gamma\cdot(p'+q)).\gamma^\mu.\gamma^5.(m_n+\gamma\cdot(p-z)).(\gamma\cdot z).\gamma^5}{4F^3(z^2-Mc^2)((p-z)^2-m_n^2)\big((p'+q)^2-m_p^2\big)}$$

h5 $$\frac{ieg_A^3(k+2z)^\mu(\gamma\cdot q).\gamma^5.(m_p+\gamma\cdot(p'+q)).(\gamma\cdot(-k-z)).\gamma^5.(m_n+\gamma\cdot(p-z)).(\gamma\cdot z).\gamma^5}{4F^3(z^2-Mc^2)((k+z)^2-Mc^2)((p-z)^2-m_n^2)\big((p'+q)^2-m_p^2\big)}$$

i1 $$0$$

i2 $$\frac{ieg_A}{2}\Bigg[\frac{(-k-2z)^\mu(\gamma\cdot(q-k)).\gamma^5\big(2((k-q)\cdot q)+2((-k-z)\cdot z)+M^2-Q^2\big)}{6F^3(z^2-Mc^2)((k-q)^2-M^2)((k+z)^2-Mc^2)}$$
$$+\frac{(k+2z)^\mu(\gamma\cdot(q-k)).\gamma^5\big(2((k-q)\cdot q)-2(z\cdot(k+z))+M^2+Q^2\big)}{6F^3(z^2-Mc^2)((k-q)^2-M^2)((k+z)^2-Mc^2)}\Bigg]$$

i3 $$0$$

Channel $\gamma^{(*)}p \longrightarrow \pi^+ n$

Topology	Integrand $f^{\mu}_{topo}(p,p',k,q,z)$
a1	$-\frac{ieg_A\gamma^\mu.(m_n+\gamma\cdot(p-q)).(\gamma\cdot q).\gamma^5}{2\sqrt{2}F^3(z^2-Mc^2)((p-q)^2-m_n^2)}$
a2	0
a3	$\frac{1}{2}\Bigg[\frac{ieg_A(-k-2z)^\mu(\gamma\cdot(-k-z)-\gamma\cdot z).(m_n+\gamma\cdot(p-q)).(\gamma\cdot q).\gamma^5}{4\sqrt{2}F^3(z^2-Mc^2)((k+z)^2-Mc^2)((p-q)^2-m_n^2)}$ $+\frac{ieg_A(k+2z)^\mu(\gamma\cdot(k+z)+\gamma\cdot z).(m_n+\gamma\cdot(p-q)).(\gamma\cdot q).\gamma^5}{4\sqrt{2}F^3(z^2-Mc^2)((k+z)^2-Mc^2)((p-q)^2-m_n^2)}\Bigg]$
b1	$\frac{ieg_A(\gamma\cdot q).\gamma^5.(\gamma\cdot(k+p)+m_p).\gamma^\mu}{6\sqrt{2}F^3(z^2-M^2)\big((k+p)^2-m_p^2\big)}$ $-\frac{ieg_A\left(\frac{-(\gamma\cdot q)-\gamma\cdot z}{6\sqrt{2}}-\frac{\gamma\cdot z}{3\sqrt{2}}\right).\gamma^5.(\gamma\cdot(k+p)+m_p).\gamma^\mu}{2F^3(z^2-Mc^2)\big((k+p)^2-m_p^2\big)}$ $-\frac{ieg_A\left(\frac{\gamma\cdot z-\gamma\cdot q}{6\sqrt{2}}+\frac{\gamma\cdot z}{3\sqrt{2}}\right).\gamma^5.(\gamma\cdot(k+p)+m_p).\gamma^\mu}{2F^3(z^2-Mc^2)\big((k+p)^2-m_p^2\big)}$
b2	$-\frac{ieg_A\gamma^\mu.\gamma^5}{6\sqrt{2}F^3(z^2-M^2)}-\frac{i\sqrt{2}eg_A\gamma^\mu.\gamma^5}{3F^3(z^2-Mc^2)}$
b3	0
b4	$-\frac{ieg_A(2q-k)^\mu(\gamma\cdot(k-q)).\gamma^5}{6\sqrt{2}F^3(z^2-M^2)((k-q)^2-Mc^2)}-\frac{ieg_A(2q-k)^\mu\left(\frac{\gamma\cdot(k-q)-\gamma\cdot z}{6\sqrt{2}}-\frac{\gamma\cdot z}{3\sqrt{2}}\right).\gamma^5}{2F^3(z^2-Mc^2)((k-q)^2-Mc^2)}$ $-\frac{ieg_A(2q-k)^\mu\left(\frac{\gamma\cdot(k-q)+\gamma\cdot z}{6\sqrt{2}}+\frac{\gamma\cdot z}{3\sqrt{2}}\right).\gamma^5}{2F^3(z^2-Mc^2)((k-q)^2-Mc^2)}$
b5	$-\frac{ieg_A(-k-2z)^\mu\left(\frac{\gamma\cdot(k+z)-\gamma\cdot q}{6\sqrt{2}}+\frac{\gamma\cdot z}{3\sqrt{2}}\right).\gamma^5}{2F^3(z^2-Mc^2)((k+z)^2-Mc^2)}-\frac{ieg_A(k+2z)^\mu\left(\frac{\gamma\cdot(-k-z)-\gamma\cdot q}{6\sqrt{2}}-\frac{\gamma\cdot z}{3\sqrt{2}}\right).\gamma^5}{2F^3(z^2-Mc^2)((k+z)^2-Mc^2)}$
c1	0
c2	$\frac{ieg_A(\gamma\cdot q).\gamma^5.(\gamma\cdot(k+p)+m_p).\gamma^\mu}{2\sqrt{2}F^3(z^2-Mc^2)\big((k+p)^2-m_p^2\big)}$
c3	$-\frac{ieg_A(-k-2z)^\mu(\gamma\cdot q).\gamma^5.(\gamma\cdot(k+p)+m_p).(\gamma\cdot(-k-z)-\gamma\cdot z)}{8\sqrt{2}F^3(z^2-Mc^2)\big((k+p)^2-m_p^2\big)((k+z)^2-Mc^2)}$ $-\frac{ieg_A(k+2z)^\mu(\gamma\cdot q).\gamma^5.(\gamma\cdot(k+p)+m_p).(\gamma\cdot(k+z)+\gamma\cdot z)}{8\sqrt{2}F^3(z^2-Mc^2)\big((k+p)^2-m_p^2\big)((k+z)^2-Mc^2)}$
d1	$-\frac{ieg_A^3(\gamma\cdot z).\gamma^5.(m_p+\gamma\cdot(p'-z)).\gamma^\mu.\gamma^5.(m_n+\gamma\cdot(p-q)).(\gamma\cdot q).\gamma^5}{2\sqrt{2}F^3(z^2-Mc^2)((p-q)^2-m_n^2)\big((p'-z)^2-m_p^2\big)}$
d2	$-\frac{ieg_A^3(\gamma\cdot z).\gamma^5.(m_p+\gamma\cdot(p'-z)).\gamma^\mu.(\gamma\cdot(-k+p'-z)+m_p).(\gamma\cdot z).\gamma^5.(m_n+\gamma\cdot(p-q)).(\gamma\cdot q).\gamma^5}{2\sqrt{2}F^3(z^2-Mc^2)((p-q)^2-m_n^2)\big((p'-z)^2-m_p^2\big)\big((-k+p'-z)^2-m_p^2\big)}$
d3	$-\frac{ieg_A^3\gamma^\mu.\gamma^5.(m_p+\gamma\cdot(p-q-z)).(\gamma\cdot z).\gamma^5.(m_n+\gamma\cdot(p-q)).(\gamma\cdot q).\gamma^5}{2\sqrt{2}F^3(z^2-Mc^2)((p-q)^2-m_n^2)\big((p-q-z)^2-m_p^2\big)}$
d4	0
d5	$\frac{ieg_A^3(-k-2z)^\mu(\gamma\cdot(-k-z)).\gamma^5.(m_p+\gamma\cdot(p-q-z)).(\gamma\cdot z).\gamma^5.(m_n+\gamma\cdot(p-q)).(\gamma\cdot q).\gamma^5}{2\sqrt{2}F^3(z^2-Mc^2)((k+z)^2-Mc^2)((p-q)^2-m_n^2)\big((p-q-z)^2-m_p^2\big)}$
e1	$\frac{ieg_A(\gamma\cdot z).\gamma^5.(m_n+\gamma\cdot(p'-z)).(\gamma\cdot q-\gamma\cdot z).(\gamma\cdot(k+p)+m_p).\gamma^\mu}{4\sqrt{2}F^3(z^2-M^2)\big((k+p)^2-m_p^2\big)\big((p'-z)^2-m_n^2\big)}$ $+\frac{ieg_A(\gamma\cdot z).\gamma^5.(m_p+\gamma\cdot(p'-z)).(\gamma\cdot q-\gamma\cdot z).(\gamma\cdot(k+p)+m_p).\gamma^\mu}{4\sqrt{2}F^3(z^2-Mc^2)\big((k+p)^2-m_p^2\big)\big((p'-z)^2-m_p^2\big)}$
e2	$-\frac{ieg_A(\gamma\cdot z).\gamma^5.(m_n+\gamma\cdot(p'-z)).\gamma^\mu}{4\sqrt{2}F^3(z^2-M^2)\big((p'-z)^2-m_n^2\big)}-\frac{ieg_A(\gamma\cdot z).\gamma^5.(m_p+\gamma\cdot(p'-z)).\gamma^\mu}{2\sqrt{2}F^3(z^2-Mc^2)\big((p'-z)^2-m_p^2\big)}$
e3	$\frac{ieg_A(\gamma\cdot z).\gamma^5.(m_p+\gamma\cdot(p'-z)).\gamma^\mu.(\gamma\cdot(-k+p'-z)+m_p).(\gamma\cdot q-\gamma\cdot z)}{4\sqrt{2}F^3(z^2-Mc^2)\big((p'-z)^2-m_p^2\big)\big((-k+p'-z)^2-m_p^2\big)}$
e4	$\frac{ieg_A\gamma^\mu.\gamma^5.(\gamma\cdot(-k+p'-z)+m_p).(\gamma\cdot q-\gamma\cdot z)}{4\sqrt{2}F^3(z^2-Mc^2)\big((-k+p'-z)^2-m_p^2\big)}$
e5	0
e6	$\frac{ieg_A(2q-k)^\mu(\gamma\cdot z).\gamma^5.(m_n+\gamma\cdot(p'-z)).(\gamma\cdot(q-k)-\gamma\cdot z)}{4\sqrt{2}F^3(z^2-M^2)((k-q)^2-Mc^2)\big((p'-z)^2-m_n^2\big)}$ $+\frac{ieg_A(2q-k)^\mu(\gamma\cdot z).\gamma^5.(m_p+\gamma\cdot(p'-z)).(\gamma\cdot(q-k)-\gamma\cdot z)}{4\sqrt{2}F^3(z^2-Mc^2)((k-q)^2-Mc^2)\big((p'-z)^2-m_p^2\big)}$
e7	$-\frac{ieg_A(-k-2z)^\mu(\gamma\cdot(-k-z)).\gamma^5.(m_p+\gamma\cdot(p-q-z)).(\gamma\cdot q-\gamma\cdot z)}{4\sqrt{2}F^3(z^2-Mc^2)((k+z)^2-Mc^2)\big((p-q-z)^2-m_p^2\big)}$

f1 $$\frac{ieg_A^3(\gamma\cdot z).\gamma^5.(m_n+\gamma\cdot(p'-z)).(\gamma\cdot q).\gamma^5.(\gamma\cdot(k+p-z)+m_p).(\gamma\cdot z).\gamma^5.(\gamma\cdot(k+p)+m_p).\gamma^\mu}{4\sqrt{2}F^3(z^2-M^2)\big((k+p)^2-m_p^2\big)\big((k+p-z)^2-m_p^2\big)\big((p'-z)^2-m_n^2\big)}$$

f2 $$0$$

f3 $$\frac{ieg_A^3(\gamma\cdot z).\gamma^5.(m_n+\gamma\cdot(p'-z)).(\gamma\cdot q).\gamma^5.(\gamma\cdot(k+p-z)+m_p).\gamma^\mu.(m_p+\gamma\cdot(p-z)).(\gamma\cdot z).\gamma^5}{4\sqrt{2}F^3(z^2-M^2)\big((p-z)^2-m_p^2\big)\big((k+p-z)^2-m_p^2\big)\big((p'-z)^2-m_n^2\big)}$$

f4 $$-\frac{ieg_A^3(\gamma\cdot z).\gamma^5.(m_n+\gamma\cdot(p'-z)).\gamma^\mu.\gamma^5.(m_p+\gamma\cdot(p-z)).(\gamma\cdot z).\gamma^5}{4\sqrt{2}F^3(z^2-M^2)\big((p-z)^2-m_p^2\big)\big((p'-z)^2-m_n^2\big)}$$

f5 $$0$$

f6 $$0$$

f7 $$0$$

f8 $$\frac{ieg_A^3(2q-k)^\mu(\gamma\cdot z).\gamma^5.(m_n+\gamma\cdot(p'-z)).(\gamma\cdot(q-k)).\gamma^5.(m_p+\gamma\cdot(p-z)).(\gamma\cdot z).\gamma^5}{4\sqrt{2}F^3(z^2-M^2)((k-q)^2-Mc^2)\big((p-z)^2-m_p^2\big)\big((p'-z)^2-m_n^2\big)}$$

f9 $$0$$

g1 $$\frac{ieg_A(\gamma\cdot q+\gamma\cdot z).(\gamma\cdot(k+p-z)+m_p).(\gamma\cdot z).\gamma^5.(\gamma\cdot(k+p)+m_p).\gamma^\mu}{4\sqrt{2}F^3(z^2-M^2)\big((k+p)^2-m_p^2\big)\big((k+p-z)^2-m_p^2\big)}$$
$$+\frac{ieg_A(\gamma\cdot q+\gamma\cdot z).(\gamma\cdot(k+p-z)+m_n).(\gamma\cdot z).\gamma^5.(\gamma\cdot(k+p)+m_p).\gamma^\mu}{4\sqrt{2}F^3(z^2-Mc^2)\big((k+p)^2-m_p^2\big)((k+p-z)^2-m_n^2)}$$

g2 $$-\frac{ieg_A(\gamma\cdot q+\gamma\cdot z).(\gamma\cdot(k+p-z)+m_n).\gamma^\mu.\gamma^5}{4\sqrt{2}F^3(z^2-Mc^2)((k+p-z)^2-m_n^2)}$$

g3 $$\frac{ieg_A(\gamma\cdot q+\gamma\cdot z).(\gamma\cdot(k+p-z)+m_p).\gamma^\mu.(m_p+\gamma\cdot(p-z)).(\gamma\cdot z).\gamma^5}{4\sqrt{2}F^3(z^2-M^2)\big((p-z)^2-m_p^2\big)\big((k+p-z)^2-m_p^2\big)}$$

g4 $$-\frac{ieg_A\gamma^\mu.(m_p+\gamma\cdot(p-z)).(\gamma\cdot z).\gamma^5}{4\sqrt{2}F^3(z^2-M^2)\big((p-z)^2-m_p^2\big)}-\frac{ieg_A\gamma^\mu.(m_n+\gamma\cdot(p-z)).(\gamma\cdot z).\gamma^5}{2\sqrt{2}F^3(z^2-Mc^2)((p-z)^2-m_n^2)}$$

g5 $$0$$

g6 $$\frac{ieg_A(2q-k)^\mu(\gamma\cdot(q-k)+\gamma\cdot z).(m_p+\gamma\cdot(p-z)).(\gamma\cdot z).\gamma^5}{4\sqrt{2}F^3(z^2-M^2)((k-q)^2-Mc^2)\big((p-z)^2-m_p^2\big)}$$
$$+\frac{ieg_A(2q-k)^\mu(\gamma\cdot(q-k)+\gamma\cdot z).(m_n+\gamma\cdot(p-z)).(\gamma\cdot z).\gamma^5}{4\sqrt{2}F^3(z^2-Mc^2)((k-q)^2-Mc^2)((p-z)^2-m_n^2)}$$

g7 $$\frac{ieg_A(k+2z)^\mu(\gamma\cdot(k+z)+\gamma\cdot q).(m_n+\gamma\cdot(p-z)).(\gamma\cdot z).\gamma^5}{4\sqrt{2}F^3(z^2-Mc^2)((-k-z)^2-Mc^2)((p-z)^2-m_n^2)}$$

h1 $$-\frac{ieg_A^3(\gamma\cdot q).\gamma^5.(m_p+\gamma\cdot(p'+q)).(\gamma\cdot z).\gamma^5.(\gamma\cdot(k+p-z)+m_p).(\gamma\cdot z).\gamma^5.(\gamma\cdot(k+p)+m_p).\gamma^\mu}{4\sqrt{2}F^3(z^2-M^2)\big((k+p)^2-m_p^2\big)\big((k+p-z)^2-m_p^2\big)\big((p'+q)^2-m_p^2\big)}$$
$$-\frac{ieg_A^3(\gamma\cdot q).\gamma^5.(m_p+\gamma\cdot(p'+q)).(\gamma\cdot z).\gamma^5.(\gamma\cdot(k+p-z)+m_n).(\gamma\cdot z).\gamma^5.(\gamma\cdot(k+p)+m_p).\gamma^\mu}{2\sqrt{2}F^3(z^2-Mc^2)\big((k+p)^2-m_p^2\big)\big((p'+q)^2-m_p^2\big)((k+p-z)^2-m_n^2)}$$

h2 $$\frac{ieg_A^3(\gamma\cdot q).\gamma^5.(m_p+\gamma\cdot(p'+q)).(\gamma\cdot z).\gamma^5.(\gamma\cdot(k+p-z)+m_n).\gamma^\mu.\gamma^5}{2\sqrt{2}F^3(z^2-Mc^2)\big((p'+q)^2-m_p^2\big)((k+p-z)^2-m_n^2)}$$

h3 $$-\frac{ieg_A^3(\gamma\cdot q).\gamma^5.(m_p+\gamma\cdot(p'+q)).(\gamma\cdot z).\gamma^5.(\gamma\cdot(k+p-z)+m_p).\gamma^\mu.(m_p+\gamma\cdot(p-z)).(\gamma\cdot z).\gamma^5}{4\sqrt{2}F^3(z^2-M^2)\big((p-z)^2-m_p^2\big)\big((k+p-z)^2-m_p^2\big)\big((p'+q)^2-m_p^2\big)}$$

h4 $$\frac{ieg_A^3(\gamma\cdot q).\gamma^5.(m_p+\gamma\cdot(p'+q)).\gamma^\mu.\gamma^5.(m_n+\gamma\cdot(p-z)).(\gamma\cdot z).\gamma^5}{2\sqrt{2}F^3(z^2-Mc^2)((p-z)^2-m_n^2)\big((p'+q)^2-m_p^2\big)}$$

h5 $$\frac{ieg_A^3(k+2z)^\mu(\gamma\cdot q).\gamma^5.(m_p+\gamma\cdot(p'+q)).(\gamma\cdot(-k-z)).\gamma^5.(m_n+\gamma\cdot(p-z)).(\gamma\cdot z).\gamma^5}{2\sqrt{2}F^3(z^2-Mc^2)((k+z)^2-Mc^2)((p-z)^2-m_n^2)\big((p'+q)^2-m_p^2\big)}$$

i1 $$-\frac{i\sqrt{2}eg_A(k-2q)^\mu(\gamma\cdot(q-k)).\gamma^5}{6F^3(z^2-M^2)((k-q)^2-Mc^2)}-\frac{i\sqrt{2}eg_A(k-2q-2z)^\mu(\gamma\cdot(q-k)).\gamma^5}{3F^3(z^2-Mc^2)((k-q)^2-Mc^2)}$$
$$-\frac{i\sqrt{2}eg_A(k-2q+2z)^\mu(\gamma\cdot(q-k)).\gamma^5}{3F^3(z^2-Mc^2)((k-q)^2-Mc^2)}$$

i2 $$\frac{ieg_A(k+2z)^\mu(\gamma\cdot(q-k)).\gamma^5\big(-2((k-q)\cdot(-k-z))+(-q-z)\cdot(q+z)+2M^2-2(q\cdot z)\big)}{6\sqrt{2}F^3(z^2-Mc^2)((k-q)^2-Mc^2)((k+z)^2-Mc^2)}$$
$$+\frac{ieg_A(-k-2z)^\mu(\gamma\cdot(q-k)).\gamma^5\big(-2((k-q)\cdot(k+z))+(q-z)\cdot(2k-q+z)+2M^2+2(q\cdot z)\big)}{6\sqrt{2}F^3(z^2-Mc^2)((k-q)^2-Mc^2)((k+z)^2-Mc^2)}$$

i3 $$\frac{ieg_A(2q-k)^\mu(\gamma\cdot(q-k)).\gamma^5\big(2((k-q)\cdot z)-2((q-k)\cdot z)+(k-q-z)\cdot(-k+q+z)+2M^2\big)}{6\sqrt{2}F^3(z^2-Mc^2)((k-q)^2-Mc^2)^2}$$
$$+\frac{ieg_A(2q-k)^\mu(\gamma\cdot(q-k)).\gamma^5\big(-2((k-q)\cdot z)+2((q-k)\cdot z)+(-k+q-z)\cdot(k-q+z)+2M^2\big)}{6\sqrt{2}F^3(z^2-Mc^2)((k-q)^2-Mc^2)^2}$$
$$+\frac{ieg_A(2q-k)^\mu(\gamma\cdot(q-k)).\gamma^5\big(2((k-q)\cdot(q-k))+M^2-2z\big)}{6\sqrt{2}F^3(z^2-M^2)((k-q)^2-Mc^2)^2}$$

Channel $\gamma^{(*)}n \longrightarrow \pi^- p$

Topology	Integrand $f^{\mu}_{topo}(p,p',k,q,z)$
a1	$\frac{ieg_A\gamma^\mu.(m_p+\gamma\cdot(p-q)).(\gamma\cdot q).\gamma^5}{2\sqrt{2}F^3(z^2-Mc^2)\left((p-q)^2-m_p^2\right)}$
a2	0
a3	$-\frac{ieg_A(-k-2z)^\mu(\gamma\cdot(-k-z)-\gamma\cdot z).(m_p+\gamma\cdot(p-q)).(\gamma\cdot q).\gamma^5}{8\sqrt{2}F^3(z^2-Mc^2)((k+z)^2-Mc^2)\left((p-q)^2-m_p^2\right)}$
	$-\frac{ieg_A(k+2z)^\mu(\gamma\cdot(k+z)+\gamma\cdot z).(m_p+\gamma\cdot(p-q)).(\gamma\cdot q).\gamma^5}{8\sqrt{2}F^3(z^2-Mc^2)((k+z)^2-Mc^2)\left((p-q)^2-m_p^2\right)}$
b1	0
b2	$\frac{ieg_A\gamma^\mu.\gamma^5}{6\sqrt{2}F^3(z^2-M^2)}+\frac{i\sqrt{2}eg_A\gamma^\mu.\gamma^5}{3F^3(z^2-Mc^2)}$
b3	$\frac{ieg_A\gamma^\mu.(m_p+\gamma\cdot(p-q)).(\gamma\cdot q).\gamma^5}{6\sqrt{2}F^3(z^2-M^2)\left((p-q)^2-m_p^2\right)}$
	$-\frac{ieg_A\gamma^\mu.(m_p+\gamma\cdot(p-q)).\left(\frac{-(\gamma\cdot q)-\gamma\cdot z}{6\sqrt{2}}-\frac{\gamma\cdot z}{3\sqrt{2}}\right).\gamma^5}{2F^3(z^2-Mc^2)\left((p-q)^2-m_p^2\right)}$
	$-\frac{ieg_A\gamma^\mu.(m_p+\gamma\cdot(p-q)).\left(\frac{\gamma\cdot z-\gamma\cdot q}{6\sqrt{2}}+\frac{\gamma\cdot z}{3\sqrt{2}}\right).\gamma^5}{2F^3(z^2-Mc^2)\left((p-q)^2-m_p^2\right)}$
b4	$-\frac{ieg_A(k-2q)^\mu(\gamma\cdot(k-q)).\gamma^5}{6\sqrt{2}F^3(z^2-M^2)((k-q)^2-Mc^2)}$
	$-\frac{ieg_A(k-2q)^\mu\left(\frac{\gamma\cdot(k-q)-\gamma\cdot z}{6\sqrt{2}}-\frac{\gamma\cdot z}{3\sqrt{2}}\right).\gamma^5}{2F^3(z^2-Mc^2)((k-q)^2-Mc^2)}$
	$-\frac{ieg_A(k-2q)^\mu\left(\frac{\gamma\cdot(k-q)+\gamma\cdot z}{6\sqrt{2}}+\frac{\gamma\cdot z}{3\sqrt{2}}\right).\gamma^5}{2F^3(z^2-Mc^2)((k-q)^2-Mc^2)}$
b5	$-\frac{ieg_A(-k-2z)^\mu\left(\frac{\gamma\cdot(-k-z)-\gamma\cdot q}{6\sqrt{2}}-\frac{\gamma\cdot z}{3\sqrt{2}}\right).\gamma^5}{2F^3(z^2-Mc^2)((k+z)^2-Mc^2)}-\frac{ieg_A(k+2z)^\mu\left(\frac{\gamma\cdot(k+z)-\gamma\cdot q}{6\sqrt{2}}+\frac{\gamma\cdot z}{3\sqrt{2}}\right).\gamma^5}{2F^3(z^2-Mc^2)((k+z)^2-Mc^2)}$
c1	0
c2	$-\frac{ieg_A(\gamma\cdot q).\gamma^5.(\gamma\cdot(k+p)+m_n).\gamma^\mu}{2\sqrt{2}F^3(z^2-Mc^2)((k+p)^2-m_n^2)}$
c3	$\frac{ieg_A(-k-2z)^\mu(\gamma\cdot q).\gamma^5.(\gamma\cdot(k+p)+m_n).(\gamma\cdot(-k-z)-\gamma\cdot z)}{8\sqrt{2}F^3(z^2-Mc^2)((k+z)^2-Mc^2)((k+p)^2-m_n^2)}$
	$+\frac{ieg_A(k+2z)^\mu(\gamma\cdot q).\gamma^5.(\gamma\cdot(k+p)+m_n).(\gamma\cdot(k+z)+\gamma\cdot z)}{8\sqrt{2}F^3(z^2-Mc^2)((k+z)^2-Mc^2)((k+p)^2-m_n^2)}$
d1	$\frac{ieg_A^3(\gamma\cdot z).\gamma^5.(m_n+\gamma\cdot(p'-z)).\gamma^\mu.\gamma^5.(m_p+\gamma\cdot(p-q)).(\gamma\cdot q).\gamma^5}{2\sqrt{2}F^3(z^2-Mc^2)\left((p-q)^2-m_p^2\right)\left((p'-z)^2-m_n^2\right)}$
d2	$-\frac{ieg_A^3(\gamma\cdot z).\gamma^5.(m_p+\gamma\cdot(p'-z)).\gamma^\mu.(\gamma\cdot(-k+p'-z)+m_p).(\gamma\cdot z).\gamma^5.(m_p+\gamma\cdot(p-q)).(\gamma\cdot q).\gamma^5}{4\sqrt{2}F^3(z^2-M^2)\left((p-q)^2-m_p^2\right)\left((p'-z)^2-m_p^2\right)\left((-k+p'-z)^2-m_p^2\right)}$
d3	$\frac{ieg_A^3\gamma^\mu.\gamma^5.(m_n+\gamma\cdot(p-q-z)).(\gamma\cdot z).\gamma^5.(m_p+\gamma\cdot(p-q)).(\gamma\cdot q).\gamma^5}{2\sqrt{2}F^3(z^2-Mc^2)\left((p-q)^2-m_p^2\right)((p-q-z)^2-m_n^2)}$
d4	$-\frac{ieg_A^3\gamma^\mu.(\gamma\cdot(p'-k)+m_p).(\gamma\cdot z).\gamma^5.(m_p+\gamma\cdot(p-q-z)).(\gamma\cdot z).\gamma^5.(m_p+\gamma\cdot(p-q)).(\gamma\cdot q).\gamma^5}{4\sqrt{2}F^3(z^2-M^2)\left((p-q)^2-m_p^2\right)\left((p'-k)^2-m_p^2\right)\left((p-q-z)^2-m_p^2\right)}$
	$-\frac{ieg_A^3\gamma^\mu.(\gamma\cdot(p'-k)+m_p).(\gamma\cdot z).\gamma^5.(m_n+\gamma\cdot(p-q-z)).(\gamma\cdot z).\gamma^5.(m_p+\gamma\cdot(p-q)).(\gamma\cdot q).\gamma^5}{2\sqrt{2}F^3(z^2-Mc^2)\left((p-q)^2-m_p^2\right)\left((p'-k)^2-m_p^2\right)((p-q-z)^2-m_n^2)}$
d5	$\frac{ieg_A^3(k+2z)^\mu(\gamma\cdot(-k-z)).\gamma^5.(m_n+\gamma\cdot(p-q-z)).(\gamma\cdot z).\gamma^5.(m_p+\gamma\cdot(p-q)).(\gamma\cdot q).\gamma^5}{2\sqrt{2}F^3(z^2-Mc^2)((k+z)^2-Mc^2)\left((p-q)^2-m_p^2\right)((p-q-z)^2-m_n^2)}$
e1	0
e2	$\frac{ieg_A(\gamma\cdot z).\gamma^5.(m_p+\gamma\cdot(p'-z)).\gamma^\mu}{4\sqrt{2}F^3(z^2-M^2)\left((p'-z)^2-m_p^2\right)}+\frac{ieg_A(\gamma\cdot z).\gamma^5.(m_n+\gamma\cdot(p'-z)).\gamma^\mu}{2\sqrt{2}F^3(z^2-Mc^2)\left((p'-z)^2-m_n^2\right)}$
e3	$-\frac{ieg_A(\gamma\cdot z).\gamma^5.(m_p+\gamma\cdot(p'-z)).\gamma^\mu.(\gamma\cdot(-k+p'-z)+m_p).(\gamma\cdot z-\gamma\cdot q)}{4\sqrt{2}F^3(z^2-M^2)\left((p'-z)^2-m_p^2\right)\left((-k+p'-z)^2-m_p^2\right)}$
e4	$\frac{ieg_A\gamma^\mu.\gamma^5.(\gamma\cdot(-k+p'-z)+m_n).(\gamma\cdot z-\gamma\cdot q)}{4\sqrt{2}F^3(z^2-Mc^2)\left((-k+p'-z)^2-m_n^2\right)}$
e5	$-\frac{ieg_A\gamma^\mu.(\gamma\cdot(p'-k)+m_p).(\gamma\cdot z).\gamma^5.(m_p+\gamma\cdot(p-q-z)).(\gamma\cdot z-\gamma\cdot q)}{4\sqrt{2}F^3(z^2-M^2)\left((p'-k)^2-m_p^2\right)\left((p-q-z)^2-m_p^2\right)}$
	$-\frac{ieg_A\gamma^\mu.(\gamma\cdot(p'-k)+m_p).(\gamma\cdot z).\gamma^5.(m_n+\gamma\cdot(p-q-z)).(\gamma\cdot z-\gamma\cdot q)}{4\sqrt{2}F^3(z^2-Mc^2)\left((p'-k)^2-m_p^2\right)((p-q-z)^2-m_n^2)}$
e6	$-\frac{ieg_A(k-2q)^\mu(\gamma\cdot z).\gamma^5.(m_p+\gamma\cdot(p'-z)).(\gamma\cdot(k-q)+\gamma\cdot z)}{4\sqrt{2}F^3(z^2-M^2)((k-q)^2-Mc^2)\left((p'-z)^2-m_p^2\right)}$
	$-\frac{ieg_A(k-2q)^\mu(\gamma\cdot z).\gamma^5.(m_n+\gamma\cdot(p'-z)).(\gamma\cdot(k-q)+\gamma\cdot z)}{4\sqrt{2}F^3(z^2-Mc^2)((k-q)^2-Mc^2)\left((p'-z)^2-m_n^2\right)}$

e7	$\frac{ieg_A(k+2z)^\mu(\gamma\cdot(-k-z)).\gamma^5.(m_n+\gamma\cdot(p-q-z)).(\gamma\cdot z-\gamma\cdot q)}{4\sqrt{2}F^3(z^2-Mc^2)((k+z)^2-Mc^2)((p-q-z)^2-m_n^2)}$
f1	0
f2	0
f3	0
f4	$\frac{ieg_A^3(\gamma\cdot z).\gamma^5.(m_p+\gamma\cdot(p'-z)).\gamma^\mu.\gamma^5.(m_n+\gamma\cdot(p-z)).(\gamma\cdot z).\gamma^5}{4\sqrt{2}F^3(z^2-M^2)((p-z)^2-m_n^2)\big((p'-z)^2-m_p^2\big)}$
f5	$\frac{ieg_A^3(\gamma\cdot z).\gamma^5.(m_p+\gamma\cdot(p'-z)).\gamma^\mu.(\gamma\cdot(-k+p'-z)+m_p).(\gamma\cdot q).\gamma^5.(m_n+\gamma\cdot(p-z)).(\gamma\cdot z).\gamma^5}{4\sqrt{2}F^3(z^2-M^2)((p-z)^2-m_n^2)\big((p'-z)^2-m_p^2\big)\big((-k+p'-z)^2-m_p^2\big)}$
f6	0
f7	$\frac{ieg_A^3\gamma^\mu.(\gamma\cdot(p'-k)+m_p).(\gamma\cdot z).\gamma^5.(m_p+\gamma\cdot(p-q-z)).(\gamma\cdot q).\gamma^5.(m_n+\gamma\cdot(p-z)).(\gamma\cdot z).\gamma^5}{4\sqrt{2}F^3(z^2-M^2)\big((p'-k)^2-m_p^2\big)((p-z)^2-m_n^2)\big((p-q-z)^2-m_p^2\big)}$
f8	$\frac{ieg_A^3(k-2q)^\mu(\gamma\cdot z).\gamma^5.(m_p+\gamma\cdot(p'-z)).(\gamma\cdot(q-k)).\gamma^5.(m_n+\gamma\cdot(p-z)).(\gamma\cdot z).\gamma^5}{4\sqrt{2}F^3(z^2-M^2)((k-q)^2-Mc^2)((p-z)^2-m_n^2)\big((p'-z)^2-m_p^2\big)}$
f9	0
g1	0
g2	$-\frac{ieg_A(-(\gamma\cdot q)-\gamma\cdot z).(\gamma\cdot(k+p-z)+m_p).\gamma^\mu.\gamma^5}{4\sqrt{2}F^3(z^2-Mc^2)\big((k+p-z)^2-m_p^2\big)}$
g3	$-\frac{ieg_A(-(\gamma\cdot q)-\gamma\cdot z).(\gamma\cdot(k+p-z)+m_p).\gamma^\mu.(m_p+\gamma\cdot(p-z)).(\gamma\cdot z).\gamma^5}{4\sqrt{2}F^3(z^2-Mc^2)\big((p-z)^2-m_p^2\big)\big((k+p-z)^2-m_p^2\big)}$
g4	$\frac{ieg_A\gamma^\mu.(m_n+\gamma\cdot(p-z)).(\gamma\cdot z).\gamma^5}{4\sqrt{2}F^3(z^2-M^2)((p-z)^2-m_n^2)}+\frac{ieg_A\gamma^\mu.(m_p+\gamma\cdot(p-z)).(\gamma\cdot z).\gamma^5}{2\sqrt{2}F^3(z^2-Mc^2)\big((p-z)^2-m_p^2\big)}$
g5	$-\frac{ieg_A\gamma^\mu.(\gamma\cdot(p'-k)+m_p).(-(\gamma\cdot q)-\gamma\cdot z).(m_n+\gamma\cdot(p-z)).(\gamma\cdot z).\gamma^5}{4\sqrt{2}F^3(z^2-M^2)\big((p'-k)^2-m_p^2\big)((p-z)^2-m_n^2)}$
	$-\frac{ieg_A\gamma^\mu.(\gamma\cdot(p'-k)+m_p).(-(\gamma\cdot q)-\gamma\cdot z).(m_p+\gamma\cdot(p-z)).(\gamma\cdot z).\gamma^5}{4\sqrt{2}F^3(z^2-Mc^2)\big((p-z)^2-m_p^2\big)\big((p'-k)^2-m_p^2\big)}$
g6	$-\frac{ieg_A(k-2q)^\mu(\gamma\cdot(k-q)-\gamma\cdot z).(m_n+\gamma\cdot(p-z)).(\gamma\cdot z).\gamma^5}{4\sqrt{2}F^3(z^2-M^2)((k-q)^2-Mc^2)((p-z)^2-m_n^2)}$
	$-\frac{ieg_A(k-2q)^\mu(\gamma\cdot(k-q)-\gamma\cdot z).(m_p+\gamma\cdot(p-z)).(\gamma\cdot z).\gamma^5}{4\sqrt{2}F^3(z^2-Mc^2)((k-q)^2-Mc^2)\big((p-z)^2-m_p^2\big)}$
g7	$-\frac{ieg_A(-k-2z)^\mu(\gamma\cdot(-k-z)-\gamma\cdot q).(m_p+\gamma\cdot(p-z)).(\gamma\cdot z).\gamma^5}{4\sqrt{2}F^3(z^2-Mc^2)((-k-z)^2-Mc^2)\big((p-z)^2-m_p^2\big)}$
h1	0
h2	$-\frac{ieg_A^3(\gamma\cdot q).\gamma^5.(m_n+\gamma\cdot(p'+q)).(\gamma\cdot z).\gamma^5.(\gamma\cdot(k+p-z)+m_p).\gamma^\mu.\gamma^5}{2\sqrt{2}F^3(z^2-Mc^2)\big((k+p-z)^2-m_p^2\big)\big((p'+q)^2-m_n^2\big)}$
h3	$-\frac{ieg_A^3(\gamma\cdot q).\gamma^5.(m_n+\gamma\cdot(p'+q)).(\gamma\cdot z).\gamma^5.(\gamma\cdot(k+p-z)+m_p).\gamma^\mu.(m_p+\gamma\cdot(p-z)).(\gamma\cdot z).\gamma^5}{2\sqrt{2}F^3(z^2-Mc^2)\big((p-z)^2-m_p^2\big)\big((k+p-z)^2-m_p^2\big)\big((p'+q)^2-m_n^2\big)}$
h4	$-\frac{ieg_A^3(\gamma\cdot q).\gamma^5.(m_n+\gamma\cdot(p'+q)).\gamma^\mu.\gamma^5.(m_p+\gamma\cdot(p-z)).(\gamma\cdot z).\gamma^5}{2\sqrt{2}F^3(z^2-Mc^2)\big((p-z)^2-m_p^2\big)\big((p'+q)^2-m_n^2\big)}$
h5	$\frac{ieg_A^3(-k-2z)^\mu(\gamma\cdot q).\gamma^5.(m_n+\gamma\cdot(p'+q)).(\gamma\cdot(-k-z)).\gamma^5.(m_p+\gamma\cdot(p-z)).(\gamma\cdot z).\gamma^5}{2\sqrt{2}F^3(z^2-Mc^2)((k+z)^2-Mc^2)\big((p-z)^2-m_p^2\big)\big((p'+q)^2-m_n^2\big)}$
i1	$-\frac{i\sqrt{2}eg_A(2q-k)^\mu(\gamma\cdot(q-k)).\gamma^5}{6F^3(z^2-M^2)((k-q)^2-Mc^2)}-\frac{i\sqrt{2}eg_A(-k+2q-2z)^\mu(\gamma\cdot(q-k)).\gamma^5}{3F^3(z^2-Mc^2)((k-q)^2-Mc^2)}$
	$-\frac{i\sqrt{2}eg_A(-k+2q+2z)^\mu(\gamma\cdot(q-k)).\gamma^5}{3F^3(z^2-Mc^2)((k-q)^2-Mc^2)}$
i2	$\frac{ieg_A(-k-2z)^\mu(\gamma\cdot(q-k)).\gamma^5\big(-2((q-k)\cdot(k+z))+(-q-z)\cdot(q+z)+2M^2-2(q\cdot z)\big)}{6\sqrt{2}F^3(z^2-Mc^2)((k-q)^2-Mc^2)((k+z)^2-Mc^2)}$
	$+\frac{ieg_A(k+2z)^\mu(\gamma\cdot(q-k)).\gamma^5\big(-2((q-k)\cdot(-k-z))+(-2k+q-z)\cdot(z-q)+2M^2+2(q\cdot z)\big)}{6\sqrt{2}F^3(z^2-Mc^2)((k-q)^2-Mc^2)((k+z)^2-Mc^2)}$
i3	$\frac{ieg_A(k-2q)^\mu(\gamma\cdot(q-k)).\gamma^5\big(2((k-q)\cdot z)-2((q-k)\cdot z)+(k-q-z)\cdot(-k+q+z)+2M^2\big)}{6\sqrt{2}F^3(z^2-Mc^2)((k-q)^2-Mc^2)^2}$
	$+\frac{ieg_A(k-2q)^\mu(\gamma\cdot(q-k)).\gamma^5\big(-2((k-q)\cdot z)+2((q-k)\cdot z)+(-k+q-z)\cdot(k-q+z)+2M^2\big)}{6\sqrt{2}F^3(z^2-Mc^2)((k-q)^2-Mc^2)^2}$
	$+\frac{ieg_A(k-2q)^\mu(\gamma\cdot(q-k)).\gamma^5\big(2((k-q)\cdot(q-k))+M^2-2z\big)}{6\sqrt{2}F^3(z^2-M^2)((k-q)^2-Mc^2)^2}$

Channel $\gamma^{(*)}n \longrightarrow \pi^0 n$

Topology	Integrand $f^{\mu}_{topo}(p,p',k,q,z)$
a1	$\frac{ieg_A\gamma^\mu.(m_n+\gamma\cdot(p-q)).(\gamma\cdot q).\gamma^5}{4F^3(z^2-Mc^2)((p-q)^2-m_n^2)}$
a2	0
a3	$-\frac{ieg_A(-k-2z)^\mu(\gamma\cdot(-k-z)-\gamma\cdot z).(m_n+\gamma\cdot(p-q)).(\gamma\cdot q).\gamma^5}{16F^3(z^2-Mc^2)((k+z)^2-Mc^2)((p-q)^2-m_n^2)}$ $-\frac{ieg_A(k+2z)^\mu(\gamma\cdot(k+z)+\gamma\cdot z).(m_n+\gamma\cdot(p-q)).(\gamma\cdot q).\gamma^5}{16F^3(z^2-Mc^2)((k+z)^2-Mc^2)((p-q)^2-m_n^2)}$
b1	0
b2	0
b3	0
b4	0
b5	$\frac{ieg_A(-k-2z)^\mu(-\gamma\cdot(-k-z)-2\gamma\cdot q-\gamma\cdot z).\gamma^5}{24F^3(z^2-Mc^2)((k+z)^2-Mc^2)}+\frac{ieg_A(k+2z)^\mu(-\gamma\cdot(k+z)-2\gamma\cdot q+\gamma\cdot z).\gamma^5}{24F^3(z^2-Mc^2)((k+z)^2-Mc^2)}$
c1	0
c2	$\frac{ieg_A(\gamma\cdot q).\gamma^5.(\gamma\cdot(k+p)+m_n).\gamma^\mu}{4F^3(z^2-Mc^2)((k+p)^2-m_n^2)}$
c3	$-\frac{ieg_A(-k-2z)^\mu(\gamma\cdot q).\gamma^5.(\gamma\cdot(k+p)+m_n).(\gamma\cdot(-k-z)-\gamma\cdot z)}{16F^3(z^2-Mc^2)((k+z)^2-Mc^2)((k+p)^2-m_n^2)}$ $-\frac{ieg_A(k+2z)^\mu(\gamma\cdot q).\gamma^5.(\gamma\cdot(k+p)+m_n).(\gamma\cdot(k+z)+\gamma\cdot z)}{16F^3(z^2-Mc^2)((k+z)^2-Mc^2)((k+p)^2-m_n^2)}$
d1	$\frac{ieg_A^3(\gamma\cdot z).\gamma^5.(m_p+\gamma\cdot(p'-z)).\gamma^\mu.\gamma^5.(m_n+\gamma\cdot(p-q)).(\gamma\cdot q).\gamma^5}{4F^3(z^2-Mc^2)((p-q)^2-m_n^2)\left((p'-z)^2-m_p^2\right)}$
d2	$\frac{ieg_A^3(\gamma\cdot z).\gamma^5.(m_p+\gamma\cdot(p'-z)).\gamma^\mu.(\gamma\cdot(-k+p'-z)+m_p).(\gamma\cdot z).\gamma^5.(m_n+\gamma\cdot(p-q)).(\gamma\cdot q).\gamma^5}{4F^3(z^2-Mc^2)((p-q)^2-m_n^2)\left((p'-z)^2-m_p^2\right)\left((-k+p'-z)^2-m_p^2\right)}$
d3	$\frac{ieg_A^3\gamma^\mu.\gamma^5.(m_p+\gamma\cdot(p-q-z)).(\gamma\cdot z).\gamma^5.(m_n+\gamma\cdot(p-q)).(\gamma\cdot q).\gamma^5}{4F^3(z^2-Mc^2)((p-q)^2-m_n^2)\left((p-q-z)^2-m_p^2\right)}$
d4	0
d5	$-\frac{ieg_A^3(-k-2z)^\mu(\gamma\cdot(-k-z)).\gamma^5.(m_p+\gamma\cdot(p-q-z)).(\gamma\cdot z).\gamma^5.(m_n+\gamma\cdot(p-q)).(\gamma\cdot q).\gamma^5}{4F^3(z^2-Mc^2)((k+z)^2-Mc^2)((p-q)^2-m_n^2)\left((p-q-z)^2-m_p^2\right)}$
e1	0
e2	$\frac{ieg_A(\gamma\cdot z).\gamma^5.(m_p+\gamma\cdot(p'-z)).\gamma^\mu}{4F^3(z^2-Mc^2)\left((p'-z)^2-m_p^2\right)}$
e3	$-\frac{ieg_A(\gamma\cdot z).\gamma^5.(m_p+\gamma\cdot(p'-z)).\gamma^\mu.(\gamma\cdot(-k+p'-z)+m_p).(\gamma\cdot q-\gamma\cdot z)}{4F^3(z^2-Mc^2)\left((p'-z)^2-m_p^2\right)\left((-k+p'-z)^2-m_p^2\right)}$
e4	$-\frac{ieg_A\gamma^\mu.\gamma^5.(\gamma\cdot(-k+p'-z)+m_p).(\gamma\cdot q-\gamma\cdot z)}{4F^3(z^2-Mc^2)\left((-k+p'-z)^2-m_p^2\right)}$
e5	0
e6	0
e7	$\frac{ieg_A(-k-2z)^\mu(\gamma\cdot(-k-z)).\gamma^5.(m_p+\gamma\cdot(p-q-z)).(\gamma\cdot q-\gamma\cdot z)}{4F^3(z^2-Mc^2)((k+z)^2-Mc^2)\left((p-q-z)^2-m_p^2\right)}$
f1	0
f2	$-\frac{ieg_A^3(\gamma\cdot z).\gamma^5.(m_p+\gamma\cdot(p'-z)).(\gamma\cdot q).\gamma^5.(\gamma\cdot(k+p-z)+m_p).\gamma^\mu.\gamma^5}{4F^3(z^2-Mc^2)\left((k+p-z)^2-m_p^2\right)\left((p'-z)^2-m_p^2\right)}$
f3	$-\frac{ieg_A^3(\gamma\cdot z).\gamma^5.(m_p+\gamma\cdot(p'-z)).(\gamma\cdot q).\gamma^5.(\gamma\cdot(k+p-z)+m_p).\gamma^\mu.(m_p+\gamma\cdot(p-z)).(\gamma\cdot z).\gamma^5}{4F^3(z^2-Mc^2)\left((p-z)^2-m_p^2\right)\left((k+p-z)^2-m_p^2\right)\left((p'-z)^2-m_p^2\right)}$
f4	0
f5	$-\frac{ieg_A^3(\gamma\cdot z).\gamma^5.(m_p+\gamma\cdot(p'-z)).\gamma^\mu.(\gamma\cdot(-k+p'-z)+m_p).(\gamma\cdot q).\gamma^5.(m_p+\gamma\cdot(p-z)).(\gamma\cdot z).\gamma^5}{4F^3(z^2-Mc^2)\left((p-z)^2-m_p^2\right)\left((p'-z)^2-m_p^2\right)\left((-k+p'-z)^2-m_p^2\right)}$
f6	$-\frac{ieg_A^3\gamma^\mu.\gamma^5.(m_p+\gamma\cdot(p-q-z)).(\gamma\cdot q).\gamma^5.(m_p+\gamma\cdot(p-z)).(\gamma\cdot z).\gamma^5}{4F^3(z^2-Mc^2)\left((p-z)^2-m_p^2\right)\left((p-q-z)^2-m_p^2\right)}$
f7	0
f8	0
f9	$\frac{ieg_A^3(-k-2z)^\mu(\gamma\cdot(-k-z)).\gamma^5.(m_p+\gamma\cdot(p-q-z)).(\gamma\cdot q).\gamma^5.(m_p+\gamma\cdot(p-z)).(\gamma\cdot z).\gamma^5}{4F^3(z^2-Mc^2)((k+z)^2-Mc^2)\left((p-z)^2-m_p^2\right)\left((p-q-z)^2-m_p^2\right)}$
g1	0
g2	$\frac{ieg_A(-(\gamma\cdot q)-\gamma\cdot z).(\gamma\cdot(k+p-z)+m_p).\gamma^\mu.\gamma^5}{4F^3(z^2-Mc^2)\left((k+p-z)^2-m_p^2\right)}$

g3	$\frac{ieg_A(-(\gamma\cdot q)-\gamma\cdot z).(\gamma\cdot(k+p-z)+m_p).\gamma^\mu.(m_p+\gamma\cdot(p-z)).(\gamma\cdot z).\gamma^5}{4F^3(z^2-Mc^2)\big((p-z)^2-m_p^2\big)\big((k+p-z)^2-m_p^2\big)}$
g4	$-\frac{ieg_A\gamma^\mu.(m_p+\gamma\cdot(p-z)).(\gamma\cdot z).\gamma^5}{4F^3(z^2-Mc^2)\big((p-z)^2-m_p^2\big)}$
g5	0
g6	0
g7	$\frac{ieg_A(-k-2z)^\mu(\gamma\cdot(-k-z)-\gamma\cdot q).(m_p+\gamma\cdot(p-z)).(\gamma\cdot z).\gamma^5}{4F^3(z^2-Mc^2)((-k-z)^2-Mc^2)\big((p-z)^2-m_p^2\big)}$
h1	0
h2	$\frac{ieg_A^3(\gamma\cdot q).\gamma^5.(m_n+\gamma\cdot(p'+q)).(\gamma\cdot z).\gamma^5.(\gamma\cdot(k+p-z)+m_p).\gamma^\mu.\gamma^5}{4F^3(z^2-Mc^2)\big((k+p-z)^2-m_p^2\big)\big((p'+q)^2-m_n^2\big)}$
h3	$\frac{ieg_A^3(\gamma\cdot q).\gamma^5.(m_n+\gamma\cdot(p'+q)).(\gamma\cdot z).\gamma^5.(\gamma\cdot(k+p-z)+m_p).\gamma^\mu.(m_p+\gamma\cdot(p-z)).(\gamma\cdot z).\gamma^5}{4F^3(z^2-Mc^2)\big((p-z)^2-m_p^2\big)\big((k+p-z)^2-m_p^2\big)\big((p'+q)^2-m_n^2\big)}$
h4	$\frac{ieg_A^3(\gamma\cdot q).\gamma^5.(m_n+\gamma\cdot(p'+q)).\gamma^\mu.\gamma^5.(m_p+\gamma\cdot(p-z)).(\gamma\cdot z).\gamma^5}{4F^3(z^2-Mc^2)\big((p-z)^2-m_p^2\big)\big((p'+q)^2-m_n^2\big)}$
h5	$-\frac{ieg_A^3(-k-2z)^\mu(\gamma\cdot q).\gamma^5.(m_n+\gamma\cdot(p'+q)).(\gamma\cdot(-k-z)).\gamma^5.(m_p+\gamma\cdot(p-z)).(\gamma\cdot z).\gamma^5}{4F^3(z^2-Mc^2)((k+z)^2-Mc^2)\big((p-z)^2-m_p^2\big)\big((p'+q)^2-m_n^2\big)}$
i1	0
i2	$-\frac{ieg_A(-k-2z)^\mu(\gamma\cdot(q-k)).\gamma^5\big(2((k-q)\cdot q)+2((-k-z)\cdot z)+M^2-Q^2\big)}{12F^3(z^2-Mc^2)((k-q)^2-M^2)((k+z)^2-Mc^2)}$
	$-\frac{ieg_A(k+2z)^\mu(\gamma\cdot(q-k)).\gamma^5\big(2((k-q)\cdot q)-2(z\cdot(k+z))+M^2+Q^2\big)}{12F^3(z^2-Mc^2)((k-q)^2-M^2)((k+z)^2-Mc^2)}$
i3	0

Appendix B

Power counting breaking terms for loop amplitudes

In the EOMS regularization scheme, the power counting breaking terms extracted in the $\mathcal{O}(p^3)$ one-loop amplitudes are given explicitly below for each reaction channel. As shown in Eq. (4.96), the PCBT derived from the $\mathcal{O}(p)$ and $\mathcal{O}(p^2)$ tree amplitudes are denoted by PCBT_1 and PCBT_2 respectively. The expressions are expanded in the Ball parametrization for electro- and photoproduction amplitudes of Eqs. (3.14), (3.74).

B.1 PCBT for pion electroproduction on nucleons

$\gamma^* + p \longrightarrow \pi^0 + p$ **channel**

$$\begin{aligned}\mathrm{PCBT}_1 =& -\frac{eg_A^3 m_N^2 \left(V_1^\mu \left(m_N^2 - s\right) + 2m_N \left(2V_2^\mu + V_3^\mu + V_4^\mu - V_5^\mu\right)\right)}{32\pi^2 F_\pi^3 \left(m_N^2 - s\right)} \\ &+ \frac{eg_A^3 m_N^2 \left(V_1^\mu \left(m_N^2 - u\right) - 2m_N \left(2V_2^\mu - V_3^\mu + V_4^\mu - V_5^\mu\right)\right)}{32\pi^2 F_\pi^3 \left(m_N^2 - u\right)}\end{aligned} \tag{B.1}$$

$$\begin{aligned}\mathrm{PCBT}_2 =& \Bigg[\frac{3eM^2 g_A^3 m_N \left(2V_2^\mu + V_3^\mu + V_4^\mu - V_5^\mu\right)}{64\pi^2 F_\pi^3 \left(m_N^2 - s\right)} \\ &- \frac{3eM^2 g_A^3 m_N^2 \left(V_1^\mu \left(m_N^2 - s\right) + 2m_N \left(2V_2^\mu + V_3^\mu + V_4^\mu - V_5^\mu\right)\right)}{32\pi^2 F_\pi^3 \left(m_N^2 - s\right)^2} \\ &+ \frac{3eM^2 g_A^3 m_N \left(2V_2^\mu - V_3^\mu + V_4^\mu - V_5^\mu\right)}{64\pi^2 F_\pi^3 \left(m_N^2 - u\right)} \\ &+ \frac{3eM^2 g_A^3 m_N^2 \left(V_1^\mu \left(m_N^2 - u\right) - 2m_N \left(2V_2^\mu - V_3^\mu + V_4^\mu - V_5^\mu\right)\right)}{32\pi^2 F_\pi^3 \left(m_N^2 - u\right)^2}\Bigg] \\ &+ \frac{eg_A^3 m_N \left(2m_N \left(-sV_1^\mu + 2V_6^\mu + V_7^\mu\right) + 2m_N^3 V_1^\mu + 3m_N^2 \left(V_4^\mu - V_5^\mu\right) + s\left(V_4^\mu - V_5^\mu\right)\right)}{64\pi^2 F_\pi^3 \left(m_N^2 - s\right)} \\ &- \frac{eg_A^3 m_N \left(-2m_N \left(uV_1^\mu + 2V_6^\mu - V_7^\mu\right) + 2m_N^3 V_1^\mu - 3m_N^2 \left(V_4^\mu - V_5^\mu\right) + u\left(V_5^\mu - V_4^\mu\right)\right)}{64\pi^2 F_\pi^3 \left(m_N^2 - u\right)}\end{aligned} \tag{B.2}$$

$$\mathrm{PCBT}_1 + \mathrm{PCBT}_2 = M^2 \Bigg[\frac{3eg_A^3 m_N^2 \left(m_N^2 V_1^\mu - 2m_N \left(2V_2^\mu - V_3^\mu + V_4^\mu - V_5^\mu\right) - uV_1^\mu\right)}{32\pi^2 F_\pi^3 \left(m_N^2 - u\right)^2}$$

$$
\begin{aligned}
&- \frac{3eg_A^3 m_N^2 \left(m_N^2 V_1^\mu + 2m_N \left(2V_2^\mu + V_3^\mu + V_4^\mu - V_5^\mu\right) - sV_1^\mu\right)}{32\pi^2 F_\pi^3 \left(m_N^2 - s\right)^2} \\
&+ \frac{3eg_A^3 m_N \left(2V_2^\mu - V_3^\mu + V_4^\mu - V_5^\mu\right)}{64\pi^2 F_\pi^3 \left(m_N^2 - u\right)} \\
&+ \frac{3eg_A^3 m_N \left(2V_2^\mu + V_3^\mu + V_4^\mu - V_5^\mu\right)}{64\pi^2 F_\pi^3 \left(m_N^2 - s\right)} \Bigg] \\
&+ \frac{eg_A^3 m_N \left(m_N^2 \left(-\left(8V_2^\mu + 4V_3^\mu + V_4^\mu - V_5^\mu\right)\right) + 2m_N \left(2V_6^\mu + V_7^\mu\right) + s\left(V_4^\mu - V_5^\mu\right)\right)}{64\pi^2 F_\pi^3 \left(m_N^2 - s\right)} \\
&+ \frac{eg_A^3 m_N \left(m_N^2 \left(-8V_2^\mu + 4V_3^\mu - V_4^\mu + V_5^\mu\right) + m_N \left(4V_6^\mu - 2V_7^\mu\right) + u\left(V_4^\mu - V_5^\mu\right)\right)}{64\pi^2 F_\pi^3 \left(m_N^2 - u\right)}
\end{aligned}
\tag{B.3}
$$

$\gamma^* + p \longrightarrow \pi^+ + n$ **channel**

$$
\begin{aligned}
\mathrm{PCBT}_1 = &- \frac{eg_A^3 m_N^2 \left(m_N^2 V_1^\mu + 2m_N \left(2V_2^\mu + V_3^\mu + V_4^\mu - V_5^\mu\right) - sV_1^\mu\right)}{16\sqrt{2}\pi^2 F_\pi^3 \left(m_N^2 - s\right)} \\
&+ \frac{eg_A^3 m_N^2 \left(-2m_N^2 V_1^\mu + m_N \left(2V_4^\mu - 4V_3^\mu\right) + V_1^\mu \left(Q^2 + s + u\right)\right)}{16\sqrt{2}\pi^2 F_\pi^3 \left(-2m_N^2 + Q^2 + s + u\right)}
\end{aligned}
\tag{B.4}
$$

$$
\begin{aligned}
\mathrm{PCBT}_2 = &\Bigg[\frac{3eM^2 g_A^3 m_N \left(2V_2^\mu + V_3^\mu + V_4^\mu - V_5^\mu\right)}{32\sqrt{2}\pi^2 F_\pi^3 \left(m_N^2 - s\right)} \\
&- \frac{3eM^2 g_A^3 m_N^2 \left(V_1^\mu \left(m_N^2 - s\right) + 2m_N \left(2V_2^\mu + V_3^\mu + V_4^\mu - V_5^\mu\right)\right)}{16\sqrt{2}\pi^2 F_\pi^3 \left(m_N^2 - s\right)^2}\Bigg] \\
&+ \frac{eg_A^3 m_N \left(2m_N \left(-sV_1^\mu + 2V_6^\mu + V_7^\mu\right) + 2m_N^3 V_1^\mu + 3m_N^2 \left(V_4^\mu - V_5^\mu\right) + s\left(V_4^\mu - V_5^\mu\right)\right)}{32\sqrt{2}\pi^2 F_\pi^3 \left(m_N^2 - s\right)} \\
&+ \frac{eg_A^3 m_N \left(-2m_N \left(uV_1^\mu + 2V_6^\mu - V_7^\mu\right) + 2m_N^3 V_1^\mu - 3m_N^2 \left(V_4^\mu - V_5^\mu\right) + u\left(V_5^\mu - V_4^\mu\right)\right)}{8\sqrt{2}\pi^2 F_\pi^3 \left(m_N^2 - u\right)}
\end{aligned}
\tag{B.5}
$$

$$
\begin{aligned}
\mathrm{PCBT}_1 + \mathrm{PCBT}_2 = M^2 &\Bigg[\frac{3eg_A^3 m_N \left(2V_2^\mu + V_3^\mu + V_4^\mu - V_5^\mu\right)}{32\sqrt{2}\pi^2 F_\pi^3 \left(m_N^2 - s\right)} \\
&- \frac{3eg_A^3 m_N^2 \left(m_N^2 V_1^\mu + 2m_N \left(2V_2^\mu + V_3^\mu + V_4^\mu - V_5^\mu\right) - sV_1^\mu\right)}{16\sqrt{2}\pi^2 F_\pi^3 \left(m_N^2 - s\right)^2}\Bigg] \\
&+ \frac{eg_A^3 m_N^2 \left(-2m_N^2 V_1^\mu + m_N \left(2V_4^\mu - 4V_3^\mu\right) + V_1^\mu \left(Q^2 + s + u\right)\right)}{16\sqrt{2}\pi^2 F_\pi^3 \left(-2m_N^2 + Q^2 + s + u\right)} \\
&+ \frac{eg_A^3 m_N \left(m_N^2 \left(-\left(8V_2^\mu + 4V_3^\mu + V_4^\mu - V_5^\mu\right)\right) + 2m_N \left(2V_6^\mu + V_7^\mu\right) + s\left(V_4^\mu - V_5^\mu\right)\right)}{32\sqrt{2}\pi^2 F_\pi^3 \left(m_N^2 - s\right)} \\
&+ \frac{eg_A^3 m_N \left(-2m_N \left(uV_1^\mu + 2V_6^\mu - V_7^\mu\right) + 2m_N^3 V_1^\mu - 3m_N^2 \left(V_4^\mu - V_5^\mu\right) + u\left(V_5^\mu - V_4^\mu\right)\right)}{8\sqrt{2}\pi^2 F_\pi^3 \left(m_N^2 - u\right)}
\end{aligned}
\tag{B.6}
$$

$\gamma^* + n \longrightarrow \pi^- + p$ **channel**

$$\begin{aligned}\mathrm{PCBT}_1 =& -\frac{eg_A^3 m_N^2 \left(-2m_N^2 V_1^\mu + m_N \left(2V_4^\mu - 4V_3^\mu\right) + V_1^\mu \left(Q^2 + s + u\right)\right)}{16\sqrt{2}\pi^2 F_\pi^3 \left(-2m_N^2 + Q^2 + s + u\right)} \\ &+ \frac{eg_A^3 m_N^2 \left(m_N^2 V_1^\mu - 2m_N \left(2V_2^\mu - V_3^\mu + V_4^\mu - V_5^\mu\right) - uV_1^\mu\right)}{16\sqrt{2}\pi^2 F_\pi^3 \left(m_N^2 - u\right)}\end{aligned} \tag{B.7}$$

$$\begin{aligned}\mathrm{PCBT}_2 =& \Bigg[\frac{3eM^2 g_A^3 m_N \left(2V_2^\mu - V_3^\mu + V_4^\mu - V_5^\mu\right)}{32\sqrt{2}\pi^2 F_\pi^3 \left(m_N^2 - u\right)} \\ &+ \frac{3eM^2 g_A^3 m_N^2 \left(V_1^\mu \left(m_N^2 - u\right) - 2m_N \left(2V_2^\mu - V_3^\mu + V_4^\mu - V_5^\mu\right)\right)}{16\sqrt{2}\pi^2 F_\pi^3 \left(m_N^2 - u\right)^2}\Bigg] \\ &- \frac{eg_A^3 m_N \left(2m_N \left(-sV_1^\mu + 2V_6^\mu + V_7^\mu\right) + 2m_N^3 V_1^\mu + 3m_N^2 \left(V_4^\mu - V_5^\mu\right) + s\left(V_4^\mu - V_5^\mu\right)\right)}{8\sqrt{2}\pi^2 F_\pi^3 \left(m_N^2 - s\right)} \\ &- \frac{eg_A^3 m_N \left(-2m_N \left(uV_1^\mu + 2V_6^\mu - V_7^\mu\right) + 2m_N^3 V_1^\mu - 3m_N^2 \left(V_4^\mu - V_5^\mu\right) + u\left(V_5^\mu - V_4^\mu\right)\right)}{32\sqrt{2}\pi^2 F_\pi^3 \left(m_N^2 - u\right)}\end{aligned} \tag{B.8}$$

$$\begin{aligned}\mathrm{PCBT}_1 + \mathrm{PCBT}_2 =& M^2 \Bigg[\frac{3eg_A^3 m_N \left(2V_2^\mu - V_3^\mu + V_4^\mu - V_5^\mu\right)}{32\sqrt{2}\pi^2 F_\pi^3 \left(m_N^2 - u\right)} \\ &+ \frac{3eg_A^3 m_N^2 \left(m_N^2 V_1^\mu - 2m_N \left(2V_2^\mu - V_3^\mu + V_4^\mu - V_5^\mu\right) - uV_1^\mu\right)}{16\sqrt{2}\pi^2 F_\pi^3 \left(m_N^2 - u\right)^2}\Bigg] \\ &- \frac{eg_A^3 m_N^2 \left(-2m_N^2 V_1^\mu + m_N \left(2V_4^\mu - 4V_3^\mu\right) + V_1^\mu \left(Q^2 + s + u\right)\right)}{16\sqrt{2}\pi^2 F_\pi^3 \left(-2m_N^2 + Q^2 + s + u\right)} \\ &- \frac{eg_A^3 m_N \left(m_N \left(-2sV_1^\mu + 4V_6^\mu + 2V_7^\mu\right) + 2m_N^3 V_1^\mu + 3m_N^2 \left(V_4^\mu - V_5^\mu\right) + s\left(V_4^\mu - V_5^\mu\right)\right)}{8\sqrt{2}\pi^2 F_\pi^3 \left(m_N^2 - s\right)} \\ &+ \frac{eg_A^3 m_N \left(m_N^2 \left(-8V_2^\mu + 4V_3^\mu - V_4^\mu + V_5^\mu\right) + m_N \left(4V_6^\mu - 2V_7^\mu\right) + u\left(V_4^\mu - V_5^\mu\right)\right)}{32\sqrt{2}\pi^2 F_\pi^3 \left(m_N^2 - u\right)}\end{aligned} \tag{B.9}$$

$\gamma^* + n \longrightarrow \pi^0 + n$ **channel**

$$\mathrm{PCBT}_1 = 0 \tag{B.10}$$

$$\begin{aligned}\mathrm{PCBT}_2 =& \frac{eg_A^3 m_N \left(2m_N \left(-sV_1^\mu + 2V_6^\mu + V_7^\mu\right) + 2m_N^3 V_1^\mu + 3m_N^2 \left(V_4^\mu - V_5^\mu\right) + s\left(V_4^\mu - V_5^\mu\right)\right)}{16\pi^2 F_\pi^3 \left(m_N^2 - s\right)} \\ &+ \frac{eg_A^3 m_N \left(2m_N \left(uV_1^\mu + 2V_6^\mu - V_7^\mu\right) - 2m_N^3 V_1^\mu + 3m_N^2 \left(V_4^\mu - V_5^\mu\right) + u\left(V_4^\mu - V_5^\mu\right)\right)}{16\pi^2 F_\pi^3 \left(m_N^2 - u\right)}\end{aligned} \tag{B.11}$$

$$\mathrm{PCBT}_1 + \mathrm{PCBT}_2 = \mathrm{PCBT}_2 \tag{B.12}$$

B.2 PCBT for pion photoproduction on nucleons

$\gamma + p \longrightarrow \pi^0 + p$ **channel**

$$\mathrm{PCBT}_1 = \frac{eq\cdot\epsilon V_N g_A^3 m_N^3}{8\pi^2 F_\pi^3\left(m_N^2-u\right)} - \frac{e\,V_{EK} g_A^3 m_N^3\left(-2m_N^2+s+u\right)}{16\pi^2 F_\pi^3\left(m_N^2-s\right)\left(m_N^2-u\right)} \tag{B.13}$$

$$\begin{aligned}\mathrm{PCBT}_2 = &\Bigg[\frac{3eM^2 q\cdot\epsilon V_N g_A^3 m_N\left(3m_N^2+u\right)}{32\pi^2 F_\pi^3\left(u-m_N^2\right)^2} \\ &+ \frac{3eM^2\,V_{EK} g_A^3\left(m_N^3\left(3s^2-4su+3u^2\right)-5m_N^5(s+u)+sum_N(s+u)+6m_N^7\right)}{64\pi^2 F_\pi^3\left(s-m_N^2\right)^2\left(u-m_N^2\right)^2} \\ &+ \frac{3eM^2\,V_E g_A^3 m_N^2(s-u)}{32\pi^2 F_\pi^3\left(s-m_N^2\right)\left(m_N^2-u\right)}\Bigg] \\ &+ \frac{e\,V_{EK} g_A^3 m_N\left(m_N^2+s\right)}{32\pi^2 F_\pi^3\left(s-m_N^2\right)} - \frac{eg_A^3 m_N^2\left(V_{EK} m_N + q\cdot\epsilon V_K\right)}{16\pi^2 F_\pi^3\left(m_N^2-u\right)}\end{aligned} \tag{B.14}$$

$$\begin{aligned}\mathrm{PCBT}_1 + \mathrm{PCBT}_2 = &\, q\cdot\epsilon V_N\left(\frac{3eM^2 g_A^3 m_N\left(3m_N^2+u\right)}{32\pi^2 F_\pi^3\left(u-m_N^2\right)^2} + \frac{eg_A^3 m_N^3}{8\pi^2 F_\pi^3\left(m_N^2-u\right)}\right) \\ &+ V_{EK}\left(\frac{3eM^2 g_A^3 m_N\left(m_N^2\left(3s^2-4su+3u^2\right)-5m_N^4(s+u)+6m_N^6+su(s+u)\right)}{64\pi^2 F_\pi^3\left(s-m_N^2\right)^2\left(u-m_N^2\right)^2}\right. \\ &\qquad\qquad\left. + \frac{eg_A^3 m_N}{32\pi^2 F_\pi^3}\right) \\ &+ \frac{3eM^2\,V_E g_A^3 m_N^2(u-s)}{32\pi^2 F_\pi^3\left(m_N^2-s\right)\left(m_N^2-u\right)} - \frac{eq\cdot\epsilon V_K g_A^3 m_N^2}{16\pi^2 F_\pi^3\left(m_N^2-u\right)}\end{aligned} \tag{B.15}$$

$\gamma + p \longrightarrow \pi^+ + n$ **channel**

$$\mathrm{PCBT}_1 = \frac{e\,V_{EK} g_A^3 m_N^3}{8\sqrt{2}\pi^2 F_\pi^3\left(m_N^2-s\right)} - \frac{eq\cdot\epsilon V_N g_A^3 m_N^3}{4\sqrt{2}\pi^2 F_\pi^3\left(-2m_N^2+s+u\right)} \tag{B.16}$$

$$\begin{aligned}\mathrm{PCBT}_2 = &\left[\frac{3eM^2\,V_E g_A^3 m_N^2}{16\sqrt{2}\pi^2 F_\pi^3\left(s-m_N^2\right)} + \frac{3eM^2\,V_{EK} g_A^3 m_N\left(3m_N^2+s\right)}{32\sqrt{2}\pi^2 F_\pi^3\left(s-m_N^2\right)^2}\right] \\ &+ \frac{eg_A^3 m_N^2\left(V_{EK} m_N + q\cdot\epsilon V_K\right)}{2\sqrt{2}\pi^2 F_\pi^3\left(m_N^2-u\right)} \\ &+ \frac{eg_A^3 m_N\left(-10s\,V_E m_N + 10\,V_E m_N^3 - 7\,V_{EK} m_N^2 + 3s\,V_{EK}\right)}{32\sqrt{2}\pi^2 F_\pi^3\left(m_N^2-s\right)}\end{aligned} \tag{B.17}$$

$$\begin{aligned}\mathrm{PCBT}_1 + \mathrm{PCBT}_2 = &\, V_{EK}\left(\frac{3eM^2 g_A^3 m_N\left(3m_N^2+s\right)}{32\sqrt{2}\pi^2 F_\pi^3\left(s-m_N^2\right)^2} + \frac{eg_A^3 m_N\left(13m_N^2+3u\right)}{32\sqrt{2}\pi^2 F_\pi^3\left(m_N^2-u\right)}\right) \\ &+ V_E\left(\frac{5eg_A^3 m_N^2}{16\sqrt{2}\pi^2 F_\pi^3} - \frac{3eM^2 g_A^3 m_N^2}{16\sqrt{2}\pi^2 F_\pi^3\left(m_N^2-s\right)}\right) \\ &- \frac{eq\cdot\epsilon V_N g_A^3 m_N^3}{4\sqrt{2}\pi^2 F_\pi^3\left(-2m_N^2+s+u\right)} + \frac{eq\cdot\epsilon V_K g_A^3 m_N^2}{2\sqrt{2}\pi^2 F_\pi^3\left(m_N^2-u\right)}\end{aligned} \tag{B.18}$$

$\gamma + n \longrightarrow \pi^- + p$ **channel**

$$\mathrm{PCBT}_1 = \frac{eq\cdot\epsilon\, V_N g_A^3 m_N^3 \left(m_N^2 - s\right)}{4\sqrt{2}\pi^2 F_\pi^3 \left(u - m_N^2\right)\left(-2m_N^2 + s + u\right)} + \frac{e\, V_{EK} g_A^3 m_N^3}{8\sqrt{2}\pi^2 F_\pi^3 \left(m_N^2 - u\right)} \tag{B.19}$$

$$\begin{aligned}\mathrm{PCBT}_2 = &\left[\frac{3eM^2 q\cdot\epsilon\, V_N g_A^3 m_N \left(3m_N^2 + u\right)}{16\sqrt{2}\pi^2 F_\pi^3 \left(u - m_N^2\right)^2} + \frac{3eM^2\, V_E g_A^3 m_N^2}{16\sqrt{2}\pi^2 F_\pi^3 \left(m_N^2 - u\right)}\right.\\ &\left. + \frac{3eM^2\, V_{EK} g_A^3 m_N \left(3m_N^2 + u\right)}{32\sqrt{2}\pi^2 F_\pi^3 \left(u - m_N^2\right)^2}\right]\\ &+ \frac{eg_A^3 m_N \left(10s\, V_E m_N - 10\, V_E m_N^3 + 13\, V_{EK} m_N^2 + 3s\, V_{EK}\right)}{32\sqrt{2}\pi^2 F_\pi^3 \left(m_N^2 - s\right)}\\ &- \frac{eg_A^3 m_N^2 \left(V_{EK} m_N + q\cdot\epsilon\, V_K\right)}{8\sqrt{2}\pi^2 F_\pi^3 \left(m_N^2 - u\right)}\end{aligned} \tag{B.20}$$

$$\begin{aligned}\mathrm{PCBT}_1 + \mathrm{PCBT}_2 = &\ V_{EK}\left(\frac{3eM^2 g_A^3 m_N \left(3m_N^2 + u\right)}{32\sqrt{2}\pi^2 F_\pi^3 \left(u - m_N^2\right)^2} + \frac{eg_A^3 m_N \left(13m_N^2 + 3s\right)}{32\sqrt{2}\pi^2 F_\pi^3 \left(m_N^2 - s\right)}\right)\\ &+ q\cdot\epsilon\, V_N\left(\frac{3eM^2 g_A^3 m_N \left(3m_N^2 + u\right)}{16\sqrt{2}\pi^2 F_\pi^3 \left(u - m_N^2\right)^2} + \frac{eg_A^3 m_N^3 \left(m_N^2 - s\right)}{4\sqrt{2}\pi^2 F_\pi^3 \left(u - m_N^2\right)\left(-2m_N^2 + s + u\right)}\right)\\ &+ V_E\left(\frac{3eM^2 g_A^3 m_N^2}{16\sqrt{2}\pi^2 F_\pi^3 \left(m_N^2 - u\right)} - \frac{5eg_A^3 m_N^2}{16\sqrt{2}\pi^2 F_\pi^3}\right) - \frac{eq\cdot\epsilon\, V_K g_A^3 m_N^2}{8\sqrt{2}\pi^2 F_\pi^3 \left(m_N^2 - u\right)}\end{aligned} \tag{B.21}$$

$\gamma + n \longrightarrow \pi^0 + n$ **channel**

$$\mathrm{PCBT}_1 = 0 \tag{B.22}$$

$$\mathrm{PCBT}_2 = \frac{e\, V_{EK} g_A^3 \left(m_N^3(s+u) + sum_N - 3m_N^5\right)}{8\pi^2 F_\pi^3 \left(m_N^2 - s\right)\left(m_N^2 - u\right)} - \frac{eq\cdot\epsilon\, V_K g_A^3 m_N^2}{4\pi^2 F_\pi^3 \left(m_N^2 - u\right)} \tag{B.23}$$

$$\mathrm{PCBT}_1 + \mathrm{PCBT}_2 = \mathrm{PCBT}_2 \tag{B.24}$$

Appendix C

Chiral expansions for physical quantities

In the evaluation of the third order amplitudes in the chiral expansion as detailed in Secs. 4.3, 4.3.2, we have used the following relevant expansions of the physical parameters within the $\widetilde{MS}$-EOMS renormalized ChPT.

C.1 Nucleon mass m_N

For the nucleon mass, m_N, we have in the EOMS scheme that [14, 25]

$$m_N = \widetilde{m} - 4\widetilde{c}_1 M_\pi^2 + \widetilde{\delta}_m^{(3)} + \mathcal{O}\left(p^4\right), \tag{C.1}$$

$$\widetilde{m}_2 = \widetilde{m} - 4\widetilde{c}_1 M_\pi^2 = m_N - \widetilde{\delta}_m^{(3)} + \mathcal{O}\left(p^4\right), \tag{C.2}$$

with

$$\widetilde{\delta}_m^{(3)} = \frac{3g_A^2 m_N M_\pi^2}{32\pi^2 F_\pi^2}\left\{\overline{B}_0\left[m_N^2, M_\pi^2, m_N^2\right] - \left(1 + \frac{\overline{A}_0\left[m_N^2\right]}{m_N^2}\right)\right\}. \tag{C.3}$$

C.2 Pion mass M_π

The pion the physical mass is expanded in terms of the chiral limit pion mass M and the $\mathcal{O}(p^4)$ low-energy constant l_3^r. In the $\widetilde{MS}$ renomalization scheme, [25, 53]

$$M_\pi^2 = M^2\left(1 + \delta_{M_\pi}^{(2)}\right) + \mathcal{O}\left(p^6\right) \tag{C.4}$$

where

$$\delta_{M_\pi}^{(2)} = \frac{2l_3^r M_\pi^2}{F_\pi^2} - \frac{\overline{A}_0[M_\pi^2]}{32\pi^2 F_\pi^2} \tag{C.5}$$

C.3 Axial coupling constant g_A

For the axial coupling constant, we have in the EOMS regularized scheme [14, 25]

$$g_A = \widetilde{g}\left(1 + \frac{4d_{16}^r M_\pi^2}{\widetilde{g}} + \widetilde{\delta}_{g_A}^{(2)}\right) + \mathcal{O}(p^4) \tag{C.6}$$

where

$$\widetilde{\delta}_{g_A}^{(2)} = \frac{1}{16\pi^2 F_\pi^2 \left(4m_N^2 - M_\pi^2\right)} \Bigg\{ 4g_A^2 M_\pi^2 \overline{A}_0 \left[m_N^2\right] + \left(\left(8g_A^2 + 4\right) m_N^2 - \left(4g_A^2 + 1\right) M_\pi^2\right) \overline{A}_0 \left[M_\pi^2\right] + M_\pi^2 \left(\left(\left(3g_A^2 + 2\right) M_\pi^2 - 8\left(g_A^2 + 1\right) m_N^2\right) \overline{B}_0 \left[m_N^2, M_\pi^2, m_N^2\right] - 4g_A^2 m_N^2\right) \Bigg\}, \tag{C.7}$$

C.4 Pion decay constant F_π

For the physical pion decay constant, the contributing terms in the chiral expansion up to $\mathcal{O}(p^4)$ and with one-loop contributions are written as follows [25, 53]

$$F_\pi = F\left(1 + \delta_{F_\pi}^{(2)} + \mathcal{O}(p^4)\right), \tag{C.8}$$

where

$$\delta_{F_\pi}^{(2)} = \frac{l_4^r M_\pi^2}{F_\pi^2} + \frac{\overline{A}_0\left[M_\pi^2\right]}{16\pi^2 F_\pi^2}. \tag{C.9}$$

Here the l_4^r and d_{16}^r are the corresponding $\widetilde{\text{MS}}$-renormalized LECs at $\mathcal{O}(p^4)$.

Appendix D

Multipole decomposition

The pion photoproduction amplitude in terms of the CGLN basis, $\mathcal{F}_i$, (3.28) can be expanded in terms of multipoles as

$$\begin{aligned}
\mathcal{F}_1 =& \sum_{l=0}^{\infty} \left[l M_l^+ + E_l^+ \right] \mathcal{P}'_{l+1}(x) + \sum_{l=2}^{\infty} \left[(l+1) M_l^- + E_l^- \right] P'_{l-1}(x), \\
\mathcal{F}_2 =& \sum_{l=1}^{\infty} \left[(l+1) M_l^+ + l M_l^l \right] \mathscr{P}'_l(x), \\
\mathcal{F}_3 =& \sum_{l=1}^{\infty} \left[E_l^+ - M_l^+ \right] \mathscr{P}''_{l+1}(x) + \sum_{l=3}^{\infty} \left[E_l^- + M_l^- \right] \mathscr{P}''_{l-1}(x), \\
\mathcal{F}_4 =& \sum_{l=2}^{\infty} \left[M_l^+ - E_l^+ - M_l^- - E_l^- \right] \mathscr{P}''_l(x),
\end{aligned} \tag{D.1}$$

where $x = \cos\theta_\pi$ indicates the pion production angle in center of mass frame, the functions $\mathscr{P}_n(x)$ are the Lengendre polynomials for angular momentum n, whilst $M_n^\pm$ and $E_n^\pm$ are the corresponding multipole functions.

For angular momenta values up to $l = 1$ in the expansion, the elementary photoproduction amplitude in Eq. (6.11) is reduced to

$$\mathcal{F} = i\vec{\sigma} \cdot \vec{\epsilon}_\lambda \left(E_{0+} + \hat{k} \cdot \hat{q} P_1 \right) + i \left(\vec{\sigma} \cdot \hat{k}\, \vec{\epsilon}_\lambda \cdot \hat{q} \right) P_2 + \left(\hat{q} \times \hat{k} \cdot \vec{\epsilon}_\lambda \right) P_3, \tag{D.2}$$

where the multipole E_{0+} correspond to the s-wave amplitude ($l = 0$) and the terms P_1, P_2 and P_3 are the p-wave contributions ($l = 1$) defined as

$$P_1 = 3E_{1+} + M_{1+} - M_{1-}, \tag{D.3}$$
$$P_2 = 3E_{1+} - M_{1+} + M_{1-}, \tag{D.4}$$
$$P_3 = 2M_{1+} + M_{1-}. \tag{D.5}$$

As discussed in Chapter. 6, the photoproduction amplitude can be generally separated into spin-dependent and independent terms $\mathcal{F} = i\vec{\sigma}\cdot\vec{K} + L$, as given in Eq. (6.12). Particularly, in the above multipolar expansion up to $l = 1$, we have that

$$\vec{K} = \vec{\epsilon}_\lambda \left(E_{0+} + \hat{k} \cdot \hat{q} P_1 \right) + \hat{k} \left(\vec{\epsilon}_\lambda \cdot \hat{q} \right) P_2 \,, \tag{D.6}$$
$$L = \hat{q} \times \hat{k} \cdot \vec{\epsilon}_\lambda \, P_3 \,. \tag{D.7}$$

Also, the expressions for the multipole functions $M_{l\pm}$ and $E_{l\pm}$ in terms of the amplitudes $\mathcal{F}_i$ are useful. These are extracted from (D.1) having

$$E_{l+} = \int_{-1}^{1} \frac{dx}{2(l+1)} \left[\mathscr{P}_l \mathcal{F}_1 - \mathscr{P}_{l+1} \mathcal{F}_2 + \frac{l}{2l+1} \left(\mathscr{P}_{l-1} - \mathscr{P}_{l+1} \right) \mathcal{F}_3 + \frac{l+1}{2l+3} \left(\mathscr{P}_l - \mathscr{P}_{l+2} \right) \mathcal{F}_4 \right],$$

$$E_{l-} = \int_{-1}^{1} \frac{dx}{2l} \left[\mathscr{P}_l \mathcal{F}_1 - \mathscr{P}_{l-1} \mathcal{F}_2 - \frac{l+1}{2l+1} \left(\mathscr{P}_{l-1} - \mathscr{P}_{l+1} \right) \mathcal{F}_3 + \frac{l}{2l-1} \left(\mathscr{P}_l - \mathscr{P}_{l-2} \right) \mathcal{F}_4 \right],$$

$$M_{l+} = \int_{-1}^{1} \frac{dx}{2(l+1)} \left[\mathscr{P}_l \mathcal{F}_1 - \mathscr{P}_{l+1} \mathcal{F}_2 + \frac{1}{2l+1} \left(\mathscr{P}_{l-1} - \mathscr{P}_{l+1} \right) \mathcal{F}_3 \right],$$

$$M_{l-} = \int_{-1}^{1} \frac{dx}{2l} \left[-\mathscr{P}_l \mathcal{F}_1 + \mathscr{P}_{l-1} \mathcal{F}_2 + \frac{1}{2l+1} \left(\mathscr{P}_{l-1} - \mathscr{P}_{l+1} \right) \mathcal{F}_3 \right]. \tag{D.8}$$

Appendix E

Nuclear form factors

Here are shown the expressions of the relevant form factors in the $^{12}\mathrm{C}(\gamma,\pi^0)$ reaction studied in Chapter 6. The matter form factor used in the coherent transitions is given in the momentum space by the Fourier transform

$$F(Q) = \langle \Psi_f | \, e^{i\vec{Q}\cdot\vec{r}} \, | \Psi_i \rangle = \int d^3r \rho(\vec{r}) e^{i\vec{Q}\cdot\vec{r}} \tag{E.1}$$

where considering $\Psi = \Psi_{i(f)}$ the ground state function of the ^{12}C nucleus, $\rho(\vec{r}) = \Psi^*(\vec{r})\Psi(\vec{r})$ is the nuclear density normalized to 1 ($F(0) = 1$). The vector $\vec{r}$ is the nucleon coordinate in the nuclear c.m. frame. In this work we adopt the closed-form expression for $F(Q)$ [161]

$$F(Q) = F_{\mathrm{Ph}}(Q) F_{c.m.}(Q) \tag{E.2}$$

where

$$F_{c.m.}(Q^2) = \exp\left[R^2 \frac{Q^2}{6A}\right] \tag{E.3}$$

is a transform function to the c.m. nuclear frame, since the nuclear density is calculated as a function of different coordinates. Assuming a symmetrized Fermi density, $F_{Ph}(Q)$ is a phenomenological function given by

$$F_{\mathrm{Ph}}(Q) = -\frac{3\pi b \left(\cos[Qc] - \pi b \sin[Qc] \coth[\pi b Q]/c\right)}{Qc^2 \sinh[\pi b Q] \left(1 + \pi^2 b^2/c^2\right)} \tag{E.4}$$

with the parameters b and c fitted to the $^{12}\mathrm{C}(e,e')$ data [184]. The values of these parameters are shown in Tab. E.1

Table E.1: Symmetrized Fermi-density parameters for the ^{12}C nuclei

b	c	R
0.478	2.220	2.462

In the incoherent $^{12}\mathrm{C}(\gamma,\pi^0)$ cross section of Eq. (6.26), the transition form factor for the 2^+ (4.4 MeV) final state is given by the model in Ref. [155] as follows

$$F_2(Q) = N y e^{-y} e^{y/A}, \tag{E.5}$$

where $y = (Qb_x/2)^2$, $b_x = 1.76$ fm is the oscillator parameter [185], $e^{y/A}$ is the c.m. correction factor, and $N = 0.345$ is a renormalization constant fitted to the electron-scattering data [155].

List of Figures

3.1 Diagram for the pion electroproduction on nucleon. The incoming nucleon and electron momenta are denoted by p and k_i, the outgoing nucleon, pion and electron momenta are given by p', q and k_f respectively. The virtual photon γ^* carries the corresponding transferred momentum k. The cross-dashed blob stands for the hadronic vertex. 26

3.2 Kinematics for a typical experiment (in the Lab. frame), leading to out-of-plane pion production. The θ_π angle indicates the deviation of pion 3-momentum from the initial virtual-photon 3-momentum, ϕ_π corresponds to the relative angle between the electron-scattering plane and the pion-nucleon final state plane. 28

3.3 General diagram for pion photoproduction on nucleons. The corresponding 4-momenta are similar to Fig. 3.1 excluding the lepton vertex and being here γ the incoming real-photon. 38

4.1 Tree Feynman diagrams contributing up to $\mathcal{O}(p^3)$ considering only pion and nucleon degrees of freedom. The numbers inside the circles denote the chiral order of the respective vertex. Diagrams from (a) to (d) correspond to the $\mathcal{O}(p^1)$ amplitudes, (e)-(h) are of $\mathcal{O}(p^2)$ order, and (i)-(t) are of $\mathcal{O}(p^3)$ order respectively. 48

4.2 One-loop Feynman diagram-generating topologies up to the nominal order $\mathcal{O}(p^3)$. Crossed-circles indicate the vertex where one incoming real- or virtual-photon may be placed to generate the corresponding Feynman diagram. Numbers provide the label to identify each diagram generated. 49

4.3 Tree Feynman diagrams for the $\gamma^{(*)} + N \longrightarrow \pi + N'$ reaction through the explicit $\Delta(1232)$ inclusion. The labels in the circles specify the chiral order of each vertex. 49

4.4 Example of Feynman diagrams generated by the topology in Fig. 4.2 -(c). 58

4.5 Feynman diagram for the one-loop diagram topology (g7) of Fig. 4.2 corresponding to the $\mathcal{O}(p^3)$ amplitude for the $\gamma^{(*)} + N \longrightarrow \pi^a + N'$ reaction. The numbers inside the circles indicate the chiral order of the vertices. The labels $\pi^{0,\pm}$ and p,n denote the possible charges of the loop lines, and z is the inner momentum in the loop integral. 60

4.6 Self energy diagrams contributing to the wave function renormalization of the external nucleon with momentum p, (a), and the external pion with momentum q, (b), (c). 71

4.7 Feynman diagrams showing the generation of amplitudes of higher orders in the chiral expansion when we substitute the nucleon mass m by m_2, Eq. (4.107), in the nucleon propagator of two $\mathcal{O}(p^1)$ amplitudes, $\mathcal{M}^{\mu\,(1)}_{(b)}$, (4.12), and $\mathcal{M}^{\mu\,(1)}_{(c)}$, (4.13). 74

4.8 Feynman diagrams indicating the generation of amplitudes the by chiral expansion when we substitute the nucleon mass m by m_2, Eq. (4.107), in the nucleon propagator of the $\mathcal{O}(p^2)$ amplitudes, $\mathcal{M}^{\mu\,(2)}_{(e)}$, Eq. (4.20) and $\mathcal{M}^{\mu\,(2)}_{(f)}$, Eq. (4.21). 75
4.9 Feynman diagrams indicating the reduction to the relevant amplitudes and LECs shown in Eq. (4.139). 82

5.1 χ^2/dof as function of the maximum W considered in the fitting procedure. Full model at $\mathcal{O}(p^3)$ with Δ (green diamonds) and without Δ (red circles). 97
5.2 Two dimensional distributions of the fixed low-energy constants $\{\widetilde{c}_6, \widetilde{c}_7, d^r_6, d^r_7, d^r_{18}, l^r_6\}$ generated via Monte Carlo simulation versus the resulting fitted LECs $\{d^r_8 + d^r_9, d^r_8 - d^r_9, d^r_{20}, d^r_{21}, d^r_{22}\}$ for $N = 1000$ samples. Each point corresponds to a particular fit where the χ^2 function is minimized. 99
5.3 Angular distribution of the virtual cross section $d\sigma_v/d\Omega^*_\pi$ at different pion angles and for several photon energies. The transfer momentum is $Q^2 = 0.10$ GeV^2, and the virtual-photon polarization $\varepsilon = 0.670$. The solid line shows the theoretical results. The inner band depicts the statistical error, Eqs. (5.4) and (5.5), from the LECs variation within 1-σ given in Table 5.1. The outer band represents the total error including also the systematical error from the chiral truncation, Eq. (5.6), added to the statistical one in quadrature, Eq. (5.7). Data from Ref. [114]. . 102
5.4 $d\sigma_{TT}/d\Omega^*_\pi$ and $d\sigma_{TL}/d\Omega^*_\pi$ at several energies as function of the c.m. pion angle θ_π for the $\gamma^* p \to \pi^0 p$ channel. Here, the momentum transfer is $Q^2 = 0.1$ GeV^2 and the virtual-photon polarization $\varepsilon = 0.713$. Data from Ref. [115]. Description of curves and bands as in Fig. 5.3. 102
5.5 Angular distribution for $(d\sigma_T/d\Omega^*_\pi + \varepsilon\, d\sigma_L/d\Omega^*_\pi)$ at different c.m. energy values, W. The transfer momenta at $Q^2 = 0.05$ GeV^2 corresponds to polarization values of $\varepsilon = 0.932$, at $Q^2 = 0.10$ GeV^2 to $\varepsilon = 0.882$ and at $Q^2 = 0.15$ GeV^2 to $\varepsilon = 0.829$. Data from Ref. [116] and description as in Fig. 5.3. 103
5.6 Angular distribution for $d\sigma_{TL}/d\Omega^*_\pi$ for different c.m. energy values, W. The transfer momenta at $Q^2 = 0.05$ GeV^2 corresponds to polarization values of $\varepsilon = 0.932$, $Q^2 = 0.10$ GeV^2 to $\varepsilon = 0.882$ and $Q^2 = 0.15$ GeV^2 to $\varepsilon = 0.829$. Data from [116] and description of curves and bands as in Fig. 5.3. 104
5.7 Energy dependence for $(d\sigma_T + \varepsilon d\sigma_L)/d\Omega^*_\pi$, $d\sigma_{TT}/d\Omega^*_\pi$, $d\sigma_{TL}/d\Omega^*_\pi$ and $A_{LT'}$ at $Q^2 = 0.05$ GeV^2, $\varepsilon = 0.933$, $\theta_\pi = 90°$. Data from [95]. 105
5.8 $d\sigma_T/d\Omega^*_\pi$, $d\sigma_L/d\Omega^*_\pi$ and $d\sigma_{TL}/d\Omega^*_\pi$ as functions of Q^2 for the $\gamma^* p \to \pi^+ n$ process. For $d\sigma_T$ and $d\sigma_L$, the pion angle is $\theta_\pi = 0°$. Magenta circles: data from [120]. Red squares: data from [117,118]. Blue triangles: data from [119]. 106

5.9 Angular cross section $d\sigma/d\Omega^*_\pi$ for the $\gamma p \to \pi^0 p$ channel at various energies. Solid line: theoretical model (full model fit from Tab. 5.1). The inner band represents the statistical errors as in Eq. (5.5). The outer band stands for the total errors where the theoretical uncertainties (due to the chiral truncation) are added to the statistical ones in quadrature, Eq. (5.7). Dashed line: results from photoproduction fit [109] in the full isospin symmetric case. Data from Ref. [125] marked as red points and from [126] as violet squares. 107
5.10 Cross section as a function of the lab. photon energy E_γ^{lab} for the $\gamma p \to \pi^0 p$ channel. Solid line: theoretical model, red circles: data from Ref. [124], blue triangles: data from Ref. [144], not included in the fit. Description same as Fig. 5.9. 108
5.11 Beam asymmetry, Σ, for the $\gamma p \to \pi^0 p$ channel at various energies. Data from Ref. [125] marked as red points and from [126] as a violet square. Description same as in Fig. 5.9. 110
5.12 Angular distribution for the target asymmetry T, reported as the product $T d\sigma/d\Omega^*_\pi$, for the $\gamma p \to \pi^0 p$ channel. Data from [23]. Description same as Fig. 5.9. 112
5.13 Angular cross section for the $\gamma p \to \pi^+ n$ channel at various energies. Going from low to high energy, the data from Ref. [145] are marked as red diamonds, [135] as black squares, [134] as blue triangles, [126] as violet squares. Finally, in the lowest right panel, data for different energies from Ref. [133] are marked as magenta circles and from [122] as dark-green squares. In this latter panel the theory has been calculated at precisely the energies and angles of the data points, and the lines and bands have been interpolated. Description same as Fig. 5.9. . . . 113
5.14 Cross section for the $\gamma p \to \pi^+ n$ channel at various energies. Data from Ref. [146] presented as red circles. In the same way as in Fig. 5.13, data from [134] as blue triangles and [135] as black squares. Description same as Fig. 5.10. 114
5.15 Beam asymmetry for the $\gamma p \to \pi^+ n$ channel at $E_\gamma^{lab} = 212.9$ MeV. Data from Ref. [126]. Description same as Fig. 5.9. 114
5.16 Angular cross section for the $\gamma n \to \pi^- p$ channel at various energies. Data from Ref. [147] are presented as red filled squares, [129] marked as black triangles, [127] as blue squares (corresponding to lab. frame energy of E_γ^{lab} =211.4 MeV in the lower-right plot), [128] as violet filled triangles and data from [130] as magenta filled diamonds. Description same as Fig. 5.10. 115
5.17 Cross section for the $\gamma n \to \pi^- p$ process. Data from [24] in magenta circles; red square, data from [148] and green dots, data from [149] (not included in the fit). Description same as Fig. 5.9. 116

6.1 Diagram representation of the $^{12}\mathrm{C}(\gamma, \pi^0)$ process with k, q, P_A and P'_A the corresponding 4-momenta in the c.m. frame. 119
6.2 Ratio of the coherent and incoherent total cross sections as a function of E_γ, the lab photon energy. The normalization factor η in Eq. (6.26) is set to 1 as in Fig. 12 of Ref. [155]. 127

6.3 Cross section of the $^{12}\mathrm{C}(\gamma,\pi^0)$ reaction as a function of the photon energy in the lab. frame. The blue/gray bands show the results of the full model, Eq. (6.29), with contribution of both coherent and the incoherent transition to the 2^+(4.4 MeV) state. Band widths correspond to the statistical error propagated from the LEC uncertainties, Tab. 4.5 and 5.2. The respective dashed curves show the effect of removing the incoherent contribution from the central values. Data below 161 MeV from [157] and the tree points at the higher energies from [183]. 128
6.4 Differential cross sections of the $^{12}\mathrm{C}(\gamma,\pi^0)$ reaction in the π-nucleus c.m. frame for various lab. energies E_γ^{lab}. The solid/dashed curves show the results of the DWIA calculation with the ChPT amplitude. The solid curve correspond to the total contribution from the coherent and incoherent transitions, whilst the dashed curve removes the incoherent part. The error bands are propagated from the LECs errors. Data points are from [157]. 129
6.5 Dependence of the function $p_3^{(+)}$ on the laboratory photon energy, comparing the full and the Δ-less model. 130

A.1 Feynman diagrams for the $\gamma NN'$, $\gamma N\pi N'$ and $NN'\pi$ vertices and corresponding to the amplitudes in Eqs. (A.11), (A.12) and (A.13) respectively. 148
A.2 Feynman diagram for the $\gamma\pi\pi$ vertex corresponding to the amplitude in (A.19). 150

List of Tables

3.1 Source of the isospin amplitudes for pion production in the isospin symmetric limit case. The tensor current operator consists of a isoscalar ($I = 0$) and a isovector ($I = 1$) component as Eq. (3.97). 44

4.1 Tree level amplitude constants for each channel at $\mathcal{O}(p^1)$. 52
4.2 Tree level amplitude constants for each channel at $\mathcal{O}(p^2)$. 53
4.3 Tree level amplitude constants for each channel at $\mathcal{O}(p^3)$. 55
4.4 Tree level amplitude constants for each channel at $\mathcal{O}(p^{5/2})$. 56
4.5 Values of the $\mathcal{O}(p^3)$ EOMS LECs determined from other processes. . . 86

5.1 Fit results for the LECs. The coupling g_M is dimensionless and d_i in units of GeV^{-2}. 95
5.2 Values of the fitted LECs in the full model. LECs are dimensionless for g_M and in units of GeV^{-2} for d's. Fit I refers to the previous fit from Tab. 5.1. Fit II refers to a new fit taking into account the uncertainties of the previously known LECs, Tab. 4.5. Both of them correspond to the full model including Δ mechanisms. 100

E.1 Symmetrized Fermi-density parameters for the ^{12}C nuclei 185

Acknowledgements

Agradecimientos

El tiempo que he trabajado en el IFIC ha sido una experiencia más que enriquecedora para mí. A pesar de la complicada situación sanitaria mundial y los confinamientos, pude aprovechar la oportunidad de asistir e impartir charlas en conferencias, congresos y workshops como en los Estados Unidos o China. Todo ello se lo debo de enormemente a las personas que me han apoyado durante todo este tiempo.

En primer lugar, quiero agradecer a mi director, Manuel José Vicente Vacas, por su constante apoyo, por su paciencia e invaluables enseñanzas durante los últimos años. Ha sido un gran mentor para mí, sus comentarios críticos siempre fueron vitales para poder mejorar en mi trabajo. He podido aprender mucho de él, tanto en el lado de la física como en el lado de la resolución de problemas y la programación. Estoy muy agradecido con él por haberme recibido en el grupo y haberme dado la oportunidad para trabajar en el fascinante tema de esta tesis.

Además quiero expresar un profundo agradecimiento a mi tutor Luis Alvarez Ruso por haberme orientado desde el inicio y por siempre estar dispuesto a ayudarme para entender los cálculos. De igual manera quiero agradecer a Astrid N. Hiller Blin y a Deliang Yao con quienes colaboré. Sus sugerencias y discusiones ayudaron a que los resultados fueran de mucho mejor calidad. Agradezco a Astrid por mantenerse siempre en contacto y por el soporte para dar charlas durante el confinamiento. Muchas gracias a M. Ostrick y a R. Lindgren por haberme falicitado el acceso a datos experimentales.

Como no podía ser de otra manera, estoy muy agradecido con mi familia, Itzel y Annita, por su comprensión durante la escritura de esta tesis, por su amor y por los momentos memorables que hemos compartido este tiempo en Valencia. Gracias a mi hermano, a mi madre y a la memoria de mi padre por el apoyo que me ofrecieron cuando elegí estudiar física.

Quiero además expresar mi gratitud a los colegas y amigos en el grupo (los que están y los que se han ido), quienes me han hecho sentir bienvenido en el grupo y tuve el placer de coincidir en el día a día: Eulogio Oset, Juan Nieves, Raquel Molina, Miguel Albaladejo, Pedro, Vinicius, Asia, Eduardo, Rafa, Shuntaro Sakai, Jorgivan Dias, Rafi Alam, Neus, Melahat, Qi-Xin Yu, Fernando Alvarado, Natsumi Ikeno, Albert, Fernando Gil, Menglin Du, Victor y Amador.

Bibliography

[1] J. Steinberger, W. Panofsky, and J. Steller, "EVIDENCE FOR THE PRODUCTION OF NEUTRAL MESONS BY PHOTONS," Phys. Rev. **78** (1950) 802–805.

[2] T. Becher and H. Leutwyler, "Baryon chiral perturbation theory in manifestly Lorentz invariant form," Eur. Phys. J. **C9** (1999) 643–671, `arXiv:hep-ph/9901384 [hep-ph]`.

[3] J. Gegelia and G. Japaridze, "Matching heavy particle approach to relativistic theory," Phys. Rev. **D60** (1999) 114038, `arXiv:hep-ph/9908377 [hep-ph]`.

[4] T. Fuchs, J. Gegelia, G. Japaridze, and S. Scherer, "Renormalization of relativistic baryon chiral perturbation theory and power counting," Phys. Rev. **D68** (2003) 056005, `arXiv:hep-ph/0302117 [hep-ph]`.

[5] T. Becher and H. Leutwyler, "Low energy analysis of pi N —> pi N," JHEP **06** (2001) 017, `arXiv:hep-ph/0103263`.

[6] T. Fuchs, J. Gegelia, and S. Scherer, "Electromagnetic form-factors of the nucleon in relativistic baryon chiral perturbation theory," J. Phys. **G30** (2004) 1407–1426, `arXiv:nucl-th/0305070 [nucl-th]`.

[7] B. C. Lehnhart, J. Gegelia, and S. Scherer, "Baryon masses and nucleon sigma terms in manifestly Lorentz-invariant baryon chiral perturbation theory," J. Phys. **G31** (2005) 89–104, `arXiv:hep-ph/0412092 [hep-ph]`.

[8] M. R. Schindler, T. Fuchs, J. Gegelia, and S. Scherer, "Axial, induced pseudoscalar, and pion-nucleon form-factors in manifestly Lorentz-invariant chiral perturbation theory," Phys. Rev. **C75** (2007) 025202, `arXiv:nucl-th/0611083 [nucl-th]`.

[9] M. R. Schindler, D. Djukanovic, J. Gegelia, and S. Scherer, "Chiral expansion of the nucleon mass to order(q**6)," Phys. Lett. **B649** (2007) 390–393, `arXiv:hep-ph/0612164 [hep-ph]`.

[10] L. S. Geng, J. Martin Camalich, L. Alvarez-Ruso, and M. J. Vicente Vacas, "Leading SU(3)-breaking corrections to the baryon magnetic moments in Chiral Perturbation Theory," Phys. Rev. Lett. **101** (2008) 222002, `arXiv:0805.1419 [hep-ph]`.

[11] L. S. Geng, J. Martin Camalich, and M. J. Vicente Vacas, "SU(3)-breaking corrections to the hyperon vector coupling f(1)(0) in covariant baryon chiral perturbation theory," Phys. Rev. **D79** (2009) 094022, `arXiv:0903.4869 [hep-ph]`.

[12] J. Martin Camalich, L. S. Geng, and M. J. Vicente Vacas, "The lowest-lying baryon masses in covariant SU(3)-flavor chiral perturbation theory," Phys. Rev. **D82** (2010) 074504, `arXiv:1003.1929 [hep-lat]`.

[13] J. M. Alarcon, J. Martin Camalich, and J. A. Oller, "The chiral representation of the πN scattering amplitude and the pion-nucleon sigma term," Phys. Rev. **D85** (2012) 051503, `arXiv:1110.3797 [hep-ph]`.

[14] J. M. Alarcon, J. Martin Camalich, and J. A. Oller, "Improved description of the πN-scattering phenomenology in covariant baryon chiral perturbation theory," Annals Phys. **336** (2013) 413–461, `arXiv:1210.4450 [hep-ph]`.

[15] T. Ledwig, J. Martin-Camalich, V. Pascalutsa, and M. Vanderhaeghen, "The Nucleon and $\Delta(1232)$ form factors at low momentum-transfer and small pion masses," Phys. Rev. **D85** (2012) 034013, `arXiv:1108.2523 [hep-ph]`.

[16] Y.-H. Chen, D.-L. Yao, and H. Q. Zheng, "Analyses of pion-nucleon elastic scattering amplitudes up to $O(p^4)$ in extended-on-mass-shell subtraction scheme," Phys. Rev. **D87** (2013) 054019, `arXiv:1212.1893 [hep-ph]`.

[17] L. Alvarez-Ruso, T. Ledwig, J. Martin Camalich, and M. J. Vicente-Vacas, "Nucleon mass and pion-nucleon sigma term from a chiral analysis of lattice QCD data," Phys. Rev. **D88** no. 5, (2013) 054507, `arXiv:1304.0483 [hep-ph]`.

[18] T. Ledwig, J. Martin Camalich, L. S. Geng, and M. J. Vicente Vacas, "Octet-baryon axial-vector charges and SU(3)-breaking effects in the semileptonic hyperon decays," Phys. Rev. **D90** no. 5, (2014) 054502, `arXiv:1405.5456 [hep-ph]`.

[19] V. Lensky, J. M. Alarcón, and V. Pascalutsa, "Moments of nucleon structure functions at next-to-leading order in baryon chiral perturbation theory," Phys. Rev. **C90** no. 5, (2014) 055202, `arXiv:1407.2574 [hep-ph]`.

[20] M. Hilt, S. Scherer, and L. Tiator, "Threshold π^0 photoproduction in relativistic chiral perturbation theory," Phys. Rev. **C87** no. 4, (2013) 045204, `arXiv:1301.5576 [nucl-th]`.

[21] A. N. Hiller Blin, T. Ledwig, and M. J. Vicente Vacas, "Chiral dynamics in the $\vec{\gamma}p \to p\pi^0$ reaction," Phys. Lett. **B747** (2015) 217–222, `arXiv:1412.4083 [hep-ph]`.

[22] A. N. Hiller Blin, T. Ledwig, and M. J. Vicente Vacas, "$\Delta(1232)$ resonance in the $\vec{\gamma}p \to p\pi^0$ reaction at threshold," Phys. Rev. **D93** no. 9, (2016) 094018, `arXiv:1602.08967 [hep-ph]`.

[23] **MAINZ-A2** Collaboration, S. Schumann et al., "Threshold $\pi 0$ photoproduction on transverse polarised protons at MAMI," Phys. Lett. B **750** (2015) 252–258.

[24] W. J. Briscoe, A. E. Kudryavtsev, I. I. Strakovsky, V. E. Tarasov, and R. L. Workman, "Threshold π^- photoproduction on the neutron," Eur. Phys. J. A **56** no. 8, (2020) 218, `arXiv:2004.01742 [nucl-th]`.

[25] D.-L. Yao, L. Alvarez-Ruso, A. N. Hiller Blin, and M. J. Vicente Vacas, "Weak pion production off the nucleon in covariant chiral perturbation theory," Phys. Rev. **D98** no. 7, (2018) 076004, `arXiv:1806.09364 [hep-ph]`.

[26] D.-L. Yao, L. Alvarez-Ruso, and M. J. Vicente Vacas, "Neutral-current weak pion production off the nucleon in covariant chiral perturbation theory," Phys. Lett. **B794** (2019) 109–113, `arXiv:1901.00773 [hep-ph]`.

[27] H. Leutwyler, "On the foundations of chiral perturbation theory," Annals Phys. **235** (1994) 165–203, `arXiv:hep-ph/9311274`.

[28] A. Pich, "Chiral perturbation theory," Rept. Prog. Phys. **58** (1995) 563–610, `arXiv:hep-ph/9502366`.

[29] G. Ecker, "Chiral perturbation theory," Prog. Part. Nucl. Phys. **35** (1995) 1–80, `arXiv:hep-ph/9501357`.

[30] S. Scherer and M. R. Schindler, "A Primer for Chiral Perturbation Theory," Lect. Notes Phys. **830** (2012) pp.1–338.

[31] V. Pascalutsa, M. Vanderhaeghen, and S. N. Yang, "Electromagnetic excitation of the Delta(1232)-resonance," Phys. Rept. **437** (2007) 125–232, `arXiv:hep-ph/0609004 [hep-ph]`.

[32] D. J. Gross and F. Wilczek, "Ultraviolet Behavior of Nonabelian Gauge Theories," Phys. Rev. Lett. **30** (1973) 1343–1346.

[33] D. J. Gross and F. Wilczek, "Asymptotically Free Gauge Theories - I," Phys. Rev. D **8** (1973) 3633–3652.

[34] **Particle Data Group** Collaboration, M. Tanabashi et al., "Review of Particle Physics," Phys. Rev. D **98** no. 3, (2018) 030001.

[35] S. L. Adler, "Axial vector vertex in spinor electrodynamics," Phys. Rev. **177** (1969) 2426–2438.

[36] S. L. Adler and W. A. Bardeen, "Absence of higher order corrections in the anomalous axial vector divergence equation," Phys. Rev. **182** (1969) 1517–1536.

[37] J. S. Bell and R. Jackiw, "A PCAC puzzle: $\pi^0 \to \gamma\gamma$ in the σ model," Nuovo Cim. A **60** (1969) 47–61.

[38] P. W. Higgs, "Broken symmetries, massless particles and gauge fields," Phys. Lett. **12** (1964) 132–133.

[39] S. Coleman, "The invariance of the vacuum is the invariance of the world," Journal of Mathematical Physics **7** no. 5, (1966) 787–787. `https://doi.org/10.1063/1.1931207`.

[40] M. Gell-Mann, "A Schematic Model of Baryons and Mesons," Phys. Lett. **8** (1964) 214–215.

[41] M. A. Shifman, A. I. Vainshtein, and V. I. Zakharov, "QCD and Resonance Physics: Applications," Nucl. Phys. B **147** (1979) 448–518.

[42] M. A. Shifman, A. I. Vainshtein, and V. I. Zakharov, "QCD and Resonance Physics. Theoretical Foundations," Nucl. Phys. B **147** (1979) 385–447.

[43] C. A. Dominguez and E. de Rafael, "Light Quark Masses in QCD from Local Duality," Annals Phys. **174** (1987) 372.

[44] A. Pich and E. de Rafael, "Four quark operators and nonleptonic weak transitions," Nucl. Phys. B **358** (1991) 311–382.

[45] T. A. DeGrand, "Short distance current correlators: Comparing lattice simulations to the instanton liquid," Phys. Rev. D **64** (2001) 094508, `arXiv:hep-lat/0106001`.

[46] S. Scherer, "Introduction to chiral perturbation theory," Adv. Nucl. Phys. **27** (2003) 277, `arXiv:hep-ph/0210398`.

[47] S. Scherer and M. R. Schindler, Quantum chromodynamics and chiral symmetry, vol. 830, pp. 1–48. 2012.

[48] A. Pich, "Effective field theory: Course," in Les Houches Summer School in Theoretical Physics, Session 68: Probing the Standard Model of Particle Interactions, pp. 949–1049. 6, 1998. `arXiv:hep-ph/9806303`.

[49] A. V. Manohar, "Effective field theories," Lect. Notes Phys. **479** (1997) 311–362, `arXiv:hep-ph/9606222`.

[50] A. Dobado, A. Gomez-Nicola, A. L. Maroto, and J. R. Pelaez, Effective lagrangians for the standard model. 1997.

[51] H. W. Griesshammer, J. A. McGovern, D. R. Phillips, and G. Feldman, "Using effective field theory to analyse low-energy Compton scattering data from protons and light nuclei," Prog. Part. Nucl. Phys. **67** (2012) 841–897, `arXiv:1203.6834 [nucl-th]`.

[52] S. Weinberg, "Phenomenological Lagrangians," Physica **A96** (1979) 327–340.

[53] J. Gasser and H. Leutwyler, "Chiral Perturbation Theory to One Loop," Annals Phys. **158** (1984) 142.

[54] J. Gasser and H. Leutwyler, "Chiral Perturbation Theory: Expansions in the Mass of the Strange Quark," Nucl. Phys. **B250** (1985) 465–516.

[55] S. R. Coleman, J. Wess, and B. Zumino, "Structure of phenomenological Lagrangians. 1.," Phys. Rev. **177** (1969) 2239–2247.

[56] J. Callan, Curtis G., S. R. Coleman, J. Wess, and B. Zumino, "Structure of phenomenological Lagrangians. 2.," Phys. Rev. **177** (1969) 2247–2250.

[57] S. Weinberg, "Nonlinear realizations of chiral symmetry," Phys. Rev. **166** (1968) 1568–1577.

[58] B. R. Holstein, "How large is f(pi)?," Phys. Lett. B **244** (1990) 83–87.

[59] J. Gasser, M. E. Sainio, and A. Svarc, "Nucleons with Chiral Loops," Nucl. Phys. **B307** (1988) 779–853.

[60] M. Gell-Mann, R. J. Oakes, and B. Renner, "Behavior of current divergences under SU(3) x SU(3)," Phys. Rev. **175** (1968) 2195–2199.

[61] J. Bijnens, G. Colangelo, and G. Ecker, "The Mesonic chiral Lagrangian of order p**6," JHEP **02** (1999) 020, `arXiv:hep-ph/9902437`.

[62] M. E. Peskin and D. V. Schroeder, An Introduction to quantum field theory. Addison-Wesley, Reading, USA, 1995.

[63] I. S. Gerstein, R. Jackiw, S. Weinberg, and B. W. Lee, "Chiral loops," Phys. Rev. D **3** (1971) 2486–2492.

[64] V. Bernard, N. Kaiser, J. Gasser, and U.-G. Meissner, "Neutral pion photoproduction at threshold," Phys. Lett. **B268** (1991) 291–295.

[65] N. Fettes, U.-G. Meißner, M. Mojzis, and S. Steininger, "The Chiral effective pion nucleon Lagrangian of order p**4," Annals Phys. **283** (2000) 273–302, `arXiv:hep-ph/0001308 [hep-ph]`. [Erratum: Annals Phys.288,249(2001)].

[66] E. E. Jenkins and A. V. Manohar, "Baryon chiral perturbation theory using a heavy fermion Lagrangian," Phys. Lett. **B255** (1991) 558–562.

[67] E. E. Jenkins and A. V. Manohar, "Chiral corrections to the baryon axial currents," Phys. Lett. **B259** (1991) 353–358.

[68] V. Bernard, "Chiral Perturbation Theory and Baryon Properties," Prog. Part. Nucl. Phys. **60** (2008) 82–160, `arXiv:0706.0312 [hep-ph]`.

[69] T. Becher, "Lorentz invariant baryon CHPT," in 3rd Workshop on Chiral Dynamics - Chiral Dynamics 2000: Theory and Experiment, pp. 66–77. 7, 2000. `arXiv:hep-ph/0011079`.

[70] V. Bernard, N. Kaiser, and U.-G. Meissner, "Chiral dynamics in nucleons and nuclei," Int. J. Mod. Phys. E **4** (1995) 193–346, `arXiv:hep-ph/9501384`.

[71] A. Krause, "Baryon Matrix Elements of the Vector Current in Chiral Perturbation Theory," Helv. Phys. Acta **63** (1990) 3–70.

[72] H.-B. Tang, "A New approach to chiral perturbation theory for matter fields," `arXiv:hep-ph/9607436`.

[73] P. J. Ellis and H.-B. Tang, "Pion nucleon scattering in a new approach to chiral perturbation theory," Phys. Rev. **C57** (1998) 3356–3375, `arXiv:hep-ph/9709354 [hep-ph]`.

[74] J. Gegelia, G. S. Japaridze, and K. S. Turashvili, "Calculation of loop integrals by dimensional counting," Theor. Math. Phys. **101** (1994) 1313–1319.

[75] D.-L. Yao, D. Siemens, V. Bernard, E. Epelbaum, A. M. Gasparyan, J. Gegelia, H. Krebs, and U.-G. Meißner, "Pion-nucleon scattering in covariant baryon chiral perturbation theory with explicit Delta resonances," JHEP **05** (2016) 038, `arXiv:1603.03638 [hep-ph]`.

[76] D. Siemens, V. Bernard, E. Epelbaum, A. Gasparyan, H. Krebs, and U.-G. Meißner, "Elastic pion-nucleon scattering in chiral perturbation theory: A fresh look," Phys. Rev. **C94** no. 1, (2016) 014620, `arXiv:1602.02640 [nucl-th]`.

[77] M. Hilt, B. C. Lehnhart, S. Scherer, and L. Tiator, "Pion photo- and electroproduction in relativistic baryon chiral perturbation theory and the chiral MAID interface," Phys. Rev. **C88** (2013) 055207, `arXiv:1309.3385 [nucl-th]`.

[78] V. Pascalutsa, "The Delta(1232) Resonance in Chiral Effective Field Theory," Prog. Part. Nucl. Phys. **61** (2008) 27–33, arXiv:0712.3919 [nucl-th].

[79] V. Bernard, E. Epelbaum, H. Krebs, and U.-G. Meißner, "New insights into the spin structure of the nucleon," Phys. Rev. **D87** no. 5, (2013) 054032, arXiv:1209.2523 [hep-ph].

[80] A. Hiller Blin, T. Gutsche, T. Ledwig, and V. E. Lyubovitskij, "Hyperon forward spin polarizability γ_0 in baryon chiral perturbation theory," Phys. Rev. **D92** no. 9, (2015) 096004, arXiv:1509.00955 [hep-ph].

[81] V. Pascalutsa and M. Vanderhaeghen, "Chiral effective-field theory in the Delta(1232) region: I. Pion electroproduction on the nucleon," Phys. Rev. **D73** (2006) 034003, arXiv:hep-ph/0512244 [hep-ph].

[82] W. Rarita and J. Schwinger, "On a theory of particles with half integral spin," Phys. Rev. **60** (1941) 61.

[83] T. R. Hemmert, B. R. Holstein, and J. Kambor, "Systematic 1/M expansion for spin 3/2 particles in baryon chiral perturbation theory," Phys. Lett. **B395** (1997) 89–95, arXiv:hep-ph/9606456 [hep-ph].

[84] V. Pascalutsa and D. R. Phillips, "Effective theory of the delta(1232) in Compton scattering off the nucleon," Phys. Rev. **C67** (2003) 055202, arXiv:nucl-th/0212024 [nucl-th].

[85] T. R. Hemmert, B. R. Holstein, and J. Kambor, "Chiral Lagrangians and delta(1232) interactions: Formalism," J. Phys. **G24** (1998) 1831–1859, arXiv:hep-ph/9712496 [hep-ph].

[86] R. H. Dalitz and D. R. Yennie, "Pion production in electron-proton collisions," Phys. Rev. **105** (1957) 1598–1615.

[87] J. S. Ball, "Application of the Mandelstam Representation to Photoproduction of Pions from Nucleons," Phys. Rev. **124** (1961) 2014–2028.

[88] P. Dennery, "Theory of the Electro- and Photoproduction of pi Mesons," Phys. Rev. **124** (1961) 2000–2010.

[89] D. Drechsel and L. Tiator, "Threshold pion photoproduction on nucleons," J. Phys. **G18** (1992) 449–497.

[90] G. F. Chew, M. L. Goldberger, F. E. Low, and Y. Nambu, "Relativistic dispersion relation approach to photomeson production," Phys. Rev. **106** (1957) 1345–1355.

[91] E. Amaldi, S. Fubini, and G. Furlan, "PION ELECTROPRODUCTION. ELECTROPRODUCTION AT LOW-ENERGY AND HADRON FORM-FACTORS," Springer Tracts Mod. Phys. **83** (1979) 1–162.

[92] B. Pasquini, D. Drechsel, and L. Tiator, "Invariant amplitudes for pion electroproduction," Eur. Phys. J. **A34** (2007) 387–403, arXiv:0712.2327 [hep-ph].

[93] J. D. Bjorken and S. D. Drell, Relativistic Quantum Mechanics. International Series In Pure and Applied Physics. McGraw-Hill, New York, 1965.

[94] G. Knochlein, D. Drechsel, and L. Tiator, "Photoproduction and electroproduction of eta mesons," Z. Phys. **A352** (1995) 327–343, `arXiv:nucl-th/9506029 [nucl-th]`.

[95] **A1** Collaboration, M. Weis et al., "Separated cross-sections in pi0 electroproduction at threshold at Q**2 = 0.05-GeV**2/c**2," Eur. Phys. J. **A38** (2008) 27–33, `arXiv:0705.3816 [nucl-ex]`.

[96] A. M. Sandorfi, S. Hoblit, H. Kamano, and T. S. H. Lee, "Determining pseudoscalar meson photo-production amplitudes from complete experiments," J. Phys. **G38** (2011) 053001, `arXiv:1010.4555 [nucl-th]`.

[97] J. Gegelia, U.-G. Meißner, D. Siemens, and D.-L. Yao, "The width of the Δ-resonance at two loop order in baryon chiral perturbation theory," Phys. Lett. **B763** (2016) 1–8, `arXiv:1608.00517 [hep-ph]`.

[98] V. Bernard, T. R. Hemmert, and U.-G. Meissner, "Cutoff schemes in chiral perturbation theory and the quark mass expansion of the nucleon mass," Nucl. Phys. A **732** (2004) 149–170, `arXiv:hep-ph/0307115`.

[99] A. N. Hiller Blin, Electromagnetic interactions of light hadrons in covariant chiral perturbation theory. PhD thesis, Valencia U., IFIC, 11, 2016.

[100] G. Passarino and M. J. G. Veltman, "One Loop Corrections for e+ e- Annihilation Into mu+ mu- in the Weinberg Model," Nucl. Phys. B **160** (1979) 151–207.

[101] R. Mertig, M. Bohm, and A. Denner, "FEYN CALC: Computer algebraic calculation of Feynman amplitudes," Comput. Phys. Commun. **64** (1991) 345–359.

[102] V. Shtabovenko, R. Mertig, and F. Orellana, "New Developments in FeynCalc 9.0" Comput. Phys. Commun. **207** (2016) 432–444, `arXiv:1601.01167 [hep-ph]`.

[103] T. Hahn and M. Perez-Victoria, "Automatized one loop calculations in four-dimensions and D-dimensions," Comput. Phys. Commun. **118** (1999) 153–165, `arXiv:hep-ph/9807565`.

[104] G. J. van Oldenborgh, "FF: A Package to evaluate one loop Feynman diagrams," Comput. Phys. Commun. **66** (1991) 1–15.

[105] V. Bernard, N. Kaiser, T. Lee, and U.-G. Meissner, "Threshold pion electroproduction in chiral perturbation theory," Phys. Rept. **246** (1994) 315–363, `arXiv:hep-ph/9310329`.

[106] H. H. Patel, "Package-X: A Mathematica package for the analytic calculation of one-loop integrals," Comput. Phys. Commun. **197** (2015) 276–290, `arXiv:1503.01469 [hep-ph]`.

[107] A. N. Hiller Blin, "Systematic study of octet-baryon electromagnetic form factors in covariant chiral perturbation theory," Phys. Rev. **D96** no. 9, (2017) 093008, `arXiv:1707.02255 [hep-ph]`.

[108] T. Bauer, J. C. Bernauer, and S. Scherer, "Electromagnetic form factors of the nucleon in effective field theory," Phys. Rev. **C86** (2012) 065206, `arXiv:1209.3872 [nucl-th]`.

[109] G. H. Guerrero Navarro, M. Vicente Vacas, A. N. H. Blin, and D.-L. Yao, "Pion photoproduction off nucleons in covariant chiral perturbation theory," Phys. Rev. D **100** no. 9, (2019) 094021, `arXiv:1908.00890 [hep-ph]`.

[110] D.-L. Yao, L. Alvarez-Ruso, and M. J. Vicente-Vacas, "Extraction of nucleon axial charge and radius from lattice QCD results using baryon chiral perturbation theory," Phys. Rev. **D96** no. 11, (2017) 116022, `arXiv:1708.08776 [hep-ph]`.

[111] V. Pascalutsa and J. A. Tjon, "Pion photoproduction on nucleons in a covariant hadron-exchange model," Phys. Rev. **C70** (2004) 035209, `arXiv:nucl-th/0407068 [nucl-th]`.

[112] V. Pascalutsa and M. Vanderhaeghen, "Electromagnetic nucleon-to-Delta transition in chiral effective-field theory," Phys. Rev. Lett. **95** (2005) 232001, `arXiv:hep-ph/0508060`.

[113] B. Kubis and U.-G. Meissner, "Low-energy analysis of the nucleon electromagnetic form-factors," Nucl. Phys. A **679** (2001) 698–734, `arXiv:hep-ph/0007056`.

[114] H. B. van den Brink et al., "Electroproduction of neutral pions on the proton," Nucl. Phys. **A612** (1997) 391–417.

[115] M. O. Distler et al., "Measurement of separated structure functions in the p(e,e' p)pi0 reaction at threshold and chiral perturbation theory," Phys. Rev. Lett. **80** (1998) 2294–2297.

[116] H. Merkel et al., "Consistent threshold pi0 electro-production at $Q^2 = 0.05$, 0.10, and 0.15 GeV^2/c^2," `arXiv:1109.5075 [nucl-ex]`.

[117] K. I. Blomqvist et al., "Precise pion electroproduction in the p (e, e-prime pi+) n reaction at W = 1125-MeV," Z. Phys. **A353** (1996) 415–421.

[118] **A1** Collaboration, A. Liesenfeld et al., "A Measurement of the axial form-factor of the nucleon by the p(e, e-prime pi+)n reaction at W = 1125-MeV," Phys. Lett. **B468** (1999) 20, `arXiv:nucl-ex/9911003 [nucl-ex]`.

[119] D. Baumann, π^+-Elektroproduktion an der Schwelle. PhD thesis, Johannes Gutenberg-Universität, Mainz, 2005. `http://wwwa1.kph.uni-mainz.de/A1/publications/doctor/baumannd.pdf`.

[120] **A1** Collaboration, I. Friščić et al., "Measurement of the $p(e, e'\pi^+)n$ reaction close to threshold and at low Q^2," Phys. Lett. **B766** (2017) 301–305, `arXiv:1606.00970 [nucl-ex]`.

[121] M. Fuchs et al., "Neutral pion photoproduction from the proton near threshold," Phys. Lett. **B368** (1996) 20–25.

[122] J. C. Bergstrom, J. M. Vogt, R. Igarashi, K. J. Keeter, E. L. Hallin, G. A. Retzlaff, D. M. Skopik, and E. C. Booth, "Measurement of the H-1 (gamma, pi0) cross-section near threshold," Phys. Rev. **C53** (1996) R1052–R1056.

[123] J. C. Bergstrom, R. Igarashi, and J. M. Vogt, "Measurement of the $H^1(\gamma, \pi^0)$ cross-section near threshold. II: Pion angular distributions," Phys. Rev. **C55** (1997) 2016–2023.

[124] A. Schmidt et al., "Test of Low-Energy Theorems for $^1H(\overrightarrow{\gamma}, \pi^0)^1H$ in the Threshold Region," Phys. Rev. Lett. **87** (2001) 232501, `arXiv:nucl-ex/0105010 [nucl-ex]`. [Erratum: Phys. Rev. Lett.110,039903(2013)].

[125] **A2, CB-TAPS** Collaboration, D. Hornidge et al., "Accurate Test of Chiral Dynamics in the $\vec{\gamma}p \to p\pi^0$ Reaction," Phys. Rev. Lett. **111** no. 6, (2013) 062004, `arXiv:1211.5495 [nucl-ex]`.

[126] G. Blanpied et al., "$\overrightarrow{N}$ Δ transition and proton polarizabilities from measurements of $p(\overrightarrow{\gamma}, \gamma)$, $p(\overrightarrow{\gamma}, \pi^0)$, and $p(\overrightarrow{\gamma}, \pi^+)$," Phys. Rev. **C64** (2001) 025203.

[127] V. Rossi et al., "Analysis of the reaction gamma n —> p pi- in the first and second resonance regions," Nuovo Cim. **A13** (1973) 59–89.

[128] **Aachen-Bonn-Hamburg-Heidelberg-Muenchen** Collaboration, P. Benz et al., "Measurement of the reaction $\gamma d \to \pi^- pp$, and determination of cross-sections for the reaction $\gamma n \to \pi^- p$, at photon energies between 0.2-GeV and 2.0-GeV," Nucl. Phys. **B65** (1973) 158–209.

[129] M. Salomon, D. F. Measday, J. M. Poutissou, and B. C. Robertson, "Radiative Capture and Charge Exchange of Negative Pions on Protons at 27.4-MeV and 39.3-MeV," Nucl. Phys. **A414** (1984) 493–507.

[130] A. Bagheri, K. A. Aniol, F. Entezami, M. D. Hasinoff, D. F. Measday, J. M. Poutissou, M. Salomon, and B. C. Robertson, "The Reaction $\pi^- p \to \gamma n$ Below the Δ Resonance," Phys. Rev. **C38** (1988) 875–884.

[131] "INS Data Analysis Center." `http://gwdac.phys.gwu.edu/`.

[132] B. Strandberg et al., "Near-threshold π^- photoproduction on the deuteron," Phys. Rev. C **101** no. 3, (2020) 035207, `arXiv:1812.03023 [nucl-ex]`.

[133] R. J. Walker, T. R. Palfrey, R. O. Haxby, and B. M. K. Nefkens, "Absolute Positive Pion Photoproduction Cross Sections from Hydrogen," Phys. Rev. **132** (1963) 2656–2663.

[134] K. G. Fissum, H. S. Caplan, E. L. Hallin, D. M. Skopik, J. M. Vogt, M. Frodyma, D. P. Rosenzweig, D. W. Storm, G. V. O'Rielly, and K. R. Garrow, "Inclusive positive pion photoproduction," Phys. Rev. **C53** (1996) 1278–1289.

[135] **GDH, A2** Collaboration, J. Ahrens et al., "Helicity dependence of the $\gamma p \to N\pi$ channels and multipole analysis in the Δ region," Eur. Phys. J. **A21** no. 2, (2004) 323–333.

[136] E. Epelbaum, H. Krebs, and U.-G. Meißner, "Improved chiral nucleon-nucleon potential up to next-to-next-to-next-to-leading order," Eur. Phys. J. **A51** no. 5, (2015) 53, `arXiv:1412.0142 [nucl-th]`.

[137] W. H. Press, S. A. Teukolsky, W. T. Vetterling, and B. P. Flannery, "Numerical Recipes in FORTRAN: The Art of Scientific Computing,".

[138] J. Nieves and E. Ruiz Arriola, "Error estimates for pi pi scattering threshold parameters in chiral perturbation theory to two loops," Eur. Phys. J. A **8** (2000) 377–384, `arXiv:hep-ph/9906437`.

[139] C. Fernandez-Ramirez and A. M. Bernstein, "Upper Energy Limit of Heavy Baryon Chiral Perturbation Theory in Neutral Pion Photoproduction," Phys. Lett. **B724** (2013) 253–258, `arXiv:1212.3237 [nucl-th]`.

[140] S. S. Kamalov, S. N. Yang, D. Drechsel, O. Hanstein, and L. Tiator, "Gamma* N —> Delta transition form-factors: A New analysis of the JLab data on p (e, e-prime p) pi0 at Q**2=(2.8-(GeV/c)**2 and 4.0-(GeV/c)**2)," Phys. Rev. C **64** (2001) 032201, `arXiv:nucl-th/0006068`.

[141] S. Kamalov, G.-Y. Chen, S.-N. Yang, D. Drechsel, and L. Tiator, "Pi0 photoproduction and electroproduction at threshold within a dynamical model," Phys. Lett. B **522** (2001) 27–36, `arXiv:nucl-th/0107017`.

[142] L. Alvarez-Ruso, Y. Hayato, and J. Nieves, "Progress and open questions in the physics of neutrino cross sections at intermediate energies," New J. Phys. **16** (2014) 075015, `arXiv:1403.2673 [hep-ph]`.

[143] V. Bernard, N. Kaiser, and U.-G. Meissner, "Threshold neutral pion electroproduction in heavy baryon chiral perturbation theory," Nucl. Phys. A **607** (1996) 379–401, `arXiv:hep-ph/9601267`. [Erratum: Nucl.Phys.A 633, 695–697 (1998)].

[144] S. Schumann et al., "Radiative pi0 photoproduction on protons in the Delta+(1232) region," Eur. Phys. J. **A43** (2010) 269–282, `arXiv:1001.3626 [hep-ex]`.

[145] E. Korkmaz et al., "Measurement of the $\gamma p \to \pi^+ n$ reaction near threshold," Phys. Rev. Lett. **83** (1999) 3609–3612.

[146] D. A. McPherson, D. C. Gates, R. W. Kenney, and W. P. Swanson, "Positive Photopion Production from Hydrogen Near Threshold," Phys. Rev. **136** (1964) B1465–B1471.

[147] K. Liu. Ph. D. thesis, University of Kentucky, 1994.

[148] D. H. White, R. M. Schectman, and B. M. Chasan, "Photoproduction of Negative Mesons in Deuterium," Phys. Rev. **120** no. 2, (1960) 614.

[149] M. Wang. Ph. D. thesis, University of Kentucky, 1992.

[150] H. B. van den Brink et al., "The $^{13}C(\gamma, \pi^-)^{13}N$ reaction at $E_\gamma \approx 184$ MeV ($T_\pi \approx 41$ MeV)," Nucl. Phys. **A587** (1995) 657–674.

[151] P. Golubev et al., "Pion emission in H-2, C-12, Al-27(gamma pi+) reactions at threshold," Nucl. Phys. A **806** (2008) 216–229, `arXiv:0801.1498 [nucl-ex]`.

[152] J. Arends, N. Floss, A. Hegerath, B. Mecking, G. Noldeke, and R. Stenz, "Experimental Investigation of the Reaction ^{12}C (γ, π^0) X in the Photon Energy Range Between Threshold and 450-MeV," Z. Phys. A **311** (1983) 367.

[153] E. Mazzucato et al., "NEUTRAL PION PHOTOPRODUCTION ON CARBON NEAR THRESHOLD," Phys. Lett. B **185** (1987) 25–28.

[154] G. Koch et al., "Cross-sections and Angular Distributions for ^{12}C (γ, π^0)," Phys. Lett. B **218** (1989) 143–147.

[155] J. Bergstrom, "Photopion P wave multipoles near threshold from C-12 (gamma, pi0) and H-1 (gamma, pi0)," Phys. Rev. C **50** (1994) 2979–2994.

[156] R. W. Gothe, W. Lang, S. Klein, B. Schoch, V. Metag, H. Stroeher, S. J. Hall, and R. O. Owens, "Measurement of the elastic pi0 photoproduction cross-sections on C-12 and C-13," Phys. Lett. B **355** (1995) 59–64.

[157] J. Bergstrom, R. Igarashi, and J. Vogt, "Measurement of the ^{12}C(γ, π^0) reaction near threshold," Phys. Rev. C **55** (1997) 2923–2930.

[158] J. C. Bergstrom, R. Igarashi, and J. M. Vogt, "Measurement of the Li-6(gamma,pi0) reaction near threshold," Phys. Rev. C **59** (1999) 2588–2602.

[159] B. Krusche et al., "Photoproduction of pi0 mesons from nuclei," Eur. Phys. J. A **22** (2004) 277–291, `arXiv:nucl-ex/0406002`.

[160] M. G. Barnett, R. Igarashi, R. E. Pywell, and J. C. Bergstrom, "Near threshold (gamma, pi0) reactions for He-4 and C-12," Phys. Rev. C **77** (2008) 064601.

[161] A. Chumbalov, R. Eramzhian, and S. Kamalov, "Dwia in the Momentum Space for (γ, π^0) Reaction Near Threshold," Z. Phys. A **328** (1987) 195.

[162] J. C. Bergstrom, "Comparing the p wave multipoles for pi0 photoproduction with low-energy predictions," Phys. Rev. C **52** (1995) 1986–1991.

[163] D. Drechsel, L. Tiator, S. S. Kamalov, and S. N. Yang, "Medium effects in coherent pion photoproduction and electroproduction on He-4 and C-12," Nucl. Phys. A **660** (1999) 423–438, `arXiv:nucl-th/9906019`.

[164] M. Lenkewitz, E. Epelbaum, H. W. Hammer, and U.-G. Meissner, "Neutral pion photoproduction off ^3H and ^3He in chiral perturbation theory," Phys. Lett. B **700** (2011) 365–368, `arXiv:1103.3400 [nucl-th]`.

[165] M. Lenkewitz, E. Epelbaum, H. W. Hammer, and U. G. Meissner, "Threshold neutral pion photoproduction off the tri-nucleon to $\mathcal{O}(q^4)$," Eur. Phys. J. A **49** (2013) 20, `arXiv:1209.2661 [nucl-th]`.

[166] V. Bernard, N. Kaiser, and U.-G. Meissner, "Threshold pion photoproduction in chiral perturbation theory," Nucl. Phys. **B383** (1992) 442–496.

[167] E. Oset and W. Weise, "Photon Nucleus Scattering and Coherent π^0 Photoproduction in the Δ Hole Model," Nucl. Phys. A **368** (1981) 375–393. [Erratum: Nucl.Phys.A 402, 612–612 (1983)].

[168] T. Takaki, T. Suzuki, and J. H. Koch, "PHOTOPRODUCTION OF NEUTRAL PIONS TO DISCRETE NUCLEAR STATES," Nucl. Phys. A **443** (1985) 570–588.

[169] R. C. Carrasco, J. Nieves, and E. Oset, "Coherent (gamma, pi0) photoproduction in a local approximation to the delta hole model," Nucl. Phys. A **565** (1993) 797–817.

[170] S. Boffi and R. Mirando, "COHERENT PI0 PHOTOPRODUCTION NEAR THRESHOLD ON CLOSED SHELL NUCLEI," Nucl. Phys. A **448** (1986) 637–651.

[171] V. Bernard, N. Kaiser, and U.-G. Meissner, "Chiral symmetry and the reaction gamma p —> pi0 p," Phys. Lett. B **378** (1996) 337–341, `arXiv:hep-ph/9512234`.

[172] R. A. Eramzhian, M. Gmitro, S. S. Kamalov, and R. Mach, "NUCLEAR PION PHOTOPRODUCTION: A THEORY AND THE O-16 (GAMMA, PI+) N-16 (BOUND) EXAMPLE," J. Phys. G **9** (1983) 605–619.

[173] M. Gmitro, J. Kvasil, and R. Mach, "PION ELASTIC AND INELASTIC SCATTERING ON S D SHELL NUCLEI IN THE DELTA (33) RESONANCE REGION. COUPLED CHANNEL ANALYSIS," Phys. Rev. C **31** (1985) 1349–1359.

[174] M. Gmitro, S. S. Kamalov, and R. Mach, "Momentum Space Second Order Optical Potential for Pion Nucleus Elastic Scattering," Phys. Rev. C **36** (1987) 1105–1117.

[175] R. H. Landau, S. C. Phatak, and F. Tabakin, "Improved theoretical pion-nucleus optical potentials," Annals Phys. **78** (1973) 299–339.

[176] R. Mach, "Galileo Invariant Theory of Low-energy Pion - Nucleus Scattering. Part 1.," Czech. J. Phys. B **33** (1983) 549.

[177] L. Tiator, A. K. Rej, and D. Drechsel, "FERMI MOTION AND OFF-SHELL EFFECTS IN THE REACTION HE-3 (GAMMA, PI+) H-3," Nucl. Phys. A **333** (1980) 343–356.

[178] R. A. Eramzhian, M. Gmitro, and S. S. Kamalov, "Momentum-space analysis of the nuclear partial transitions in the charged pion photoproduction," Phys. Rev. C **41** (1990) 2865–2877.

[179] L. Tiator and L. E. Wright, "Δ Resonance and Nonlocal Effects in Pion Photoproduction From Nuclei," Phys. Rev. C **30** (1984) 989.

[180] I. Sick and J. S. Mccarthy, "Elastic electron scattering from c-12 and o-16," Nucl. Phys. A **150** (1970) 631–654.

[181] F. Lenz, M. Thies, and Y. Horikawa, "ISOBAR HOLE DESCRIPTION OF PION NUCLEUS INELASTIC SCATTERING," Annals Phys. **140** (1982) 266–340.

[182] M. Pfeiffer. Diploma Thesis, Giessen U., 1988.

[183] R. W. Gothe. Ph.D. thesis, University of Mainz, 1990.

[184] V. V. Burov and V. K. Lukyanov Preprint JINR-P4-11098, Dubna (1977) .

[185] J. B. Flanz, R. S. Hicks, R. A. Lindgren, G. A. Peterson, A. Hotta, B. Parker, and R. C. York, "Convection currents and spin magnetization in $e2$ transitions of ^{12}C," Phys. Rev. Lett. **41** (Dec, 1978) 1642–1645. `https://link.aps.org/doi/10.1103/PhysRevLett.41.1642`.